University of Nevada, Reno

Degradation of Structural Alloys in Molten LiCl-Li_2O-Li

A dissertation submitted in partial fulfillment of the requirements for the degree of Doctor of Philosophy in Materials Science and Engineering

By

William Phillips

Dr. Dev Chidambaram - Dissertation Advisor

May 2019

THE GRADUATE SCHOOL

We recommend that the dissertation
prepared under our supervision by

WILLIAM C PHILLIPS

Entitled

Degradation Of Structural Alloys In Molten LiCl-Li2O-Li

be accepted in partial fulfillment of the
requirements for the degree of

DOCTOR OF PHILOSOPHY

Dev Chidambaram, Advisor

Nicholas Tsoulfanidis, Committee Member

Dhanesh Chandra, Committee Member

Qi An, Committee Member

Miles Greiner, Graduate School Representative

David W. Zeh, Ph. D., Dean, Graduate School
May, 2019

Abstract

The necessity to curtail carbon emissions to limit anthropogenic climate change is at odds with the continued increase in energy demand caused by economic and population growth in the developing world. In order to simultaneously increase the standard of living for billions of people while limiting greenhouse gas emissions, it is necessary to develop and implement carbon free sources of energy on a large scale. Such energy sources should cover increases in capacity and replace legacy coal and nuclear power plants. Nuclear fission provides a powerful, compact, and reliable source of electricity and process heat. However, the long-term storage of nuclear waste poses a number of environmental and nuclear weapons proliferation concerns. Reprocessing of used nuclear fuel (UNF) offers the promise of reducing both the longevity and volume of waste, while simultaneously reducing nuclear security concerns and increasing the energy generated by a given quantity of mined uranium.

Pyroprocessing technology has been developed to separate the fission products from the remaining actinide elements using electrochemical separations in a molten salt electrolyte. The incorporation of oxide based nuclear fuels from light water reactors requires the reduction of this material to a metallic form. Currently, the state-of-the-art process for this reaction is electroreduction in a molten LiCl-Li_2O electrolyte maintained at 650°C. In order to achieve a high reduction efficiency, the applied potential necessarily surpasses the reduction potential of Li_2O, causing the formation of metallic Li at the cathode. As metallic

Li is soluble in molten LiCl, the electrolyte becomes a ternary mixture of LiCl, Li_2O, and Li. While the increasing concentration of Li during the electrolytic reduction of UNF has been widely observed, little work has been performed thus far to investigate the effect of metallic Li on the corrosion of the structural materials used to contain the electrolyte. This is the first study to explore the long-term effect of metallic Li dissolved in LiCl-Li_2O on alloys.

Knowledge of the corrosion rate of a material in a given environment is necessary in order to accurately predict the expected lifetime of a component, thus preventing expensive and potentially hazardous failures. As such, the work presented in this dissertation was performed to elucidate the corrosion mechanisms and the rate of material degradation of structural materials during extended exposure to molten LiCl containing varying concentrations of Li_2O and Li. Stainless Steel 316L (SS316L) was studied since the current containers for engineering scale oxide reduction processing are constructed of this material. Inconel 625 (I625) was also studied as an alternative to SS316L due to its high temperature corrosion performance in other systems, and previous short-term studies that have shown good performance in the LiCl-Li_2O-Li system. Duplicate samples of each material were exposed to molten LiCl containing 1 or 2wt% Li_2O and 0, 0.3, 0.6, or 1wt%Li for periods of 500 and 1000 hours, at a temperature of 650°C inside an Ar glovebox. Post exposure analysis of the sample surfaces was conducted via scanning electron microscopy (SEM) coupled with energy dispersive X-ray analysis (EDS) and focused ion beam (FIB) milling, X-ray diffraction, X-ray photoelectron spectroscopy, and Raman spectroscopy. SEM-

EDS analysis was also performed on the sample cross section after both FIB milling and mechanical cross sectioning.

Both SS316L and I625 formed a protective oxide layer composed primarily of $LiCrO_2$ in the absence of metallic Li, which limited the degradation of both alloys. However, the presence of metallic Li in the molten salt solution prevented the formation of this protective oxide layer, resulting in extensive attack of the base materials. In both cases, selective dissolution of minor alloying elements was observed. In SS316L, intergranular attack of the base alloy resulted from the selective dissolution of Cr, Mo, and Mn, while I625 showed the selective dissolution of Cr, Mo and Nb, and a porous, Ni foam like microstructure was observed. Corrosion rates were approximately an order of magnitude greater in the tertiary LiCl-Li_2O-Li electrolyte than observed in LiCl-Li_2O in the absence of Li. Thus, these results should be taken into consideration when designing systems for the oxide reduction of UNF.

Acknowledgements

I thank my advisor Dr. Dev Chidambaram for providing me the opportunity to grow as both a researcher and as an individual over the course of my graduate studies. His guidance has been invaluable to my academic and personal development, and I am grateful to have had the pleasure of working with him over the last several years.

I acknowledge my committee members: Professors Nicholas Tsoulfanidis, Dhanesh Chandra, Qi An, and Miles Greiner for taking the time to assist me in my pursuit of higher education and for their invaluable comments and suggestions. Specifically, I also thank Professor Tsoulfanidis for inspiring my passion in nuclear energy and for the wisdom and experience he has shared with me and countless other students during his distinguished tenure as a professor of nuclear engineering. I also thank Professor Chandra for the wealth of knowledge on materials and metallurgy that he has imparted to me while I have been his student, and also for his compassion and good-hearted nature. To be able to study under such great minds is truly an honor.

The funding for this work was provided by the Department of Energy (DOE) under contracts DE-NE0008262 and DE-NE0008236, and the US Nuclear Regulatory Commission (NRC) under contracts NRCHQ-11-G-38-0039 and NRC-HQ-13-G-38-0027. I acknowledge the Fellowship Award from the USNRC. Dr. Kenny Osborne serves as the program manager for the DOE award and Ms. Nancy Hebron-Isreal serves as the grants program officer for the NRC awards.

Additionally, I thank my colleagues with whom I have had the pleasure of sharing time with while working in the Materials and Electrochemistry Research Lab: Dr. Augustus Merwin, Dr. David Rodriguez, Dr. Ruchi Gakhar, Dr. Akira Nordmeier, Dr. Thorunn Snorradottir, Zachary Karmiol, Sarah Yang, Kodi Summers, Vickram Singh, Mary Lou Lindstrom, McKenzie Parker, James Mulcahey, Christopher Bruneau, Gabrielle Blanchard, Gabriel Martins, and the numerous undergraduate students as well. Their knowledge, experience, humor, and friendship are what have made it possible for me to accomplish what I have over the course of this work. Specifically, I thank Gus for laying the groundwork for my studies and for his friendship during our shared time at the lab, and Zach for his friendship and unwavering dedication to do the right thing.

Most importantly, I thank my family for their unconditional love, support, and encouragement throughout my life. It is because of them that I am here, and it is because of the opportunities that they have given me that I am who I am now. I thank them from the bottom of my heart.

Contents

List of Figures

List of Tables

Scholarly Work

Publications

6) Phillips, W., & Chidambaram, D., Corrosion of Stainless Steel 316L in molten LiCl-Li2O-Li. Journal of Nuclear Materials 517, 241-253, (2019)

5) Phillips, W., Karmiol, Z., & Chidambaram, D., Effect of metallic Li on the Corrosion Behavior of I625 in Molten LiCl-Li2O-Li, Journal of the Electrochemical Society, 166 (6) C162-C168, (2019)

4) Phillips, W., & Chidambaram, D., Effect of metallic Li on the Surface Chemistry of I625 Exposed to LiCl-Li_2O-Li, Journal of the Electrochemical Society, 166 (11) C3193-C3199, (2019)

3) Phillips, W., Merwin, A. & Chidambaram, D. On the Corrosion Performance of Monel 400 in Molten LiCl-Li2O-Li at 923 K. Metallurgical and Materials Transactions A 49, 2384-2392, (2018).

2) Merwin, A., Phillips, W, Williamson, M.A., Willit, J.L., Motsegood, P.N., & Chidambaram, D. Presence of Li Clusters in Molten LiCl-Li. Scientific Reports 6, 25435, (2016).

1) Phillips, W. Corrosion behavior of Monel 400 and electrochemical performance of Li-Bi reference electrode in molten LiCl-Li2O-Li. Master's Thesis, Materials Science and Engineering, University of Nevada, Reno (2015)

Professional Presentations

6) W. Phillips, and D. Chidambaram, 'Long-term corrosion testing of Inconel alloy 625 in molten LiCl-Li2O-Li,' 233rd Meeting of the Electrochemical Society, Seattle, WA, May 13-17 (2018)

5) W. Phillips, and D. Chidambaram, 'Long-term corrosion performance of stainless steel 316 in molten LiCl-Li2O-Li' in Session C03: State-of-the-Art Surface Analytical Techniques in Corrosion 3: in Honor of Hugh Isaacs – Spectroscopy and Characterization 3 of the 232nd Meeting of the Electrochemical Society, National Harbor, MD, October 1-5 (2017).

4) W. Phillips, A. Merwin, V. Singh, and D. Chidambaram, 'Characterization of the Electrochemical Behavior of a Li-Bi Reference Electrode for the

Molten LiCl-Li' in Session L02: Molten Salts and Ionic Liquids 20 – Materials of the 230th Meeting of the Electrochemical Society, Honolulu, HI, October 2-7 (2016).

3) A. Merwin, W. Phillips, and D. Chidambaram, 'On the Formation of Clusters of Li8 in Molten Solutions of LiCl-Li' in Session L02: Molten Salts and Ionic Liquids 20 – Solute and Solvent Properties II of the 230th Meeting of the Electrochemical Society, Honolulu, HI, October 2-7 (2016).

2) W. Phillips, A. Merwin, and D. Chidambaram, Electrochemical Performance of the Li-Bi Reference Couple in Molten LiCl-Li2O-Li, Abstract number 969 in High Temperature Corrosion in Complex Environments, Session of the 229th Meeting of the Electrochemical Society, San Diego, May 29th-June 2nd (2016).

1) W. Phillips, A. Merwin, and D. Chidambaram Corrosion behavior of Monel 400 in Molten LiCl-Li2O-Li, Abstract number 970 in High Temperature Corrosion in Complex Environments, Session of the 229th Meeting of the Electrochemical Society, San Diego, May 29th-June 2nd (2016).

Chapter 1 : Introduction

1.1: Global Energy Needs

Throughout human history, increased standards of living have directly correlated to increased energy usage. The industrial revolution exploited the vast quantities of energy contained in the hydrocarbons of fossil fuels, which has allowed for the improvements in quality of life, standard of living, and life expectancy that have occurred in the past two centuries. As the benefits of high energy consumption make their way to the developing regions of the world, total energy consumption continues to rise, along with economic prosperity. Combined with continued population growth, particularly in sub-Saharan Africa and Asia, global energy demand is projected by the International Energy Agency to increase by at least 50% between 2019 and 2040 [1].

As the scientific understanding of the earth's climate has grown, so too has our knowledge that the carbon emissions associated with the burning of fossil fuels have multiple deleterious effects on the environment [2]. Anthropogenic climate change is a direct result of the large quantities of fossil fuels that have been burned for energy production and their associated carbon emissions over the past two centuries. In order to limit the rise in global average temperatures, a concerted global effort to limit greenhouse gas emissions is necessary. Technologies such as wind, solar, geothermal, hydro, and nuclear power are capable of providing vast quantities of carbon free energy, and growth in generation capacity for all of these resources must occur over the next few

decades if we are to successfully curtail the worst predictions of climate scientists.

1.2: Nuclear Energy

While renewable energy sources such as wind, solar, geothermal, and hydro power should all be implemented to the full extent possible, they all have limitations: wind and solar are intermittent and unreliable, while geothermal and hydroelectric are highly localized. Full decarbonization of the world energy supply necessitates the inclusion of nuclear in the mix, due to its high reliability, energy density, safety, and baseload power capability [3, 4]. In addition to growth in production capacity to account for increased energy demand, it is also necessary to replace generating capacity that is being phased out, such as legacy nuclear plants that are reaching their design lifetimes, and coal fired power plants. Nuclear power is uniquely suited to supplying the baseload demand due to its high average capacity factor and the economy of operation once installed [4].

1.3: Used Nuclear Fuel

Along with concerns over the possible proliferation of nuclear weapons, long term storage of used nuclear fuel (UNF) is an issue that must be dealt with in an environmentally responsible way. The back end of the fuel cycle is an essential component of a sustainable and environmentally responsible nuclear industry, but is often hampered by concerns of nuclear weapons proliferation and unfavorable economics. Currently, the preferred solution to deal with UNF is to

deposit the fuel in a geologic repository, where it should be maintained undisturbed and intact until the residual radioactivity decays to background levels. Due to the high levels of transuranic (TRU) isotopes present in UNF such as Pu^{239} and Am^{241} and their long half-lives, this means a once through fuel cycle will necessitate the assurance of safe storage for tens of thousands of years [4]. Concerns with our abilities to design for these time frames has meant that the licensing of a permanent geological storage facility has been beset with controversies since the beginning of the nuclear industry in the U.S. [5]

1.4: Reprocessing

While a once through fuel cycle results in extremely long-lived waste, it is possible to separate the TRU elements and unburned uranium from UNF through chemical and metallurgical means and recycle them into freshly fabricated fuel for use in a suitably designed reactor. The so-called closed fuel cycle with complete recycle of transuranic elements theoretically results in a decrease in the longevity of the final waste form from tens of thousands of years to approximately 300 years, while simultaneously reducing the volume stored by a factor of 20 and increasing the energy extracted from a given amount of mined material, although this has yet to be implemented commercially [5, 6].

Two general methods for reprocessing have been developed. The first process developed was the plutonium-uranium redox extraction (PUREX) process, which is based on aqueous chemical separations. PUREX was developed as part of the Manhattan project for the production of high purity

plutonium for weapons cores [4]. Consequently, this process poses a significant proliferation risk due to the stream of pure fissile material. Despite this, both France and Japan have developed commercial reprocessing capabilities based on the PUREX process, and have successfully demonstrated the ability to recycle a significant amount of the fissile inventory of UNF through the use of mixed oxide (MOX) fuel. Unfortunately, the neutronic limitations of thermal spectrum light water reactors (LWR) limit the ability to continually reprocess MOX fuel due to the buildup of the heavier TRU isotopes, meaning that complete recycle of all TRU is not possible without the implementation of other reactor types [4].

1.5: The Integral Fast Reactor and Pyroprocessing

The integral fast reactor (IFR) concept was conceived by Argonne National Laboratory (ANL) in the 1970's as a way to close the nuclear fuel cycle at a single site via the use of a sodium cooled fast reactor (SFR) using metallic fuel and an on-site fuel processing plant to reprocess used fuel and manufacture new fuel for reuse in the reactor [5, 6]. The reprocessing technology was based on molten salt electrochemical methods, and the central operation was termed the electro refiner (ER). Fast spectrum reactors operate without the use of a moderator, and fission occurs primarily via high energy neutron capture. This allows for the efficient burning of fertile as well as fissile heavy isotopes.

The experimental breeder reactor 2 (EBR-II) was built at the desert site of ANL West, which is now the current location of Idaho National Laboratory (INL).

EBR-II served as the reactor for the IFR concept, with a hot cell built adjacent to the reactor that included the operations necessary to take fuel from the reactor core, de-clad the sodium bonded fuel, reprocess the fuel and cast new fuel rods. By all accounts, the IFR project was successful in demonstrating the technical viability of a closed fuel cycle based on a SFR and molten salt based reprocessing technologies [5, 6].

1.6: Electroreduction of Used Nuclear Fuel in LiCl-Li_2O-Li

Molten salt based pyrochemical reprocessing methods necessitate a metallic feedstock in order to facilitate the separation of U and TRU from the fission products. Consequently, the reduction of UO_2 is an important head-end process for the incorporation of oxide used nuclear fuel (UNF) into a pyrometallurgical-based fuel cycle. The most widely researched UNF reduction method is a high temperature, molten salt based electrochemical reduction process that was originally developed by ANL [7, 8]. In addition to ongoing work at ANL, this technology is currently being investigated by researchers at INL, the Korean Atomic Energy Research Institute (KAERI) in South Korea, the Central Research Institute of Electric Power Industry (CRIEPI) in Japan, the Indira Gandhi Center for Atomic Research (ICGAR) in India, and at a small number of research universities in the United States.

The electroreduction of UO_2, as well as various fission products and actinide oxides, is accomplished by loading de-clad UNF pellets into a stainless steel 316L (SS316L) basket, which is then immersed in a molten LiCl-Li_2O

electrolyte maintained at 650°C. The fuel basket is then cathodically polarized against an anode made of suitable material, typically Pt. A reference electrode is employed for accurate monitoring of the applied potentials and process control. A schematic diagram of the this process is shown in Figure 1.1 [9].

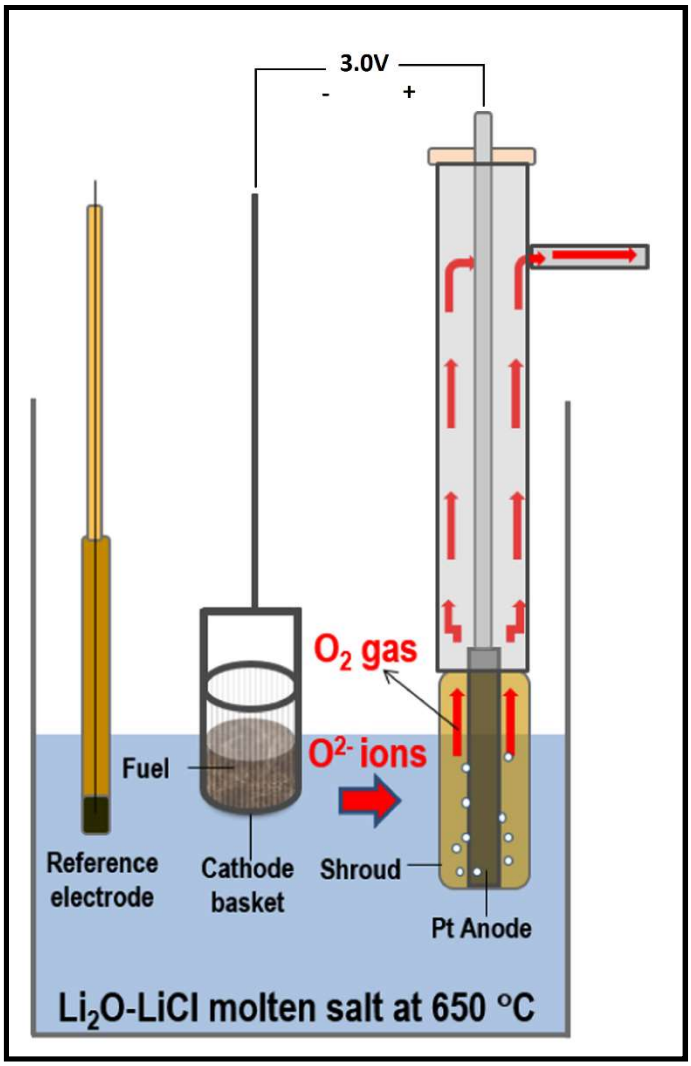

Figure 1.1: Schematic diagram of the electroreduction process for UNF [9].

The applied potential must be beyond the reduction potential of UO_2, which is -2.40V vs. Pt. During the first stage of the reduction process, the

reduction of UO_2 proceeds directly via an electrochemical reduction pathway represented by the half-cell reactions given in Equations 1 and 2:

$$Cathode:\ U^{4+} + 4e^- \rightarrow U \quad (1)$$

$$Anode:\ 2O^{2-} \rightarrow O_2 + 4e^- \quad (2)$$

The reduction of UO_2 begins at the edge of the basket, and progresses radially inward [10, 11]. As the reduction proceeds, the process becomes diffusion limited and the over-potential required to maintain a desired current increases during galvanostatic operation [10, 11]. This increasing over-potential eventually reaches the reduction potential of Li_2O, which is at -2.47V vs. Pt. Attempts to completely reduce UO_2 to metallic form potentiostatically below the reduction potential of Li_2O have been unsuccessful at producing acceptable yields [8, 12]. Consequently, metallic Li is generated at the cathode as the reduction proceeds. This metallic Li acts as an additional chemical reduction pathway for UO_2, represented by Equation 3 [8]:

$$UO_2 + 4Li \rightarrow U + 2Li_2O \quad (3)$$

It has been suggested that in theory, if the applied electrolytic current is interrupted upon completion of the reduction of UO_2, minimal excess Li will be produced, as Li will be consumed quickly in the presence of UO_2 via Reaction 3. However, a reliable method to determine the correct cutoff point has not yet been devised, and the typical practice is to terminate the process when approximately 150-200% of the theoretical charge required for the complete reduction of UO_2 has been passed [13]. This has been shown by leading researchers in the U.S.

and Korea to be effective at producing a high reduction yield [8, 14]. Additionally, the underpotential deposition (UPD) of Li at the surface of U_3O_8 at potentials more noble than required to reduce bulk Li has been reported to occur, indicating that the generation of some quantity of Li may be unavoidable [15].

Unfortunately, the presence of metallic Li in the system introduces complications in materials compatibility and solution chemistry that must be taken into account during the design and operation of an electroreduction cell. Due to the non-zero solubility of Li in LiCl, some of the Li generated at the cathode dissolves into the electrolyte, forming a ternary LiCl-Li_2O-Li system, the properties of which differ greatly from LiCl-Li_2O [13, 16, 17]. As stated above, significant quantities of Li are generated *in-situ*, and as such, it can be assumed that the electrolyte is saturated with Li after extended periods of operation. The nature of the dissolution mechanism of Li in LiCl has been debated in the literature. In addition to physical dissolution via Bredig's F^- centered model [18], some researchers have hypothesized a colloidal suspension or metal fog [19, 20], while others have suggested the presence of excessively reduced sub-halide compounds such as Li_2Cl [21]. Sub-halide compounds have been shown to be present in other molten metal-halide salt systems where the salt cation is identical to the dissolved metal, as is the case with Bi-BiI_3 [18]. Previous work by our group detected the presence of Li_8 nanoclusters in LiCl-Li_2O-Li solutions at 650° via *in-situ* Raman spectroscopy, and hypothesized that the dipole of the Li_8 nanocluster structure is responsible for the colloidal dissolution of Li into LiCl-Li_2O [22]. The possible presence of multiple dispersion mechanisms in addition

to physical dissolution may partially explain the difficulty other researchers have experienced while attempting to quantify the solubility limit of Li in LiCl, which has been shown to vary depending on differences in experimental parameters employed, such as agitation and sampling technique [17]. Although the absolute limit of Li dispersion in LiCl is not known and may not be possible to quantify, 0.3wt%Li is a useful approximation for the apparent solubility limit [17, 20, 23, 24]. While the dissolution mechanism of Li in LiCl is not the focus of this work, it is useful to understand the nature of the solution chemistry to inform the experimental design and interpret the results of the present investigation.

The generation of Li concurrently with the reduction of UO_2 also leads to current inefficiencies and consumption of Li_2O as the process proceeds [17]. Upon dissolution into the electrolyte, Li can spontaneously recombine with the O_2 generated at the anode, resulting in a reduction in efficiency. Dissolved Li can also be consumed through reaction with most other oxides present in the system, such as MgO anode shrouds and reference electrode sheaths, or the oxide layers on alloy surfaces [17, 25]. Additionally, the presence of Li in LiCl increases its electrical conductivity, allowing electrons to pass from the anode to the cathode directly through the salt. Any electron that passes through the electrolyte directly will not contribute to the reduction of UO_2 and thus reduces current efficiency. The combination of all of these effects are responsible for the necessity for passing large excess charge beyond that predicted theoretically.

The presence of dissolved Li also leads to challenges with the degradation of materials that must come into contact with the electrolyte. Common engineering ceramics such as Al_2O_3 and MgO [17, 26, 27] have been shown to undergo severe degradation when exposed to LiCl-Li_2O-Li solutions, while ZrO_2 has been shown to be reduced to a combination of Zr and Li_2ZrO_3 in LiCl-1wt%Li_2O melts [28]. The corrosion of structural alloys is also greatly affected by the presence of Li metal, and is the primary focus of this dissertation. The following discussion is intended to offer background on the processes responsible for the corrosion of metals in molten salts and liquid metals.

1.7: Corrosion in Molten Salts

Understanding of the effect the solution chemistry has on materials exposed to the molten LiCl-Li_2O-Li system is important for the safe and economical design of vessels and other components for use during the electrolytic reduction of used nuclear fuel. Fortunately, much work has been conducted on corrosion of materials used for the construction of molten salt reactors (MSR), particularly during the molten salt reactor experiment (MSRE) of the 1960's and 1970's, and this work can serve to inform the present study.

The high temperature molten salt environment of MSRs and other molten salt systems imposes severe demands on the corrosion performance of the materials used to construct the vessels and components exposed to the salt. Fluoride salts are typically considered as the fuel and/or coolant salts due to their favorable neutronic properties [29, 30], however, some newer designs for fast

spectrum MSRs are focused on isotopically enriched chloride salts [31]. Consequently, much of the discussion below uses fluoride salts as examples, but these concepts are generally applicable to corrosion in chloride salts. Typically, the molten salt in a salt fueled MSR is composed of fluorides of Li, Be, Zr, or Na, with additions of UF_3/UF_4, ThF, as well as the fluorides of the fission products that form stable compounds with fluorine [29, 30]. Temperatures in typical MSR designs routinely exceed 550°C, with some designs, such as the very high temperature reactor (VHTR), exceeding 850°C during routine operation to achieve higher thermodynamic efficiency and provide high temperature process heat for chemical facilities [32]. Consequently, it is critical that the corrosion mechanisms affecting structural materials be well understood and the corrosion rate of these alloys be minimized prior to the construction of a reactor. The following sections highlight the different mechanisms by which corrosion occurs and the ways in which a material can be designed to withstand these conditions. Emphasis is placed on the corrosion of Hastelloy-N in molten LiF-BeF_2, as this system has been the subject of the majority of corrosion studies in molten salts. LiF-NaK-KF and LiCl-NaCl molten salts have also been proposed and tested for MSR primary and secondary loop service. There are many similarities between the corrosion behavior of alloys in these salts and LiF-BeF_2 salts, which have been studied extensively, but there are important departures for each class of molten salt that bear on the selection of container materials, the development of cleaning procedures and on the development of chemistry controls.

1.7.1: Corrosion - Thermodynamic Considerations

The high temperatures in these molten salt systems accelerate the kinetics of reaction between the salt and the reactor materials. Additionally, molten fluoride and chloride salts both act as a flux to remove most oxide layers present on the surface of a material, largely negating the usefulness of the protective surface oxides of active elements such as Cr, Al, or Si typically relied on for corrosion protection for stainless steels and many nickel alloys [33]. Consequently, corrosion typically occurs rapidly at the beginning of exposure to molten salts as the oxide layers dissolve into the solution and impurities are consumed. Table 1.1 gives the Gibbs free energy of formation for various fluoride compounds of interest for MSR designs, with salt fluoride compounds given in the left two columns, and fluoride compounds of common alloying elements given in the right two columns [33].

Table 1.1 Gibbs free energies of formation per mole of fluorine for various fluoride compounds at 727°C (* indicates value is at 754°C). Compounds with more negative Gibbs free energies of formation are more thermodynamically stable and are likely to form at the expense of compounds with less negative Gibbs free energies of formation (6).

Compound	ΔG_f Kcal/mol·F	Compound	ΔG_f Kcal/mol·F
LiF	-125	AlF_3	-90
MgF_2	-113	CrF_2	-75.2
NaF	-112	CrF_3	-72.3
RbF	-112	FeF_2	-66.5
KF	-109	FeF_3	-60.6*
BeF_2	-104	WF_6	-56.8
ZrF_4	-94	NiF_2	-55.3
HF	-66.2	MoF_3	-52.5*

Thermodynamically, compounds with more negative free energies will form more readily than compounds with less negative free energies. Consequently, once the initial surface oxide layer is removed from the alloy, corrosion proceeds by attack of the most active element in the material. This was observed during the material exposure tests performed concurrently with the Aircraft Reactor Experiment (ARE), where the corrosion rate of the alloys studied was directly proportional to the chromium content in the alloy [29, 30, 34]. This led to the reduction of chromium contents in the composition of Hastelloy-N, which was developed following the ARE, to levels just sufficient to provide

adequate resistance to corrosion in the high temperature air environment experienced outside of the reactor vessel [29, 30].

1.7.2: Corrosion – Impurity Effects

Although pure fluoride and chloride salts are thermodynamically stable with respect to container materials, and corrosion is minimal in these conditions, small amounts of impurities present during the preparation or introduced during the processing of the salt can greatly impact the corrosion rates observed. Impurities such as water, oxygen, or hydroxides can be present in the salt if proper purification techniques are not followed. These impurities can produce HF or HCl through the reactions given below, which is a highly corrosive acid and will rapidly etch structural materials [33]. Here, Me is used to represent any metallic element.

$$MeF(l) + H_2O(g) = MeOH(l) + HF(g) \quad (4)$$

$$2MeF(l) + H_2O(g) = MeO(l) + 2HF(g) \quad (5)$$

Impurities of Ni and Fe fluorides present in the salt due to the manufacturing process can react with Cr present in the alloy due to the thermodynamic considerations listed above and lead to accelerated corrosion at the beginning of exposure [33]. Fortunately, the effects of impurities are limited to the initial exposure to the molten salt environment, and after the initial period of rapid corrosion during which time the impurities are consumed, the corrosion rate settles to a slow and stable rate that is limited by the diffusion of Cr to the surface [30, 33, 35].

1.7.3: Corrosion – Thermal Gradients

The large temperature gradients inherent to a MSR can also lead to corrosion problems. Since the solubility limits of the corrosion products in a molten fluoride are highly temperature dependent, it has been observed that there can be mass transport loops that develop in the MSR from areas of high temperature to areas of low temperature [30, 33]. The cold areas, such as heat exchangers, act as sinks where precipitation and accumulation of corrosion products occur. Thus, the concentration of the corrosion products in the system is limited by the solubility limit in the cold side of the loop. Consequently, the solubility limit in the hot side is never reached, leading to a continuous flux of material from the hot side of the reactor to the cold side. In addition to the constant level of corrosion experienced on the hot surfaces in the reactor, the buildup of precipitated corrosion products in the heat exchanger can impede the flow of coolant, causing blockages and possibly localized salt freezing [30, 33]. While this is less of a concern in the batch processes employed during pyroprocessing, large vessels containing many kilograms of molten salt will inherently have some temperature gradient that may play a minor role in the corrosion of the vessel.

1.7.4: Corrosion – Dissimilar Materials

The use of dissimilar materials within a MSR is unavoidable in practice, as the moderator will be constructed of graphite, and there will be at least one metallic alloy used to construct the reactor vessel, piping, and other ancillary

equipment. The use of multiple alloy compositions and/or other materials, such as SiC composites for heat exchangers, is likely [36]. In the oxide reduction operation, the majority of components can be constructed from a single alloy, with the primary exception being the anode which is typically a noble metal such as Pt. The effects that the use of dissimilar materials have on the corrosion mechanisms at play in a reactor have been studied, however, the full extent to which these material choices affect the long term performance of reactor materials is not certain [30, 33].

Activity gradients caused by the presence of dissimilar materials can lead to the depletion of an element from an alloy with high concentration and deposition of that element on another alloy with low concentration of the element of interest. This mechanism can accelerate corrosion of the alloy with high activity, and lead to preferential leaching of specific elements. Another possibility is the formation of compounds that are thermodynamically more stable than the constituent species, as has been observed with the formation of chromium carbides on the surface of graphite when both graphite and Cr containing alloys are exposed to the same melt [33]. This mechanism acts as a sink for Cr, leading to the depletion of Cr from the base alloy at accelerated rates.

1.7.5: Corrosion – Redox control

By controlling the oxidation state of species in the salt with multiple soluble valence states, for example U which can form UF_3 and UF_4 corresponding to U^{3+} and U^{4+}, respectively, it is possible to control the aggressiveness of the corrosive

attack by the salt on the container materials [33]. The control of the oxidation state of the salt changes the electrochemical potential of the salt, and is termed the redox control. The Nernst equation relates the ratio of oxidation states to electrochemical potential, as shown below in equations 6 and 7.

$$M^{n+} + ne^- \leftrightarrow M \quad (6)$$

$$E = E^0 + 2.3 * \frac{RT}{nF} \log\left(\frac{[M^{n+}]}{[M]}\right) \quad (7)$$

By controlling the ratio of U^{3+}/U^{4+} it is possible to favor reducing conditions, whereby the corrosive attack of the salt on container materials is reduced [36]. However, it is important that the conditions do not become so reducing that the precipitation of dissolved species becomes problematic, such as is the case with the formation of uranium carbide compounds under highly reducing conditions [33]. The ideal ratio whereby corrosion and precipitation were both minimized was found to be a U^{3+}/U^{4+} ratio of 0.005 to 0.06 [30]. This corresponds to a U^{4+}/U^{3+} ratio of 200-16:1. Figure 1.2 shows clearly how the redox potential of the salt affects the intensity of intergranular cracking observed on Hastelloy-N [36].

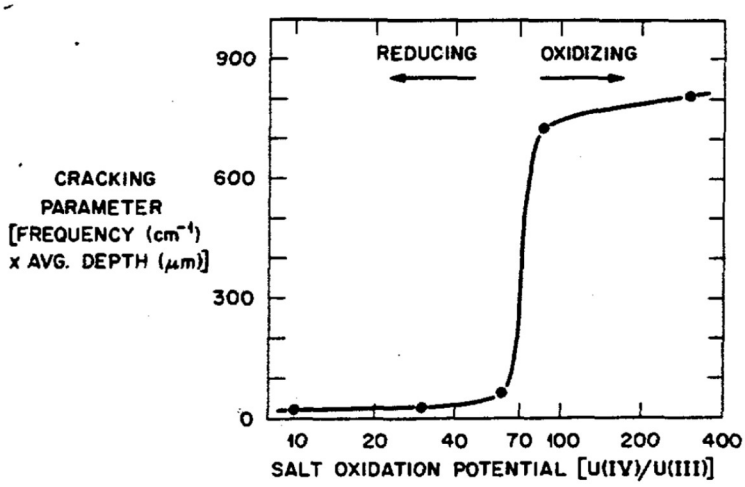

Figure 1.2: Crack intensity as a function of salt oxidation potential. The ratio of U^{4+}/U^{3+} is highly influential on the corrosive behavior of

1.7.6: Corrosion – Tellurium based intergranular corrosion and embrittlement

An important and unforeseen corrosion problem encountered during the MSRE was the reaction of the base alloy with fission products contained in the fuel salt, most notably Te [30]. As a chalcogen, Te exhibits similar properties to Se, S, and O, and readily forms compounds with negative valence states, however, it is somewhat unique in that it can also form compounds where it has a positive charge. In fluoride salts, Te forms compounds with Ni and Cr through the reactions given in equations 8 and 9 below due to the instability of tellurium fluoride [33].

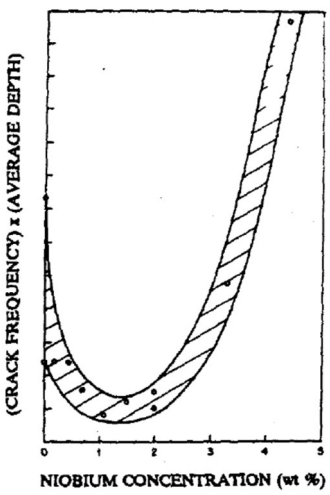

Figure 1.3: Effect of Nb concentration on the observed crack severity in modified Hastelloy-N compositions following exposure to tellurium. The ideal fraction of Nb in the alloy is between 1-2wt% (8).

$$xTe + yNi \rightarrow Ni_yTe_x \quad (8)$$

$$xTe + yCr \rightarrow Cr_yTe_x \quad (9)$$

These reactions occur preferentially at the grain boundaries, leading to intergranular corrosion and stress corrosion cracking that significantly weakens the alloy.

The deleterious effects of Te on the long term performance of Hastelloy-N and other Ni base alloys lead to development efforts at ORNL to minimize the effects of Te [36]. Two methods were found to be effective at limiting the crack

intensity: redox control to keep the salt under reducing conditions, and the addition of Nb as an alloying element at concentrations between 1-2wt%, as shown in Figure 1.3 [36]. The redox control method limits the formation of Te compounds by limiting the potential for oxidation in the system, while the mechanism by which Nb acts to limit the effects of Te induced cracking is not entirely known, but one possible explanation is the formation of Nb_xTe_y surface layers on the alloy preferentially to the diffusion of Te into the grain boundaries [30]. These investigations indicated that the use of Nb modified Hastelloy-N in conjunction with redox control would sufficiently limit corrosion over the design lifetime of a MSR [30].

1.7.7: Corrosion in Chloride Molten Salts

Chloride molten salts have also been proposed for MSR service as they have high stability and low vapor pressures, and can provide a harder neutron spectrum than fluoride salts for fast reactor designs. Oak Ridge National Lab prepared a very comprehensive review of these salts properties for use in assessing their use for the NGNP heat transfer loop and their results are summarized here [37]. The corrosion databases for these classes of salts are insufficiently developed and contain data based upon salts with large and unquantified impurity inventories. There has not been extensive characterization of the effect of moisture and impurities on the corrosion of alloys in these salts and cleaning procedures have not been developed to the same standard as for fluoride salts, which had the advantage of being extensively developed through Oak Ridge National Laboratory's (ORNL) molten salt reactor experiment. In

addition to the unreliability of the data on corrosion in these salts due to impurity content, there is little high temperature data for corrosion with these salts above 800°C.

Chloride molten salts behave similarly to more common fluoride salts in that they flux passive layers from container walls and have a similar electrochemical sequence to fluoride salts. Despite this, passive oxide layers are in general more stable in chloride salts than in fluoride melts. There are many important differences in corrosion chemistry however, and chloride molten salts for MSR applications still require extensive exploration. The thermodynamic driving force for corrosion in Cl salts seems to be slightly greater that for fluoride salts based on a comparison of the free energy of formation of halide compounds, but it is noted that this analysis is highly simplistic and ignores deviations from ideal solution behavior; this is an area requiring further study. Additionally, there will be important differences in coordination chemistry as the most stable form of uranium is UCL_3 in chlorides and UF_4 in fluorides.

Extensive research is required to further characterize chloride molten salt corrosion behavior and interactions with candidate container materials. The author of the ORNL assessment of chloride salts for use in MSR systems recommends that an improved method for purification of chloride salts be developed and implemented as a standard method for corrosion tests [37]. Once impurity factors can be controlled, the thermodynamic driving force and propensity for corrosion must be examined more extensively and compared with

fluoride salts. In conjunction with this effort, corrosion controls, especially redox buffers for chloride salt systems, can be explored and more conclusive decisions about the suitability of chloride salts and appropriate materials can be made if there are advantages for chloride salts when compared with fluoride salts.

1.8: Lithium induced corrosion

Some research has been performed on the corrosion of structural materials to be used for the containment of metallic lithium. Lithium is considered as both a coolant and tritium source for fusion reactors due to the n, α reaction with Li^6 that yields both tritium and helium; however, most work for fusion reactors has focused on refractory metals such as Ta and W due to the high temperatures involved in fusion confinement.

The primary consideration when selecting a metal or alloy for the containment of metallic Li is the solubility of certain metallic elements in molten Li. Consequently, examination of the binary phase diagrams of Li with Al, Cd, Cu, Pb, Mg, Ag, Sn, and Zn reveals that these elements are not suitable for inclusion in the alloys used to contain metallic Li due to their mutual solubility [38]. Similar examination reveals that the elements Ti, V, Cr, Ni, Fe, Zr, Nb, Mo, Ta, and W do not have appreciable solubility in molten Li and can thus be considered for use in structural alloys. Our previous work on the corrosion of Monel 400, which is a Ni-Cu based alloy, in molten LiCl-Li_2O-Li showed increased degradation of the base material as the Li concentration was increased, implying the solubility of alloying elements in metallic Li is of great importance when selecting an alloy for

containment in this system [39]. A review written by Chopra et al. on the corrosion by liquid metals for fusion applications showed that the primary effects of molten Li on the corrosion of austenitic stainless steels, such as SS316, was the selective dissolution of Ni and Cr from the base alloy, accompanied by the formation of a ferrite layer on the surface of the material over the course of 5000hr, with corrosion rates being highly influenced by the impurity level of the molten metal [40]. This indicates that even elements without appreciable solubility in pure metallic Li may be corroded by the presence of impurities, similar to the case with corrosion in molten salts.

A second, and perhaps more relevant consideration for the present work, is the lack of data on the thermodynamic stability of oxide films in the presence of metallic Li. The primary corrosion prevention mechanism of stainless steels and Ni-based super alloys is through the formation of a Cr oxide-based surface film. The highly reducing nature of metallic Li means that most oxide films will react with Li, thus negating their usefulness at preventing corrosion. In the case of containment of pure metallic Li, if the underlying base material is compatible with metallic Li, this is not of major concern; however, in the present study, the elimination of the oxide film by metallic Li solvated in LiCl-Li_2O exposes the base material to the molten salt. As will be shown in Chapters 2, 3, and 4, this results in much higher corrosion rates than would be otherwise observed during exposure to pure metallic Li or pure molten salt conditions.

Intergrannular corrosion was the primary method of attack observed by DeVries in low carbon and alloy steels, which was assisted by the formation of Li carbides and sulfides at the grain boundaries [38]. Dissolution of Fe and Ni at the grain boundaries was also observed, while stress corrosion cracking was observed in all Ni-based alloys, rendering them incompatible with molten Li. This leads to consideration of the phenomena of liquid metal embrittlement (LME) whereby the exposure of a metal or alloy to a liquid metal leads to the severe degradation of the structural properties of that alloy [41]. The factors influencing the appearance of LME include, but aren't limited to, the metallurgical structure of the base material, grain boundary structure, and point defects, along with the thermodynamics of new surface formation, applied stress, impurities present in the base material, and the liquid metal to which the alloy is exposed. In depth discussion of the LME of alloys is beyond the scope of this work, but the reader is directed to a recent book published by E. Schukin, et al. on this effect if more information is desired [41].

1.9: Corrosion in Molten LiCl-Li_2O-Li

While the literature concerning corrosion in molten halide salts is rich in diversity and discussion of corrosion mechanisms, very few studies have investigated the effect of solvated lithium metal in lithium chloride [25, 39, 42-47]. The studies that have been reported have been mainly of short term duration and have been conducted under widely varying experimental parameters. Consequently, these studies conflict in their analysis on the effect of Li^0 on the

corrosion of various materials in the molten LiCl-Li_2O-Li system. Initial studies by Indacochea at ANL under inert atmosphere conditions showed minimal corrosion, however, due to the evaporation of both Li and Li_2O over the course of these experiments the solution chemistry was likely not maintained as that which was intended to be studied [42]. A following study, also by Indacochea et al., was performed under an Ar atmosphere containing 10% O_2 and showed much higher corrosion rates, and the formation of multiple metallic oxides on the sample surfaces, which may serve to inform the corrosion expected during a possible atmospheric contamination[43]. Recent work by Choi, et al. showed drastic degradation of pure metallic Ni in molten LiCl-Li_2O in the presence of either metallic Li or O_2 gas, but minimal degradation if neither impurity was present [47]

Previous work in our laboratory has attempted to elucidate the effect of Li^0 and Li_2O on the corrosion of Stainless Steel 316L (SS316L), Inconel 625, and Monel 400 by parametrically varying the concentrations of Li_2O, Li, and impurity H_2O independently [25, 39, 46]. These studies showed that material degradation depends on the concentration of Li_2O and Li, and the presence of impurity H_2O. These studies also showed that the mechanism of material degradation changes depending upon the concentration of Li in the system. At low concentrations of Li, the attack is based primarily on the O^{2-} activity in the melt, while corrosion more similar to liquid metal attack occurs at high Li^0 concentrations. In the absence of Li metal, Merwin noted the formation of bulk $LiCrO_2$ on the sample surface in the absence of Li, and detected small amounts of this compound via XPS up to Li concentrations of approximately 0.6wt% [25, 46]. While these studies are

extremely valuable for identification of the corrosion products and informing the mechanisms responsible for material degradation in the LiCl-Li_2O-Li system, the short-term nature of these exposure tests necessitated the continuation of this work to verify these findings.

1.10: Overview

This dissertation is thus primarily focused on the long-term effect of solvated metallic Li on the corrosion behavior of structural materials in the LiCl-Li_2O-Li system. Both Stainless Steel 316L (SS316L) and Inconel 625 (I625) were studied via exposure testing for periods of 500 and 1000 hours. Further experimental details are noted in each chapter. Chapter 2 presents the findings from the work performed on SS316L while Chapters 3 and 4 present the findings on the corrosion behavior of I625 in LiCl-Li_2O-Li. Chapter 5 summarizes the conclusions of these studies with a discussion of the general mechanisms observed and gives possible paths forward with suggestions for future work. Additionally, the appendices present additional work performed over the course of this doctoral dissertation that have not been yet been submitted for publication, and the supplemental information file for the publication of chapter 4. Specifically, Appendix 1 contains the supplemental information file for Chapter 4. Appendix 2 discusses the necessity and theoretical background of reference electrode development for the LiCl-Li_2O-Li system and presents several theoretical options for further investigation, along with preliminary results. Appendix 3 briefly discusses the degradation of ceramic materials in the LiCl-Li_2O-Li system and

presents the theoretical considerations necessary for development of ceramics in this system. Appendices 4 and 5 contain supplemental information and data collected from the long-term corrosion studies of SS316L and I625, respectively. Finally, Appendix 6 shows the results of the Li evaporation study used to determine the salt replacement interval for the long-term corrosion studies of SS316L and I625.

Chapter 2 : High Temperature Corrosion of Stainless Steel 316L in LiCl-Li2O-Li

As published in the Journal of Nuclear Materials, Volume 517, Issue 15, Pages 241-253, April 2019

Authors: William Phillips and Dev Chidambaram

https://doi.org/10.1016/j.jnucmat.2019.02.007

Abstract:

Exposure testing of Stainless Steel 316L was performed in LiCl-Li_2O-Li solutions at 650°C for periods of 500 and 1000 hours to investigate the effect of metallic Li on corrosion of materials used to contain the LiCl-Li_2O electrolyte for the electrolytic reduction of used nuclear fuel. Melt compositions studied consisted of LiCl containing 1 or 2 wt% Li_2O and 0, 0.3, 0.6, or 1wt% Li. Post exposure surface analysis was performed using scanning electron microscopy coupled with energy dispersive X-ray spectroscopy, Raman spectroscopy, X-ray photoelectron spectroscopy, and X-ray diffraction. Cross sections of the samples and gravimetric analyses were performed to determine the time-averaged corrosion rate for each sample. Lithium metal induced attack rates were found to be as high as 2.91 mm/y. In the absence of solvated Li in the LiCl-Li_2O system, $LiCrO_2$, Li_2CrO_4, and $NiFe_xCr_{2-x}O_4$ were observed to be the primary corrosion products. When Li was present in the melt, the oxidized alloying elements were only detectable via X-ray photoelectron spectroscopy, and the surface was primarily comprised of bare metal.

2.1: Introduction

Reduction of used oxide-based nuclear fuel is a necessary step for the incorporation of the large stockpile of used fuel from light water reactors into a pyrometallurgical-based fuel cycle [7, 8, 48]. The electrolytic oxide reduction operation developed by ANL is the preferred method for the reduction of used nuclear fuel (UNF) and has been the subject of continued development [7, 11, 12, 49-55]. In this process, declad, crushed, and pelletized UNF is placed in a stainless steel basket and cathodically polarized versus a suitable anode at a potential sufficient to reduce the oxides present at the cathode [55]. Li_2O is added in concentrations of 1-2wt% to provide an initial source of O^{2-} ions, which are then oxidized at the anode to form oxygen gas. The concentration of Li_2O must be carefully controlled, as the reduction of the lanthanides and minor actinides becomes thermodynamically unfavorable at high O^{2-} activities, and the anodic dissolution of Pt becomes problematic at low O^{2-} activities [11, 56-58]. As the reduction proceeds, the actinide and lanthanide oxides are reduced to metallic form, while the salt soluble fission products (i.e. Cs, Sr, I, Br, etc.) form salts and dissolve into the electrolyte. Due to the close reduction potentials of Li_2O and UO_2 of -2.40V and -2.47V vs. $O^{2-}|O_2$, respectively, and the necessity of applying a high overpotential to achieve a high reduction yield, metallic Li is generated at the cathode [8, 13, 17, 55].

The Li generated at the cathode acts as an additional reduction pathway for UO_2 through direct chemical means; however, due to the solubility of Li in

LiCl, some of the metallic Li dissolves into the electrolyte [17, 20, 21, 58-62]. Dissolution of Li into LiCl has been noted by a number of researchers, and causes a number of changes in physical, electrical, and chemical properties of the electrolyte, as well as causing current inefficiency [17]. The exact solubility limit of Li in LiCl has proven to be experimentally difficult to determine [16, 59, 60]. A number of different dissolution mechanisms have been proposed by other researchers, but a consensus has yet to be reached within the community. The f-center model proposed by Bredig, *et Al.* treats the excess electron from solvated Li^0 as an anion vacancy, with the electron delocalized from any individual Li^+ ion core [18, 59]. In this model, the solution behaves somewhat similarly to a liquid metal, with free electrons contributing to increased electrical conductivity. This model has successfully predicted the increase in solution conductivity for other alkali halide – alkali metal systems, however, the solution conductivity of the LiCl-Li system is anomalous in that it does not increase at the rate predicted by the f-center model [17, 59]. Previous work in our laboratory using *in-situ* Raman spectroscopy has provided evidence of the presence of Li_8 nanoclusters in solution as a colloidal suspension [22]. If Li_8 clusters are present in the LiCl-Li system, they would act to keep the valence electrons of the Li_8 cluster localized, thus reducing the rate of electrical conductivity increase associated with the progressive addition of Li^0 to LiCl. As the clusters would be present as a colloid, the solubility of Li^0 in LiCl would be dependent on the specific experimental parameters, leading to the variation in the measured values for solubility reported by other researchers [22].

Regardless of the molecular interactions at place within the LiCl-Li system, understanding of the effect the solution chemistry has on materials exposed to the molten LiCl-Li_2O-Li system is important for the safe and economical design of vessels and other components for use during the electrolytic reduction of used nuclear fuel. Corrosion in LiCl-Li_2O under oxidizing conditions has been widely investigated [63-70]. The most successful model of corrosion in this system is based on the Lux-Flood model of salt basicity where the rate of material degradation is dependent upon the activity of the O^{2-}anion [33, 63, 71]. In addition to O^{2-} activity, corrosion in molten salts is also governed by the inclusion of impurities in the melt, such as moisture or metal chlorides [33]. While the literature concerning corrosion in chloride salts is rich in diversity and discussion of corrosion mechanisms, very few studies have investigated the effect of solvated lithium metal in lithium chloride [25, 39, 42-47]. The studies that have been reported have been mainly of short term duration and have been conducted under widely varying experimental parameters. Consequently, these studies conflict in their analysis on the effect of Li^0 on the corrosion of various materials in the molten LiCl-Li_2O-Li system.

Previous work in our laboratory has attempted to elucidate the effect of Li^0 and Li_2O on the corrosion of Stainless Steel 316L (SS316L), Inconel 625, and Monel 400 by parametrically varying the concentrations of Li_2O, Li, and impurity H_2O independently [25, 39, 46]. These studies showed that material degradation depends on the concentration of H_2O, Li_2O and Li, and that a transition from corrosion based primarily on the O^{2-} activity in the melt at low Li^0 concentrations

to corrosion more similar to liquid metal attack occurs at high Li^0 concentrations. However, the short-term nature of these exposure tests necessitated the continuation of this work to verify our previous findings. In this light, the current study focuses on the corrosion of SS316L over extended time periods when exposed to LiCl containing Li_2O and Li at various concentrations. This paper presents the information gathered from SEM-EDS of the sample surfaces and cross sections, as well as XRD, XPS, and Raman spectroscopy of the surfaces to elucidate the mechanisms responsible for material degradation.

2.2: Materials and Methods

All experiments were performed in a Vacuum Atmospheres OMNI-LAB glovebox under an Ar atmosphere containing less than 2ppm O_2 and less than 1ppm H_2O. Anhydrous LiCl and Li_2O were obtained from Alfa-Aesar and were of 99% and 99.5% purity, respectively. Li metal of 99% purity was purchased from Strem Chemicals. 99% purity Ni crucibles were obtained from Alfa-Aesar. SS316L coupons were cut from a 3.048mm plate obtained from McMaster-Carr, with the certified composition given in Table 2.1.

Table 2.1: Certified composition of the SS316L plate used in this study.

Fe	Cr	Ni	Mo	Mn	C
70.1	16.5	10	2	1.3	0.014

The salt compositions studied consisted of LiCl containing 1 and 2wt% Li_2O and 0, 0.3, 0.6, and 1wt% Li, with exposure periods of 500 and 1000 hours.

Total salt mass contained in each crucible was 50g. Duplicate samples were exposed for each data point, and 500 hour and 1000 hour exposures were conducted in parallel, with the 500 hour samples removed from the experiment upon completion of the allotted exposure period. The furnace configuration used for this study is shown in Figure 2.1. A 6.5 inch inner diameter, 6 inch tall cylindrical heater from Watlow (1500 watts) was used to maintain a temperature of 650±5°C for the duration of the exposure period. A 6 inch diameter graphite block was machined to accommodate 5 Ni crucibles, with slots machined to accommodate the sample hanging rods. This configuration allowed for repeatable placement of the samples within the melt during the salt replacement procedure outlined below. Two identical furnaces were constructed to maximize the number of experiments that could be ran in parallel. In operation, four experiments were ran simultaneously in each furnace, which allowed for an additional crucible location to be used for salt replacement purposes.

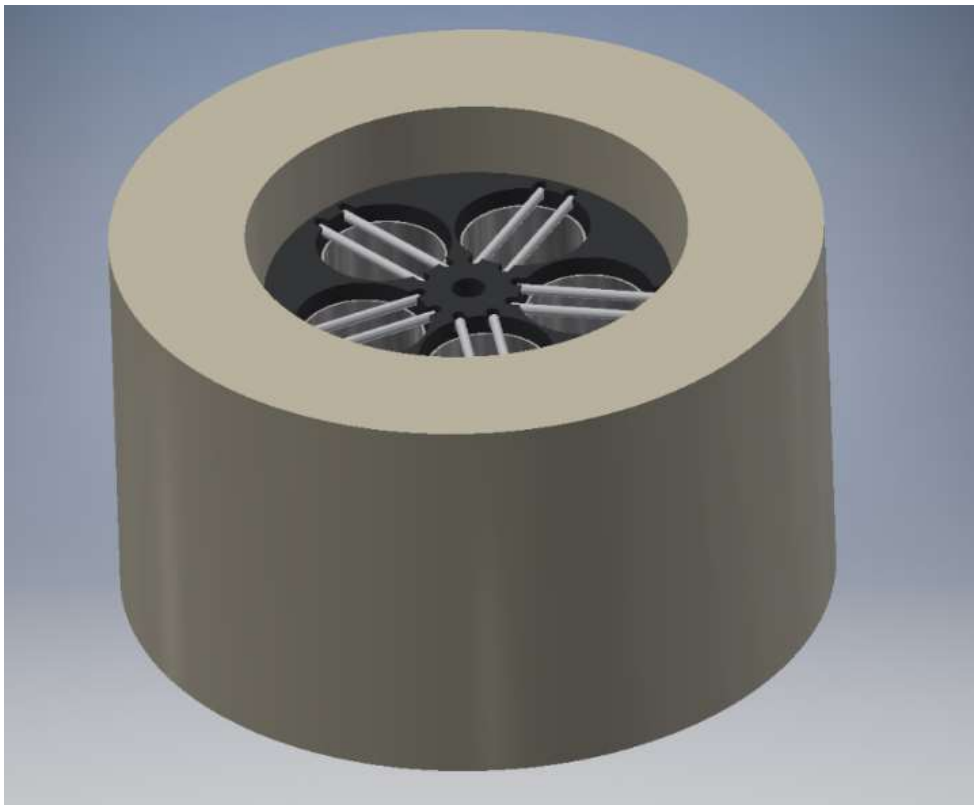

Figure 2.1: A model of the long-term exposure furnace, graphite crucible holder, Ni crucibles, and sample hanging rods.

Prior to exposure, the metal samples were cut into 1.27cm by 1.27cm squares using a CO_2 laser. The samples were then polished to a 1 μm surface finish on both sides using a diamond abrasive and spot welded to loops of SS316L wire for suspension from the sample hanging rods, as was performed in our previous studies [25, 39, 46]. Sample hanging rods were made of like material to the samples, as alumina rods proved to be incapable of withstanding the highly reducing atmosphere directly over the molten solutions containing metallic Li for the duration of these experiments. The mass of each sample was recorded immediately prior to exposure using a high precision balance.

2.3: Experimental

Due to the evaporation of Li and Li_2O over time and the extended exposure periods of this study, the salt charge for each test was replaced once every 96 hours to maintain the solution chemistry. To minimize the effects of impurity H_2O, LiCl was dried in a vacuum oven in air at 200°C for 24 hours before being transferred into the glovebox for storage [19, 25]. Immediately prior to insertion in the primary furnace, a cleaned Ni crucible (99% purity, Alfa Aesar) containing the weighed amount of LiCl was dried under Ar for 2hr in a dedicated furnace maintained at 550°C. After insertion into the primary furnace, the LiCl was allowed 1 hour to reach thermal equilibrium, after which time the required mass of Li_2O and Li were added to the molten salt. The melt was allowed to equilibrate for another hour prior to the transfer of the corrosion specimens from the old salt charge to the new salt charge. Sample transfer was accomplished through the use of specially fabricated tongs. Following transfer of the samples to the new salt charge, the old salt charge was removed from the furnace and allowed to cool to room temperature.

Following completion of the exposure period, the samples were removed from the furnace and allowed to cool to room temperature in the glovebox atmosphere. All samples were stored in the Ar glovebox between analytical procedures. As it was unknown if the surface films formed on the corrosion specimens would be stable in atmosphere, surface analysis was performed both prior to and following removal of the residual salt layer. Following the initial

surface analytical procedures, residual LiCl was removed by placing each sample in 25ml of HPLC grade methanol for 15 minutes with constant agitation. Prior to the methanol rinsing procedure, all surface analysis was performed under inert atmosphere or vacuum conditions, depending on technique. The data presented here was collected following the methanol rinsing procedure, as the residual salt layer significantly interfered with surface analysis. No chemical or morphological changes were observed as a result of the methanol rinsing procedure. Gravimetric weight change measurements were performed following the methanol rinsing procedure.

Post exposure surface analysis was performed using scanning electron microscopy (SEM) coupled with energy dispersive X-ray spectroscopy (EDS), Raman Spectroscopy, X-ray diffraction (XRD), and X-ray photoelectron spectroscopy (XPS). Following the completion of all surface analytical techniques performed in this study, the samples were cross sectioned to investigate the nature and depth of degradation of the samples. Initially, focused ion beam (FIB) milling was used to mill a trench in the samples to minimize possible morphological and chemical changes to the internal structure of the samples; however, it was found that the depth of attack for samples exposed to melts containing Li was much greater than practical to investigate using this technique alone. Consequently, all samples exposed to Li containing melts were cross sectioned using a Buehler cubic-BN wafering blade on a slow speed saw and polished according to Buehler's recommended polishing techniques to a 0.05μm surface finish prior to analysis. Samples exposed to LiCl-Li_2O in the absence of

Li were investigated using only FIB milling for cross sectional analysis due to the relatively shallow depth of attack.

SEM of the sample surfaces was performed using a Hitachi S-4700, while EDS data was collected via the attached Oxford Instruments energy dispersive X-ray spectrometer. The W cold field emission source was operated at an accelerating voltage of 5kV for surface morphology images, while 20kV was used for collection of EDS spectra. Emission current was maintained at 10mA. FIB milling and subsequent SEM-EDS analysis for cross sectional images was performed using a FEI Scios dual-beam FIB/SEM equipped with a TEAM Pegasus Integrated EDS-EBSD. The same dual-beam FIB/SEM was used to perform the SEM-EDS analysis of all of the cross sectioned samples, including those mechanically cross sectioned and polished. The electron beam was operated at 20kV for both imaging and EDS analysis.

Following the methanol rinsing procedure, the final mass of each sample was recorded, and the exposed surface area was calculated based on the measured submersion depth of each sample. The average corrosion rate in mm/year and the mass loss rate in mg cm^{-1} hr^{-1} was then calculated based on the mass change, density of the alloy, exposed surface area, and length of exposure.

X-ray diffraction was performed using a Rigaku Smartlab X-ray diffractometer with a Cu kα source operating at 44kV and 40mA. Parallel beam optics in a grazing incidence angle configuration were used for detection of the

thin surface films formed on the samples in this study. The incidence angle was set at 1°, and the diffraction pattern was recorded over a 2θ range of 10° to 90° for all diffraction patterns. For each diffraction pattern, the scan speed was optimized to yield an intensity of 5000 counts for the highest peak, while the step size was varied to give 5 steps at the full width at half-maximum intensity of the narrowest peak.

Raman spectroscopy was performed using a Thermo-Scientific DXR Raman microscope utilizing a 10mW 532nm continuous wave laser. Spectra were collected through the 50x objective lens of the microscope using a 50μm incident beam slit. The collection time was 4 seconds per spectra, and 16 individual spectra were averaged to give the spectra reported here.

X-ray photoelectron spectroscopy was performed using a PHI 5600 spectrometer equipped with an Al-Kα source with a photon energy of 1486.6eV. The source was operated at an accelerating voltage of 14kV and an anode power of 300W. The spectrometer dispersion and work function were calibrated to the Au $4f_{7/2}$ peak at 84.00eV and the Cu $2p_{3/2}$ peak at 932.67eV to an accuracy of ±0.05eV. Survey spectra were recorded with a step size of 0.5eV, while narrow scans were collected at a step size of 0.025eV for the elements detected on the sample surfaces. Peak fitting was performed with SDP version 4.6 Gaussian fitting software. Charge correction was performed to the adventitious C 1s peak at 284.8eV.

2.4: Results

2.4.1: Scanning Electron Microscopy

The morphologies observed via SEM were highly dependent on the Li concentration in the molten salt solution. The SEM micrographs obtained from SS316L samples exposed to LiCl-2wt% Li_2O containing 0, 0.3, 0.6, and 1wt% Li at 650°C for 1000hr and washed with methanol are shown in Figure 2.2, while the area averaged EDS composition of the primary constituents of the sample surface for these regions are given in Figure 2.3. The differences in the surface morphology caused by the varying concentrations of Li in LiCl-2wt% Li_2O correlates to the changes in surface chemistry observed via Raman, XPS, and XRD presented below. The unique surface morphology observed at 0.3wt% Li may be indicative of the simultaneous action of electrochemical corrosion and liquid metal attack, while the similarity between the morphologies observed at 0.6 and 1wt% Li indicate that corrosion at these concentrations is firmly within the liquid metal attack regime. Morphologies similar to those observed here were reported in a recent publication by researchers at KAERI who investigated the corrosion behavior of Ni in molten LiCl-Li_2O-Li [47]. A number of void spaces were also observed on the surface of all samples exposed to melts containing metallic Li, indicating possible locations where the intergranular corrosion observed on the sample cross sections was initiated. These voids were typically located at high angle grain boundaries, further supporting this hypothesis.

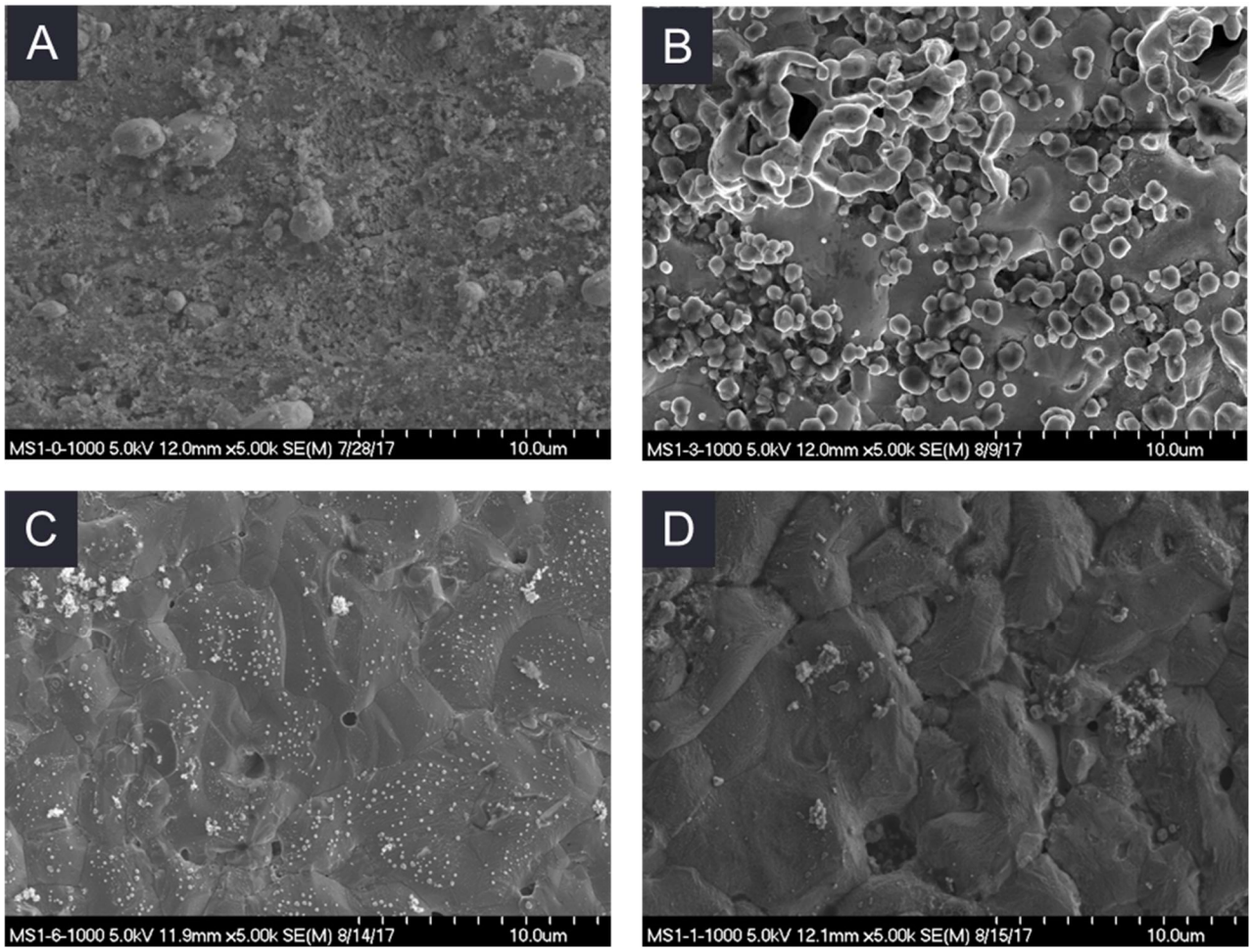

Figure 2.2: SEM micrographs of SS316L exposed to LiCl-1wt% Li2O at 650°C containing A) no Li, B) 0.3wt% Li, C) 0.6wt% Li, and D) 1wt% Li for 1000hr, following the methanol rinsing procedure.

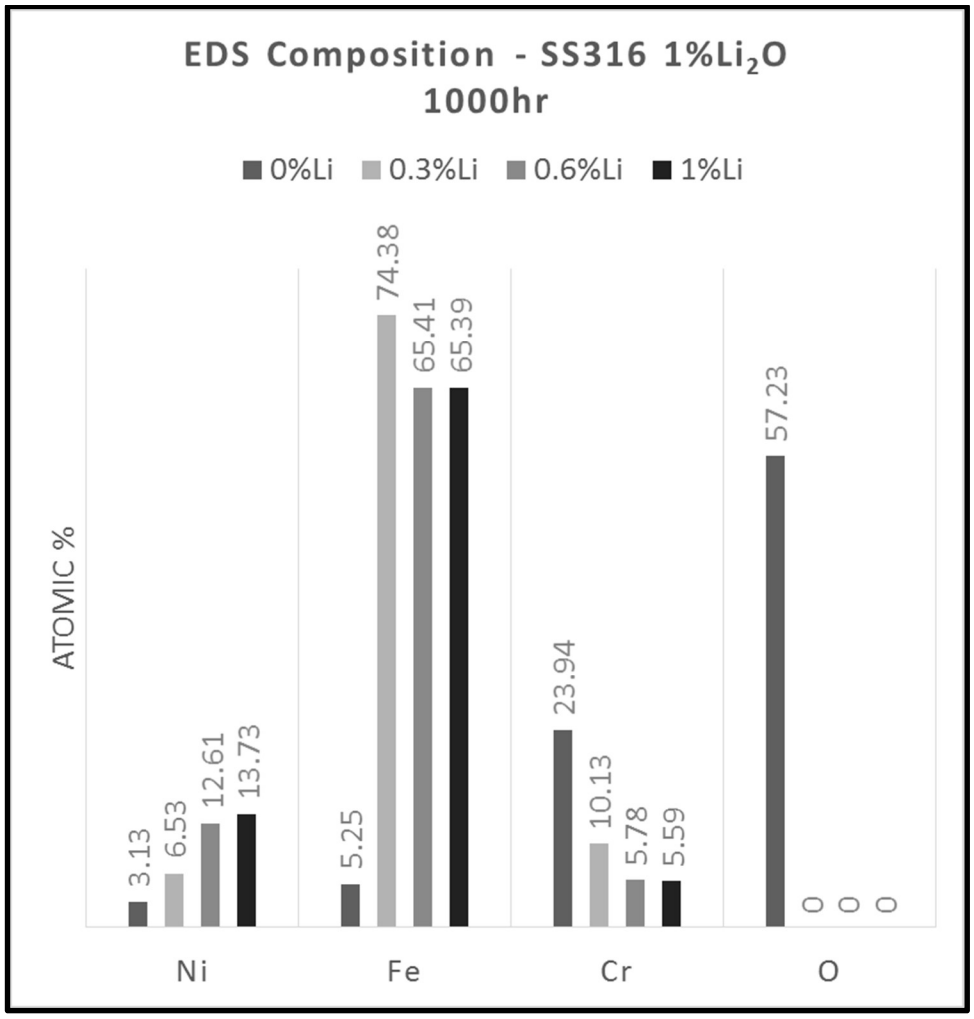

Figure 2.3: Average composition of the SS316L samples exposed to LiCl-1wt% Li_2O-Li solutions for 1000hr for the regions shown in Figure 2.2.

From Figure 2.3, it can be observed that the surface of the SS316L sample exposed to LiCl-1wt% Li_2O-0wt% Li at 650°C for 1000hr is primarily composed of Cr-based oxide films, with minor contributions of Ni and Fe. This is in good agreement with the Raman, XRD, and XPS data presented in their respective sections, which all indicate that these surfaces are composed primarily of $LiCrO_2$, while small quantities of Li_2CrO_4 and $NiFe_xCr_{2-x}O_4$ are predicted by Raman and XPS. When the Li concentration in the molten salt solution is 0.3wt%, the Cr content of the surface is depleted compared to the

base alloy while the Fe content is increased. Beyond the solubility limit of Li, at 0.6 and 1wt% Li, Cr is depleted slightly further and O is not detectable, while both Fe and Ni are present at levels nominal for SS316L, indicating a bare metallic surface. A slight enrichment of Ni on the SS316L sample exposed to LiCl-2wt% Li-1wt% Li for 1000hr is in agreement with our previous work, and is indicative of liquid metal like attack by Li [25]. Similar trends were observed for samples exposed to LiCl-Li_2O-Li containing 1 and 2wt% Li_2O and 0, 0.3, 0.6, and 1wt% Li for 500 and 1000hr.

Also of interest is the observation of sensitization on a small area on the SS316L sample exposed to LiCl-2wt% Li_2O-0.6wt% Li at 650°C for 1000hr. Sensitization of austenitic stainless steels is a well-known issue at high temperatures, where the formation of chromium carbides and their subsequent concentration at the grain boundaries leads to intergranular corrosion and loss of strength [72]. The characteristic enrichment of Cr at the grain boundaries typical of sensitization can clearly be observed in the Cr Kα EDS map in Figure 2.4, while the specific compositions for spots 1 and 2 marked on the SEM micrograph and EDS map are given in Table 2.2.

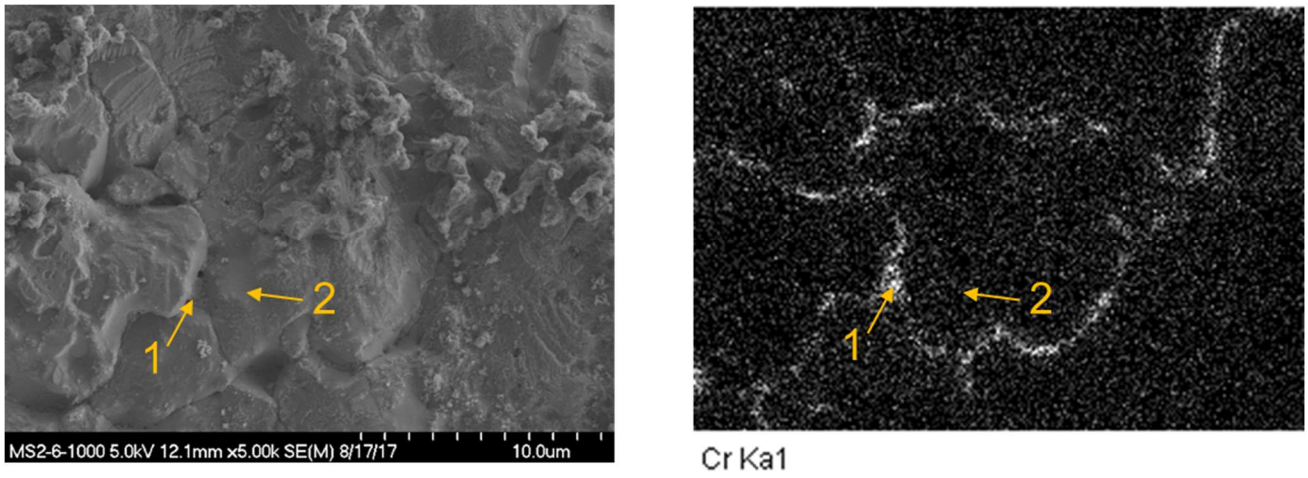

Figure 2.4: SEM micrograph (left) and EDS map of Cr of the same location (right) for the SS316L sample exposed to LiCl-2wt% Li_2O-0.6wt% Li at 650°C for 1000hr. The elemental compositions obtained via EDS analysis for spots 1 and 2 are given in Table 2.2.

Table 2.2: EDS composition spot analysis for the locations marked on the SEM micrograph in Figure 2.4, above.

Element	Spot 1 Atomic%	Spot 2 Atomic%
C	26.69	-
S	1.21	-
Cr	27.05	4.28
Mn	1.09	1.46
Fe	28.52	50.05
Ni	15.44	44.21

The detection of S along with chromium carbide formation at Spot 1 is in good agreement with literature, as S is known to accelerate the sensitization of austenitic stainless steels [72]. As expected, the vicinity of spot 1 area (spot 2) has much lower concentration of chromium, which is below the concentration in base alloy. The low carbon content of the SS316L used for this study is intended to minimize this issue by preventing the formation of carbides. Of great importance to the present work, the operating temperature of the electrolytic reduction of UNF at 650°C is also ideal to cause sensitization of austenitic

stainless steels, as chromium carbides are insoluble at this temperature and the diffusion of C through the microstructure allows for their formation and migration to the grain boundaries.

2.4.2: Cross Section SEM-EDS

The SEM image obtained for the FIB milled trench from the SS316L samples exposed to LiCl-1wt% Li_2O-0% Li for 500hr and 1000hr are shown in Figure 2.5. It can be observed that the attack first proceeds inward from the sample surface in an intergranular fashion prior to consuming the grains themselves, likely assisted by the sensitization of the material seen in Figure 2.4. The depth of attack into the sample is approximately linear with length of exposure, with the total depth of attack being 13μm and 27μm for 500hr and 1000hr, respectively, while the thickness of the outer oxide layer is approximately 3μm for the 500hr sample and 7.5μm for the 1000hr sample.

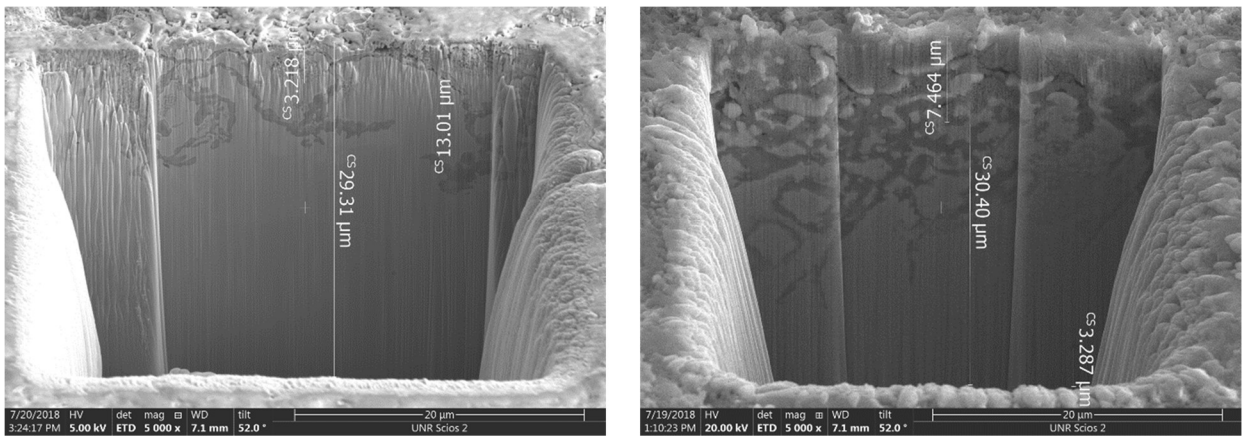

Figure 2.5: FIB milled and SEM imaged cross sections of SS316L samples exposed to LiCl-1wt% Li_2O for 500hr (left) and 1000hr (right).

EDS mapping results for the corroded region of the SS316L sample exposed to LiCl-1wt% Li_2O for 1000hr are shown in Figure 2.6. Here, it can be observed that the corrosion products (dark regions) are enriched in Cr, Mo and O, while the bulk material is relatively depleted in Cr and Mo. This agrees with the findings of previous studies that corrosion in LiCl-Li_2O occurs primarily through preferential attack of the most active alloying elements, namely Cr and Mo [25, 33].

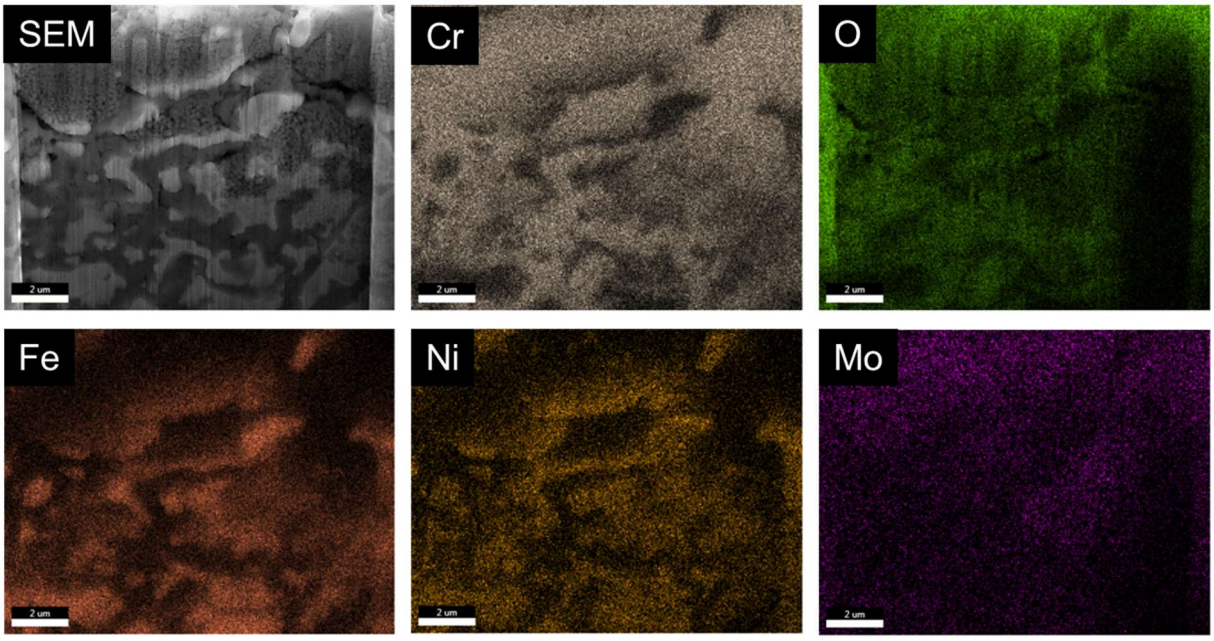

Figure 2.6: EDS mapping results for the SS316L sample exposed to LiCl-1wt% Li_2O for 1000hr.

In the presence of Li, intergranular corrosion was again observed to be the primary method of material degradation, as can be observed in Figure 2.7. However, the lack of a protective oxide layer severely accelerated the attack of the base material.

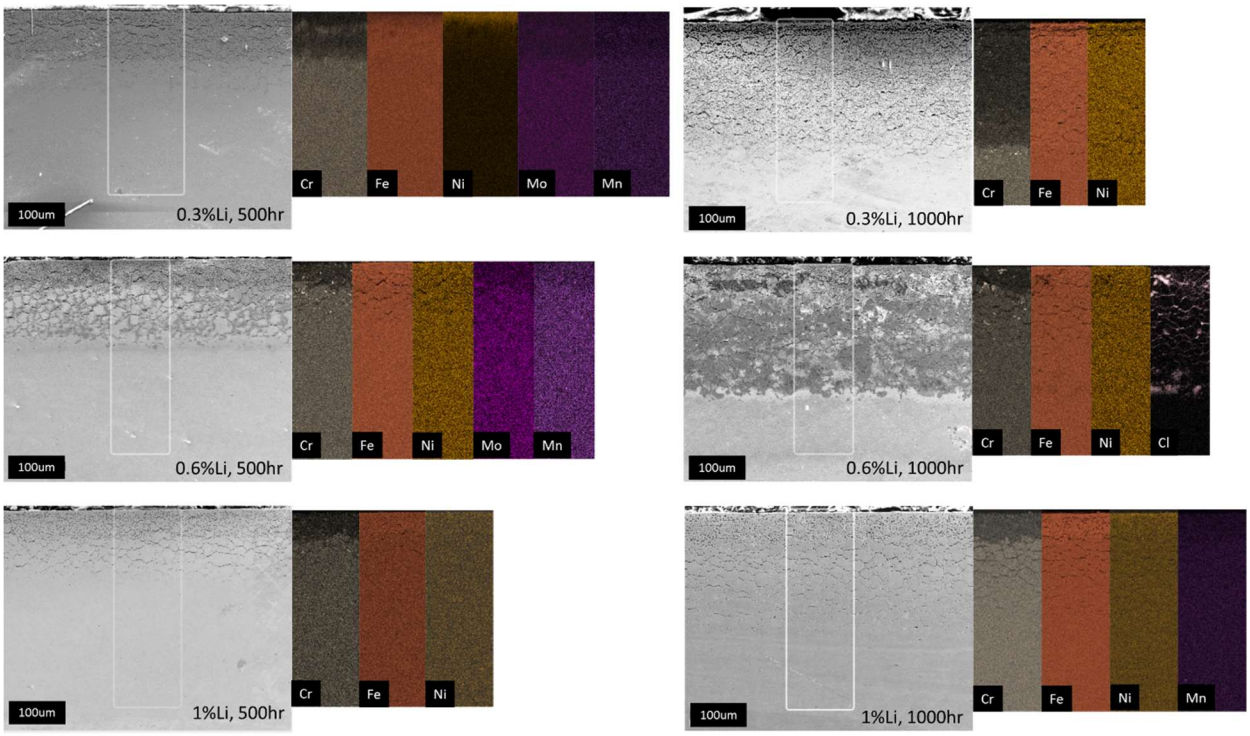

Figure 2.7: Cross section SEM images and EDS maps of SS316L samples exposed to LiCl-1wt% Li_2O containing 0.3, 0.6, and 1wt% Li for 500 and 1000hr. Areas selected for EDS mapping are delimited in SEM image. Brightness has been adjusted for clarity.

From Figure 2.7, it can be observed that the depth of attack on the base material is approximately linear with time and does not depend on the concentration of Li; however, the severity of the degradation is proportional to the Li concentration in the melt. In all cases, the rate of attack was approximately 2.2 to 2.9mm/year in the presence of Li. The outer layers of the SS316L samples exposed to melts containing Li were depleted in Cr, while small, localized areas of high Cr concentration were observed in intergranular regions, further corroborating the observations of sensitization made in Figure 2.4. A high magnification EDS map of one of these regions on the SS316L sample exposed to LiCl-1wt%Li_2O-0.6wt%Li for 500hr is shown in Figure 2.8, while the spot EDS analysis for the area highlighted in red in the SEM image is given in Table 2.3.

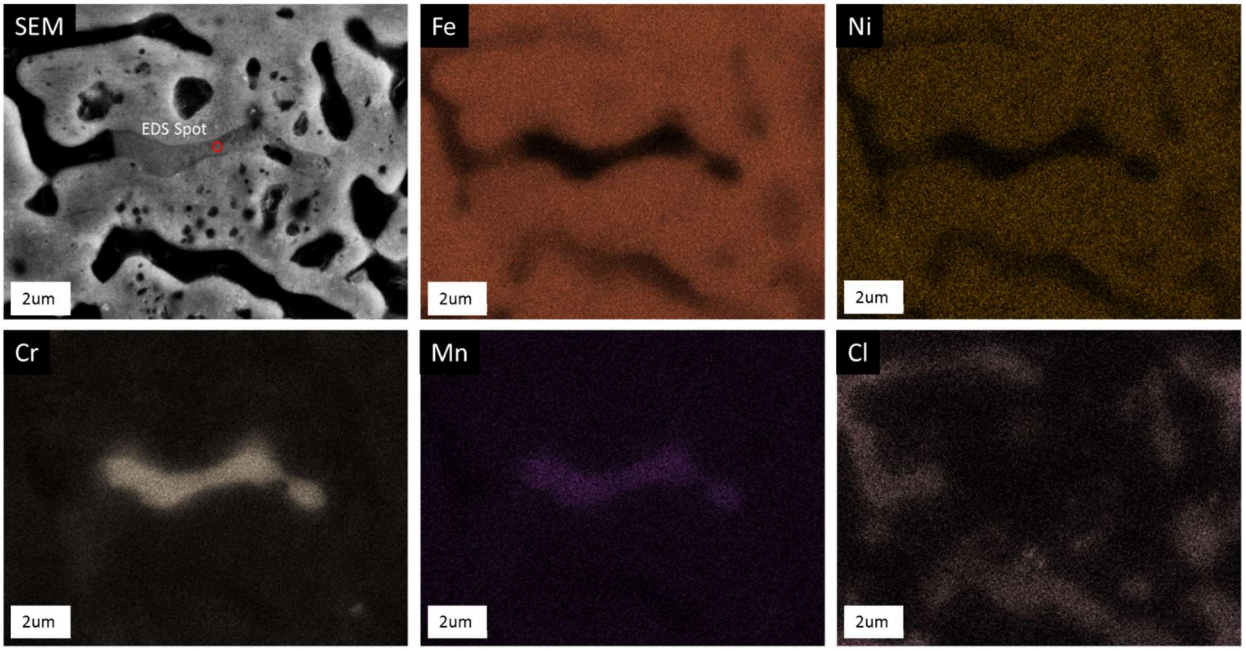

Figure 2.8: Hi-magnification SEM-EDS maps of Fe, Ni, Cr, Mn, and Cl for a Cr rich region of the SS316L sample exposed to LiCl-1wt%Li_2O-0.6wt%Li for 500hr. The red spot on the SEM image indicates the location of the spot EDS analysis summarized in Table 2.3

Table 2.3: Spot EDS analysis for the location on the SS316L sample exposed to LiCl-1wt%Li_2O-0.6%Li for 500hr shown in Figure 2.8.

Element	Weight %	Atomic %	Error %
C	9.72	26.31	8.88
N	10.88	25.23	8.87
Cr	53.57	33.48	1.64
Mn	1.36	0.81	7.84
Fe	21.91	12.75	2.74
Ni	2.56	1.42	5.82

From the SEM-EDS images in Figure 2.8 and spot analysis in Table 2.3, it is apparent that corrosion of the base material is facilitated by the precipitation of Cr and Mn at the grain boundaries in the form of metal carbides and nitrides. These carbides and nitrides are then preferentially attacked by the molten salt, leaving a channel for further intrusion of the salt along the grain boundary. N was

likely incorporated as an impurity from the glovebox atmosphere which reacted with Li^0 to form Li_3N, which is known to accelerate corrosion in the LiCl-Li_2O-Li system [73]. Also, titanium nitride surface films were observed in previous studies, as well as during XPS analysis of these samples [26]. Some of these samples were observed to spontaneously form droplets of water from the cross sectioned surface when exposed to atmosphere, implying LiCl was entrapped within the sample. LiCl is extremely hygroscopic, and will absorb enough water to form a solution, even in relatively dry air, so the formation of water droplets on the cross sectioned surface is indicative of the entrapment of LiCl within the bulk sample. As most other metal chlorides are not hygroscopic to the same extent as Li, this indicates that the Cl observed in Figures 2.7 and 2.8 is primarily in the form of LiCl.

2.4.3: Depth of Attack Analysis

Based on the depth of attack observed in Figure 2.7, the depth of lithium attack was calculated for each sample and are tabulated in Table 2.4. For comparison, the corrosion rates based on gravimetric analysis are presented in Table 2.5.

Table 2.4: Depth of attack observed for SS316L samples exposed to LiCl-1wt% Li_2O solutions containing 0, 0.3, 0.6, and 1wt% Li for 500 and 1000hr, and the corrosion rate based on this depth of attack.

Li Concentration in Salt (wt%)	Exposure Duration (hr)	Depth of Attack (µm)	Depth of Attack Rate (mm/year)
0	500	13	0.23
0	1000	27	0.24
0.3	500	140	2.45
0.3	1000	275	2.41
0.6	500	166	2.91
0.6	1000	250	2.19
1	500	120	2.10
1	1000	225	1.97

The lack of spallation of the material based on the gravimetric analysis presented below, along with the morphological changes to the base material shown above indicates that simple mass loss or thickness measurements are not sufficient for assessing corrosion damage in this system. The maximum corrosion rate observed gravimetrically was for the SS316L sample exposed to LiCl-1wt% Li_2O-1wt% Li for 500hr, where the corrosion rate was 0.665mm/year, which is well below the attack rate calculated for this sample based on the ingress of attack observed in cross sectional imaging. The high variance observed is thought to be a result of the relatively low absolute weight change per sample, which was on the order of 10s of mg for most samples, as well as ingress of salt into the material. No overall trend in gravimetric weight loss as a function of material, Li_2O concentration, Li concentration, or exposure period was observed.

Table 2.5: Calculated corrosion rates for SS316L samples exposed to LiCl-Li_2O-Li solutions at 650°C for 500hr and 1000hr. Positive corrosion rates indicate weight loss, while negative corrosion rates indicate weight gain.

Wt% Li2O	Wt% Li	Exposure (hr)	Mass Loss Rate (mg cm^{-1} hr^{-1})	Corrosion Rate (mm $year^{-1}$)
1	0	500	0.000	-0.005
1	0.3	500	-0.019	0.211
1	0.6	500	-0.012	0.126
1	1	500	-0.061	0.665
2	0	500	-0.010	0.115
2	0.3	500	-0.005	0.055
2	0.6	500	-0.001	0.016
2	1	500	0.012	-0.134
1	0	1000	-0.005	0.050
1	0.3	1000	-0.006	0.062
1	0.6	1000	-0.016	0.179
1	1	1000	-0.010	0.112
2	0	1000	-0.008	0.082
2	0.3	1000	-0.012	0.130
2	0.6	1000	-0.009	0.101
2	1	1000	-0.007	0.073

2.4.4: X-ray Diffraction

Figure 2.9 shows the diffraction pattern obtained for SS316L exposed to LiCl-2wt%Li_2O-0wt%Li at 650°C for 500hr. Peaks characteristic of $LiCrO_2$, based on PDF card number 01-072-7839, and the base material were observed [74]. No other phases were detected on the sample surface, indicating that the $NiFe_xCr_{2-x}O_4$ and Li_2CrO_4 phases predicted by Raman spectroscopy, SEM-EDS, and XPS observations presented below are minor components of the oxide layer present on samples exposed to LiCl-Li_2O solutions in the absence of Li. Similar patterns were obtained for all samples exposed to LiCl-Li_2O solutions in the absence of Li^0.

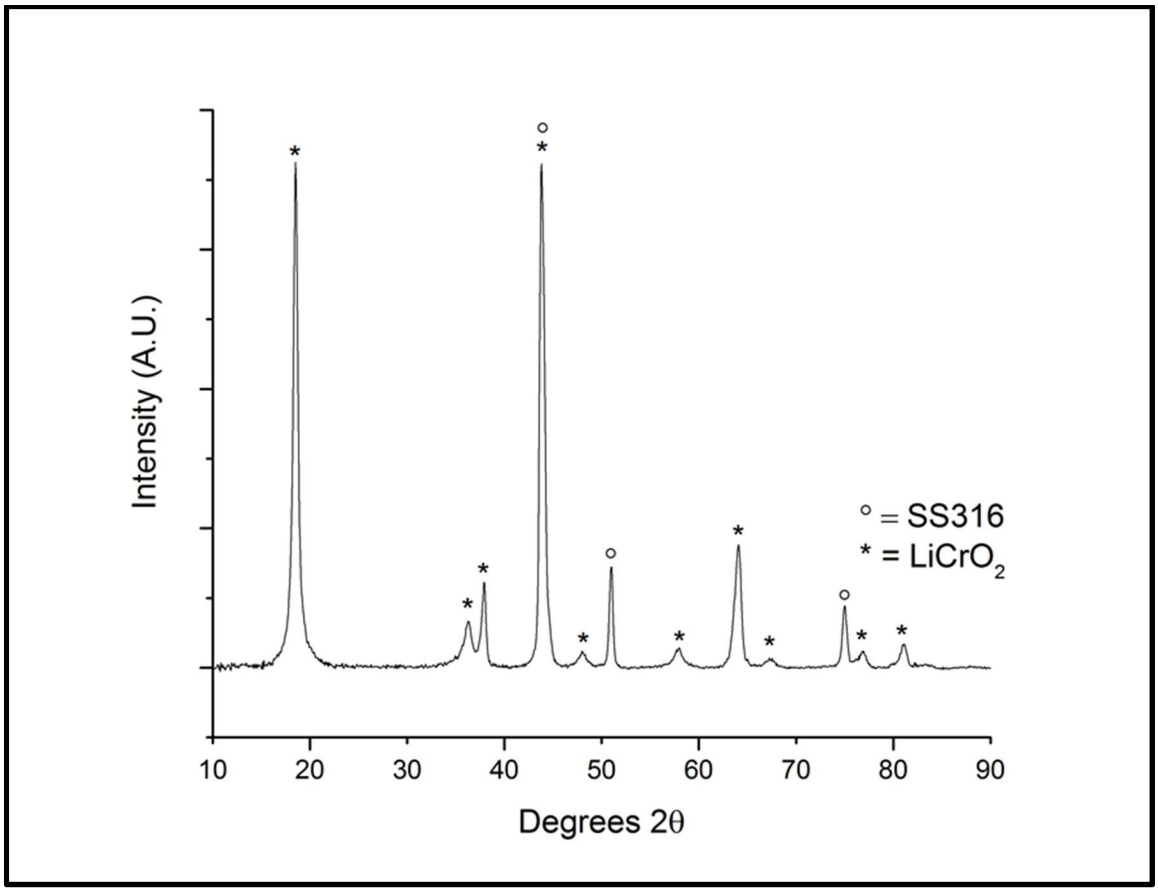

Figure 2.9: GI-XRD pattern of SS316L exposed to LiCl-2%Li_2O-0%Li for 500hr after methanol rinsing. Peaks corresponding to $LiCrO_2$ and the base material were observed.

The XRD patterns for SS316L samples exposed to LiCl-1wt%Li_2O solutions containing 0, 0.3, 0.6, or 1wt%Li at 650°C for 500hr are shown in Figure 2.10, while Figure 2.11 shows the diffraction patterns for SS316L samples exposed to identical conditions for 1000hr.

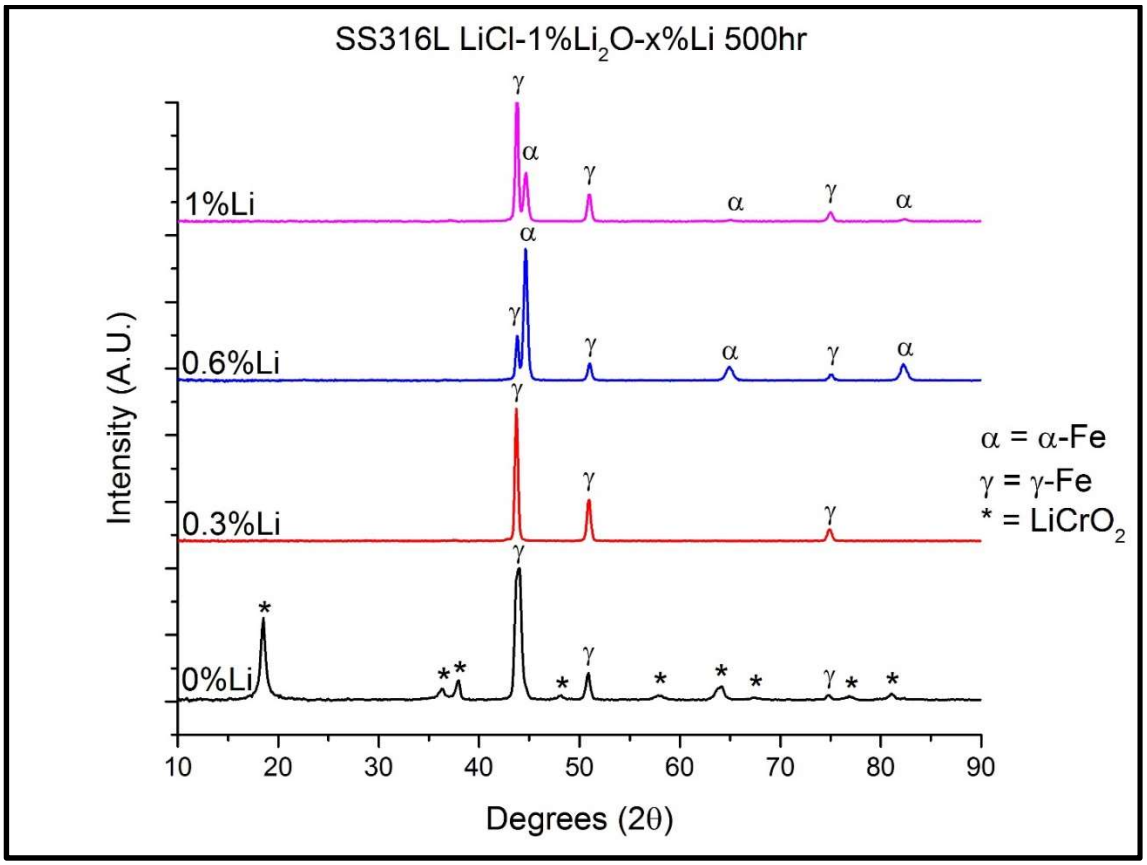

Figure 2.10: High resolution grazing incidence XRD patterns for SS316L samples exposed to LiCl-1wt%Li_2O solutions containing 0, 0.3, 0.6, or 1wt%Li at 650°C for 500hr. The diffraction pattern for the SS316L sample exposed to LiCl-1wt%Li_2O-0wt%Li shows the peaks identified as $LiCrO_2$ in Figure 2.10, above. The peaks of $LiCrO_2$ were not observed on any sample exposed to LiCl-Li_2O in the presence of Li. De-austenization of samples exposed to LiCl-1wt%Li_2O containing 0, 0.6, and 1wt%Li for 500hr was observed.

From these figures, it can be observed that the $LiCrO_2$ surface films that form in the absence of Li are not detectable via XRD in the presence of Li, corroborating SEM-EDS as well as the Raman spectroscopy and XPS analysis presented in this work [25]. These techniques all show that the presence of Li prevents the formation of appreciable oxide surface films, resulting in severe degradation to the base material. Additionally, de-austenization of the base material was observed on the SS316L samples exposed to LiCl-1wt%Li_2O containing 0, 0.6, and 1wt%Li for 500hr, and LiCl-1wt%Li_2O containing 0 and

0.3wt%Li for 1000hr. This effect was also observed in short term testing of SS316L in molten LiCl-Li_2O-Li [25]. The inconsistency with which this phenomena was observed indicates that the solution chemistry does not affect the probability that a particular sample will undergo de-austenization. This is particularly highlighted by the SS316L samples exposed to LiCl-1wt%Li_2O containing 0.3, 0.6, and 1wt%Li for 500 or 1000hr, as the samples exposed to identical solution chemistries for different exposure periods did not display similar de-austenization behavior.

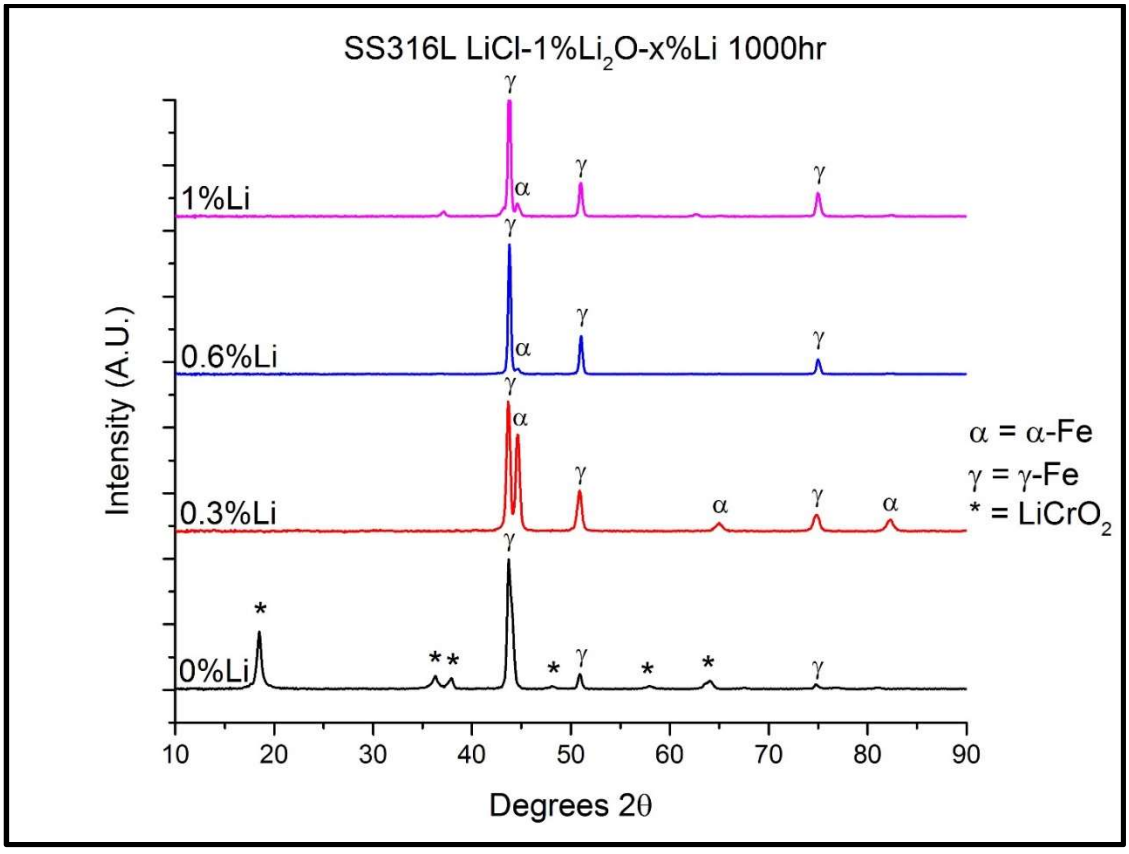

Figure 2.11: High resolution grazing incidence XRD patterns for SS316L samples exposed to LiCl-1wt%Li_2O solutions containing 0, 0.3, 0.6, or 1wt%Li at 650°C for 1000hr. The diffraction pattern for the SS316L sample exposed to LiCl-1wt%Li_2O-0wt%Li shows the peaks identified as $LiCrO_2$ in Figure 2.9, above. The extent of de-austenization of the base material varied among

samples exposed to identical conditions, but otherwise the trends observed in Figure 2.10 remain consistent at longer exposure periods.

The samples exposed to LiCl-2wt%Li_2O solutions containing 0, 0.3, 0.6, and 1wt% Li displayed similar diffraction patterns as those presented above.

2.4.5: Raman Spectroscopy

The Raman spectrum of SS316L sample exposed to LiCl-1wt%Li_2O-0wt%Li at 650°C for 500hr is shown in Figure 2.12. This spectrum displays peaks that were observed in various ratios on all samples exposed to LiCl-Li_2O solutions in the absence of Li and is therefore used here as representative of the samples exposed to similar conditions. Both the A_{1g} mode at 572cm^{-1} and the E_g mode at 445cm^{-1} of $LiCrO_2$ are clearly defined [75]. Broad peaks centered at 250cm^{-1}, 690cm^{-1}, and 845cm^{-1} were also observed. Based on EDS and XPS analysis shown in their respective sections, the peak at 690cm^{-1} can be attributed to the A_{1g} mode of a mixed Ni, Fe, Cr spinel of the form $NiFe_xCr_{2-x}O_4$, although the exact composition of this oxide is not easily identified [76]. The position of this peak was also observed to shift slightly on other samples, which can likely be attributed to variations in the stoichiometry of the spinel due to differing exposure periods, melt compositions, and base materials. The peak at 845cm^{-1} is hypothesized to originate from Li_2CrO_4, based on the presence of Cr^{6+} in the XPS spectra collected from SS316L samples exposed to LiCl-Li_2O solutions in the absence of Li. The broad feature centered around 250cm^{-1} could not be positively attributed to any single compound, but may be caused by the

combination of the minor modes of Li_2CrO_4 and minor components of the $NiFe_xCr_{2-x}O_4$ spectrum.

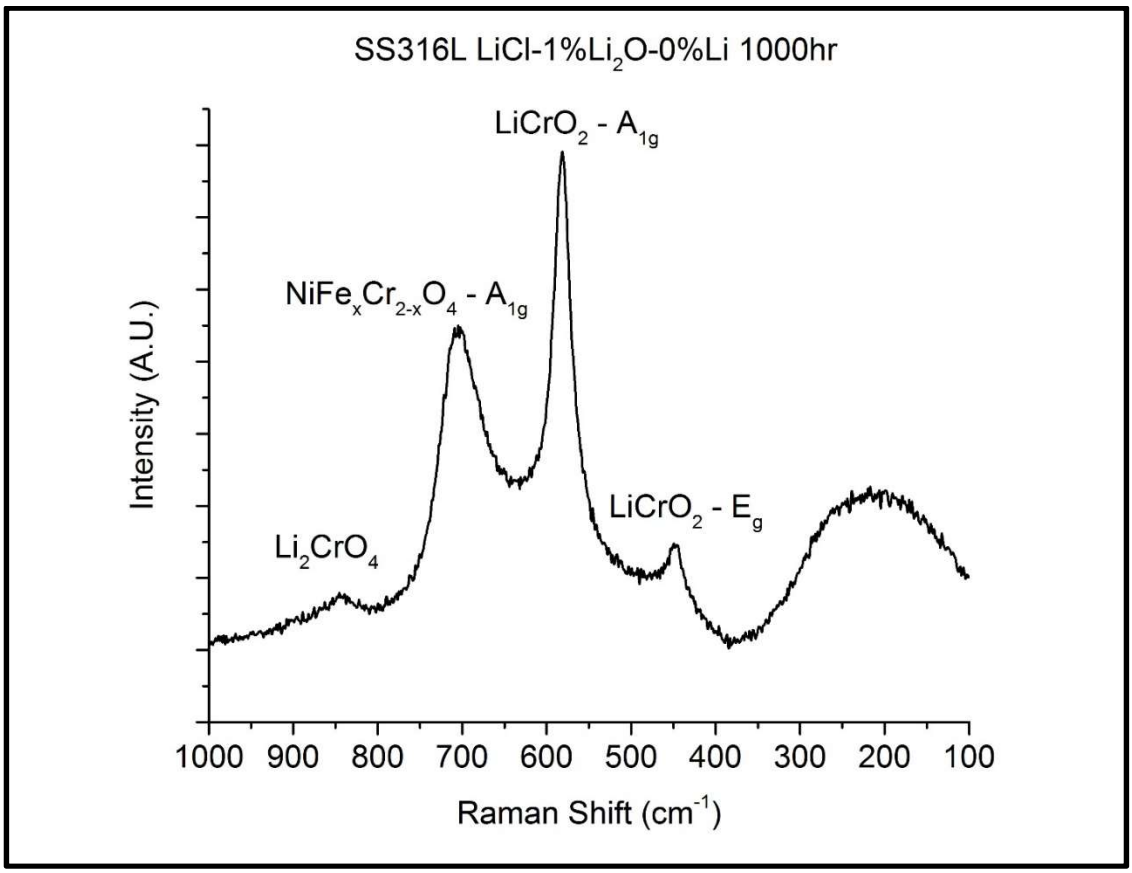

Figure 2.12: Raman spectra of the SS316L sample exposed to LiCl-1wt%Li_2O in the absence of Li for 1000hr.

When exposed to LiCl-Li_2O solutions containing Li, these oxide based surface films are destabilized due to the highly reducing nature of metallic Li. To illustrate the changes to the surface layer present on samples exposed to LiCl-Li_2O solutions as a function of Li concentration, Figure 2.13 shows the Raman spectra obtained from SS316L samples exposed to LiCl-1wt%Li_2O solutions containing 0, 0.3, 0.6, and 1wt%Li at 650°C for 500hr. The spectra collected from samples exposed to LiCl-Li_2O in the presence of Li do not display any discernible

features indicative of the well-developed oxide layer observed in Figure 2.12. Rather, the features observed are broad and are close to the baseline of the instrument, indicating that the oxide layer is tenuously present on these samples.

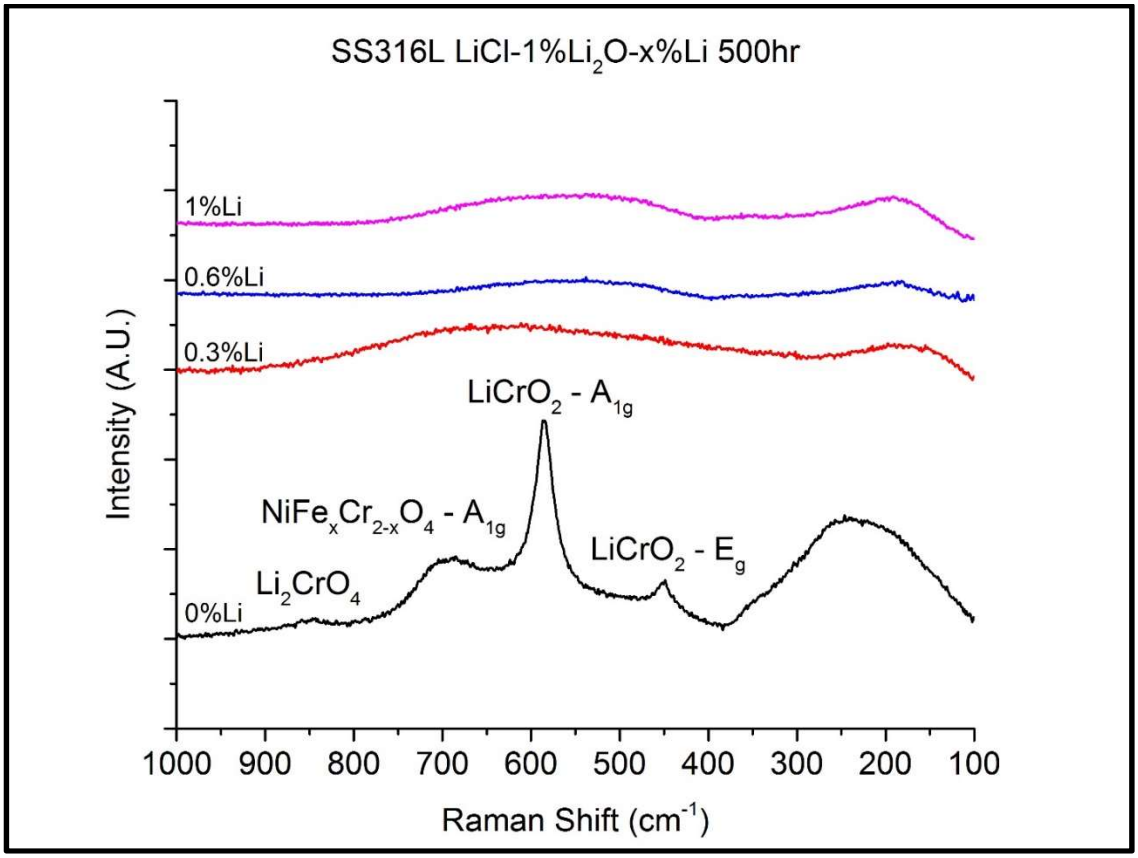

Figure 2.13: Raman spectra of SS316L samples exposed to molten LiCl-1wt% Li_2O containing 0, 0.3, 0.6, and 1wt% Li for 500 hours. The distinctive peaks characteristic of $LiCrO_2$, Li_2CrO_4 and $NiFe_xCr_{2-x}O_4$ observed on samples exposed to LiCl-Li_2O in the absence of Li are seen to be eliminated by the presence of Li in the melt.

As no investigations into the Raman spectra of Li_2CrO_4 could be found in literature, the spectra of a commercially purchased Li_2CrO_4 standard was collected to confirm that the peak seen at 845cm^{-1} in Figures 2.12 and 2.13 could be attributed to this compound. The Raman spectrum collected from pure Li_2CrO_4 is shown in Figure 2.14. The assignment of specific vibrational and rotational modes to each of the peaks observed in Figure 2.14 is beyond the

scope of this study. However, it can be seen that the primary features of pure Li_2CrO_4 occur between 1000cm^{-1} and 800cm^{-1}, with the dominant peak occurring at approximately 850cm^{-1}. Additional minor features are present between 450cm^{-1} and 275cm^{-1}. As the oxide layer of the samples is non-homogenous and consists primarily of $LiCrO_2$ with small amounts of $NiFe_xCr_{2-x}O_4$ and Li_2CrO_4, the smearing of the features of the Li_2CrO_4 spectrum to form the single, broad peak centered around 850cm^{-1} observed on the samples exposed to LiCl-Li_2O is plausible [76].

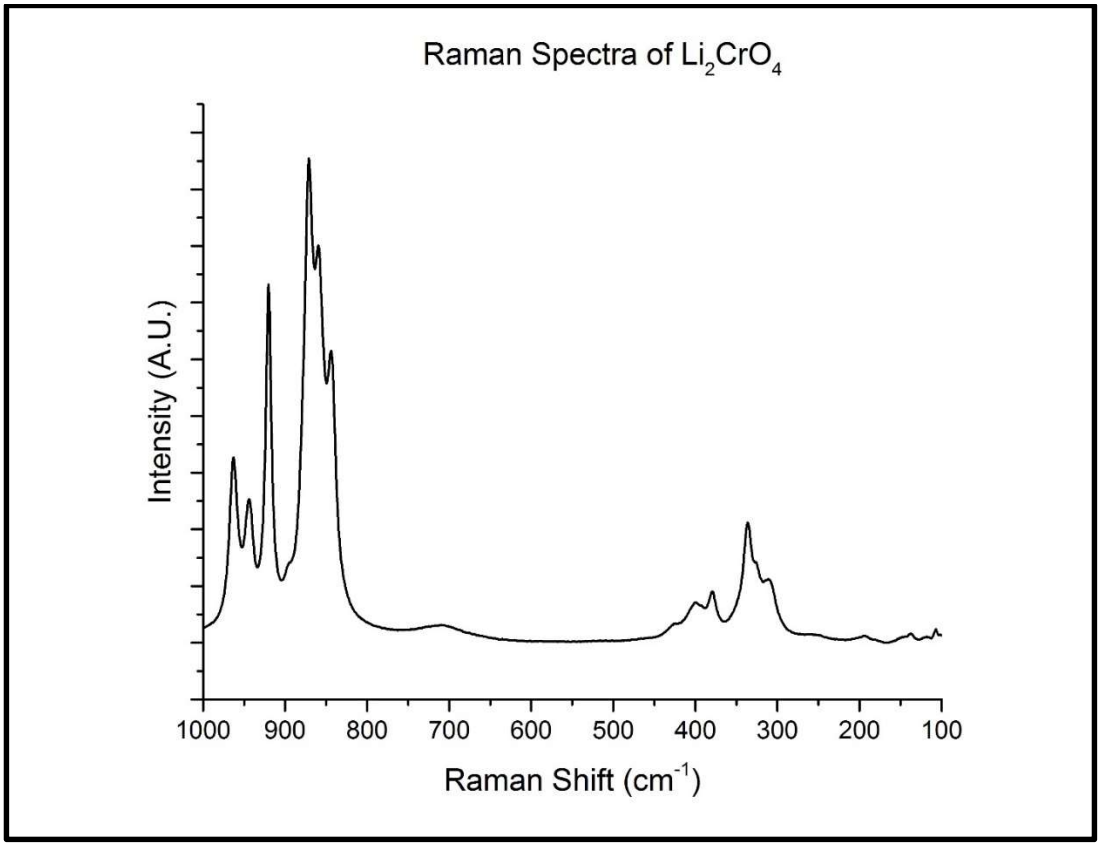

Figure 2.14: Raman spectrum obtained from Li_2CrO_4. Collection parameters were identical to those used for methanol rinsed samples. The primary features of the Li_2CrO_4 spectrum occur around 850cm^{-1}, with minor features in the range of 450cm^{-1} to 300cm^{-1}.

2.4.6: X-ray Photoelectron spectroscopy

XPS survey scans of the SS316L samples exposed to LiCl-1wt%Li_2O containing 0, 0.3, 0.6, and 1wt% Li at 650°C for 1000hr are shown in Figure 2.15. For the SS316L sample exposed to LiCl-1wt%Li_2O at 650°C for 1000hr in the absence of Li, the surface is primarily composed of Cr and O, with Ni and Fe detectable in small quantities. For the SS316L samples exposed to LiCl-1wt%Li_2O containing 0.6 and 1wt% Li at 650°C for 1000hr, the surface shows a relatively thick Ti-based surface deposit, with high quantities of N and O present. In the case of the SS316L sample exposed to LiCl-1wt%Li_2O-0.6wt%Li for 1000hr, this Ti surface film was sufficiently thick to prevent the analysis of the underlying base material. TiO_2 is a common impurity in Li_2O, and the deposition of Ti based compounds on samples exposed to LiCl-Li_2O in the presence of Li was extensively studied during our previous short term studies [26].

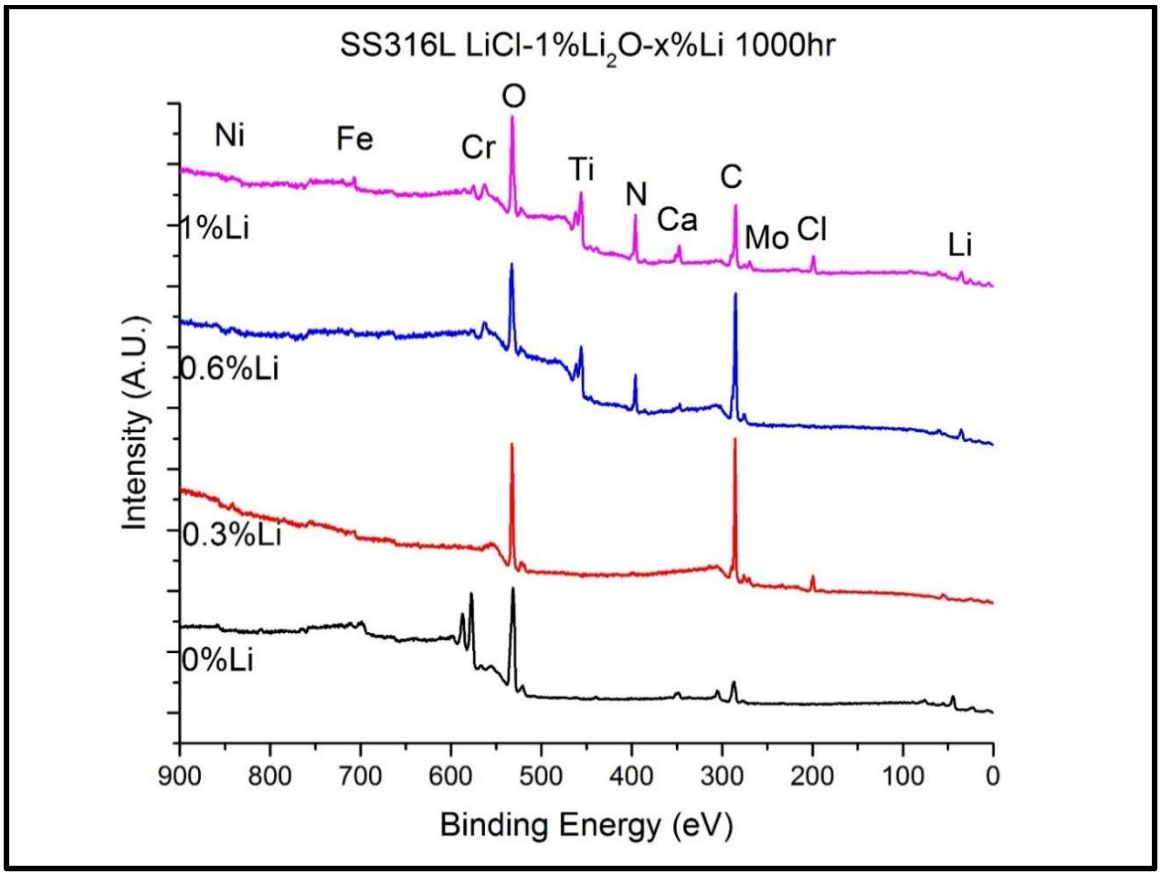

Figure 2.15: XPS survey spectra recorded on SS316L samples exposed to LiCl-1wt%Li_2O containing 0, 0.3, 0.6, and 1wt%Li at 650°C for 1000hr after rinsing in methanol.

Analysis of the alloying elements, especially the Cr 2p spectra, is necessary to determine the corrosion mechanisms of SS316L in LiCl-Li_2O-Li, as Cr is the primary element responsible for the formation of oxide films in the absence of Li. Identification of the oxidation state of Cr present on the surface of the SS316L sample exposed to LiCl-1wt%Li_2O-Li at 650°C for 500hr was performed by peak fitting the Cr $2p_{3/2}$ spectra using previously published peak fitting parameters [77]. The peak fit data for all Cr spectra collected on the samples in this study are shown in Figure 2.16, while the peak fitting parameters are given in Table 2.6 [77].

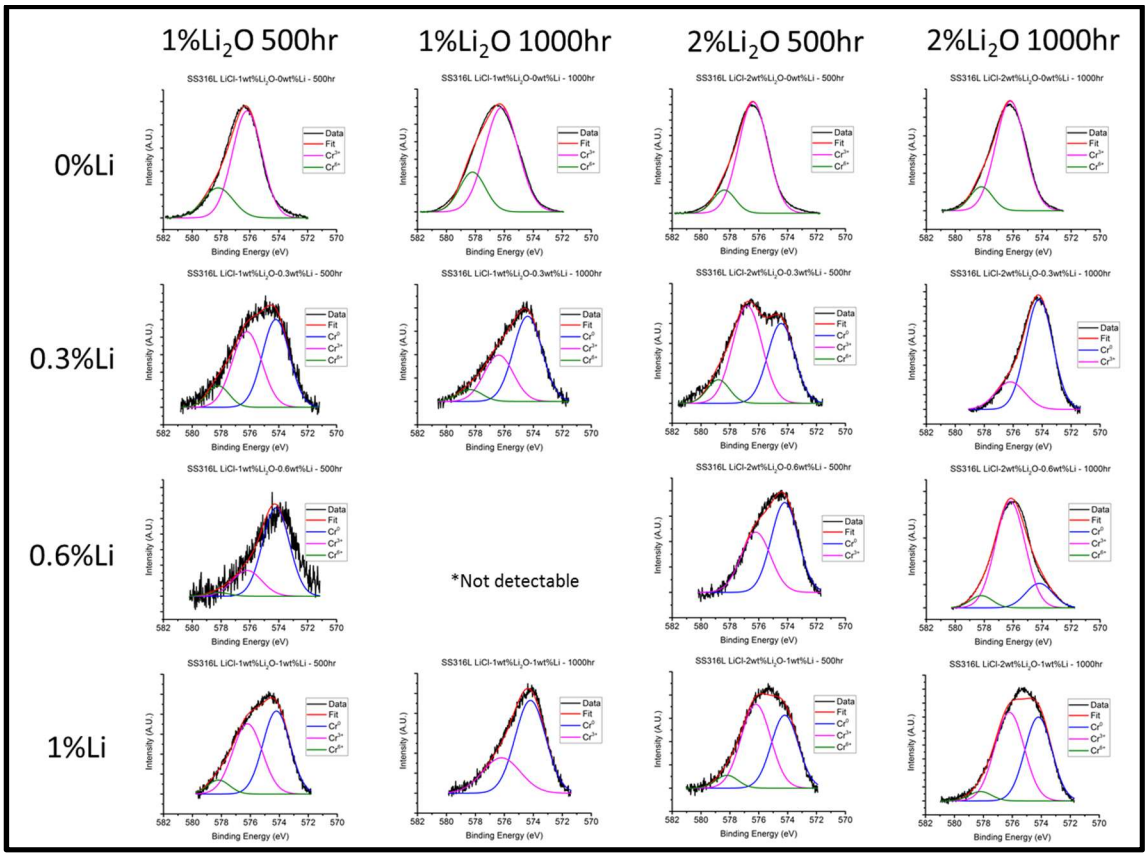

Figure 2.16: Cr 2p XPS spectra collected from SS316L samples exposed to all LiCl-Li_2O-Li compositions and exposure periods studied in this work. Charge correction was performed to the adventitious C 1s peak at 284.8eV, and peak fitting parameters for Cr^0, Cr^{3+}, and Cr^{6+} listed in Table 2.6 were used for all spectra. Cr^{3+} and Cr^{6+} are the only species present in the absence of Li. Cr spectra of SS316L samples exposed to molten LiCl-Li_2O in the presence of Li indicate both metallic and oxidized components; however, no discernible trend in oxidation state based on Li concentration, Li_2O concentration or exposure period could be determined. Cr was not detectable on the SS316L sample exposed to LiCl-1wt% Li_2O-0.6wt%Li for 1000hr due to the thickness of the overlying TI surface deposit.

Table 2.6: Peak fitting parameters used for Cr $2p_{3/2}$ spectra reported in Figure 2.16 [77].

Peak	BE	FWHM
Cr^0	574.2	2.2
Cr^{3+}	576.2	2.4
Cr^{6+}	578.2	1.8

As can be observed in Figure 2.16, both Cr^{3+} and Cr^{6+} are simultaneously present on all SS316L samples exposed to LiCl-Li_2O solutions in the absence of Li^0. The presence of Cr^{3+} and Cr^{6+} on the samples further supports the presence of both $LiCrO_2$ (Cr^{3+}) and Li_2CrO_4 (Cr^{6+}) on the surfaces of samples exposed to LiCl-Li_2O solutions in the absence of Li. In the presence of Li, the highly reducing nature of metallic Li destabilizes the oxide films that are present on the sample surfaces in the absence of Li. However, the transition between electrochemical oxidation of the samples in the absence of Li and liquid metal attack in the presence of high Li concentrations is not abrupt. Our previous short term studies have shown that at concentrations at or below the apparent solubility limit of Li in the system (around 0.3wt%Li) [16], there exists a transition region where both modes of attack occur simultaneously[25, 46]. The Cr $2p_{3/2}$ spectra shown in Figure 2.16 give further evidence for this hypothesis, although there was no discernible trend in the relative ratios of Cr^0, Cr^{3+}, and Cr^{6+} based on the concentration of Li, Li_2O, or exposure period.

The presence of Cr^{3+} is also required for the formation of $NiFe_xCr_{2-x}O_4$, as both Fe and Cr are in the 3+ oxidation state in this compound, while Ni is present in the 2+ oxidation state. Further confirmation of the presence of $NiFe_xCr_{2-x}O_4$ is given by the narrow scans of the Ni 2p and Fe 2p spectra for SS316L exposed to LiCl-1wt%Li_2O-0wt%Li for 500hr, which are shown in Figure 2.17, along with the Ni 2p and Fe 2p narrow scans for the SS316L sample exposed to LiCl-1wt%Li_2O-0.3wt%Li for 500hr. In the absence of Li, the Ni $2p_{3/2}$ peak is located at 853.5eV, while the Fe $2p_{3/2}$ peak is located at 710.1eV. These binding energies

and peak shapes correspond to Ni^{2+} and Fe^{3+}, respectively [78]. Neither element was detected in the metallic state, confirming the presence of Ni and Fe based oxides on the sample surface. In conjunction with Raman spectroscopy and EDS analysis, this is further evidence supporting the presence of a $NiFe_xCr_{2-x}O_4$ based spinel present on the surface of the samples exposed to LiCl-Li_2O in the absence of Li. However, when Li was present in the molten salt, only metallically bonded Ni and Fe are present on the sample surface. No charge correction was necessary for the Ni and Fe 2p spectra, indicating that these elements were in direct electrical contact with the base material. Similar spectra were recorded for all other SS316L samples exposed to LiCl-Li_2O-Li, indicating that any quantity of Li^0 in the melt is sufficient to reduce $NiFe_xCr_{2-x}O_4$.

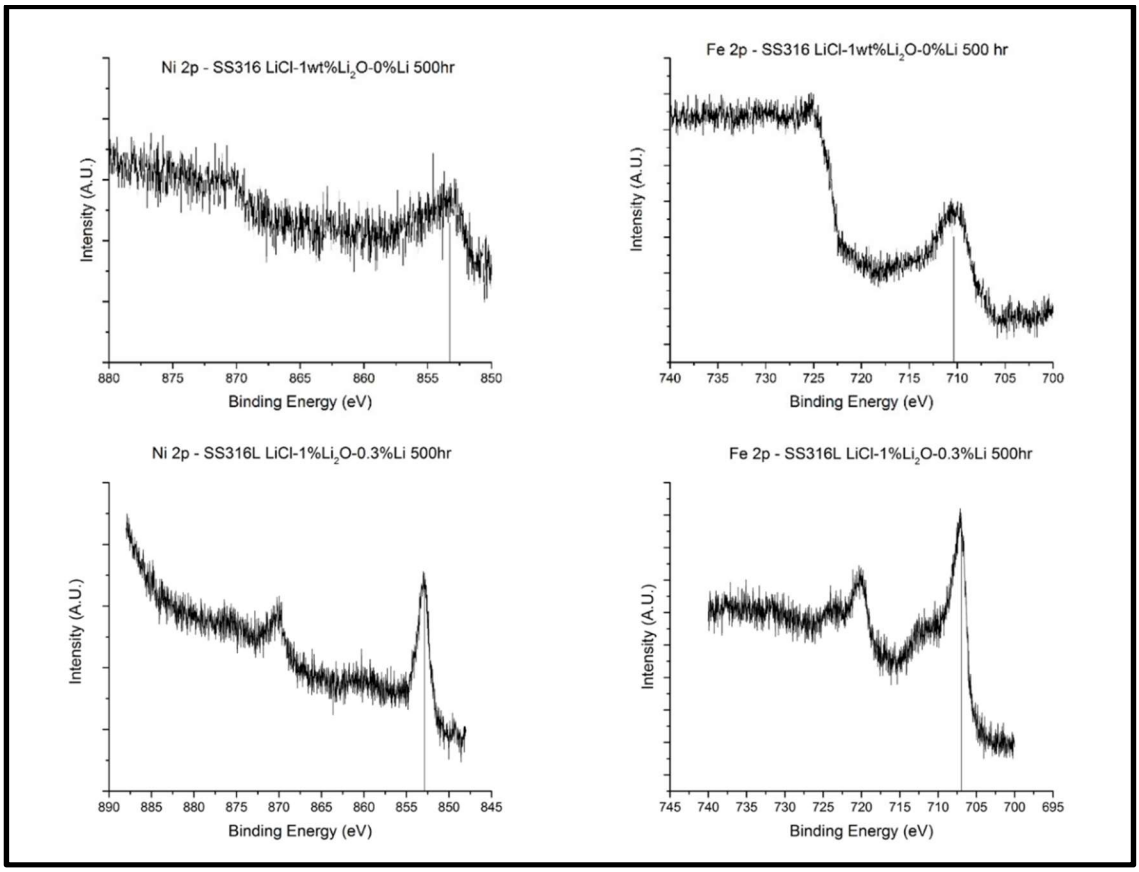

Figure 2.17: XPS narrow scans for Ni 2p (left) and Fe 2p (right) collected from SS316L exposed to LiCl-1%Li_2O-0%Li (Top) and LiCl-1wt%Li_2O-0.3wt%Li (Bottom) at 650°C for 500hr. In the absence of Li, Ni is present in the 2+ oxidation state and Fe is present in the 3+ oxidation state based on their binding energies of 853.5eV and 710.1eV, respectively. However, in the presence of Li, all Ni and Fe spectra indicate the presence only of metallic Ni and Fe.

In our previous work, Mo was observed to behave similarly to Cr in some respects, becoming enriched on the surface in the absence of Li, and depleted at higher Li concentrations. As Mo is a minor alloying element of SS316L at around 2wt%, Mo was not observed on all samples. Additionally, in the absence of Li, Mo was not detectable via XPS on any sample due to the thick $LiCrO_2$ surface layer. However, the samples exposed to molten LiCl-2wt%Li_2O solutions containing 0.3, 0.6, and 1wt%Li for 500hr all had detectable levels of Mo, the narrow scans of which are presented in Figure 2.18. From the spectra in Figure

2.18, it can be observed that when 0.3wt% Li is present in solution, Mo^{6+} is the only Mo species observable on the sample surface [79]. However, as Li concentration increases the stability of oxidized Mo is decreased, resulting in a mixed Mo^{6+}/Mo^{0} spectra at 0.6wt% Li and a fully metallic Mo^{0} spectra at 1wt% Li [79, 80]. The observation of Mo^{6+} on samples exposed to high concentrations of Li indicates that Mo is highly active in the LiCl-Li_2O-Li system, which could explain the depletion of Mo from the surface of SS316L observed via SEM-EDS analysis of the cross section of these samples in section 4.2.

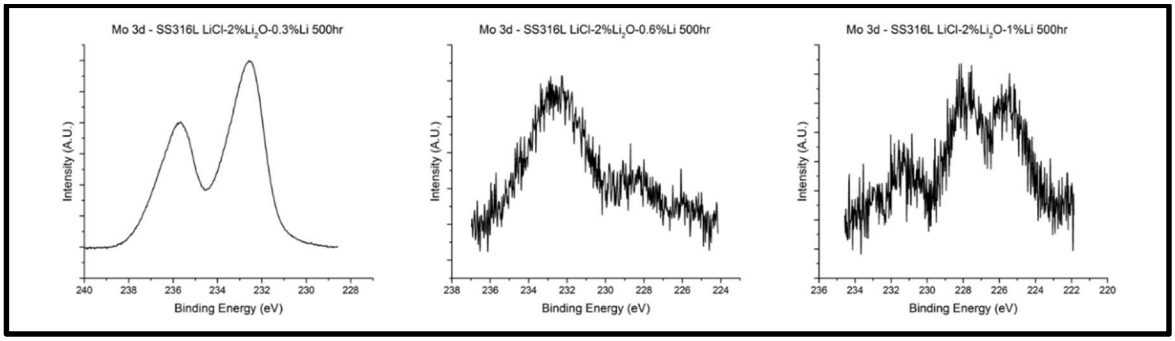

Figure 2.18: Mo 3d XPS spectra of SS316L samples exposed to molten LiCl-2wt%Li_2O solutions containing 0.3, 0.6, and 1wt%Li for 500hr. As Li concentration in the melt is increased, the Mo oxidation state shifts towards more reduced species. The peak shape for the SS316L sample exposed to LiCl-2wt%Li_2O-1wt%Li for 500hr is likely the result of differential charging and the charge correction performed to the adventitious C 1S peak at 284.8eV.

Co was also observed on some samples exposed to LiCl-Li_2O in the presence of Li. Co is not an alloying element of SS316L, but is present as the primary impurity in the Ni crucibles used for these studies at concentrations of less than 1wt%. Consequently, the presence of Co on the surface of the samples exposed to LiCl-Li_2O solutions in the presence of Li indicates that there is mass transport from the crucible to the samples. Mass transport of Co from the crucible to the samples had not been observed in our previous short term experiments

[25, 39, 46]. The Co 2p spectra of the SS316L sample exposed to LiCl-1wt%Li_2O-0.3wt%Li for 500hr is presented in Figure 2.19, and is typical of Co^{3+}, due to its binding energy and peak shape [78]. The cause of the transport of Co from the crucible to the samples and its implications to the degradation of materials in the LiCl-Li_2O-Li system as a whole requires further investigation.

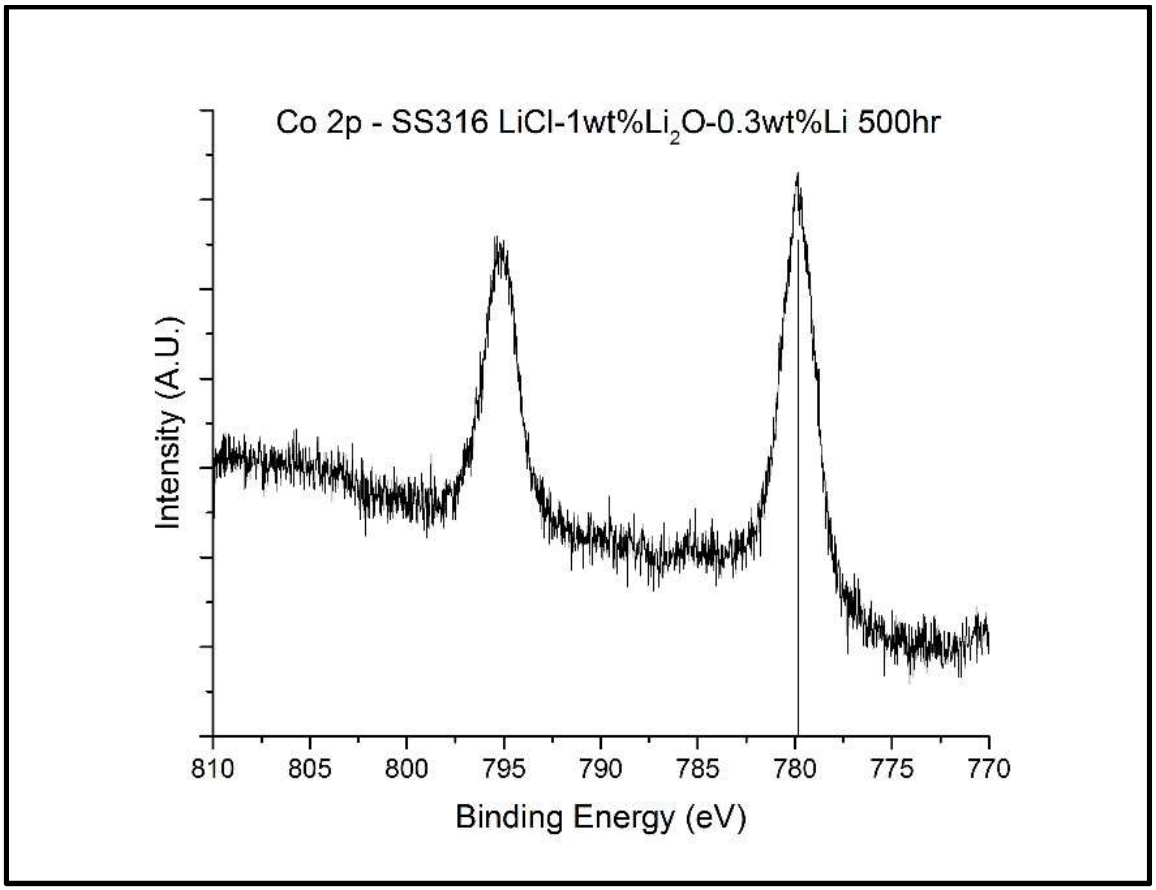

Figure 2.19: XPS narrow scan of the Co 2p peak observed on SS316L exposed to LiCl-1wt%Li_2O-0.3wt%Li at 650°C for 500hr and rinsed with methanol. The binding energy and shape of the $2p_{3/2}$ peak of 789.8eV is consistent with the presence of Co^{3+}.[81]

2.5: Conclusions

Exposure testing of SS316L samples was performed for 500 and 1000hr intervals in molten LiCl-Li_2O-Li solutions containing 1 and 2wt% Li_2O and 0, 0.3,

0.6, and 1wt% Li. Morphological and elemental changes to the sample surfaces and cross sections were investigated via SEM and EDS, respectively, while XRD, Raman spectroscopy, and XPS were used to provide further insight into the effect of Li^0 on the degradation mechanisms of materials in LiCl-Li_2O-Li. Upon exposure to LiCl-Li_2O solutions in the absence of Li, SS316L was observed to form a $LiCrO_2$ based surface film, with minor contributions of Li_2CrO_4 and $NiFe_xCr_{2-x}O_4$. The oxide layer limited corrosion to a rate of approximately 0.24mm/year during exposure to molten LiCl-Li_2O solutions. The presence of Li in the melt resulted in the destabilization of the protective oxide film formed in LiCl-Li_2O solutions, causing substantial damage to the samples in the form of intergranular corrosion. XPS analysis observed that metallically bonded Ni and Fe were present on the surface of all SS316L samples exposed to LiCl-Li_2O in the presence of Li, however both Cr and Mo displayed varying degrees of oxidation in the presence of Li. Mass loss rates were low, but cross sectioned samples displayed significant ingress of LiCl and damage to the sample surface, indicating that mass loss measurements alone are not sufficient to characterize corrosion in this system. Intergranular corrosion was facilitated by the precipitation of metal carbides and nitrides along the grain boundaries, resulting in the selective depletion of alloying elements, such as Cr, Mo, and Mn. The rate of material damage was on the order of 2-3mm/year, indicating that the presence of high concentrations of Li during the electrolytic reduction of UNF will dramatically reduce the lifetime of any SS316L components exposed to the electrolyte. The ingress of intergranular corrosion into the material will likely have

a marked effect on the strength of the material due to the effective loss of structural thickness, however, further investigation would be necessary to validate this hypothesis. From the combination of analytical techniques presented in this work, it is hypothesized that cyclical oxidation by O^{2-} ions and reduction by Li^{0} is responsible for the high levels of material degradation in the LiCl-Li_2O-Li system.

Chapter 3 : Effect of metallic Li on the corrosion behavior of Inconel 625 in molten LiCl-Li2O-Li

As published in the Journal of the Electrochemical Society

Volume 166, Issue 6, Pages C162-C168, April 2019

Authors: William Phillips and Dev Chidambaram

https://doi.org/10.1149/2.0201906jes

Abstract:

The corrosion behavior of Inconel 625 in molten LiCl solutions maintained at 650°C and containing various quantities of Li_2O and metallic Li was studied for possible application in the electroreduction of used oxide-based nuclear fuel. This study focusses on the morphological and elemental changes on the surface of the samples with an emphasis on cross-sectional analyses conducted using focused ion beam microscopy. In the absence of metallic Li, a stable oxide film is formed that limits the corrosion of the base material to 0.07mm/year. However, in the presence of metallic Li, the formation of this film is impeded, resulting in dealloying of the base material and the formation of a highly porous microstructure composed primarily of Ni.

Keywords: Hot corrosion, Pyroprocessing, FIB.

3.1: Introduction

In order to reprocess used nuclear fuel (UNF) from light water reactors using pyrometallurgical techniques, a reduction operation is necessary to convert UO_2-based UNF into a metallic product that can then be processed in subsequent unit operations [7, 8, 48, 50, 82]. The prototypical process by which the reduction of UO_2 is conducted is via the electrolytic reduction operation developed at Argonne National Laboratory (ANL) [7, 49]. In this process, LiCl containing 1 to 2wt% Li_2O and maintained at 650°C serves as the electrolyte [56, 83]. The reduction is performed with UNF loaded in a stainless steel cathode basket which is polarized vs. a suitable anode, typically made of Pt, either galvanostatically or potentiostatically [8, 17]. To achieve high reduction yields, it has been shown by a number of researchers that it is necessary to polarize UO_2 at potentials beyond the electrochemical window of Li_2O, which results in the formation of metallic Li at the cathode [8, 13, 17]. Some of the metallic Li thus generated then metalothermically reduces the UNF in the cathode; however, LiCl is capable of solvating Li to a limited degree, which leads to the formation of a tertiary LiCl-Li_2O-Li electrolyte [8, 13, 17]. As the process goes to completion, the electrolyte eventually reaches Li saturated conditions, and may even form and be present as clusters [22]

The dissolution of alkali metals in their respective alkali halides has been well studied over the last century, notably by M.A. Bredig at Oak Ridge National Laboratory, among others [59, 84, 85]. The two primary models of alkali metal –

alkali halide systems are the f- center model and the sub-halide model [84]. In the f- center model typical for alkali metal – alkali halide systems, the excess electron is delocalized from any particular cation core, leaving a free electron that imparts a metallic character to the molten solution [84]. This leads to several orders of magnitude increase in electrical conductivity of solution as the concentration of the alkali metal increases towards saturation, as well as causing a number of other changes in physical and chemical properties. The sub-halide model is typically representative of transition metals and post-transition metals in their respective halides and gives rise to the formation of abnormally reduced species due to the formation of complex molecules that keep electrons localized to the molecular scale, as is typical for the Bi-$BiCl_3$ system [84]. Sub-halide forming systems are not associated with an increase in electrical conductivity in the same manner as the f- center model predicts. Other dissolution mechanisms have also been reported, such as the formation of colloidal suspensions of nanoclusters of Na_2 or Li_8 in the Na-NaCl and Li-LiCl systems, respectively [22, 84]. It is important to note that none of these effects are mutually exclusive, and it is possible that the simultaneous action of multiple dissolution mechanisms may occur simultaneously in the same system. Of the alkali metal – alkali halide systems, the Li-LiCl system has proven to be particularly challenging in the determination of the solubility limit of the metal in the metal salt, with the apparent solubility limit seeming to vary depending on the experimental methods; however, approximately 0.3wt% has been shown to be a useful estimate at the temperatures of the electrolytic reduction operation [16, 20, 24, 59, 60, 84, 86].

Importantly, the concentration of Li_2O has been shown to have minimal effect on the measured solubility limit of Li in LiCl-Li_2O [86]. The discrepancy between the various reported values of the solubility limit of Li in LiCl may be due to the simultaneous action of the various dissolution mechanisms theorized for this system [22].

For the electrolytic reduction of UNF to be implemented on a large scale, knowledge of the degradation of materials in contact with the electrolyte is necessary, particularly for the container material. Corrosion in molten LiCl-Li_2O under inert or oxidizing atmospheres has been fairly well studied, and the corrosion of various materials has been found to follow similar mechanisms to those observed in other molten salt systems [63-66, 68, 69, 87]. Primarily, the dissolution of alloying elements, and consequently the corrosion rate, is governed primarily by the activity of the O^{2-}ion in the solution according to the Lux-Flood model of salt basicity, as well as by the presence of impurities such as moisture or transition metal halides [33, 63, 71]. For the electroreduction process, such models are insufficient to completely describe corrosion due to the presence of dissolved Li. To date, very few investigations into the effects of Li on the corrosion of materials exposed to this system have been performed [25, 39, 42, 44, 46, 47]. The initial studies conducted by Indocochea, *et al.* conflicted with studies conducted by Mishra and Olson due to widely varying experimental parameters, leading to confusion about the effect Li had on the degradation observed [42, 44]. Recent studies have been performed to address these issues, but were of short term in nature and did not investigate the degradation of the

materials studied in cross section [25, 39, 46]. These studies showed that a transition from molten salt based corrosion to a liquid metal attack induced degradation occurred at approximately 0.6wt%Li, and that the concentration of both Li and Li_2O affected the corrosion processes that were observed. Recent work by researchers at the Korean Atomic Energy Research Institute showed that Ni displayed minimal corrosion in the absence of Li, but underwent significant degradation in the presence of metallic Li [47]. In this light, the current study investigates the corrosion behavior of Inconel 625 (I625) in the LiCl-Li_2O-Li system at 650°C. To understand the effect of oxide concentration, metal concentration and the period of exposure, the solution chemistries studied consisted of LiCl containing 1 or 2wt% Li_2O and 0, 0.3, 0.6, or 1wt% Li, with samples exposure periods of 500 and 1000hr. This study focusses on the observed degradation of I625 under these conditions by determining the changes to the microstructure and elemental composition using scanning electron microscopy (SEM) coupled with energy dispersive X-ray spectroscopy (EDS) of the sample surfaces as well as their cross sections.

3.2: Experimental

Experiments were conducted in a Vacuum Atmospheres OMNI-LAB glovebox under Ar containing less than 2ppm O_2 and less than 1ppm H_2O. Anhydrous LiCl, Li_2O, and Ni crucibles were obtained from Alfa-Aesar and were of 99%, 99.5%, and 99% purity, respectively. Li metal of 99% purity was purchased from Strem Chemicals. I625 coupons were cut from a 3.175mm thick

plate obtained from High Performance Alloys.. The composition of this alloy as measured via the EDS used for cross sectional investigation was 62.3wt% Ni 23.5wt% Cr, 6.5wt% Mo, 5.1% Fe, and 2.6wt% Nb.

Studies were conducted using duplicate samples, and 500 hour and 1000 hour exposures were conducted in parallel, with the 500 hour samples removed from the experiment upon completion of the allotted exposure period. A 6.5 inch inner diameter, 6 inch tall cylindrical heater from Watlow (1500 watts) was used to maintain a temperature of 650±5°C for the duration of the exposure period. A 6 inch diameter graphite block was machined to accommodate 5 Ni crucibles, with slots machined to accommodate the sample hanging rods. This configuration allowed for repeatable placement of the samples within the melt during the salt replacement procedure outlined below. Two identical furnaces were constructed to maximize the number of experiments that could be ran in parallel. In operation, four experiments were ran simultaneously in each furnace, which allowed for the extra 5^{th} crucible location to be used for salt replacement purposes.

Prior to exposure, the metal samples were cut into 1.27cm by 1.27cm squares using a CO_2 laser. The samples were then polished to a 1 µm surface finish on both sides using a diamond abrasive and spot welded to loops of SS316L wire for suspension from the sample hanging rods, as was performed in our previous studies [25, 39, 46]. Sample hanging rods were made of like material to the samples, as alumina rods proved to be incapable of withstanding the highly reducing atmosphere directly over the molten solutions containing

metallic Li for the duration of these experiments. The mass of each sample was recorded immediately prior to exposure.

Considering the evaporation of Li and Li_2O over time that was observed in other short-term studies and the extended exposure periods of this study, the salt charge for each test was replaced at a period of once every 96 hours to maintain the solution chemistry [25, 26, 39, 46, 88]. To minimize the effects of impurity H_2O, LiCl was dried in a vacuum oven in air at 200°C for 24 hours before being transferred into the glovebox for storage [19, 25]. Immediately prior to insertion in the primary furnace, a cleaned Ni crucible containing the weighed amount of LiCl was dried under Ar for 2hr in a dedicated furnace maintained at 550°C. After insertion into the primary furnace, the LiCl was allowed 1 hour to reach thermal equilibrium, after which time the required mass of Li_2O and Li were added to the molten salt by placing the Li_2O powder and Li pellets on top of the solution. Total salt mass contained in each crucible was 50g. The melt was allowed to equilibrate for another hour prior to the transfer of the corrosion specimens from the old salt charge to the new salt charge. As the concentration of Li was above the solubility limit for the 0.6 and 1wt% tests, a significant fraction was likely present as a colloidal suspension. Sample transfer was accomplished via specially fabricated tongs, which allowed for the transfer time to be less than 5 seconds on average. Following transfer of the samples to the new salt charge, the old salt charge was removed from the furnace and allowed to cool to room temperature. The cooled salt ingot was then dissolved in deionized (DI) water. The Ni crucible was then sanded with 600 grit SiC paper, rinsed with DI water,

cleaned with isopropyl alcohol, and dried under vacuum prior to re-use for the next salt charge for the same solution chemistry conditions. Two Ni crucibles were alternated between for each solution chemistry.

Following completion of the exposure period, the samples were removed from the furnace and allowed to cool to room temperature in the glovebox atmosphere. All samples were stored in the Ar glovebox between analytical procedures. As it was unknown if the surface films formed on the corrosion specimens would be stable in atmosphere, surface analysis was performed both prior to and following removal of the residual salt layer. Following the initial surface analytical procedures, residual LiCl was removed by placing each sample in 25ml of HPLC grade methanol for 15 minutes with constant agitation. Prior to the methanol rinsing procedure, all surface analysis was performed under inert atmosphere or vacuum conditions, depending on technique. The data presented here were collected following the methanol rinsing procedure, as the residual salt layer significantly interfered with surface analysis as has been described earlier [25]. No chemical or morphological changes were observed as a result of the methanol rinsing procedure. Gravimetric weight change measurements were performed following the methanol rinsing procedure.

All samples exposed to Li containing melts were cross sectioned using a Buehler cubic-BN wafering blade on a slow speed saw and polished according to Buehler's recommended polishing techniques to a 0.05μm surface finish prior to analysis. Samples exposed to LiCl-Li_2O in the absence of Li were investigated

using only FIB milling for cross sectional analysis due to the relatively shallow depth of attack.

SEM of the sample surfaces was performed using a Hitachi S-4700 and EDS data was collected via the attached Oxford Instruments energy dispersive X-ray spectrometer. The electron beam was operated at an accelerating voltage of 5kV for surface morphology images, while 20kV was used for collection of EDS spectra. Emission current was maintained at 10mA. FIB milling and subsequent SEM-EDS analysis for cross sectional images was performed using a FEI Scios dual-beam FIB/SEM equipped with a TEAM Pegasus Integrated EDS-EBSD. The same dual-beam FIB/SEM was used to perform the SEM-EDS analysis of all of the cross sectioned samples, including those mechanically cross sectioned and polished. The electron beam was operated at 20kV for both imaging and EDS analysis.

The exposed surface area was calculated based on the measured submersion depth of each sample. The average corrosion rate in mm/year and the mass loss rate in mg cm^{-2} hr^{-1} was then calculated based on the mass change, density of the alloy, exposed surface area, and length of exposure

3.3: Results

The surface of I625 samples exposed to LiCl-Li_2O solutions in the absence of Li displayed a high degree of crystallinity indicative of a well-formed oxide layer, while the surfaces of samples exposed to LiCl-Li_2O in the presence

of metallic Li showed a very porous, almost sponge-like microstructure. To illustrate these points, the SEM micrographs taken of the I625 samples exposed to LiCl-1wt%Li_2O containing 0, 0.3, 0.6, or 1wt%Li for 500hr are shown in Figure 3.1.

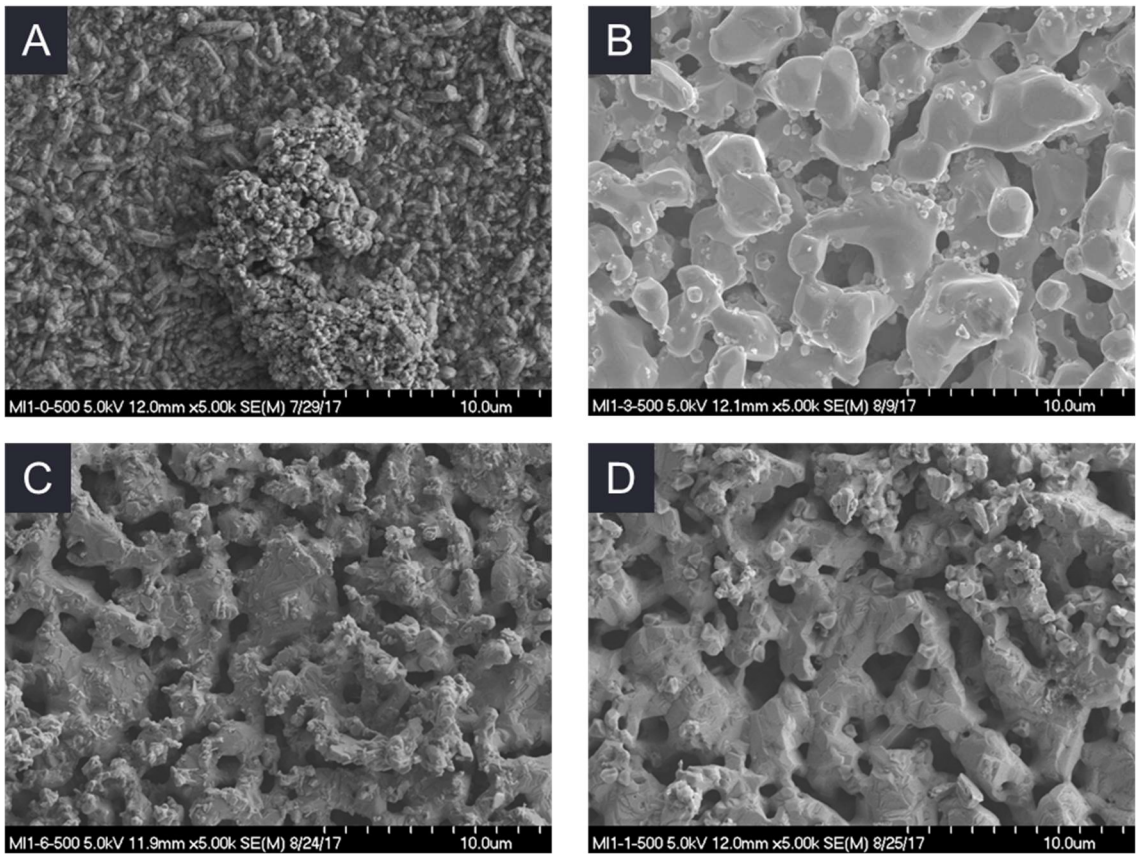

Figure 3.1: SEM micrographs of I625 exposed to LiCl-1wt%Li2O at 650°C containing A) no Li, B) 0.3wt%Li, C) 0.6wt%Li, and D) 1wt%Li for 500hr and rinsed with methanol.

In the absence of Li, the oxide layer is well formed and shows evidence of a multi layered structure that is discussed in greater detail below. EDS analysis of the area shown in Figure 3.1(a) showed that the surface was composed of 22at% Cr, 66at%O, and 13at%Ni, with minor quantities of other elements, indicating a primarily Cr based oxide layer. Li is not detectable via EDS, however,

spectroscopic analysis has definitively shown this compound to be $LiCrO_2$ [89]. The presence of Li in the molten LiCl-Li_2O solution destabilizes the oxide layer and forms a very porous microstructure that is similar in appearance to a Ni foam. EDS analysis of these areas consistently showed greater than 80at%Ni, with high depletion of Cr, Mo, and Nb, although the Ni:Fe ratio remained close to that of the base material. There was little difference between the microstructures observed at low and high Li concentrations, with the microstructure of the I625 samples exposed to melts containing 0.3wt%Li displaying microstructures nearly identical to samples exposed to melts containing 1wt%Li. Exposure periods of 500hr and 1000hr both yielded nearly indistinguishable microstructures, as can be observed by comparing the micrographs of I625 samples exposed to LiCl-1wt%Li_2O containing 0, 0.3, 0.6, and 1wt%Li for 1000hr shown in Figure 3.2 to the micrographs presented in Figure 3.1.

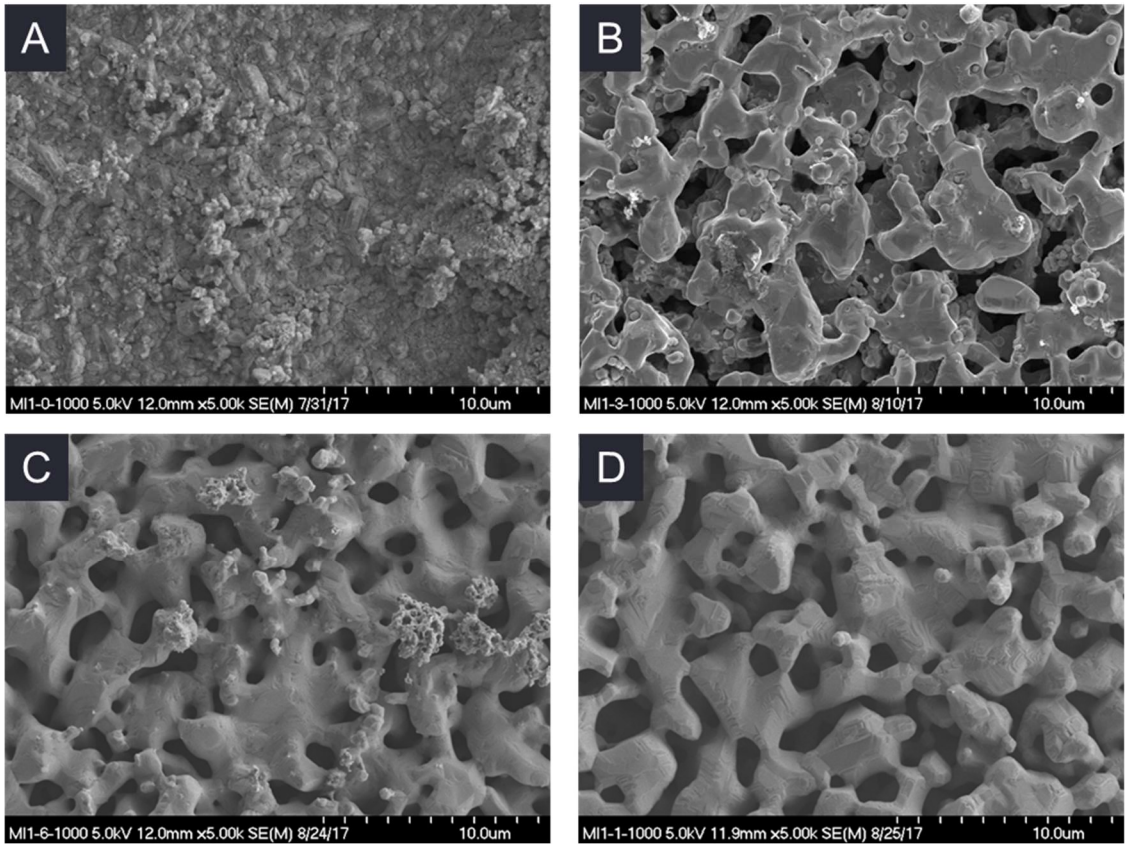

Figure 3.2: SEM micrographs of I625 exposed to LiCl-1wt%Li2O at 650°C containing A) no Li, B) 0.3wt%Li, C) 0.6wt%Li, and D) 1wt%Li for 1000hr and rinsed with methanol.

Variations in Li_2O concentration and exposure length did not dramatically alter the morphology observed on I625 samples exposed to LiCl-Li_2O-Li compared to those shown in Figures 3.1 and 3.2. Consistent morphology was observed in the presence of Li, with all samples displaying similar structures. Likewise, in the absence of Li, a well-developed, highly crystalline oxide layer was consistently observed. Additionally, the surface of the I625 sample exposed to LiCl-2wt%Li_2O-0wt%Li for 500hr had a small number of locations where the oxide layer had partially delaminated, which allowed for direct observation of the layered structure of the oxide films formed on I625 during exposure to LiCl-Li_2O in the absence of Li. SEM micrographs of one of these locations are shown in

Figure 3.3, and the compositions of locations 1 through 4 detected via EDS are given in Table 3.1.

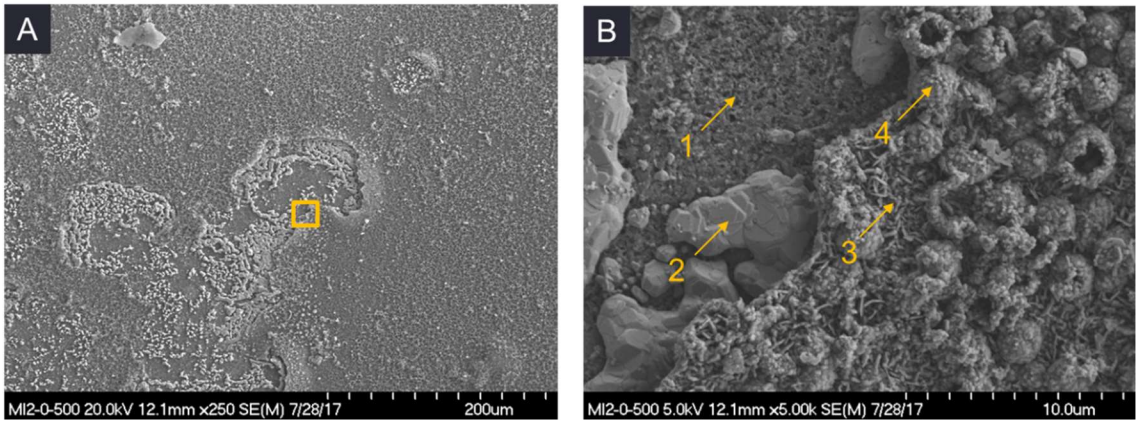

Figure 3.3: SEM micrographs taken at (A) low magnification and (B) high magnification of the highlighted area on the I625 sample exposed to LiCl-2wt%Li_2O-0wt%Li at 650°C for 500hr after methanol rinsing. The delamination of the outer surface layer on this sample provided a unique opportunity to examine the layered structure of the oxide films that form on I625 upon exposure to molten LiCl-Li_2O in the absence of Li. The compositions of Layers 1 through 4 in image B were obtained via EDS analysis and are given in Table 3.1, below.

Table 3.1: EDS compositional analysis obtained for locations 1 through 4 marked in Figure 3.3B for the I625 sample exposed to LiCl-2wt%Li_2O-0wt%Li at 650°C for 500hr.

Element	Layer 1 Atomic%	Layer 2 Atomic%	Layer 3 Atomic%	Layer 4 Atomic%
C				5.07
O	62.43	11.22	61.07	65.48
Mg	1.35		2.56	3.14
Cl	0.41		0.27	0.47
Cr	18.34	3.33	12.99	20.07
Fe	0.61	3.74	1.21	0.32
Ni	15.23	80.97	21.44	5.13
Nb	0.9			
Mo	0.73	0.74		
Ti			0.46	0.32

The presence of a multilayered oxide structure is easily discernable in this image. Each layer was analyzed using EDS at the spots marked by the arrows. The layers were numbered 1 through 4 starting with the innermost and proceeding outward. Due to the composition of Layer 2 and the lack of Ti in both Layers 1 and 2, which is present as an impurity in the Li_2O used in this study, it is thought that Layer 1 is the result of the inward diffusion of O into the base material. The O concentration of Layer 2 is much lower than in any of the other layers observed here, and its composition is the most similar to the base alloy, although all areas analyzed were notably depleted in Mo and Nb. The size of the grains in Layer 2 and their relative orientations are also similar to the morphology of the I625 samples exposed to LiCl-Li_2O in the presence of Li, as can be

observed by comparison with Figures 3.1 and 3.2, indicating that this is likely the base material which has been depleted in Cr to facilitate the outward growth of Layers 3 and 4. These outermost layers differ in both morphology and composition, suggesting a difference in the compounds that compose them. Layer 3 is the layer closest to the base material, and has a plate-like morphology. The high Ni content of Layer 3 compared to Layer 4 implies that Layer 3 is composed of primarily $NiFe_xCr_{2-x}O_4$ with a relatively low value of x, while Layer 4 is primarily $LiCrO_2$ based. Both Layer 3 and Layer 4 have incorporated Ti from the impurities present in the Li_2O used in this study. The spheroidal morphology of Layer 4 suggests that its growth begins at specific nucleation sites. Some of these spheroids from Layer 4 appear to be broken or incompletely formed, showing that they are hollow. Figure 3.4 shows the results of EDS mapping of Ni, Fe, Cr, and O for the same location shown in Figure 3.3 which further highlights the differences between the layers observed on this sample.

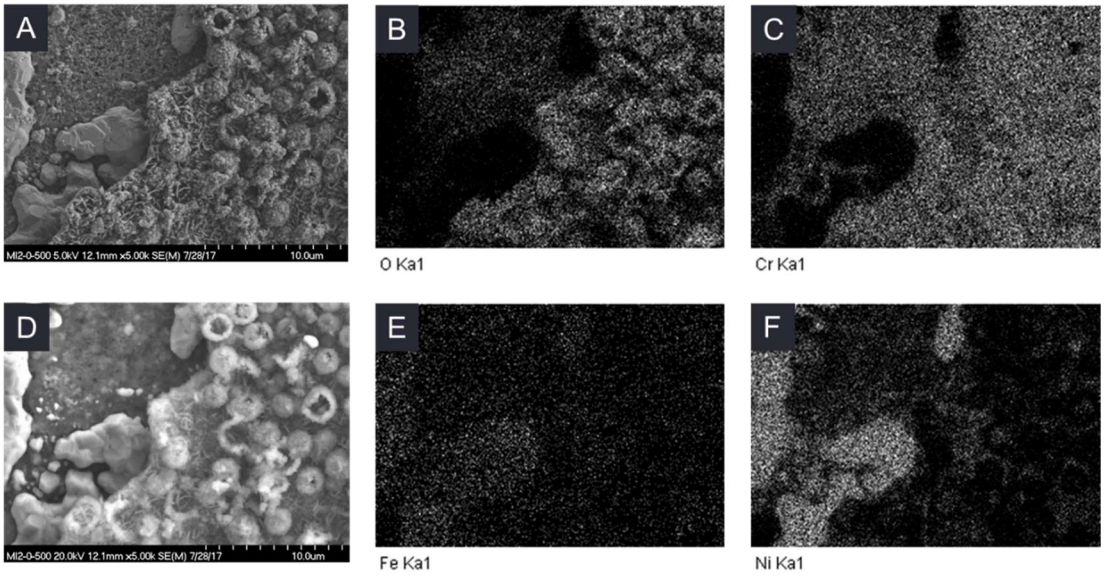

Figure 3.4: SEM images and EDS maps of the same area for the I625 sample exposed to LiCl-2wt%Li_2O-0wt%Li for 500hr. (A) SEM micrograph same as in Figure 3.3B given for reference, taken at 5kV accelerating voltage, (B) EDS map of O Kα, (C) EDS map of Cr Kα, (D) SEM micrograph of same area, taken at 20kV accelerating voltage (E) EDS map of Fe Kα, and (F) EDS map of Ni Kα. For the EDS maps, lighter tones indicate higher concentrations of that element.

Cross Section SEM-EDS.– The cross sections of the samples were investigated to determine the depth to which the degradation of the surface penetrated into the bulk of the sample. In the absence of Li, the penetration into the bulk of the sample was minimal, as evidenced by Figures 3.5 and 3.6, which show the FIB milled cross section of the I625 samples exposed to LiCl-1wt%Li_2O-0wt%Li at 650°C for 500hr and 1000hr, respectively. Small pores of less than 2μm in diameter were observed immediately below the outer oxide layer for the 500hr sample, corresponding to a layer of Mo enrichment as evidenced in Figure 3.5 (d). As shown in the EDS analysis of this sample previously, the oxide layer does not incorporate a significant amount of Mo, indicating that the surface enrichment of Mo is deleterious to the integrity of the base material. At an exposure period of 500hr, the thickness of the oxide layer is

approximately 1μm, while the thickness of the Mo enriched layer containing the pores is approximately 2μm. Based on a total thickness of 3μm, the corrosion rate was calculated to be 0.05mm/year.

Careful observation of the EDS maps in figure 3.5(b through f) show that Cr is depleted in this region. Consequently, our hypothesis is that the pores are a result of the diffusion of Cr towards the surface to form the outer oxide layer, causing contraction of the base material at the interface between the base alloy and the oxide layer. As corrosion proceeds, the diffusion of Cr from the bulk alloy becomes the limiting factor, and the surface of these voids then offer the path of least resistance to allow reaction of Cr with the salt to form the Cr-based oxide layer. The increased volume of the oxide eventually fills in the void space. The growth and subsequent infill of these voids may give rise to the multi-layered oxide structure observed on the samples exposed to identical conditions for 1000hr in Figure 3.6. The lack of voids observed in Figure 3.6 may be due to the path required for diffusion of Cr from the alloy. This is supported by near complete depletion of Cr in the Ni and Fe rich layers between the Cr-based oxides.

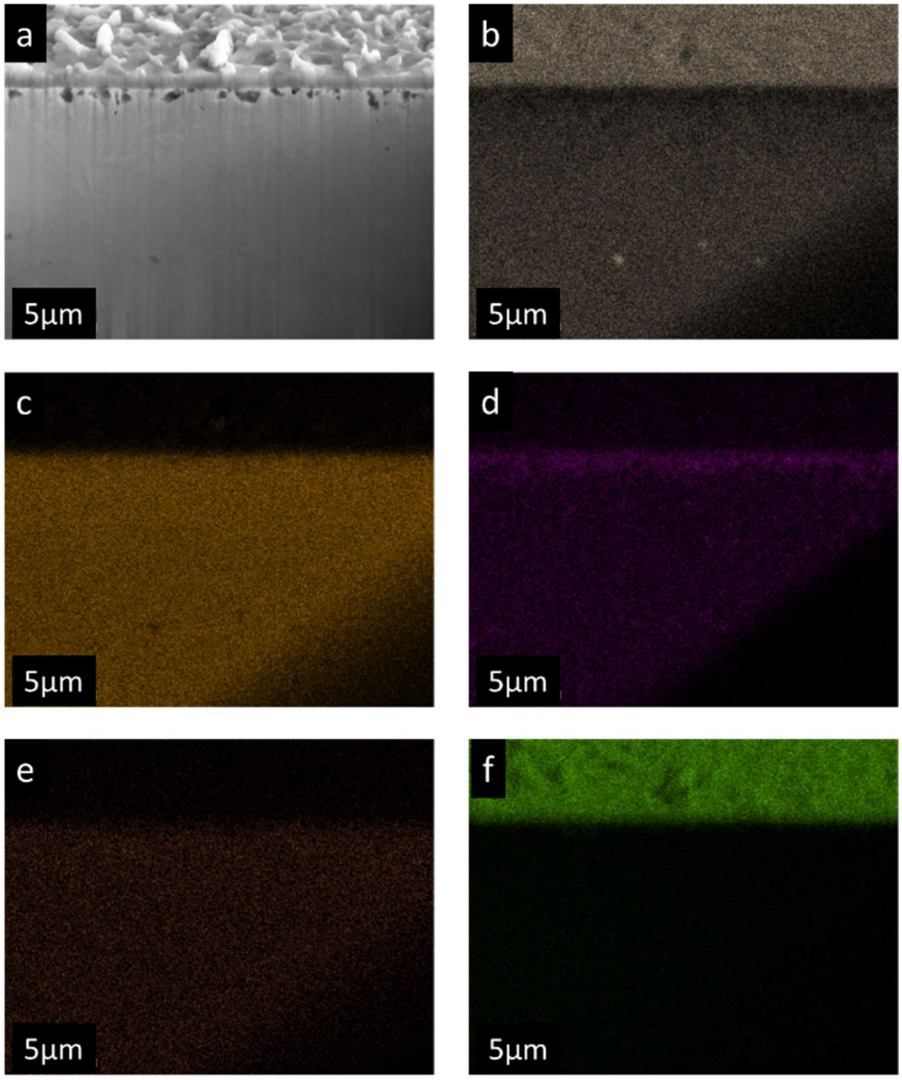

Figure 3.5: SEM micrograph (a) and EDS mapping analysis of the FIB milled trench on the I625 sample exposed to LiCl-1wt%Li_2O-0wt%Li for 500hr showing variations in concentration of (b) Cr, (c) Ni, (d) Mo, (e) Fe, and (f) O. The sample surface is observed as the image was taken at an angle of 52° from normal to the plane of the sample. The delineation between sample surface and cross section is demarked by the location of the abrupt change in intensity of all elements. Cr is seen to be enriched on the surface of the sample, while Mo is slightly enriched just below the outer corrosion layer. Oxide thickness is approximately 1µm, while the depth to the bottom of the lowest void space is 2.25µm.

For the I625 sample exposed to LiCl-1wt%Li_2O-0wt%Li for 1000hr, the corrosion rate was approximately 0.07mm per year, indicating that corrosion was approximately linear for these experiments. The oxide film was well developed, and showed a multi-layered structure similar to that shown for the I625 sample

exposed to LiCl-2wt%Li_2O-0wt%Li for 500hr in Figures 3.3 and 3.4. The Mo enriched layer below the outer corrosion layer was still observed, however, there were no voids located in this area as there were on the 500hr sample. Mo accumulation was also observed at the grain boundaries, along with Cr and Nb, which is likely due to thermal aging of the microstructure, rather than a result of exposure to the molten LiCl-Li_2O solution [90]. Although enrichment of Cr, Mo, and Nb were observed along the grain boundaries, carbon was not observed at these locations, so it cannot be concluded that sensitization was observed. Corrosion did not proceed along the grain boundaries, so it seems that the enrichment of the grain boundaries in Cr, Mo, and Nb did not negatively impact the observed corrosion rate. However, sensitization followed by intergranular corrosion was observed in our previous work on SS316L under similar conditions [88].

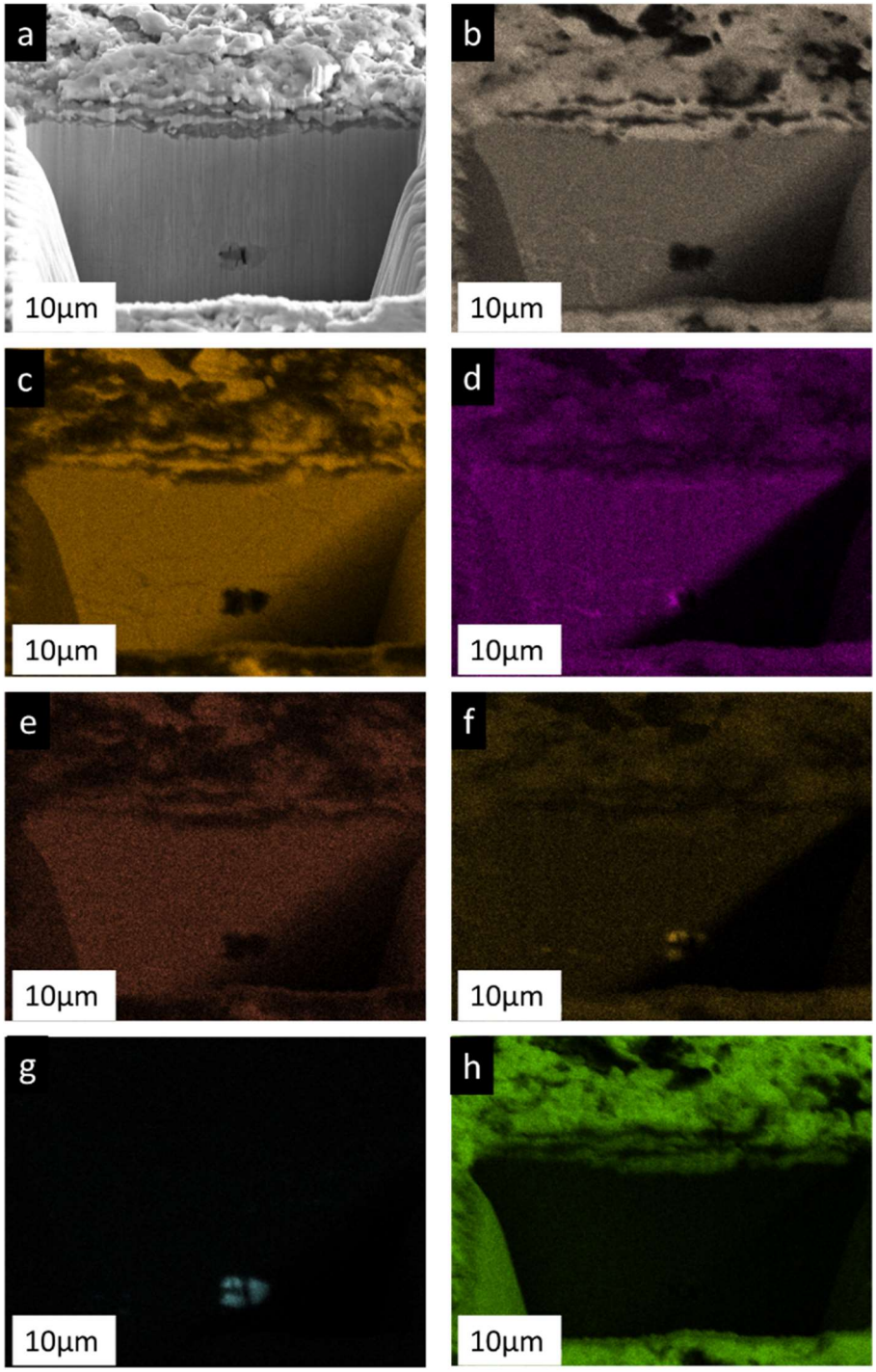

Figure 3.6: SEM micrograph (a) and EDS mapping analysis of the FIB milled trench on the I625 sample exposed to LiCl-1wt%Li_2O-0wt%Li for 1000hr showing variations in concentration of (b) Cr, (c) Ni, (d) Mo, (e) Fe, (f) Nb, (g) Ti, and (h) O. The multi-layered structure observed here corresponds to a similar oxide layer structure observed in Figures 3.3 and 3.4. Again, Mo enrichment is seen immediately below the corrosion layer, without significant incorporation of Mo into the oxide layer itself. The precipitate seen at a depth of 17µm consists largely of Ti, Mo, and Nb. Cr, Mo, and Nb were also observed to be enriched along the grain boundaries.

As was observed via SEM imaging of the sample surfaces, the cross sections of the I625 samples exposed to LiCl-Li_2O in the presence of Li were consistent in morphology and showed an outer layer of a highly porous Ni rich foam-like structure. The formation of this porous layer is believed to be a result of the selective dissolution of Cr, Mo, and Nb from the base material, leaving the Ni-Fe matrix in place, similar to the formation of Rainey Nickel by the selective dissolution of Al from Ni-Al alloys [91]. This mechanism is likely similar to the void formation observed in Figure 3.5(a), as diffusion of elements within the alloy is unlikely to be affected by the solution chemistry. The SEM images of the cross sections of the I625 samples exposed to LiCl-1wt%Li_2O containing 0.3, 0.6, or 1wt% Li at 650°C for 500 and 1000hr are shown in Figure 3.7. For the sample exposed to LiCl-1wt%Li_2O-0.3wt%Li for 500hr, the porosity penetrated into the surface to a depth of approximately 30μm, corresponding to a corrosion rate of 0.53mm/year. However, all other samples consistently showed a penetration depth of 15μm, regardless of Li concentration or period of exposure, indicating that a direct measure of the corrosion rate is not necessarily applicable for these specimens. The similarity in the morphology and depth of attack regardless of Li concentration or exposure period indicates that there may be a threshold concentration of Li necessary to cause this morphology and that threshold is likely below 0.3wt%, and the reactions responsible for pore formation may not be diffusion controlled. Further studies at Li concentrations below 0.3wt% would be necessary to determine at what concentration this morphology begins to be observed as well as the mechanisms responsible for pore formation. Due to the

presence of metallic Li, liquid metal embrittlement may play a role in the formation of the microstructures observed here, although verification of this hypothesis would require further investigation.

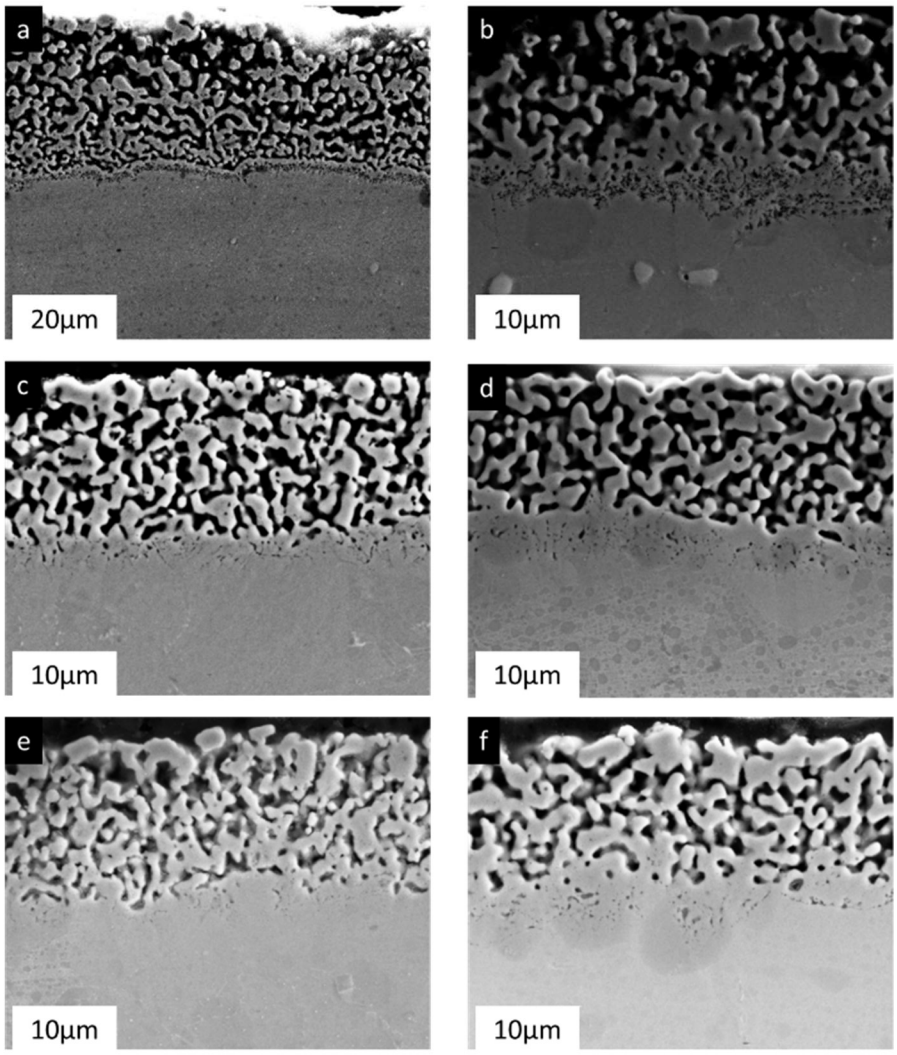

Figure 3.7: Cross section SEM images for I625 samples exposed to LiCl-1wt%Li_2O containing 0.3wt% Li for (a) 500hr or (b) 1000hr, 0.6wt%Li for (c) 500hr or (d) 1000hr, or 1wt%Li for (e) 500hr or (f) 1000hr. The porous microsctructure observed via SEM of the sample surface was also observed in cross section, and was consistent amongst sample exposed to LiCl-Li_2O in the presence of Li.

The variation in composition as a function of depth was investigated via EDS of the cross sections. As all samples exposed to LiCl-Li_2O in the presence

of Li displayed similar variations in composition, the SEM-EDS results for the I625 sample exposed to LiCl-1wt%Li_2O-1wt%Li at 650°C for 1000hr are shown in Figure 3.8, while spot EDS analysis for the locations shown in Figure 3.8(a) are given in Table 3.2. Cr, Mo, and Nb are all significantly depleted from the material remaining in the porous layer, leaving primarily Ni, with Fe remaining at approximately the same ratio as in the base material. The depletion of Cr, Mo, and Nb was also observed to irregularly penetrate into the sample beyond the depth of the porous layer. The loss of the amount of Cr, Mo, and Nb necessary to reach the composition of spot 1 shown in Figure 3.8(a) represents the loss of a significant fraction of the material, which may account for the porous microstructure seen on this sample and other I625 samples exposed to LiCl-Li_2O in the presence of Li.

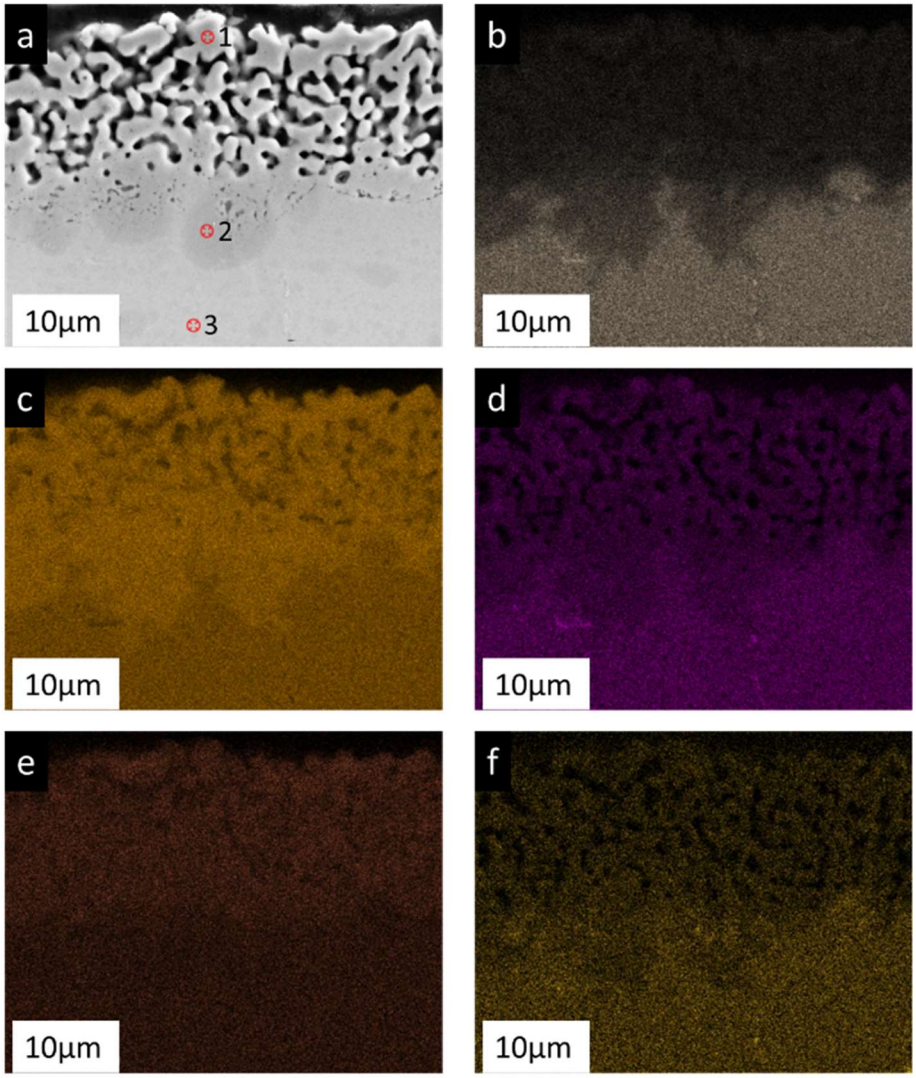

Figure 3.8: SEM micrograph (a) and EDS mapping analysis of the cross section of the I625 sample exposed to LiCl-1wt%Li_2O-1wt%Li for 1000hr showing variations in concentration of (b) Cr, (c) Ni, (d) Mo, (e) Fe, and (f) Nb. Locations marked 1, 2, and 3, were analyzed via point analysis, which is presented in Table 3.2.

Table 3.2: EDS spot analysis of the locations demarked in Figure 3.8(a) for the I625 sample exposed to LiCl-1wt%Li_2O-1wt%Li for 1000hr. The outermost layer was depleted in Cr compared to the base material, while the dark spots seen in some locations on these samples did not show any observable variation in composition compared to the base material.

Element	Spot 1 (wt%)	Spot 2 (wt%)	Spot 3 (wt%)
Nb	-	2.87	2.97
Mo	4.86	7.18	7.19
Cr	5.31	22.34	23.7
Fe	8.35	5.17	5.17
Ni	81.48	62.45	60.98

3.4: Conclusions

I625 samples were exposed to molten LiCl solutions containing 1 or 2wt% Li_2O and 0, 0.3, 0.6, or 1wt% Li maintained at 650°C for periods of 500 and 1000hr to investigate the effect of metallic Li on the degradation of the material. In the absence of metallic Li, I625 formed a highly crystalline, stable oxide film with a multi-layered structure that limited corrosion to approximately 0.05 to 0.07mm/year. The presence of metallic Li in solution prevented the formation of any substantial oxide film, resulting in a highly porous, foam-like structure. The depletion of Cr, Mo, and Nb from the surface was also observed on these samples via EDS, indicating that these elements were preferentially leached from the base material by the molten solution. The loss of these elements from the sample surface, which together constitute one-third of the material, is likely responsible for the highly porous microstructure observed.

Chapter 4 : Effect of metallic Li on the Surface Chemistry of Inconel 625 Exposed to molten LiCl-Li_2O-Li

As published in the Journal of the Electrochemical Society

Volume 166, Issue 11, April 2019

Authors: William Phillips, Zachary Karmiol, and Dev Chidambaram

Abstract:

This study explores the surface chemistry of Inconel 625 samples exposed to molten LiCl-Li_2O-Li solutions at 650°C for 500 and 1000hr and aims to understand the effect of solvated Li on corrosion behavior in molten LiCl-Li_2O-Li. The surfaces of Inconel 625 samples were analyzed using X-ray diffraction, Raman spectroscopy, and X-ray photoelectron spectroscopy. The oxide films formed on the surface of the samples in the absence of Li is composed of $LiCrO_2$, with small contributions of Li_2CrO_4 and $NiFe_xCr_{2-x}O_4$. The presence of Li was observed to destabilize these compounds, resulting in a primarily metallic surface with trace amounts of oxidized Cr, Mo, and Nb present depending on the concentration of Li in solution.

Keywords: High temperature corrosion, Lithium chromate, Electrolytic reduction, Pyroprocessing

4.1: Introduction

This study discusses the effect of metallic Li dissolved in molten LiCl-Li_2O solutions on the corrosion behavior of Inconel alloy 625 (I625), as applies to the electrolytic reduction of oxide based used nuclear fuel (UNF). A thorough introduction including the motivation and background for this work is provided in an earlier study [92]. Briefly, the formation of metallic Li in the molten LiCl-Li_2O electrolyte used for the electrolytic reduction of oxide based UNF has been noted by a number of researchers to occur [8, 17]. Formation of metallic lithium is a side reaction that occurs as a result of the high reduction potential in the process that is necessary to reduce uranium oxide to uranium metal. As the reduction proceeds, it can be assumed that the concentration of Li in the electrolyte approaches saturated conditions [17]. While the dissolution mechanism of Li in LiCl and its effects on the physical chemistry of the solution have been well studied, corrosion in this tertiary LiCl-Li_2O-Li solution has not been extensively studied [22, 59, 60, 84]. Additionally, the studies that have been conducted have been of short duration and have shown conflicting results due to widely varying experimental conditions employed [25, 39, 42, 44, 46, 47]. Consequently, this study was performed to elucidate the mechanisms responsible for material degradation in conditions applicable to the electrolytic reduction of UNF.

Previous work from our group reported the morphological and elemental changes to the base material surface and cross section via scanning electron microscopy (SEM) coupled with energy dispersive X-ray spectroscopy (EDS) for

both stainless steel 316 (SS316) and I625 [88, 92]. The results presented there showed that a stable Cr-based oxide film forms on the surface of I625 upon exposure to molten LiCl-Li_2O solutions at 650°C in the absence of Li^0 [92]. This oxide film was found to limit the corrosion of these samples to a rate of approximately 0.05 to 0.07 mm/year [92]. However, in the presence of Li, this oxide film was destabilized, resulting in the preferential dissolution of the active alloying elements, namely Cr, Mo, and Nb, and a porous microstructure at the sample surface (92, Appendix 1 Figs. A1-4 and A1-5). This porous structure extended into the surface to a depth of 15 to 30μm [92]. This study aims to better understand the corrosion mechanisms involved by understanding the surface chemistry of I625 using X-ray diffraction (XRD), Raman spectroscopy, and X-ray photoelectron spectroscopy (XPS). The results of these surface analytical techniques are presented in this work.

4.2: Experimental

I625 coupons were cut from a 3.175mm plate obtained from High Performance Alloys with the following nominal composition: 58wt% Ni, 20-23wt% Cr, 5wt% Fe, 8.0-10.0wt% Mo, 3.15-4.15wt% Nb, 0.5wt% Mn, 0.4wt% Al, 0.4wt% Ti, and 0.5wt% Si. The composition of this alloy as measured via the EDS used for cross sectional investigation was 62.3wt% Ni 23.5wt% Cr, 6.5wt% Mo, 5.1% Fe, and 2.6wt% Nb. Duplicate coupons were exposed molten solutions of LiCl containing either 1 or 2wt% Li_2O, and either 0, 0.3, 0.6, or 1wt% Li over exposure periods of either 500 or 1000 hours. Considering the evaporation of Li and Li_2O

over time that was observed in other short-term studies and the extended exposure periods of this study, the salt charge for each test was replaced at a period of once every 96 hours to maintain the solution chemistry [25, 26, 39, 46, 88]. To minimize the effects of impurity H_2O, LiCl was dried in a vacuum oven in air at 200°C for 24 hours before being transferred into the glovebox for storage. Additionally, the LiCl was baked for 2 hours at 550°C immediately prior to melting and subsequent addition of Li_2O and Li [19, 25]. The surface analysis presented here was conducted on the samples prepared for our previous work [92]. More details on the experimental procedure and morphology of these samples can be found in that publication [92]. All surface analysis was performed prior to removal of the residual salt layer, as well as following removal of the salt layer, which was accomplished by rinsing the sample in 25mL of ACS grade methanol for 15 minutes with continuous agitation.

Great care was taken to maintain sample integrity at all times during analyses. Prior to methanol rinsing, all surface analyses was conducted under inert or ultra-high vacuum (UHV) conditions, as dictated by each technique. Raman studies were performed inside the Ar glovebox using a fiber optic coupled probe. For XPS analyses, the samples were transferred from the glove box to the UHV chamber in a sealed transfer chamber to prevent atmospheric contamination (PHI Model 04-110). This transfer vessel has been extensively verified to protect reactive samples from atmospheric contamination during transfer under various conditions [93]. A glove bag was installed on the transfer port of the XPS and purged with dry nitrogen for 30 minutes prior to sample

removal to reduce atmospheric contamination of the samples during removal from the instrument. The samples were then re-sealed inside the PHI 04-110 transfer chamber for transfer back to the glovebox. As described in our earlier work, XRD studies were then conducted on samples which were sealed in plastic bags in the argon atmosphere of the glovebox [25, 26, 39, 46, 88]. No hydrated LiCl peaks were detected via XRD, indicating that there was insignificant moisture contamination on the samples to this point, however, peaks indicative of $LiCrO_2$ were observed on the samples exposed to LiCl-Li_2O in the absence of Li (see supplemental information, Appendix A1). Finally, sample surfaces were studied using SEM-EDS prior to methanol rinsing [92]. Due to the design of the transfer port of this instrument, it was necessary to momentarily expose the samples to atmosphere prior to pumping down of the SEM entry chamber. Total exposure time to atmosphere was less than 30 seconds. After SEM studies, the samples were then immediately rinsed with methanol as described above to remove the residual salt layer. Moisture content of the methanol was not analyzed, but typical moisture concentration was specified to be lower than 100 ppm. Following removal of the salt layer, the samples were immediately re-analyzed via SEM-EDS. No morphological or compositional changes were detected following methanol rinsing. Samples were stored inside the Ar glovebox at all times other than for analysis. The surface analytical results from post methanol rinse were consistent with the results from pre-methanol rinse; however, the removal of the residual salt allowed for more accurate determination of the surface chemistry, as in many cases, the residual salt layer

partially obscured the surface from analysis, particularly with XPS (see supplemental information, Appendix A1). The lack of substantial surface oxides on the samples exposed to LiCl-Li_2O solutions containing Li indicate that the surface analysis procedures outlined above had minimal impact on the surface chemistry of these samples. As has been shown previously, no chemical or morphological changes to the sample surface were observed to result from the methanol rinsing procedure [25, 26, 57]. As such, the spectra reported here were collected from the sample surfaces following removal of the salt layer due to the improved data quality afforded by the increased signal to noise ratio.

X-ray diffraction was performed using a Rigaku Smartlab X-ray diffractometer with a Cu kα source operating at 44kV and 40mA. Parallel beam optics in a grazing incidence angle configuration were used for detection of the thin surface films formed on the samples in this study. The incidence angle was set at 1°, and the diffraction pattern was recorded over a range of 10° to 90° 2θ for all diffraction patterns. For each diffraction pattern, the scan speed was optimized to yield an intensity of 5000 counts for the highest peak, while the step size was varied to give 5 steps at the full width at half-maximum intensity of the narrowest peak.

Raman spectroscopy was performed using a Thermo-Scientific DXR Raman microscope utilizing a 10mW 532nm continuous wave laser. Spectra were collected through the 50x objective lens of the microscope using a 50μm

incident beam slit. The collection time was 4 seconds per spectra, and 16 individual spectra were averaged to give the spectra reported here.

X-ray photoelectron spectroscopy was performed using a PHI 5600 spectrometer equipped with an Al-Kα source with a photon energy of 1486.6eV. The source was operated at an accelerating voltage of 14kV and an anode power of 300W. The spectrometer dispersion and work function were calibrated to the Au $4f_{7/2}$ peak at 84.00eV and the Cu $2p_{3/2}$ peak at 932.67eV to an accuracy of ±0.05eV. Survey spectra were recorded with a step size of 0.5eV, while narrow scans were collected at a step size of 0.025eV for the elements detected on the sample surfaces. Peak fitting was performed with SDP version 4.6 Gaussian fitting software. Charge correction was performed to the adventitious C 1s peak at 284.8eV.

4.3: Results

4.3.1: XRD

The X-ray diffraction pattern collected for the I625 sample exposed to LiCl-1wt% Li_2O-0wt% Li at 650°C for 1000hr is shown in Figure 4.1. The peaks displayed in this pattern are representative of those collected for all samples exposed to molten LiCl-Li_2O solutions in the absence of Li^0. The only crystalline phases detected on these samples were the base material and peaks consistent with $LiCrO_2$ [74]. When this result is considered along with Raman and XPS analysis of these samples shown below, it can be concluded that the oxide scale

is composed largely of $LiCrO_2$ when I625 is exposed to molten LiCl-Li_2O solutions in the absence of Li.

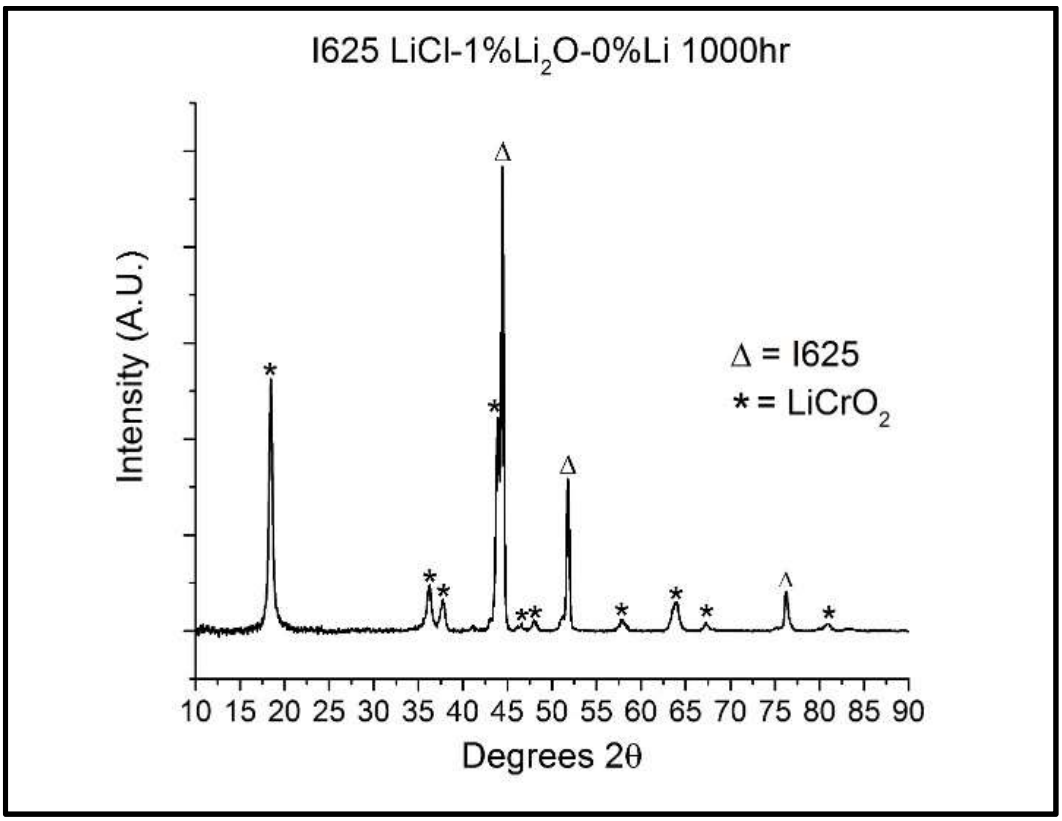

Figure 4.1: XRD pattern collected from the I625 sample exposed to LiCl-1wt% Li_2O-0wt% Li at 650°C for 1000hr. Peaks indicative of the base material and $LiCrO_2$ were observed.

The presence of Li^0 in solution creates a very reducing environment, preventing the formation of the well-developed $LiCrO_2$ films observed on these samples in the absence of Li. Consequently, the diffraction patterns for all samples exposed to LiCl-Li_2O solutions containing Li displayed diffraction patterns indicative only of the base material, as can be observed in Figures 4.2 and 4.3. These figures show the diffraction patterns of I625 samples exposed to LiCl-1wt% Li_2O solutions containing 0, 0.3, 0.6, or 1wt% Li for 500hr (Figure 4.2) or 1000hr (Figure 4.3). This corresponds with the observation made using SEM

of the highly porous metallic surfaces on I625 samples exposed to LiCl-Li_2O in the presence of Li [92].

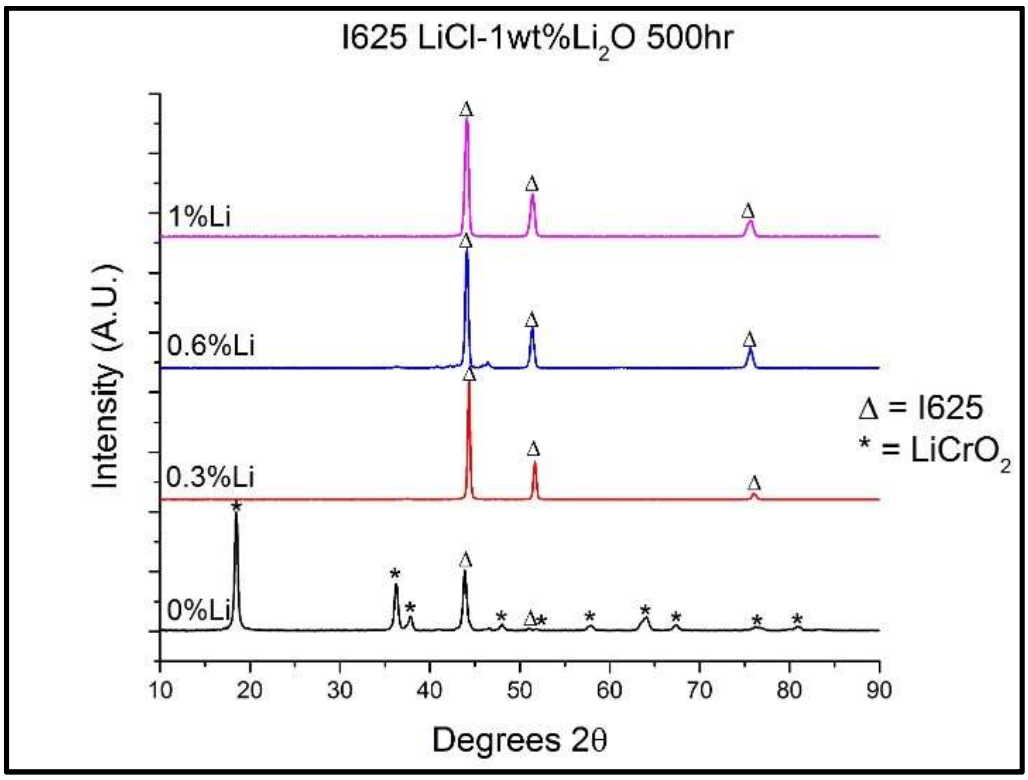

Figure 4.2: XRD spectra of I625 samples exposed to LiCl-1wt% Li_2O containing 0, 0.3, 0.6, and 1wt% Li at 650°C for 500hr. In the absence of Li, both $LiCrO_2$ and the base material were observed; however, in the presence of Li, on the base material was present.

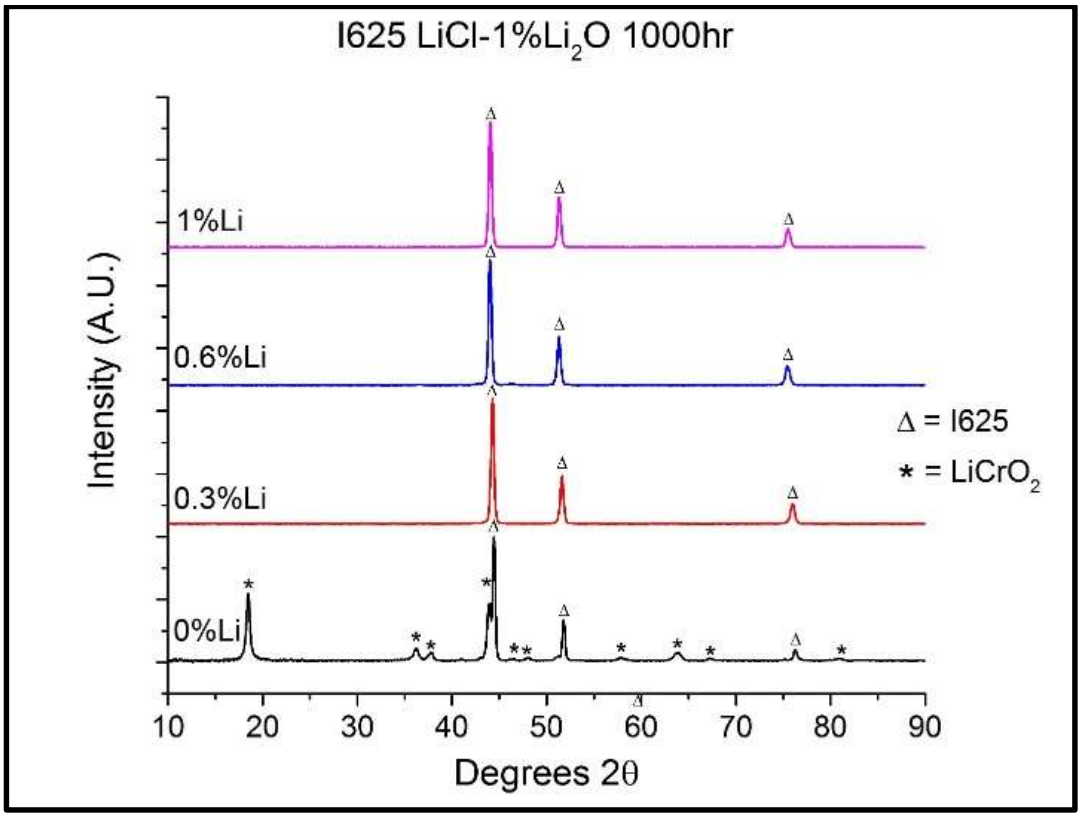

Figure 4.3: XRD spectra of I625 samples exposed to LiCl-1wt% Li_2O containing 0, 0.3, 0.6, and 1wt% Li at 650°C for 1000hr. In the absence of Li, both $LiCrO_2$ and the base material were observed; however, in the presence of Li, only the base material was present.

4.3.2: Raman Spectroscopy

Raman spectra, shown in Figure 4.4, also confirms the presence of $LiCrO_2$ in the absence of Li, with the Raman spectra of the four samples exposed to molten LiCl-Li_2O solutions in the absence of Li displaying prominent peaks of both the $LiCrO_2$ A_{1g} and E_g modes at 572cm^{-1} and 445cm^{-1}, respectively [75]. An additional hump on the shoulder of the $LiCrO_2$ A_{1g} peak is believed to be indicative of a spinel of the type $NiFe_xCr_{2-x}O_4$ based on the work of Hosterman [76]. The exact composition of this compound is unknown, but is likely skewed towards Cr-rich compounds, due to the relatively low concentration of Fe in the I625 alloy. The I625 sample exposed to LiCl-1wt% Li_2O at 650°C also displayed

features at 845cm^{-1} and 340cm^{-1} that indicate the presence of Li_2CrO_4 based on the collection of Raman spectra of this compound in our laboratory. It is currently unknown why the other I625 samples exposed to similar conditions did not display the features of Li_2CrO_4.

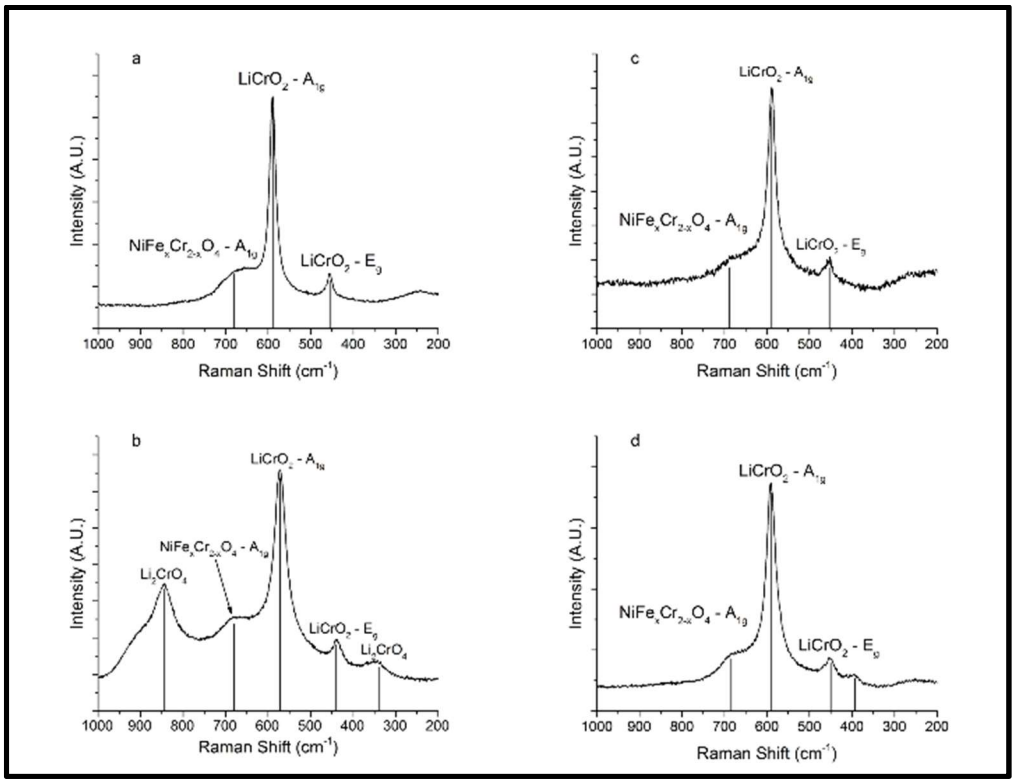

Figure 4.4: Raman spectra of I625 samples exposed at 650°C to LiCl containing a) 1wt% Li_2O for 500hr, b) 1wt% Li_2O for 1000hr, c) 2wt% Li_2O for 500hr and d) 2wt% Li_2O for 1000hr. The A_{1g} and E_g peaks of $LiCrO_2$ and a hump indicative of the A_{1g} peak of $NiFe_xCr_{2-x}O_4$ were observed on all samples exposed to LiCl-Li_2O solutions in the absence of Li. Additionally, the I625 sample exposed to LiCl-1wt% Li_2O for 1000hr displayed peaks indicative of Li_2CrO_4.

The effect of Li on the Raman spectra of I625 exposed to LiCl-Li_2O-Li solutions can be observed in Figure 4.5, which shows the Raman spectra of I625 samples exposed to LiCl-1wt% Li_2O solutions containing 0, 0.3, 0.6, and 1wt% Li at 650°C for 500hr. The well-defined Raman modes observed in Figure 4.4 are seen to be largely absent in the presence of Li. The broad features that roughly

align with the positions of the compounds observed in the absence of Li may indicate minute quantities of these compounds on the sample surface. XPS analysis presented below confirms the presence of small amounts of oxidized Cr, Mo, and Nb on the surface of the I625 samples exposed to LiCl-Li_2O in the presence of Li.

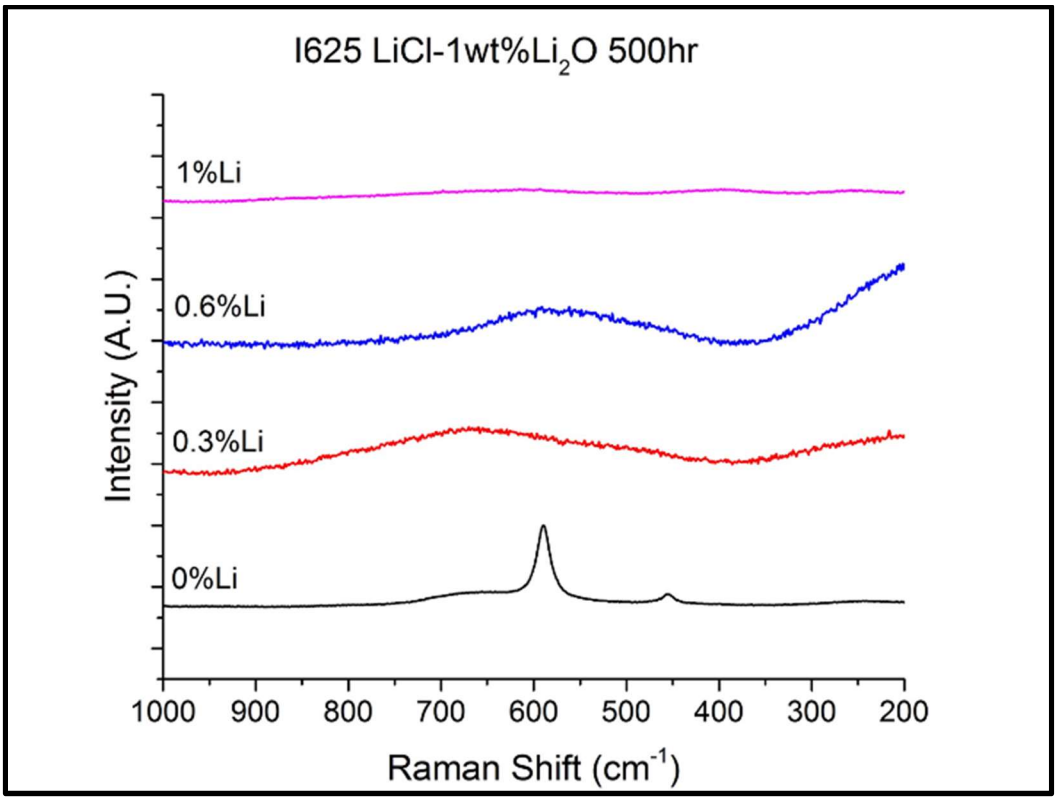

Figure 4.5: Raman spectra obtained from the surfaces of I625 samples exposed to LiCl-1wt% Li_2O containing 0, 0.3, 0.6, or 1wt% Li at 650°C for 500hr. The clearly defined Raman modes present in Raman spectra of samples exposed to LiCl-Li_2O in the absence of Li are not observed on the surface of samples exposed to LiCl-Li_2O in the presence of Li.

4.3.3: XPS

The surface sensitivity and chemical state analysis provided by XPS allowed for the investigation of the corrosion products present on the surface of

the samples, even at the low thicknesses observed on the I625 samples exposed to molten LiCl-Li_2O solutions containing Li. Comparison of spectra taken prior to and following methanol rinsing showed no change in surface chemistry caused by the rinsing procedure (see supplemental information, Appendix A1), allowing for the chemical analysis presented below; however, the presence of a Ti-based deposit on some of the samples prevented accurate quantitative analysis of the surface composition. Figure 4.6 shows the XPS survey spectra recorded from the I625 samples exposed to LiCl-1wt% Li_2O solutions containing 0, 0.3, 0.6, and 1wt% Li at 650°C for 1000hr. Survey spectra of the I625 samples exposed to varying Li_2O concentrations and exposure periods showed similar features and trends. In the case of the samples exposed to LiCl-Li_2O solutions in the absence of Li, the surface was primarily composed of Cr, O, and Li, further confirming the presence of $LiCrO_2$ on these samples. For the I625 sample exposed to LiCl-1wt% Li_2O for 1000hr, Ni was also detected via XPS; however, Ni was not detected on the surface of the other samples exposed to LiCl-Li_2O solutions in the absence of Li, further indicating that this sample had somewhat different surface chemistry when compared to the other samples exposed to similar conditions.

For I625 samples exposed to LiCl-Li_2O in the presence of Li, Ni was the primary element present, while the Cr level was depleted and most of the primary alloying elements were detected in trace amounts. Our previous work has shown these compounds were also detected on the surface of numerous samples that do not contain Ti as an alloying element, notably SS316L (14,15) and thus must be the be a result of electroless deposition of Ti oxide and nitride compounds

from Ti impurities present in the Li_2O used in these studies [26]. This will not be discussed further in the present work.

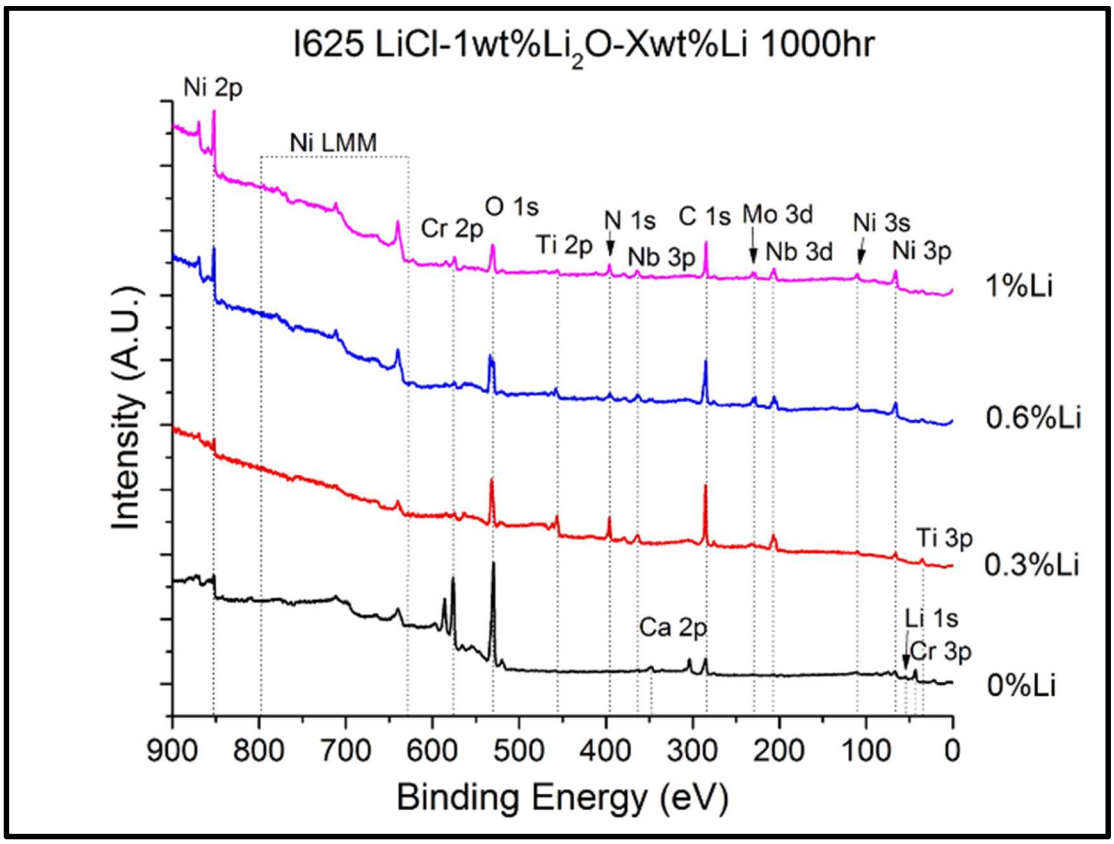

Figure 4.6: XPS survey spectra of I625 samples exposed to LiCl-1wt% Li_2O containing 0, 0.3, 0.6, or 1wt% Li at 650°C for 1000hr. Vertical lines denote the peak position of the spectral lines indicated.

The chemistry of Cr, being the primary alloying element in I625 as well as being responsible for corrosion inhibition through the formation of stable oxide films, is important to understand thoroughly. XPS narrow scans of the Cr $2p_{3/2}$ spectra obtained from the surface of the I625 samples exposed to LiCl containing 1 or 2wt% Li_2O and 0, 0.3, 0.6, or 1wt% Li for 500hr are shown in Figure 4.7, while the Cr $2p_{3/2}$ spectra of I625 samples exposed to similar conditions for 1000hr are shown in Figure 4.8. Peak fitting was performed using previously

published fitting parameters, with charge correction performed to the adventitious C 1s peak at 284.8eV [77]. In the absence of Li, the Cr spectra consistently showed the presence of Cr^{3+}, which is necessary for the formation of $LiCrO_2$, confirming the observations made via XRD and Raman spectroscopy that show this compound is present on the surface of these samples. Additionally, Cr^{6+} is also present to a minor degree on these samples, which supports the observation via Raman of the presence of Li_2CrO_4 in small amounts in the oxide film. As both Li_2O concentration and exposure period increase, the proportion of Cr^{6+} to Cr^{3+} increases, indicating that the formation of $LiCrO_2$ and Li_2CrO_4 are governed by the activity of the O^{2-} ion in solution, and that $LiCrO_2$ may be converted to Li_2CrO_4 over time. In the presence of Li^0, neither of these compounds are stable in bulk form, as indicated by XRD, Raman, and SEM-EDS observations; however, a nominal amount of Cr^{3+} and to a lesser extent Cr^{6+} were observed via XPS alongside metallic Cr^0, indicating that O^{2-} in solution continues to play a role in the corrosion process at concentrations of Li in solution of at least 1wt%. Cr^{6+} was not observed on all samples when Li metal was present in solution. While the formation of Cr^{6+} is unlikely from a thermodynamic perspective in pure LiCl-Li_2O, it was consistently observed in this study, as shown both via XPS and Raman. The formation of Li_2CrO_4 was also hypothesized to be the dissolution mechanism of the Cr-based oxide film by researchers at KAERI [63]. The solubility of CrO_4^{2-} in LiCl-Li_2O may lower the activation energy necessary to facilitate the formation of the Cr^{6+} oxidation state. Due to the difficulty associated with completely removing moisture from highly

hygroscopic LiCl, the source of oxygen for the formation of the oxide layers observed in the absence of metallic Li was likely from impurity moisture remaining in the molten salt. In the case of the samples exposed to melts containing metallic Li, the excess Li would react with any moisture present in the salt to form Li_2O and H_2 gas, effectively eliminating this source of oxygen. The mechanism for the formation of the trace quantities of oxides present on the surface of the samples exposed to LiCl-Li_2O melts containing Li is currently unknown, and will require further investigation.

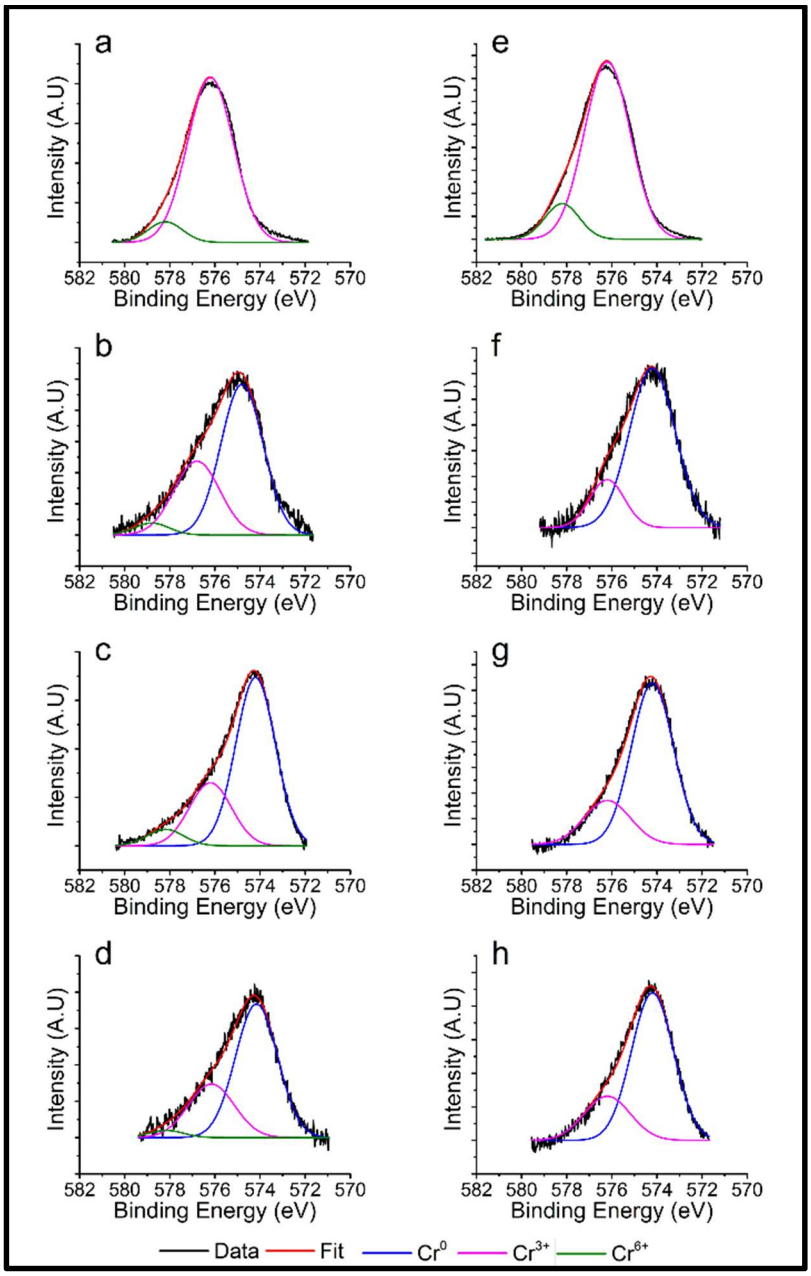

Figure 4.7: Cr $2p_{3/2}$ XPS spectra of I625 samples exposed for 500hr to LiCl containing a) 1% Li_2O 0% Li, b) 1% Li_2O 0.3% Li, c) 1% Li_2O 0.6% Li, d) 1% Li_2O 1% Li, e) 2% Li_2O 0% Li, f) 2% Li_2O 0.3% Li, g) 2% Li_2O 0.6% Li, and h) 2% Li_2O 1% Li.

Table 4.1: Peak fitting parameters for Cr $2p_{3/2}$ spectra shown in Figures 4.7 and 4.8. Charge correction to the adventitious C 1s line at 284.6eV was performed.

Peak	BE	FWHM
Cr^0	574.2	2.2
Cr^{3+}	576.2	2.4
Cr^{6+}	578.2	1.8

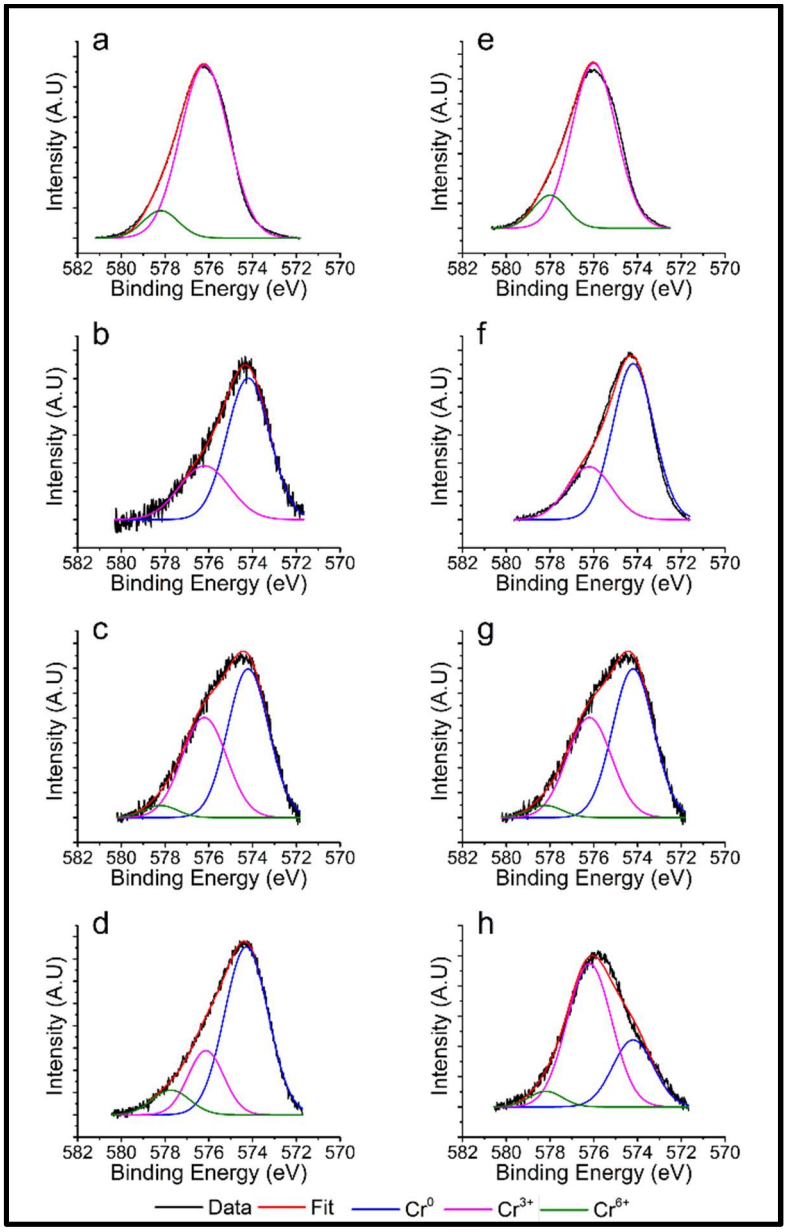

Figure 4.8: Cr $2p_{3/2}$ XPS spectra of I625 samples exposed for 1000hr to LiCl containing a) 1% Li_2O 0% Li, b) 1% Li_2O 0.3% Li, c) 1% Li_2O 0.6% Li, d) 1% Li_2O 1% Li, e) 2% Li_2O 0% Li, f) 2% Li_2O 0.3% Li, g) 2% Li_2O 0.6% Li, and h) 2% Li_2O 1% Li.

While Ni was not observed on the surface of most of the samples exposed to LiCl-Li_2O in the absence of Li, it was observed on the I625 sample exposed to LiCl-1wt% Li_2O for 1000hr, as well as on all samples exposed to LiCl-Li_2O-Li

solutions. As shown in Figure 4.9, in the absence of Li, Ni was observed in a mixed valence state, showing both metallic as well as oxidized character. The presence of oxidized Ni on the surface of this sample supports the observations made via Raman of the presence of a spinel of the form $NiFe_xCr_{2-x}O_4$ in the oxide film of these samples. Fitting of these spectra was not performed due to the known difficulties associated with peak fitting Ni 2p XPS spectra without precise parameters obtained from standards with identical composition [78]. Peaks shapes and positions consistent with metallic Ni were observed on all samples exposed to LiCl-Li_2O in the presence of Li. No charge correction was necessary for the Ni spectra.

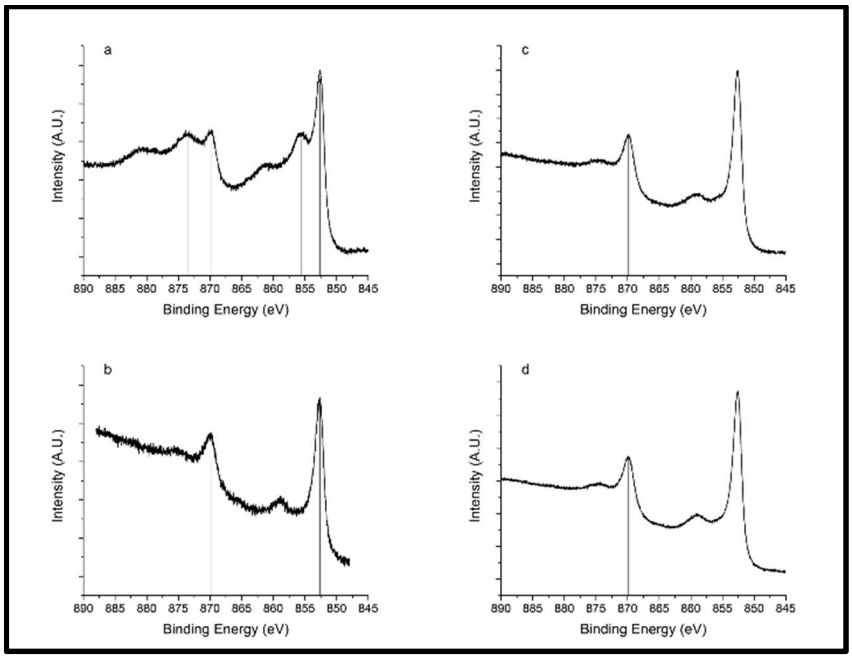

Figure 4.9: Ni 2p XPS narrow scans obtained from the I625 samples exposed to LiCl-1wt% Li_2O containing a) 0wt% Li, b) 0.3wt% Li, c) 0.6wt% Li, and d) 1wt% Li at 650°C for 1000hr. In the absence of Li, Ni is observed in a mixed metallic and oxidized state, indicating the presence of small amounts of Ni compounds in the oxide layer. In the presence of Li, Ni was only observed in the pure metallic state. No charge correction was performed necessary for Ni, indicating that it was consistently in electrical contact with the base material.

While Mo was not observed in detectable quantities via XPS of the surfaces of I625 samples exposed to LiCl-Li_2O solutions in the absence of Li due to the thick $LiCrO_2$ surface film and the relatively low concentration of Mo in the base alloy, it was observed on the surface of the majority of the samples exposed to LiCl-Li_2O in the presence of Li. The XPS narrow scans of the Mo 3d region are shown in Figure 4.10. At 0.3wt% Li, Mo behaved similarly to Cr in that it was present in a mixed metallic and oxidized state [79, 80]. Due to the noise, presence of multiple overlapping peaks on these spectra, and the known tendency for photoreduction of Mo, peak fitting was not performed, although the apparent positions of the primary peaks are demarked by vertical lines on the charts in Figure 4.10. The I625 samples exposed to LiCl-Li_2O in the presence of 0.6 and 1wt% Li showed only the characteristic asymmetric peaks of metallic Mo. This transition from mixed metallic and oxidized character at low Li concentrations to a purely metallic state at higher Li concentrations indicates that the activity of Li in solution is not unity until beyond the solubility limit.

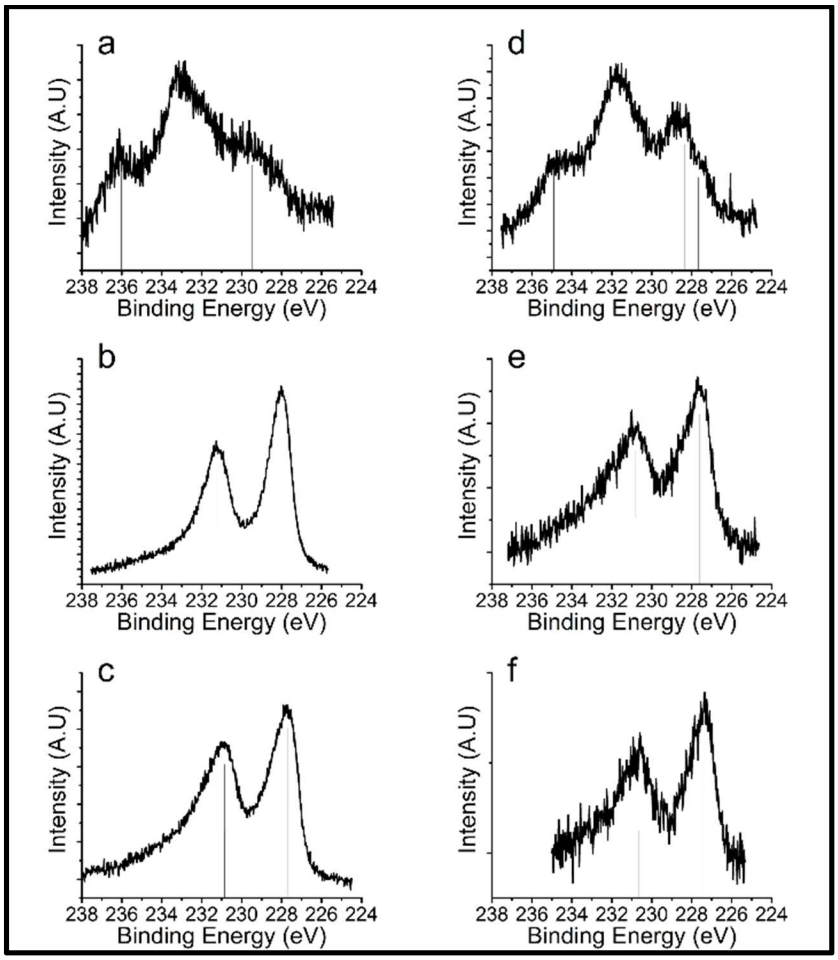

Figure 4.10: Mo 3d XPS narrow scans obtained from the surface of I625 samples exposed for 1000hr to molten LiCl containing a) 1wt% Li_2O and 0.3wt% Li, b) 1wt% Li_2O and 0.6wt% Li, c) 1wt% Li_2O and 1wt% Li, d) 2wt% Li_2O and 0.3wt% Li, e) 2wt% Li_2O and 0.6wt% Li, and f) 2wt% Li_2O and 1wt% Li. At concentrations of 0.3wt% Li Mo shows a mixed oxide state

While both Cr and Mo were observed to be present in a mixed state containing oxidized and reduced species in the presence of Li, Nb was only observed in oxidized states [94]. The narrow scans of the Nb 3d region obtained from the surface of I625 samples exposed to molten LiCl solutions containing 1 or 2wt% Li_2O and 0.3, 0.6, or 1wt% Li for 1000hr are shown in Figure 4.11, with the exception of the I625 sample exposed to LiCl-1wt% Li_2O-1wt% Li for 1000hr, as Nb was not detected on this sample. The presence of only oxidized Nb even

in the presence of high Li concentrations is counter intuitive, as work by Jeong, *et al.* showed that the reduction of Nb_2O_5 to metallic Nb was able to be accomplished in LiCl-Li_2O, primarily through the indirect reaction with Li which was electrolytically generated at the cathode, similar to the reduction of UO_2 [95].

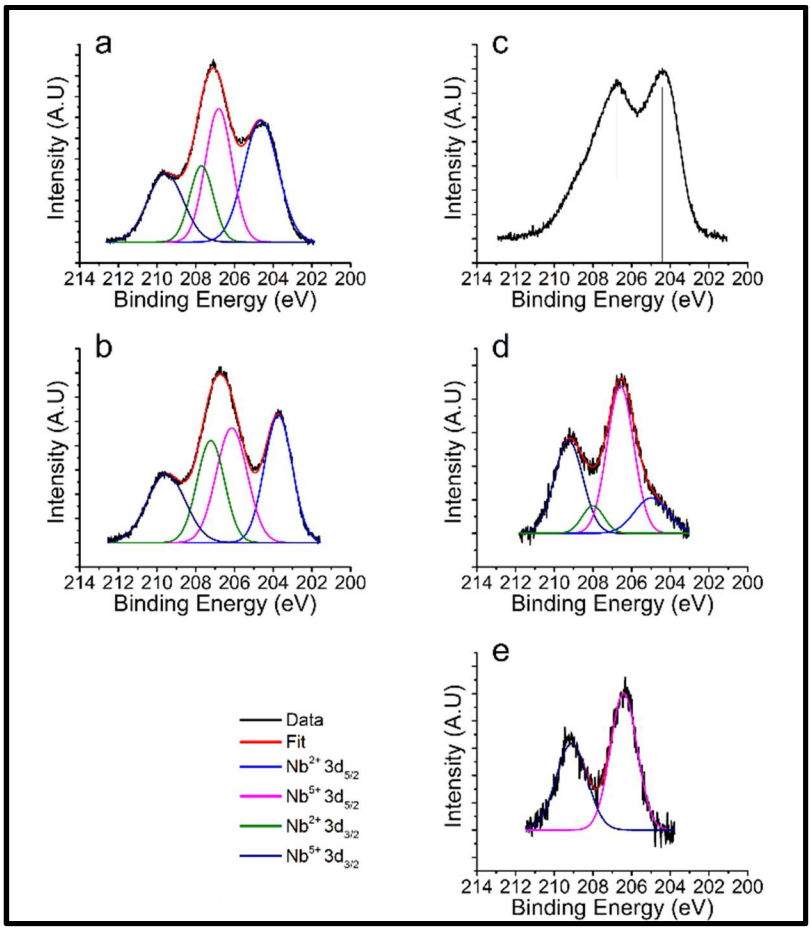

Figure 4.11: Nb 3d XPS narrow scans obtained from the surface of I625 samples exposed for 1000hr to molten LiCl containing a) 1wt% Li_2O and 0.3wt% Li, b) 1wt% Li_2O and 0.6wt% Li, c) 2wt% Li_2O and 0.3wt% Li, d) 2wt% Li_2O and 0.6wt% Li, and e) 2wt% Li_2O and 1wt% Li. Nb was not observed on the I625 sample exposed to LiCl-1wt% Li_2O-1wt% Li for 1000hr. Nb was observed to be present as Nb^{2+} and Nb^{5+}, however, metallic Nb was not observed.

Minor alloying elements, Fe and Al, were not analyzed in this study. The oxide film on the samples exposed to LiCl-Li_2O in the absence of Li did not have detectable quantities of Fe on its surface, however Fe was detected in extremely

small quantities on some of the samples exposed to LiCl-Li_2O solutions containing Li. Auger electrons from Ni using the Al Kα source interfered with these peaks, and switching the X-ray source to Mg Kα X-rays did not provide adequate signal intensity to reliably peak fit the Fe 2p spectra. Detection was not consistent from sample to sample. Consequently, interpretation of the Fe 2p spectra was not attempted. Al was not detected on the surface of any sample via XPS, regardless of X-ray source.

4.4: Conclusions

Investigation of the surface chemistry of I625 samples exposed to molten LiCl-Li_2O-Li solutions at 650°C for 500 and 1000hr was performed via XRD, Raman spectroscopy, and XPS. In the absence of solvated Li^0, the surface of I625 forms a stable $LiCrO_2$ based surface film with minor inclusions of Li_2CrO_4 and $NiFe_xCr_{2-x}O_4$ which acts to limit corrosion of the base alloy. Corrosion of the base alloy in molten LiCl-Li_2O is thus expected to be dictated by the O^{2-} activity and the presence of impurities, similar to the corrosion processes typical in other molten salt systems [33]. When Li is dissolved in the molten LiCl-Li_2O system, the formation of a bulk oxide film is not possible due to the highly reducing conditions caused by metallic Li; however, XPS analysis showed that the active alloying elements Cr, Mo, and Nb were all present to varying degrees in oxidized states on the sample surfaces, even up to high concentrations of Li in solution. This indicates that there is a synergistic effect between the oxidation caused by the O^{2-} ions and the reducing nature of solvated Li^0 that allows for the effective

dissolution of Cr, Mo, and Nb, although further investigation would be necessary to confirm this hypothesis. Our earlier work showed that the alloy was depleted of these elements at the sample surface and in the regions displaying the highly porous microstructure seen via SEM-EDS. Consequently, it is likely that the diffusion of Cr, Mo, and Nb through the alloy microstructure and their subsequent dissolution in to the molten LiCl-Li_2O-Li system is responsible for the porosity observed in that study.

Chapter 5 : Conclusions and Future Work

5.1: Conclusions

Both SS316L and I625 exhibited similar corrosion phenomena, with a protective $LiCrO_2$ based oxide film forming on the surface upon exposure to LiCl-Li_2O in the absence of dissolved Li. Minor components of Li_2CrO_4 and $NiFe_xCr_{2-x}O_4$ were also observed on these samples, with I625 forming the most fully developed oxide layer with a well-defined crystalline structure. These oxide films were successful in limiting corrosion to an acceptable level, with SS316L showing a corrosion rate of approximately 0.2mm/year, while the corrosion rate was approximately 0.1mm/year for I625. A multilayered oxide structure was observed on I625, with the outermost layer being composed primarily of $LiCrO_2$ and the inner layers incorporating progressively more Ni and Fe oxides.

While both SS316L and I625 performed acceptably upon exposure to LiCl-Li_2O containing no metallic Li, the addition of Li metal to the solution resulted in a very reducing environment, and protective oxide layers were not found to form on the sample surface. The removal of the oxide layer resulted in the exposure of the base material directly to the highly corrosive LiCl-Li_2O-Li solution, and severely accelerated corrosion. For both SS316L and I625, this resulted in the selective dissolution of certain alloying elements. Particularly, Cr, Mo, Nb, and Mn were all depleted from the sample surfaces, depending on alloy composition. For SS316L, this resulted in intergranular corrosion that penetrated the sample at a rate of approximately 2-3mm/year. Evidence of salt intrusion into the base

material was also observed on SS316L, as were Cr carbides immediately preceding the intruded salt. This indicates that, similar to corrosion by pure metallic Li, intergranular attack of metallic carbides is the primary corrosion mechanism. In I625, the selective dissolution of Cr, Mo, and Nb lead to the formation of a highly porous microstructure, similar in nature to a Ni foam. Evidence of oxidized Cr, Mo, Nb, and Mn was observed via XPS analysis, depending on the alloy composition. Both Ni and Fe were always observed in the metallic state on samples exposed to LiCl-Li_2O-Li solutions. This indicates that there may be a cyclical oxidation-reduction pathway that leads to the selective dissolution of these alloying elements into the molten salt.

These results indicate that the corrosion mechanisms responsible for material degradation in the LiCl-Li_2O-Li system are a combination of the corrosion mechanisms that have been observed by other researchers during corrosion studies of alloys in molten salts and liquid metals. The combined effects of molten salt and liquid metal corrosion result in a more severe attack of the base material than would be observed in the isolated cases of pure molten salt or liquid metal corrosion.

These findings have direct impact on the operation and design of engineering scale and production scale UNF oxide reduction systems utilizing LiCl-Li_2O based electrolytes. The obvious solution to the problem of accelerated corrosion is to simply increase the wall thickness of the vessel in order to account for the degradation over time. However, a more elegant approach would be to

limit the activity of Li in the melt. This goal could be accomplished by a number of means, however, the most elegant and reliable solution would likely be the simple addition of another cathode basket of UNF that has yet to be reduced. The presence of UO_2 in direct contact with the melt would prevent the activity of Li from becoming high enough to cause severe degradation of the vessel, and would also increase the overall current efficiency of the system.

5.2: Future Work

Although these studies represent a significant advancement in the understanding of corrosion in molten LiCl-Li_2O-Li, numerous avenues for remain uncharted that could help further understand the effect metallic Li has on materials exposed to the conditions present during oxide reduction of UNF. Of these pathways forward for future work, *In-situ* spectroscopy of the surface of corrosion samples would shed light on the nature of the corrosion products at temperature. Advanced fiber coupled Raman probes, high temperature inert atmosphere XRD, and other x-ray spectroscopies could allow for the analysis of corrosion products as they form, rather than the post exposure studies presented in this work. It is possible that chemical or morphological changes occur during cooling or the removal of the residual salt layer, so these *in-situ* studies would be invaluable for understanding the mechanisms responsible for material degradation in LiCl-Li_2O-Li.

The difficulty associated with detecting Li was a major limitation in this investigation. Direct chemical analysis of Li is difficult due to its low atomic

number, which results in extremely low energy x-rays and photoelectrons of 52 eV. Typical X-ray detectors for chemical analysis utilize Be windows to isolate the detector from the sample chamber, resulting in the absorption of the characteristic X-rays of Li. Numerous elements exhibit outer shell X-ray and photoelectron emission in this region, further complicating analysis. Secondary ion mass spectroscopy (SIMS) and electron energy loss spectroscopy (EELS) allow for the detection of Li, as do some advanced EDS and wavelength dispersive spectroscopy (WDS) instruments, and the use of these instruments would provide extremely valuable information on the chemical structure and spatial distribution of Li and its compounds on these samples. Particularly with the extreme level of corrosion observed in the presence of metallic Li, it would be useful to be able to determine the distribution of Li through the sample cross sections.

Computational modelling has led to many recent advancements in other fields of materials science but has been slow to be adopted in the field of corrosion research, primarily due to the inherently large multiphase systems that must be simulated for accurate modeling of corrosion environments. However, the continuous increase in the power of high-performance computers has increased the accuracy and number of atoms able to be simulated in atomistic modeling. Application of multiscale computational modeling methods to the corrosion of alloys in molten salts could help to quickly identify potential materials capable of withstanding the demands of these systems. Models verified by experimental results would lead to a deeper understanding of the reaction

pathways, thermodynamics, and kinetics of the corrosion mechanisms in these complicated systems.

Accelerated corrosion testing via electrochemical means is well established as a viable method of estimating corrosion rates in aqueous systems and has been applied to other molten salt systems. The presence of Li and the associated rise in electrical conductivity of the electrolyte complicates the analysis of electrochemical methods for the LiCl-Li_2O-Li system, and the lack of a universally accepted reference electrode for this system introduces further complications. The development of reference electrodes was attempted during these studies and is detailed in the appendices, but this work remains unfinished. Additionally, it would likely be necessary to re-derive the Tafel equations for the LiCl-Li_2O-Li system to account for the simultaneous action of ionic and electronic conduction in order to fully deconvolute their independent effects on the current-potential curves.

In operation, the oxide reduction electrolyte chemistry is much more complicated than the ternary LiCl-Li_2O-Li system studied in this work. High variations in cover gas atmosphere may occur due to both reduction operations which generate O_2 gas at the anode and the difficulty of maintaining the atmosphere of a working hot cell. The result of this is a vessel intermittently exposed to relatively high levels of O_2 and H_2O while at high temperatures. Additionally, salt soluble fission products such as I, Ba, Cs, Te, etc. will all be dissolved into the electrolyte and accumulate as used fuel is processed [8, 50].

While this is a benefit for the overall pyroprocessing flow sheet and simplifies later processing operations, the addition of these elements to the electrolyte complicates the solution chemistry during oxide reduction. Particularly, Te was shown to be of great concern to the corrosion of materials during the molten salt reactor experiment, where it caused intergranular corrosion of various Ni based alloys even at relatively low concentrations [29]. Effect of fission products on the corrosion of structural materials in an operating OR vessel are of great interest, and should be investigated further.

Experimentally studying each of these parameters independently would help to shed light on the mechanisms involved and could keep many graduate students busy; however, it would also be beneficial to study materials exposed to the conditions present concurrently with engineering scale testing of oxide reduction operations. These studies should be long term in nature, with the goal of predicting the expected service life of components used during oxide reduction operations. An economic analysis of the overall oxide reduction operation, with expected service intervals, cost of disposal and replacement of vessels and other components, and operations should also be conducted.

References

[1] "World Energy Outlook 2018," ed: International Energy Agency, 2018.

[2] Pachauri, R.K. *et al., "*Climate Change 2014 Synthesis Report", Intergovernmental Panel on Climate Change, 2015.

[3] "World Statistics - Nuclear Energy Around the World." Nuclear Energy Institute. http://www.nei.org/Knowledge-Center/Nuclear-Statistics/World-Statistics (accessed Jul 16, 2015).

[4] N. Tsoulfanidis, *The Nuclear Fuel Cycle*, 2 ed. American Nuclear Society, 2013, p. 463.

[5] C. E. Till and Y. I. Chang, *Plentiful Energy: The Story of the Integral Fast Reactor*. 2011.

[6] C. E. Till, Y. I. Chang, and W. H. Hannum, "The Integral Fst Reactor - An Overview," *Progress in Nuclear Energy,* vol. 31, no. 1-2, pp. 3-11, 1997.

[7] K. Gourishankar, L. Redey, and M. Williamson, "Electrolytic Reduction of Metal Oxides in Molten Salts," in *Light Metals, The Minerals, Metals & Materials Society*, W. A. Schneider, Ed., 2002.

[8] S. D. Herrmann, S. X. Li, and M. F. Simpson, "Electrolytic Reduction of Spent Oxide Fuel - Bench-Scale Test Results," in *GLOBAL 2005*, Tsukuba, Japan, 2005.

[9] E.-Y. Choi and S. M. Jeong, "Electrochemical processing of spent nuclear fuels: An overview of oxide reduction in pyroprocessing technology," *Progress in Natural Science: Materials International,* vol. 25, no. 6, pp. 572-582, 2015.

[10] S. Phongikaroon, S. Herrmann, and M. Simpson, "Diffusion Model for Electrolytic Reduction of Uranium Oxides in Molten LiCl-Li_2O Salt," *Nuclear Technology,* vol. 174, no. 1, pp. 85-93, 2010.

[11] S. Herrmann, S. Li, and B. Serrano-Rodriguez, "Observations of Oxygen Ion Behavior in the Lithium-Based Electrolytic Reduction of Uranium Oxide," in *GLOBAL 2009*, Paris, France, 2009: Idaho National Labs, pp. 1198-1206.

[12] B. H. Park, I. W. Lee, and C. S. Seo, "Electrolytic reduction behavior of U_3O_8 in a molten LiCl–Li2O salt," *Chemical Engineering Science,* vol. 63, no. 13, pp. 3485-3492, 2008.

[13] W. Park *et al.*, "An experimental study for Li recycling in an electrolytic reduction process for UO_2 with a Li_2O–LiCl molten salt," *Journal of Nuclear Materials,* vol. 441, no. 1–3, pp. 232-239, 2013.

[14] E. Y. Choi *et al.*, "Electrochemical reduction behavior of a highly porous SIMFUEL particle in a LiCl molten salt," *Chemical Engineering Journal (Lausanne),* vol. 207-208, pp. 514-520, 2012.

[15] W. Xiao and D. Wang, "The electrochemical reduction processes of solid compounds in high temperature molten salts," *Chemical Society Reviews,* vol. 43, no. 10, pp. 3215-3228, 2014.

[16] T. N. Nakajima, K. and N. Watanabe, "The Dissolution of Lithium in Molten Lithium Chloride," *Nippon Kagaku Kaishi,* vol. 1974, pp. 401-404, 1974.

[17] A. Merwin, M. A. Williamson, J. L. Willit, and D. Chidambaram, "Review - Metallic Lithium and the Reduction of Actinide Oxides," *Journal of the Electrochemical Society,* vol. 164, no. 8, pp. H5236-H5246, 2017.

[18] M. A. Bredig, in *Molten Salt Chemistry*, M. Blander Ed.: John Wiley and Sons, 1964, 1964, pp. 367-425.

[19] N. J. Gese, "The Electrochemistry of Li-LiCl-Li2O Molten Salt Systems and the role of Moisture," Nuclear Engineering, University of Idaho, 2015.

[20] T. Nakajima, K. Nakanishi, and N. Watanabe, "The Dispersion of Metallic Lithium in Various Molten Salts," *Nippon Kagaku Kaishi,* vol. 1975, pp. 617-621, 1975.

[21] J. Liu and J. C. Poignet, "Measurement of the activity of lithium in dilute solutions in molten lithium chloride between 650°C and 800°C," (in English), *Journal of Applied Electrochemistry,* vol. 20, no. 5, pp. 864-867, 1990.

[22] A. Merwin, W. C. Phillips, M. A. Williamson, J. L. Willit, P. N. Motsegood, and D. Chidambaram, "Presence of Li Clusters in Molten LiCl-Li," *Scientific Reports,* vol. 6, p. 25435, 2016.

[23] N. Watanabe, K. Nakanishi, and T. Nakajima, "The Dissolution of Lithium in Molten Lithium Chloride," *Nippon Kagaku Kaishi,* vol. 1974, no. 3, pp. 401-404, 1974.

[24] T. N. Nakajima, K. and N. Watanabe, "Study of Emulsions in Molten Salts III. The concentration stability and particle-size distribution of dispersed lithium in molten lithium chloride," *Bulletin of the Chemical Society of Japan,* vol. 49, pp. 994-997, 1975.

[25] A. Merwin and D. Chidambaram, "The effect of Li^0 on the corrosion of stainless steel alloy 316L exposed to molten LiCl-Li_2O-Li," *Corrosion Science,* vol. 126, pp. 1-9, 2016.

[26] A. Merwin, "Material Interactions with Molten LiCl-Li_2O-Li," Doctor of Philosophy in Materials Science and Engineering, Materials Science and Engineering, University of Nevada, Reno, 2016.

[27] E. Y. Choi *et al.*, "Electrochemical reduction of UO2 in LiCl–Li2O molten salt using porous and nonporous anode shrouds," *Journal of Nuclear Materials,* vol. 444, pp. 261-269, 2014.

[28] Y. Sakamura, M. Iizuka, S. Kitawaki, A. Nakayoshi, and H. Kofuji, "Formation and reduction behaviors of zirconium oxide compounds in LiCl–Li2O melt at 923 K," *Journal of Nuclear Materials,* vol. 466, pp. 269-279, 2015.

[29] P. N. Haubenreich and J. R. Engel, "Experience with the molten-salt reactor experiment," *Nuclear Technology,* vol. 8, no. 2, pp. 118-136, 1970.

[30] V. Ignatiev and A. Surenkov, "Material Performance in Molten Salts," in *Comprehensive Nuclear Materials*, vol. 5: Material Performance and Corrosion/Waste Materials, R. J. M. Konings Ed. Amsterdam, The Netherlands: Elsevier, 2012, ch. 5.10, pp. 221-250.

[31] J. Latkowski, "TerraPower and the Molten Chloride Fast Reactor," ed: TerraPower, 2015.

[32] (2014). *Technology Roadmap Update for Generation IV Nuclear Energy Systems*.

[33] T. R. Allen and K. Sridharan, F. G. Lantelme, H, Ed. *Corrosion in Molten Salts, in Molten salts chemistry from lab to applications*, 1 ed. Burlington, MA: Elsevier, 2013.

[34] E. S. Bettis, R. W. Schroeder, G. A. Cristy, H. W. Savage, R. G. Affel, and L. F. Hemphill, "The aircraft reactor experiment—design and construction," *Nucl. Sci. Eng,* vol. 2, no. 6, pp. 804-825, 1957.

[35] G. Zheng, B. Kelleher, G. Cao, M. Anderson, T. Allen, and K. Sridharan, "Corrosion of 316 stainless steel in high temperature molten Li_2BeF4 (FLiBe) salt," *Journal of Nuclear Materials,* vol. 461, no. 0, pp. 143-150, 2015.

[36] J. H. DeVan, I. R. DiStefano, W. P. Eatherly, J. R. Keiser, and R. L. Klueh, "Materials considerations for molten salt accelerator-based plutonium conversion systems," 1995, pp. 476-487.

[37] D. F. Williams, "Assessment of candidate molten salt coolants for the NGNP/NHI Heat-Transfer Loop," Oak Ridge National Laboratory, ORNL/TM-2006/69, 2006/06// 2006. [Online]. Available: https://www.researchgate.net/publication/237299958_Assessment_of_candidate_molten_salt_coolants_for_the_NGNPNHI_Heat-Transfer_Loop

[38] G. DeVries, "The Corrosion of Metals by Molten Lithium," in *Proceedings of the Sessions on Corrosion by Liquid Metals of the 1969 Fall Metting of the Metallurgical Society of AIME*, Philadelphia, Pennsylvania, J. E. Draley and J. R. Weeks, Eds., 1969: Springer Science and Business Media, LLC.

[39] W. Phillips, A. Merwin, and D. Chidambaram, "On the Corrosion Performance of Monel 400 in Molten LiCl-Li_2O-Li at 923 K," *Metallurgical and Materials Transactions A,* vol. 49, no. 6, pp. 2384-2392, 2018.

[40] O. K. Chopra, D. L. Smith, P. F. Tortorelli, J. H. DeVan, and D. K. Sze, "Liquid-Metal Corrosion," *Fusion Technology,* vol. 8, no. 2P1, pp. 1956-1969, 1985.

[41] E. Shchukin, Z. Polukarova, and V. Savenko, *Liquid metal embrittlement in solids LME-effect*. Lambert Academic Publishing, 2018.

[42] J. E. Indacochea, J. L. Smith, K. R. Litko, and E. J. Karell, "Corrosion performance of ferrous and refractory metals in molten salts under reducing conditions," *Journal of Materials Research,* vol. 14, no. 05, pp. 1990-1995,1999.

[43] J. E. Indacochea, J. L. Smith, K. R. Litko, E. J. Karell, and A. G. Raraz, "High-Temperature Oxidation and Corrosion of Structural Materials in Molten Chlorides," *Oxidation of Metals,* vol. 55, no. 12, pp. 1-16, 1999.

[44] B. Mishra and D. L. Olson, "Corrosion of Refractory Alloys in Molten Lithium and Lithium Chloride," *Mineral Processing and Extractive Metallurgy Reviews,* vol. 22, pp. 369-388, 2001.

[45] S. H. Cho, S. B. Park, J. H. Lee, J. M. Hur, and H. S. Lee, "Corrosion behavior of Ni-based structural materials for electrolytic reduction in lithium molten salt," *Journal of Nuclear Materials,* vol. 412, no. 1, pp. 157-164, 2011.

[46] A. Merwin and D. Chidambaram, "Corrosion of Inconel Alloy 625 in Molten LiCl-Li_2O-Li," *Nuclear Technology,* vol. 195, no. 2, pp. 204-212, 2016.

[47] E.-Y. Choi and J. Lee, "Feasibility tests of nickel as a containment material of molten Li_2O-LiCl salt containing Li metal at 650°C during electrolytic reduction," *Journal of Nuclear Materials,* vol. 495, no. Supplement C, pp. 85-90, 2017.

[48] H. Lee *et al.*, "Pyroprocessing Technology Development at KAERI," *Nuclear Engineering and Technology,* vol. 43, no. 4, pp. 317-328, 2011.

[49] M. Kurata, T. Inoue, J. Serp, M. Ougier, and J. P. Glatz, "Electro-chemical reduction of MOX in LiCl," *Journal of Nuclear Materials,* vol. 328, pp. 97-102, 2004.

[50] S. D. Herrmann, S. X. Li, M. F. Simpson, and S. Phongikaroon, "Electrolytic Reduction of Spent Nuclear Oxide Fuel as Part of an Integral Process to Separate and Recover Actinides from Fission Products," *Separation Science and Technology,* vol. 41, pp. 1965-1983, 2006.

[51] M. Iixzuka, Y. Sakamura, and T. Inoue, "Electrochemical reduction of (U-40Pu-5Np)O_2 in molten LICl electrolyte," *Journal of Nuclear Materials,* vol. 359, pp. 102-113, 2006.

[52] B. Park, S. Park, S. Jeong, and C. Seo, "Electrolytic reduction of spent oxide fuel in a molten LiCl-Li_2O system," *Journal of Radioanalytical and Nuclear Chemistry,* vol. 270, pp. 575-583, 2006.

[53] C. S. Seo, S. B. Park, B. H. Park, K. J. Jung, S. W. Park, and S. H. Kim, "Electrochemical Study on the Reduction Mechanism of Uranium Oxide in a LiCl-Li_2O Molten Salt," *Journal of Nuclear Science and Technology,* vol. 43, no. 5, pp. 587-595, 2006.

[54] S. Jeong *et al.*, "An Electrochemical Reduction of Uranium Oxide in the Advanced Spent Fuel Conditioning Process," *Nuclear Technology,* vol. 162, pp. 184-191, 2007.

[55] S. Herrmann, S. Li, D. Sell, and B. Westphal, "Electrolytic Reduction of Spent Nuclear Oxide Fuel – Effects of Fuel Form and Cathode Containment Materials on Bench-Scale Operations," Idaho National Laboratory, 2007.

[56] S. X. Li, M. F. Simpson, and S. D. Hermann, "Oxygen Ion Oxidation Process on a Platinum Electrode in LiCl-Li_2O At 650C," in *Electrochemical Society Proceedings*, R. A. Mantz, Ed., 2004, vol. 24.

[57] A. Merwin and D. Chidambaram, "Alternate Anodes for the Electrolytic Reduction of UO_2," *Metallurgical and Materials Transactions A,* vol. 46, no. 1, pp. 536-544, 2015.

[58] T. Usami *et al.*, "Lithium reduction of americium dioxide to generate americium metal," *Journal of Nuclear Materials,* vol. 304, no. 1, pp. 50-55, 2002.

[59] A. S. Dworkin, H. R. Bronstein, and M. A. Bredig, "Miscibility of Metals with Salts. VI. Lithium-Lithium Halide Systems," *The Journal of Physical Chemistry,* vol. 66, pp. 572-573, 1962.

[60] T. Nakajima, R. Minami, K. Nakanishi, and N. Watanabe, "Miscibility of Lithium with Lithium Chloride and Lithium Chloride - Potassium Chloride Eutectic Mixture," *Bulletin of the Chemical Society of Japan,* vol. 47, no. 8, pp. 2071-2072, 1974.

[61] T. Nakajima, K. Nakanishi, and N. Watanabe, "Study of Emulsions in Molten Salts III. The concentration stability and particle-size distribution of dispersed lithium in molten lithium chloride," *Bulletin of the Chemical Society of Japan,* vol. 49, no. 4, pp. 994-997, 1975.

[62] T. Usami, M. Kurata, T. Inoue, H. E. Sims, S. A. Beetham, and J. A. Jenkins, "Pyrochemical reduction of uranium dioxide and plutonium dioxide by lithium metal," *Journal of Nuclear Materials,* vol. 300, no. 1, pp. 15-26, 2002.

[63] S. H. Cho, J. S. Zhang, Y. J. Shin, S. W. Park, and H. S. Park, "Corrosion behavior of Fe–Ni–Cr alloys in the molten salt of LiCl–Li_2O at high temperature," *Journal of Nuclear Materials,* vol. 325, no. 1, pp. 13-17, 2004.

[64] R. Y. Liu, X. Wang, J. S. Zhang, and X. M. Wang, "Corrosion of nickel in molten LiCl–Li_2O at 750°C," *Journal of Nuclear Materials,* vol. 327, no. 2–3, pp. 194-201, 2004.

[65] C. Soo-Haeng, L. Jong-Ho, P. Sung-Bin, J. Ki-Jung, and P. Seong-Won, "Hot corrosion behavior of superalloys in lithium molten salt," *Journal of the Korean Institute of Metals and Materials,* Jour vol. 43, no. 6, pp. 449-54, 2005.

[66] Q. Gao, R. Y. Liu, J. S. Zhang, and J. T. Guo, "Corrosion behavior of intermetallic compound of TiAl–5Nb in molten LiCl–Li_2O," *Materials Letters,* vol. 59, no. 16, pp. 2052-2058, 2005.

[67] S. H. Cho, S. B. Park, J. H. Lee, J. M. Hur, and H. S. Lee, "Hot corrosion behavior of ZrO_2–MgO coatings in LiCl–Li_2O molten salt," *Materials Chemistry and Physics,* vol. 131, no. 3, pp. 743-751, 2012.

[68] C. Soo-Haeng, P. Seong-Bin, L. Jong-Hyeon, H. Jin-Mok, and L. Han-Soo, "Cyclic Corrosion Behavior of Ni-Based Superalloys in Hot Lithium Molten Salt," *Oxidation of Metals,* Jour vol. 78, no. 3-4, pp. 153-65, 2012.

[69] P. SangKyu, L. TaeHyuk, S. MoonSoo, N. JaeSoo, C. SooHaeng, and L. JongHyeon, "Alloy design of new Ni-based structural materials for electrolytic reduction and its corrosion behavior in lithium molten salt," *Advanced Materials Research,* vol. 886, pp. 41-44, 2014.

[70] H.-Y. Lee and K.-H. Baik, "Comparison of corrosion resistance between Al_2O_3 and YSZ coatings against high temperature LiCl-Li_2O molten salt," (in English), *Metals and Materials International,* vol. 15, no. 5, pp. 783-787, 2005.

[71] Y. S. Zhang, "Solubilities of Cr_2O_3 in Fused Na_2SO_4 at 1200K," *Journal of The Electrochemical Society,* vol. 133, p. 655, 1986.

[72] D. A. Jones, *Principles and Prevention of Corrosion*, 2 ed. Upper Saddle River, NJ: Prentice Hall, 1996.

[73] J. E. Indacochea, J. L. Smith, K. R. Litko, E. J. Karell, and A. G. Rarez, "High-Temperature Oxidation and Corrosion of Structural Materials in Molten Chlorides," *Oxidation of Metals,* vol. 55, no. 1, pp. 1-16, 2001.

[74] "PDF Card No. : 01-072-7839," ed: The International Centre for Diffraction Data.

[75] M. Suzuki, I. Yamada, H. Kadowaki, and F. Takei, "A Raman scattering investigation of the magnetic ordering in the two-dimensional triangular lattice antiferromagnet $LiCrO_2$," *Journal of Physics: Condensed Matter,* vol. 5, pp. 4225-4232, 1993.

[76] B. D. Hosterman, "Raman Spectroscopic Study of Solid Solution Spinel Oxides," Doctor of Philosophy in Physics, Physics and Astronomy, UNLV, 2011.

[77] D. Chidambaram, C. R. Clayton, and G. P. Halada, "A Duplex Mechanism-Based Model for the Interaction Between Chromate Ions and the Hydrated Oxide Film on Aluminum Alloys," *Journal of the Electrochemical Society,* vol. 150, no. 5, pp. B224-B237, 2003.

[78] M. C. Biesinger, B. P. Payne, A. P. Grosvenor, L. W. M. Lau, A. R. Gerson, and R. S. C. Smart, "Resolving surface chemical states in XPS analysis of first row transition metals, oxides and hydroxides: Cr, Mn, Fe, Co and Ni," *Applied Surface Science,* vol. 257, no. 7, pp. 2717-2730, 2011.

[79] B. Brox and I. Olefjord, "ESCA Studies of MoO_2 and MoO_3," *Surface and Interface Analysis,* vol. 13, no. 1, pp. 3-6, 1988.

[80] J. Baltrusaitis *et al.*, "Generalized molybdenum oxide surface chemical state XPS determination via informed amorphous sample model," *Applied Surface Science,* vol. 326, pp. 151-161, 2015.

[81] M. C. Biesinger, B. P. Payne, A. P. Grosvenor, L. W. M. Lau, A. R. Gerson, and R. S. C. Smart, "Resolving surface chemical states in XPS analysis of first row transition metals, oxides and hydroxides: Cr, Mn, Co and Ni," *Applied Surface Science,* vol. 257, no. 7, pp. 2717-2730, 2011.

[82] J. J. Laidler, J. E. Battles, W. E. Miller, J. P. Ackerman, and E. L. Carls, "Development of Pyroprocessing Technology," *Progress in Nuclear Energy,* vol. 31, no. 1-2, pp. 131-140, 1997.

[83] S. M. Jeong, H. S. Shin, S. H. Cho, J. M. Hur, and H. S. Lee, "Electrochemical behavior of a platinum anode for reduction of uranium oxide in a LiCl molten salt," *Electrochimica Acta,* vol. 54, pp. 6335-6340, 2009.

[84] M. A. Bredig, "Mixtures of Metals with Molten Salts," United States, 1963-08-15 1963. [Online]. Available: https://www.osti.gov/servlets/purl/4658668

[85] L. M. Ferris, M. A. Bredig, and F. J. Smith, "Equilibrium distribution of lithium and bismuth between liquid lithium-bismuth alloys and molten lithium chloride at 650-800.deg," *The Journal of Physical Chemistry,* vol. 77, no. 19, pp. 2351-2357, 1973.

[86] A. J. Burak and M. F. Simpson, "Measurement of Solubility of Metallic Lithium Dissolved in Molten LiCl–Li_2O," *JOM,* vol. 68, no. 10, pp. 2639-2645, 2016.

[87] S.-H. Cho, S.-K. Lee, D.-Y. Kim, J.-H. Lee, and J.-M. Hur, "Effects of alloying elements of nickel-based alloys on the hot-corrosion behavior in an electrolytic reduction process," *Journal of Alloys and Compounds,* vol. 695, no. Supplement C, pp. 2878-2885, 2017.

[88] W. Phillips and D. Chidambaram, "Corrosion of stainless steel 316L in molten LiCl-Li_2O-Li," *Journal of Nuclear Materials,* vol. 517, pp. 241-253, 2019.

[89] W. Phillips and D. Chidambaram, "Effect of Metallic Li on the Surface Chemistry of Inconel 625 Exposed to molten LiCl-Li_2O-Li," *Journal of the Electrochemical Society,* vol. 166, no. 11, pp. C3193-C3199, 2019.

[90] S. Malej, J. Medved, B. Šetina Batič, F. Tehovnik, and M. Godec, *Microstructural evolution of inconel 625 during thermal aging*. 2017, pp. 319-322.

[91] H. Lei *et al.*, "Preparation of novel Raney-Ni catalysts and characterization by XRD, SEM and XPS," *Applied Catalysis A: General,* vol. 214, no. 1, pp. 69-76, 2001.

[92] W. Phillips, Z. Karmiol, and D. Chidambaram, "Effect of metallic Li on the corrosion behavior of Inconel 625 in molten LiCl-Li_2O-Li," *Journal of the Electrochemical Society,* vol. 166, no. 6, pp. C162-C168, 2019.

[93] U. Vogel, E. Brachmann, S. Oswald, S. Menzel, T. Gemming, and J. Eckert, "Evaluation of a mobile vacuum transfer system for in vacuo XPS analysis using as-deposited Ti thin-films," *Vacuum,* vol. 117, pp. 81-84, 2015.

[94] Z. P. Hu, Y. P. Li, M. R. Ji, and J. X. Wu, "The interaction of oxygen with niobium studied by XPS and UPS," *Solid State Communications,* vol. 71, no. 10, pp. 849-852, 1989.

[95] S. M. Jeong, H. Y. Yoo, J.-M. Hur, and C.-S. Seo, "Preparation of metallic niobium from niobium pentoxide by an indirect electrochemical reduction in a LiCl-Li_2O molten salt," *Journal of Alloys and Compounds,* vol. 452, no. 1, pp. 27-31, 2008.

[96] A. J. Bard and L. R. Faulkner, *Electrochemical Methods: Fundamentals and Applications*, 2nd Edition ed. Wiley, 2000.

[97] D. J. G. Ives and G. Janz, *Reference Electrodes: Theory and Practice*. 111 Fifth Avenue, New York, New York 10003: Academic Press, Inc., 1961.

[98] S. Herrmann, S. Li, and M. Simpson, "Electrolytic Reduction of Spent Light Water Reactor Fuel Bench-Scale Experiment Results," *Journal of Nuclear Science and Technology,* vol. 44, no. 3, pp. 361-367, 2007.

[99] M. Iizuka, Y. Sakamura, and T. Inoue, "Electrochemical reduction of (U-40Pu-5Np)O_2 in molten LiCl electrolyte," *Journal of Nuclear Materials,* vol. 359, pp. 102-113, 2006.

[100] V. Pavlyuk, M. Sozanskyi, G. Dmytriv, S. Indris, and H. Ehrenberg, "Amendment of the Li-Bi Phase Diagram Crystal and Electronic Structure of Li_2Bi," *Journal of Phase Equilibria and Diffusion,* journal article vol. 36, no. 6, pp. 544-553, 2015.

[101] M. S. Foster, S. E. Wood, and C. E. Crouthamel, "Thermodynamics of Binary Alloys. I. The Lithium-Bismuth System," *Inorganic Chemistry,* vol. 3, no. 10, pp. 1428-1431, 1964.

[102] *ANL/CMT/CP-96844, Synthesis and casting of a lithium-bismuth compound for an ion-replacement electrorefiner*, 1999.

[103] J. Sangster, "C-Li (Carbon-Lithium) System," *Journal of Phase Equilibria and Diffusion,* vol. 28, no. 6, pp. 561-570, 2007.

[104] J. Miettinen, "Thermodynamic description of Cu–Mg–Ni and Cu–Mg–Zn systems," *Calphad,* vol. 32, no. 2, pp. 389-398, 2008.

[105] P. Gao, X. Jin, D. Wang, X. Hu, and G. Z. Chen, "A quartz sealed Ag/AgCl reference electrode for CaCl2 based molten salts," *Journal of Electroanalytical Chemistry,* vol. 579, no. 2, pp. 321-328, 2005.

[106] F. Mansfeld, S. Lin, Y. C. Chen, and H. Shih, "Minimization of High-Frequency Phase Shifts in Impedance Measurements," *Journal of The Electrochemical Society,* vol. 135, no. 4, pp. 906-907, 1988.

[107] R. N. Singh, "Compatibility of Ceramics with Liquid Na and Li," *Journal of the American Ceramic Society,* vol. 59, no. 3-4, pp. 1

Appendices

Appendix 1 : Supplemental Information for Chapter 4

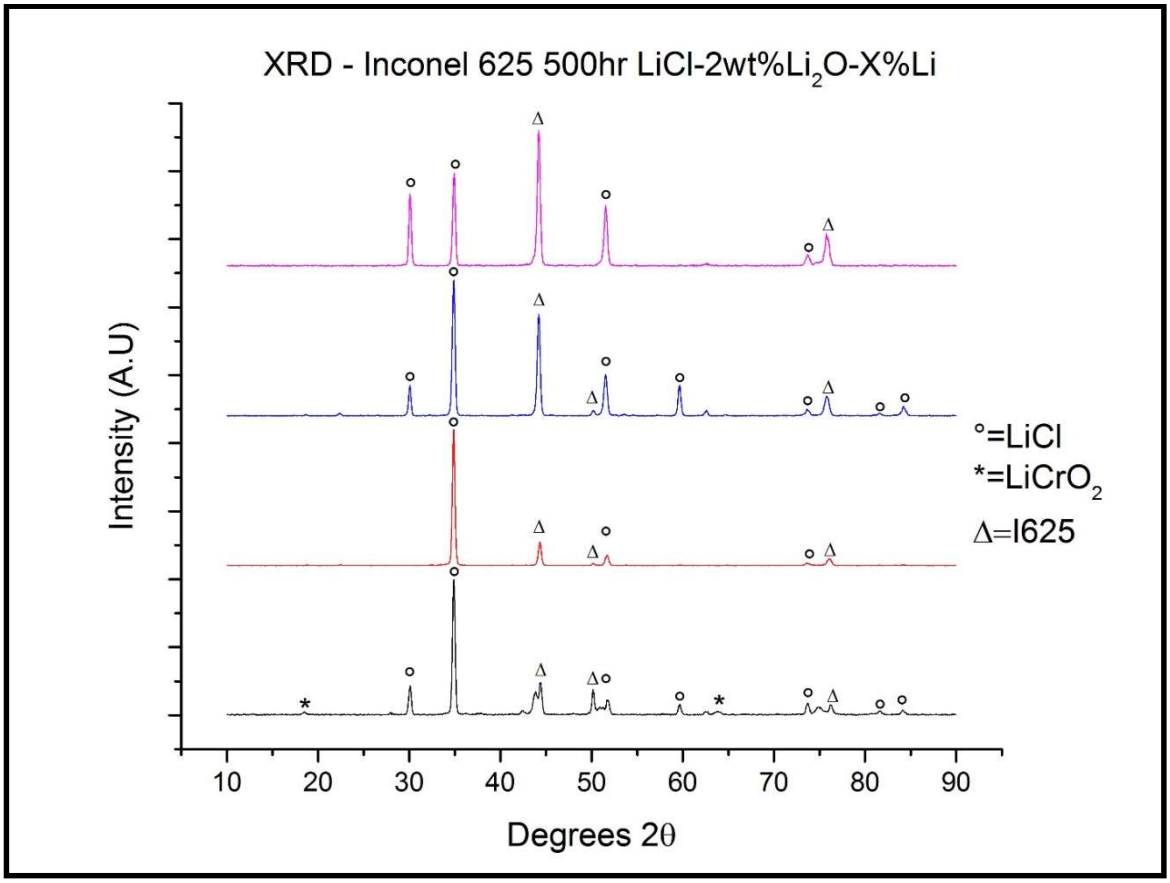

Figure A1-1: GI-XRD patterns obtained from the I625 samples exposed to LiCl-2wt%Li_2O containing 0, 0.3, 0.6, and 1wt% Li for 500hr prior to removal of the residual salt layer via methanol rinsing. Phases identified consist of LiCl, the base material and small amounts of $LiCrO_2$. The residual salt layer significantly obscures the sample surface when compared to the methanol rinsed data. No peaks characteristic of hydrated LiCl were observed, indicting the samples were not contaminated with moisture.

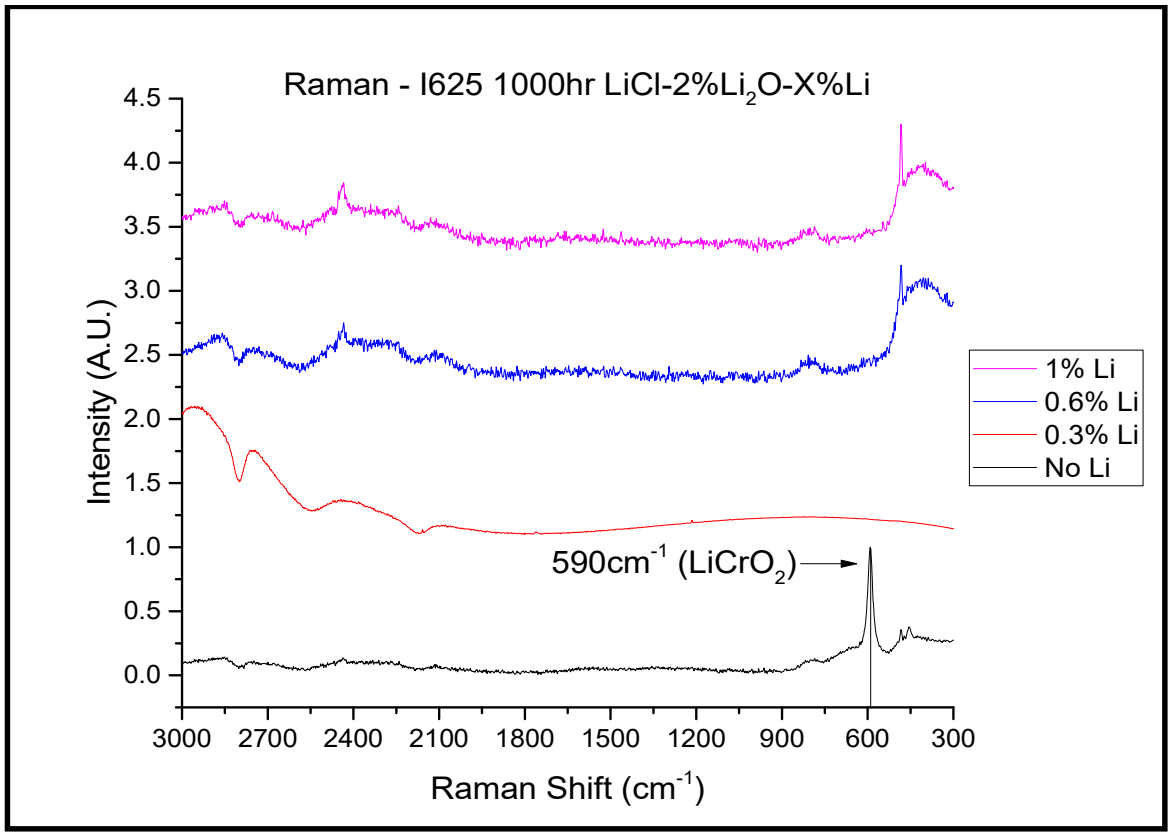

Figure A1-2: Raman spectra obtained from the I625 samples exposed to LiCl-2wt%Li_2O containing 0, 0.3, 0.6, and 1wt% Li for 500hr prior to removal of the residual salt layer via methanol rinsing. $LiCrO_2$ was identified on the surface of the I625 sample exposed to LiCl-2wt%Li_2O in the absence of Li metal. The spectra of the samples exposed to LiCl-Li_2O containing Li are indicative of the spectral artifacts caused by the fiber optic probe. These are present in the spectra of the sample exposed to LiCl-Li_2O in the absence of Li, but are overpowered by the $LiCrO_2$ peak. Consequently, the spectra of the I625 samples exposed to LiCl-Li_2O-Li can be interpreted as being a bare metallic surface covered by the residual layer of salt.

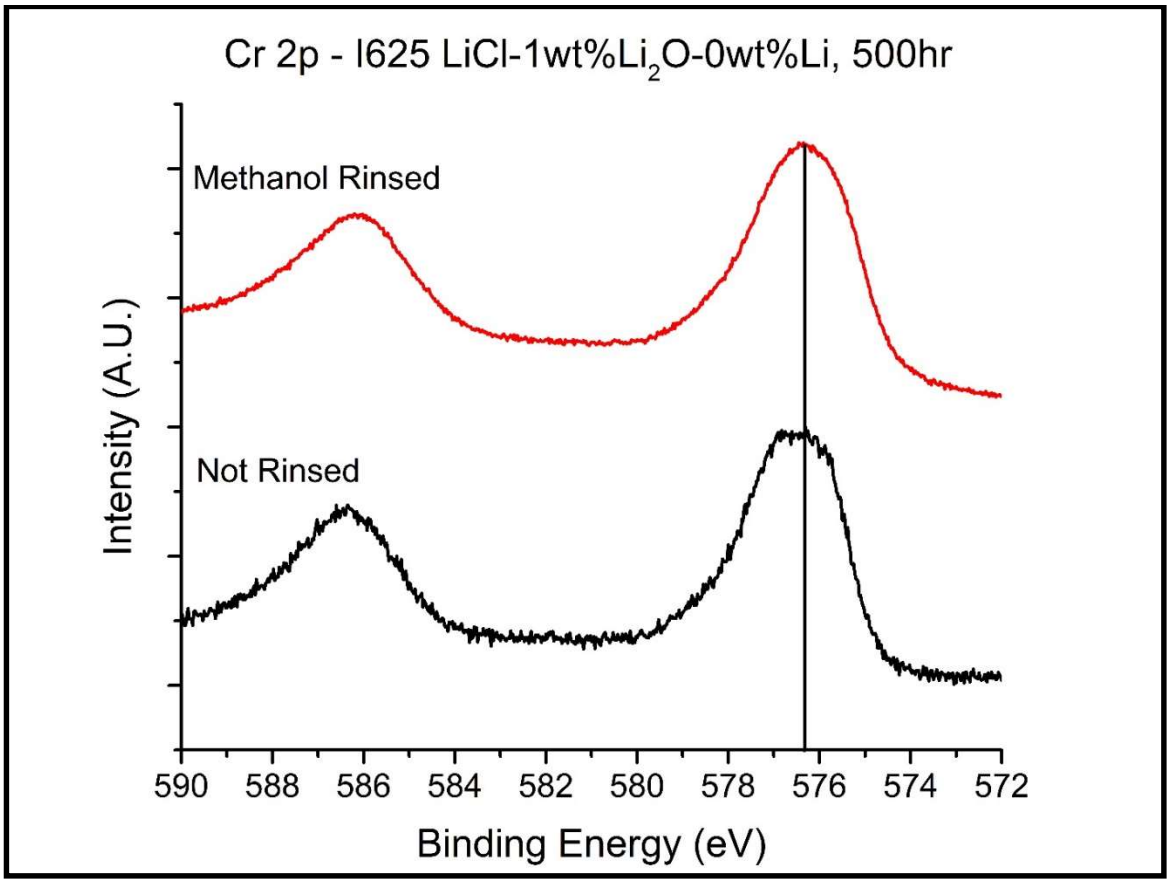

Figure A1-3: XPS Cr 2p spectra obtained from the I625 sample exposed to LiCl-1wt%Li_2O in the absence of Li at 650°C for 500 hr prior to and following methanol rinsing. Identical collection parameters were used, and both spectra were charge corrected to the adventitious C 1s peak at 284.8eV. It can be observed that no significant changes to the Cr 2p spectra occurred as a result of the methanol rinsing procedure, although a significant reduction in noise was realized as a result of the removal of the residual salt layer. The residual salt layer completely obscured the sample surface from XPS analysis on some of the other samples in this study, necessitating the methanol rinsing procedure for their analysis.

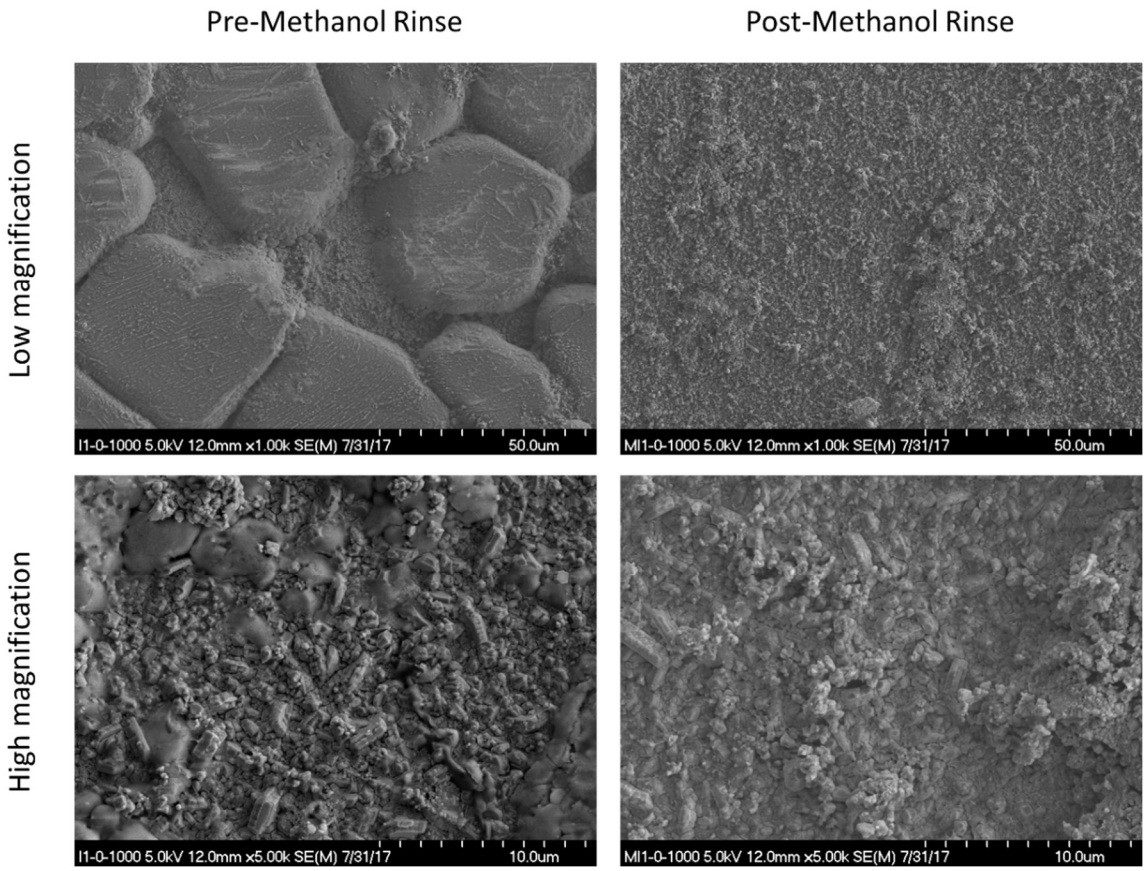

Figure A1-4: SEM images taken at low and high magnifications of the I625 sample exposed to LiCl-1wt%Li_2O-0wt%Li at 650°C for 1000hr taken prior to and following the methanol rinsing procedure to remove the residual salt layer. The top left image shows the high coverage of the sample surface by the residual salt layer, which prevented accurate surface analysis by XPS, XRD, and Raman. This sample had several locations where the oxide layer was possible to view through gaps in the residual salt layer, allowing for direct comparison of the pre and post-methanol rinsing surface morphology. Comparison of the two images taken at high magnification shows that the morphology of the oxide layer remained unchanged following the methanol rinsing procedure. Please refer to our previous study for further morphological and cross sectional analysis of these samples [92].

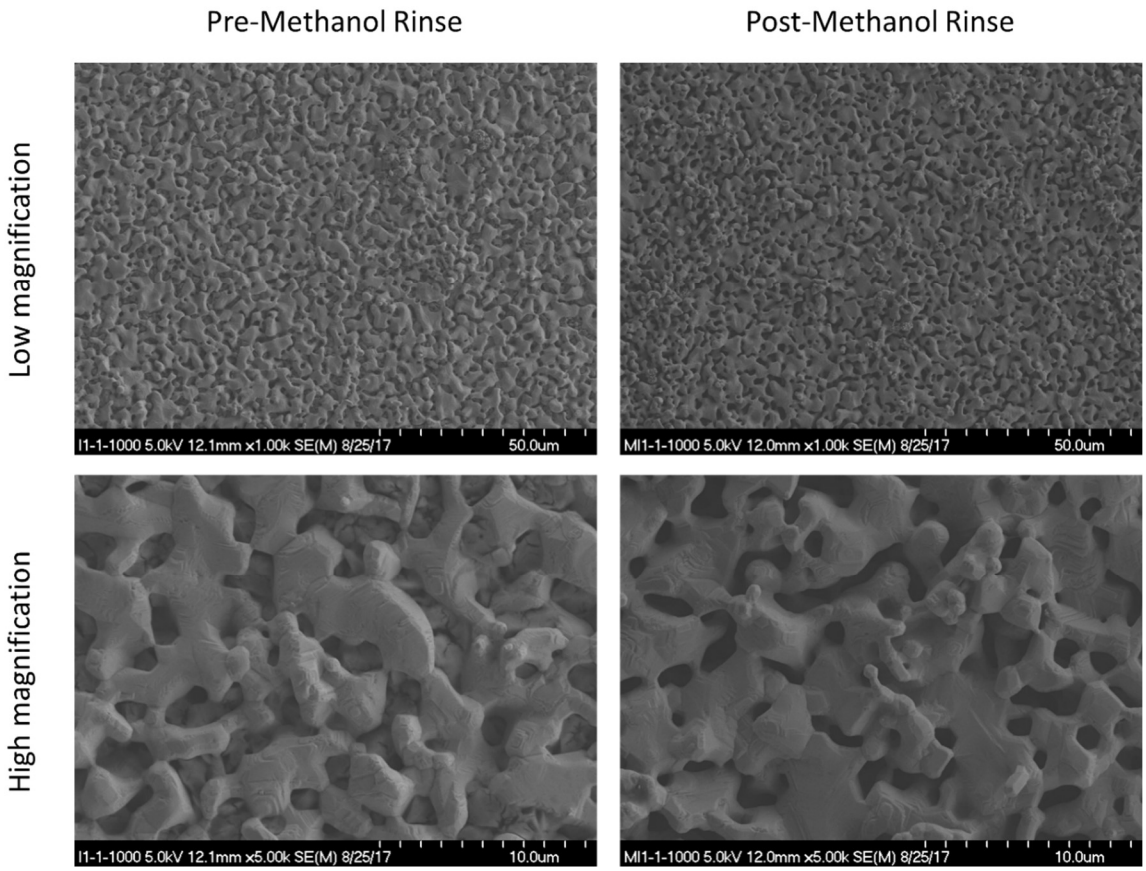

Figure A1-5: SEM images taken at low and high magnifications of the I625 sample exposed to LiCl-1wt%Li_2O-1wt%Li at 650°C for 1000hr taken prior to and following the methanol rinsing procedure to remove the residual salt layer. For this sample, the consistent surface morphology prior to and following the methanol rinsing procedure is readily apparent, as the salt was largely occluded within the pores of the sponge-like structure of the sample. No formation of an oxide layer or change in morphology were observed to occur as a result of the methanol rinsing procedure, although the residual salt was successfully removed from within the pores. Please refer to our previous study for further morphological and cross sectional analysis of these samples [92].

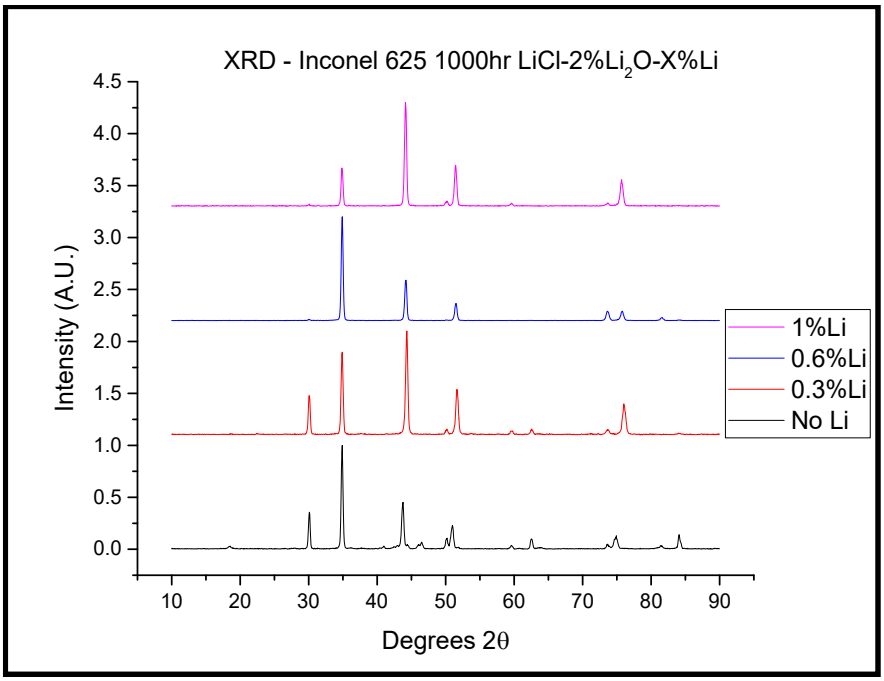

Figure A1-6: GI-XRD patterns collected from I625 samples exposed to LiCl-2wt%Li_2O containing 0, 0.3, 0.6, and 1wt%Li at 650°C for 1000hr prior to the removal of the residual salt layer by rinsing with methanol.

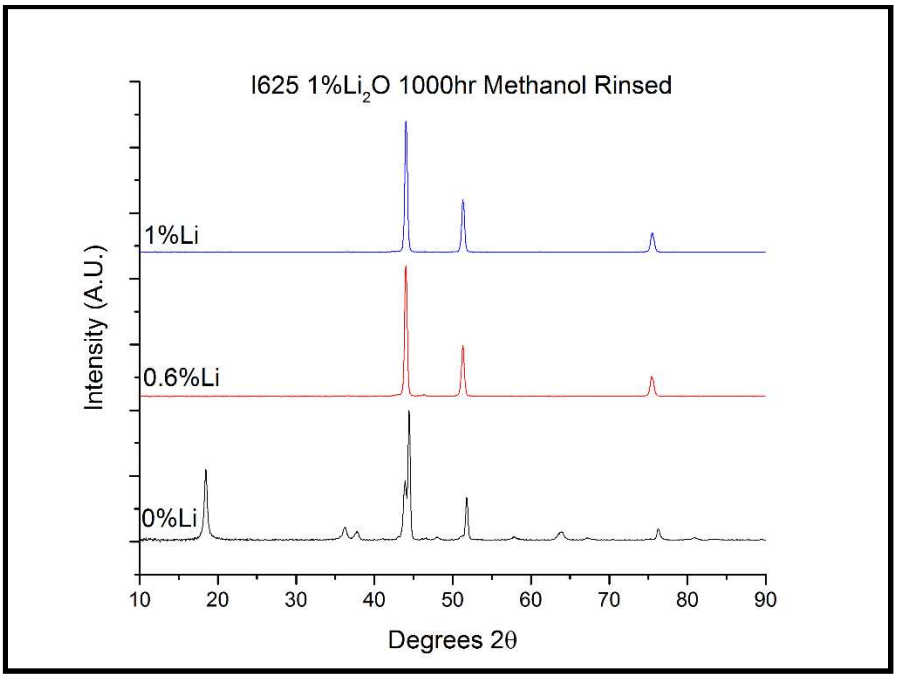

Figure A1-7: GI-XRD patterns collected from I625 samples exposed to LiCl-1wt%Li_2O containing 0, 0.6, and 1wt%Li at 650°C for 1000hr following the removal of the residual salt layer by rinsing with methanol.

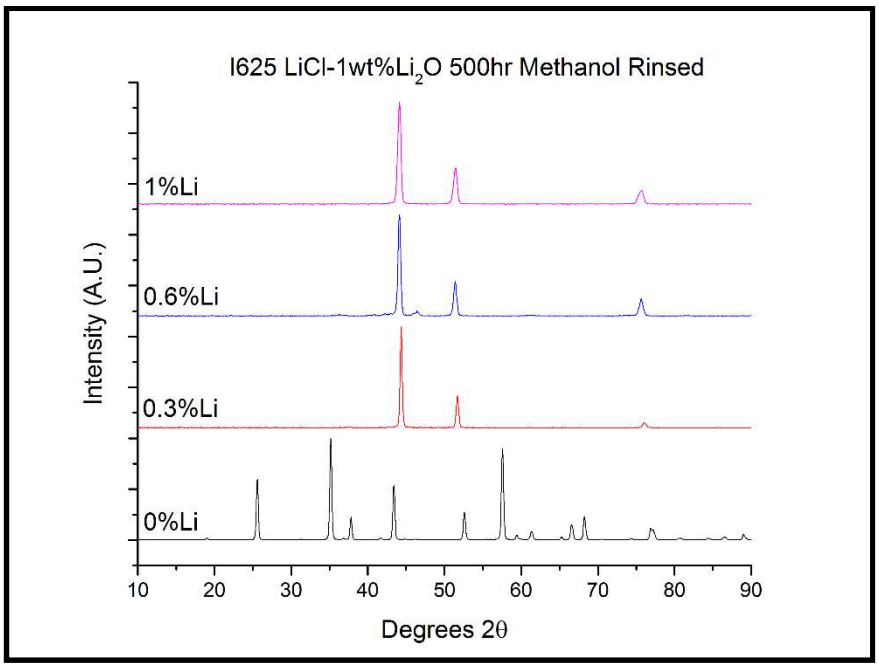

Figure A1-8: GI-XRD patterns collected from I625 samples exposed to LiCl-1wt%Li_2O containing 0, 0.3, 0.6, and 1wt%Li at 650°C for 500hr following the removal of the residual salt layer by rinsing with methanol.

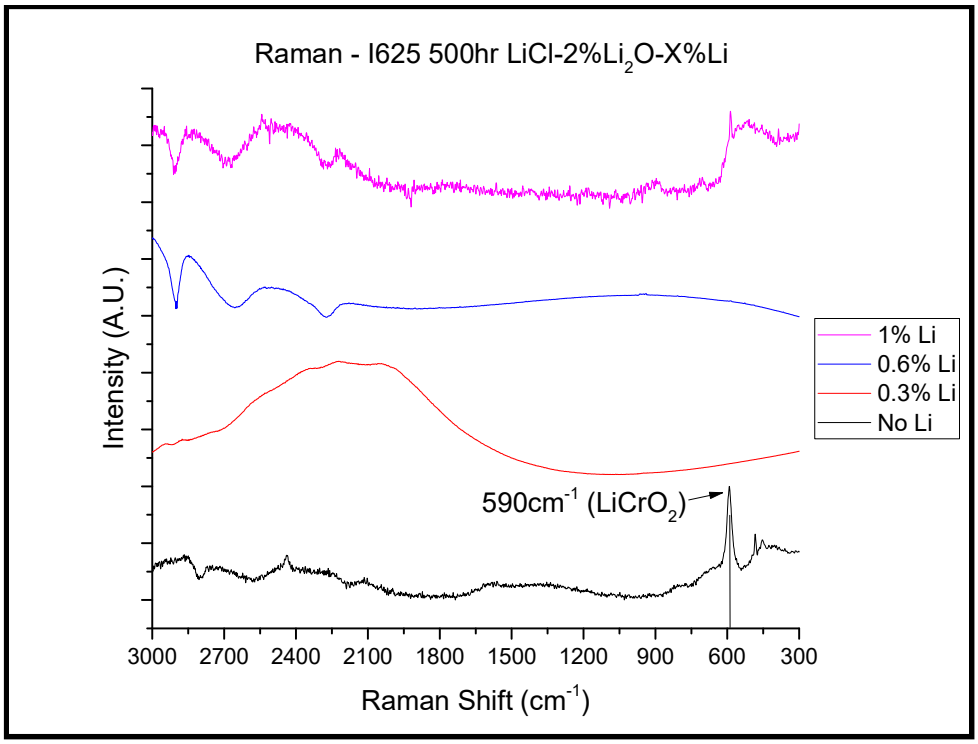

Figure A1-9: Raman spectra collected from I625 samples exposed to LiCl-2wt%Li_2O containing 0, 0.3, 0.6, and 1wt%Li at 650°C for 500hr prior to the removal of the residual salt layer by rinsing with methanol.

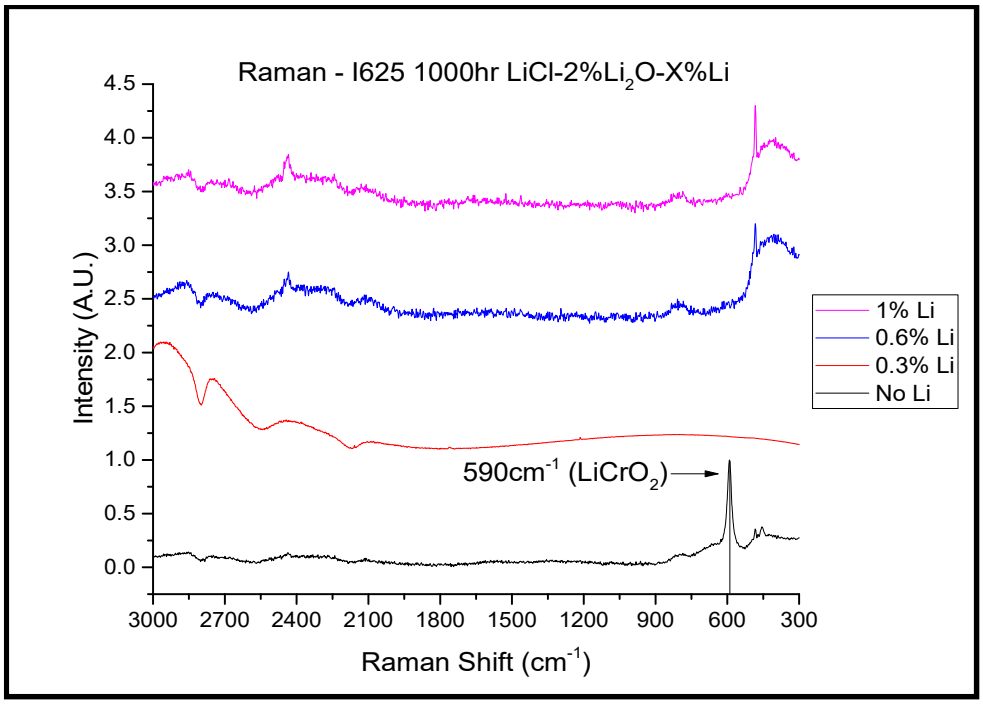

Figure A1-10: Raman spectra collected from I625 samples exposed to LiCl-2wt%Li_2O containing 0, 0.3, 0.6, and 1wt%Li at 650°C for 1000hr prior to the removal of the residual salt layer by rinsing with methanol.

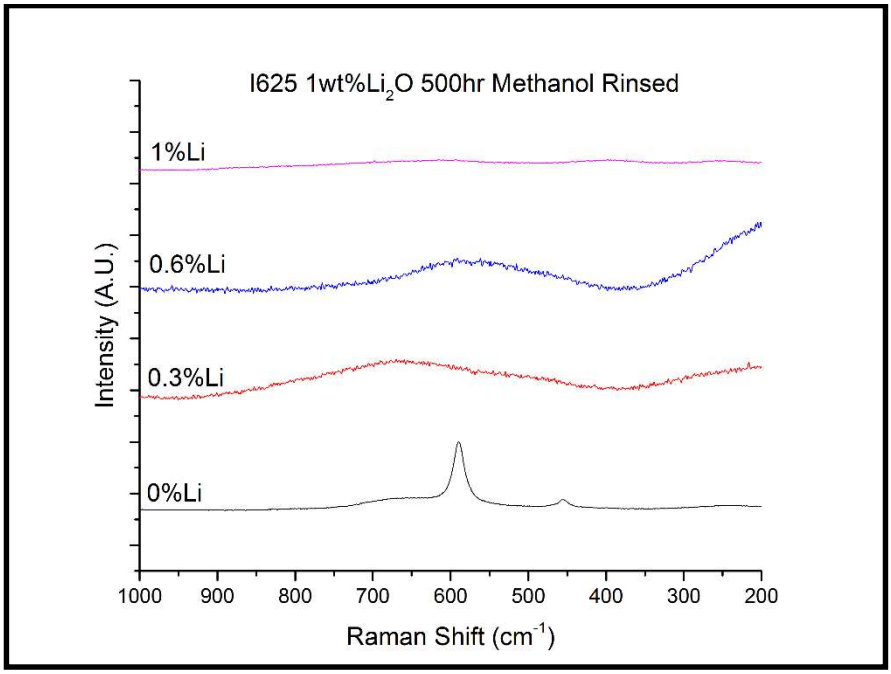

Figure A1-11: Raman spectra collected from I625 samples exposed to LiCl-1wt%Li_2O containing 0, 0.3, 0.6, and 1wt%Li at 650°C for 500hr following the removal of the residual salt layer by rinsing with methanol.

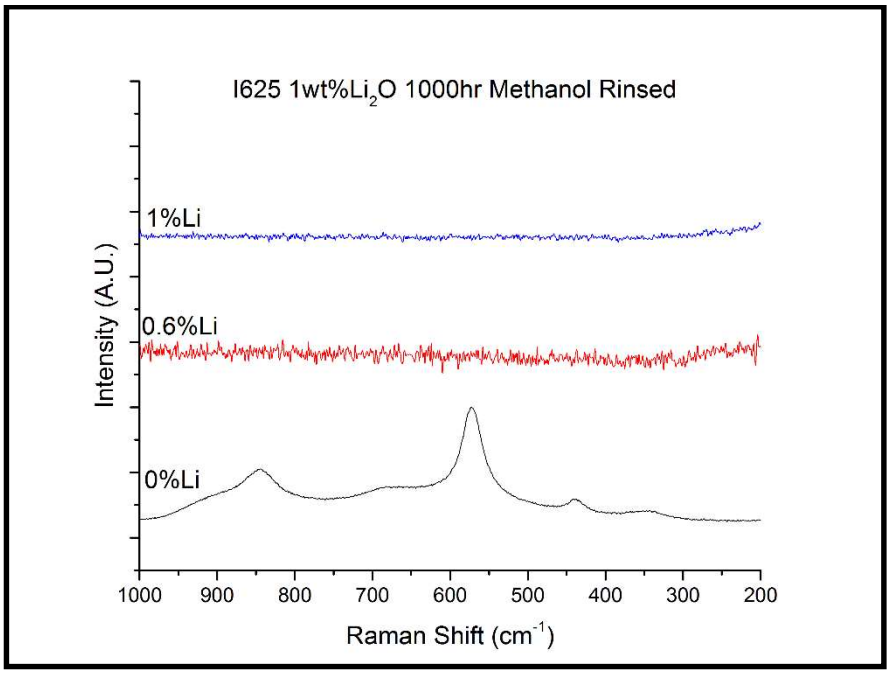

Figure A1-12: Raman spectra collected from I625 samples exposed to LiCl-1wt%Li_2O containing 0, 0.3, 0.6, and 1wt%Li at 650°C for 1000hr following the removal of the residual salt layer by rinsing with methanol.

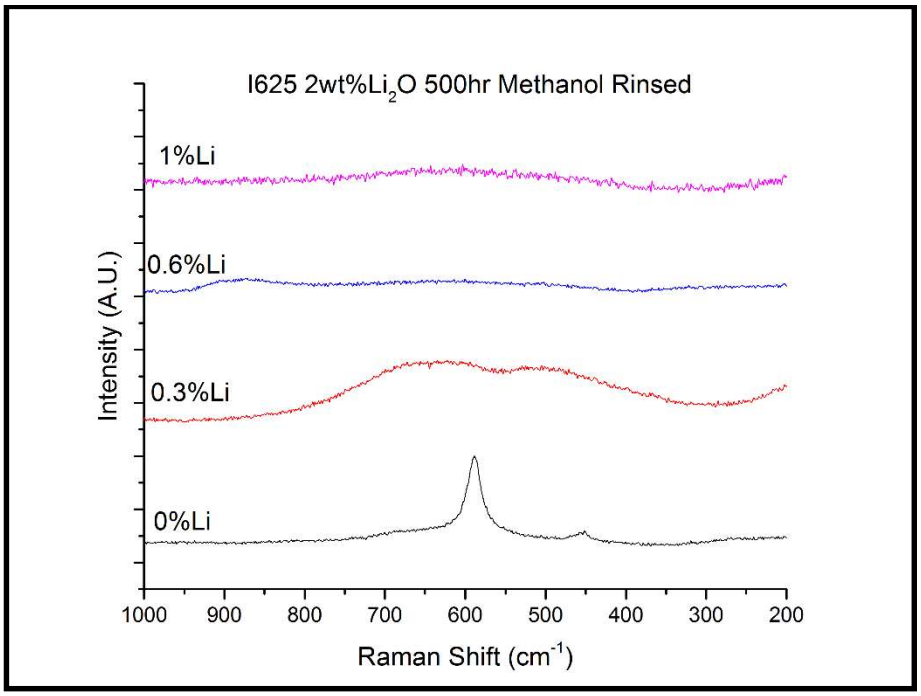

Figure A1-13: Raman spectra collected from I625 samples exposed to LiCl-2wt%Li_2O containing 0, 0.3, 0.6, and 1wt%Li at 650°C for 500hr following the removal of the residual salt layer by rinsing with methanol.

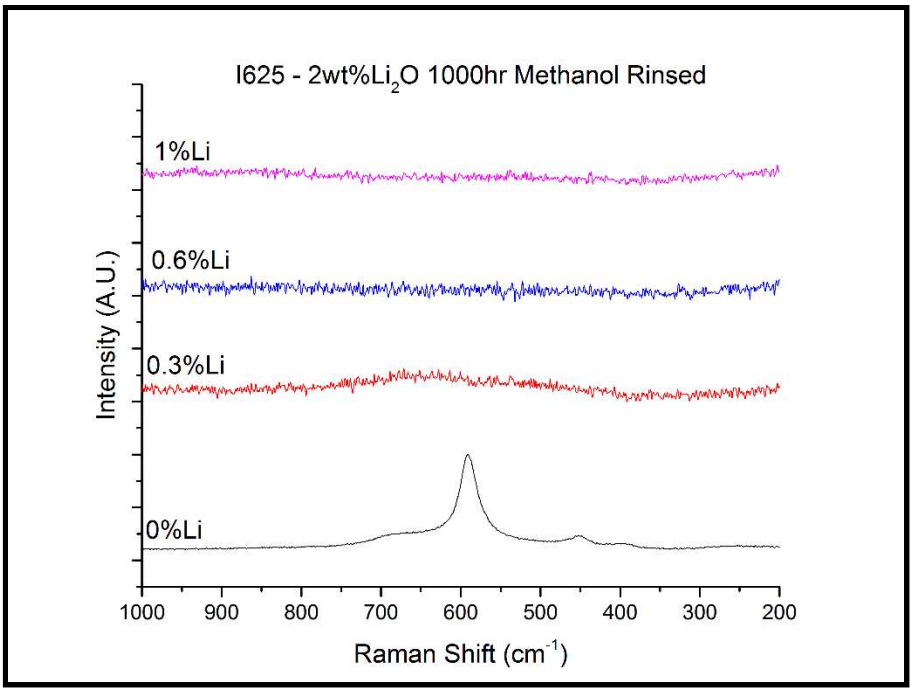

Figure A1-14: Raman spectra collected from I625 samples exposed to LiCl-2wt%Li_2O containing 0, 0.3, 0.6, and 1wt%Li at 650°C for 1000hr following the removal of the residual salt layer by rinsing with methanol.

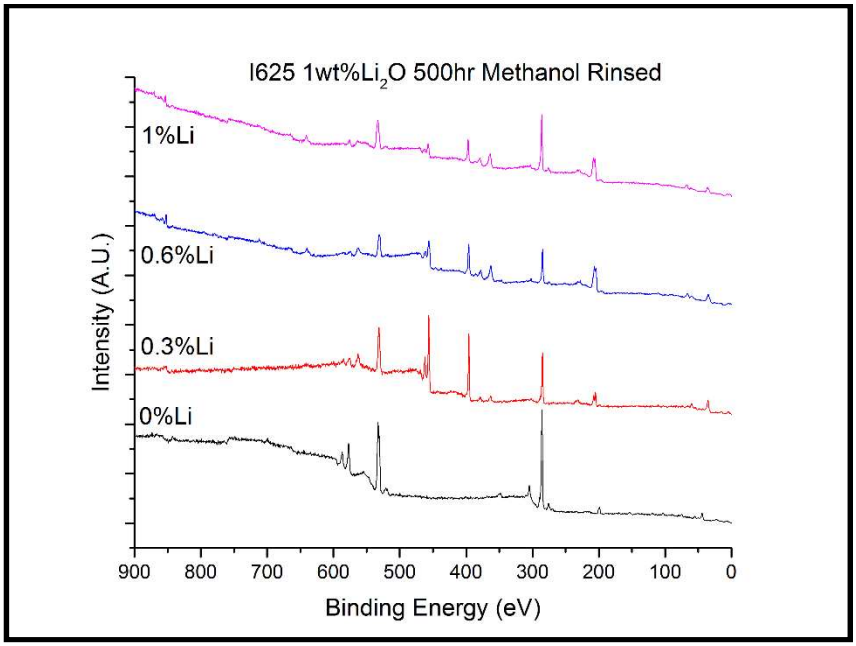

Figure A1-15: XPS spectra collected from I625 samples exposed to LiCl-1wt%Li_2O containing 0, 0.3, 0.6, and 1wt%Li at 650°C for 500hr following the removal of the residual salt layer by rinsing with methanol.

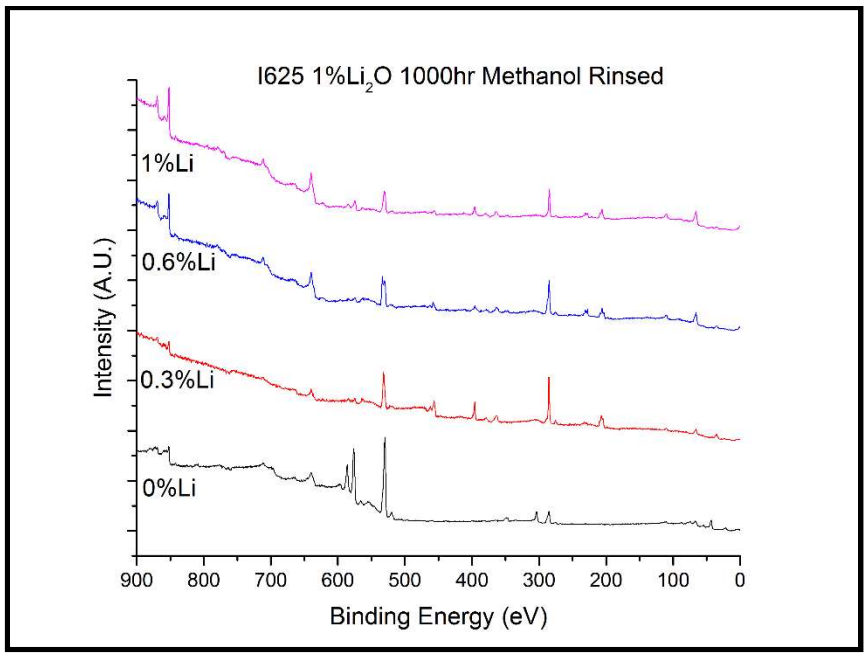

Figure A1-16: XPS spectra collected from I625 samples exposed to LiCl-1wt%Li_2O containing 0, 0.3, 0.6, and 1wt%Li at 650°C for 1000hr following the removal of the residual salt layer by rinsing with methanol.

Appendix 2 Reference Electrode Development for Molten LiCl-Li_2O-Li

A2.1: Background

Due to the uniquely challenging chemical conditions present during the oxide reduction of UNF, a reference electrode that remains stable and usable over an extended period of time has not yet been developed. The most commonly used electrode is the Ni|NiO reference, encased in an MgO sheath with a porous MgO frit at the bottom. Neither MgO nor NiO are stable under Li saturated conditions that are reached upon completion of the reduction of UO_2, leading to the electrode's degradation. Consequently, studies were conducted to develop an improved reference electrode design for this system. No conclusive results were obtained, but progress was made on the understanding of the challenges that must be overcome in pursuit of a stable, repeatable reference design.

Theoretically, the design of a reference electrode can be broken down into two main parts: the first being the reference couple, $M \mid M^{n+}$, and the second being the ion conducting membrane to separate the reference electrode cell from the bulk electrolyte [96, 97]. The present work was concerned with both of these parts, and multiple options exist for both reference couple and ion conducting membrane or electrode sheath for the system in question. This Appendix is concerned with the choice of the reference couple, while Appendix 2 is concerned with the choice of the electrode sheath.

While common reference electrodes for use in aqueous systems at room temperature or slightly elevated temperatures (less than 100°C) are not suitable for use in a high temperature molten salt electrolyte, the theory of operation of a reference electrode in molten salt electrolytes is largely unchanged from those developed for aqueous systems [97]. The choice of a reference couple is guided by the need for a reversible and stable chemical equilibrium to exist between the oxidized and reduced species present in the system [97]. Any material when placed in a solution capable of ionic dissolution, whether it be aqueous or molten salt based, will attempt to reach thermodynamic equilibrium with that solution and the other materials that are exposed to the system by undergoing redox reactions to equalize the chemical activity of each species across the phases present, the general form of which is given in Equation A1.1 and A1.2, below.

Oxidation: $M \leftrightarrow M^{n+} + ne^{-}$ (A1.1)

Reduction $A + ye^{-} \leftrightarrow A^{y-}$ (A1.2)

As these reactions require an exchange of electrons, it can be inferred that an electric potential will be generated based on the materials in the system and the design of the cell, whether intentional or not. This manifests in a number of ways, depending on the solution and materials in question, and is the basis for the field of electrochemistry [96]. For the design of a reference electrode, it is necessary that the electrode be in a stable thermodynamic equilibrium with the solution that is not easily perturbed by changes in solution chemistry or is sufficiently isolated from the bulk solution to prevent contamination. At

equilibrium, the Nernst equation, given in Equation A1.3 below, provides a convenient means of calculating the potential of a given electrochemical system [96].

$$E = E^0 - \frac{RT}{nF}\ln\left(\frac{[a_{red}]}{[a_{ox}]}\right) \quad \text{(A1.3)}$$

Here, E^0 is the standard potential for a given redox couple compared to a standard electrode (the standard hydrogen electrode in the case of aqueous systems), R is the ideal gas constant, T is the temperature in Kelvin, n is the number of electrons transferred in the half-cell reaction, F is Faraday's constant, while a_{red} and a_{ox} are the activities of the reduced and oxidized species, respectively. Consequently, if the activity of both the oxidized and reduced species present in the system are thermodynamically constrained through the choice of the proper electrochemical couple, the electrode will provide a stable potential that will only vary linearly as a function of temperature.

Constraining the chemical activity of a given species in a system can be achieved in several different ways. First, the activity of a solid metal is defined as being unity as long as it is in its standard state and not actively corroding [96]. It is important to note here that the processing history of the metal, such as cold work, surface preparation, etc. can affect the thermodynamic properties of the metal surface through dislocations, defects, and other surface phenomena, and hence its chemical activity in solution can depart from unity depending on the surface chemistry. Consequently, it is important to ensure that the metal is in its lowest energy state through annealing and/or various means to deposit a pure

metal on a bulk metal substrate. Therefore, most common reference electrode designs rely on an inert metal whose surface has been deposited in a defined and repeatable manner to function as both the reduced species as well as the electrical contact for the electrode [96]. The activity of the oxidized species can then be constrained by saturating the electrolyte with the corresponding cation. For example, in the $Ag|Ag^+$ electrode commonly used in aqueous systems, a Ag rod coated in AgCl is immersed in an aqueous solution saturated with AgCl. As AgCl is only sparingly soluble in water, very little AgCl is needed to saturate the solution with Ag^+. However, saturation of the solution with the corresponding anion is also required, and therefore the solution is typically saturated with KCl to ensure that the activity of Cl^- in the electrode is also unity, although other KCl concentrations can be used as long as the change in electrode potential caused by the change in Cl^- activity and AgCl solubility is taken into account [96, 97]. The addition of KCl also serves to increase the conductivity of the electrode and balance the charge transfer between positive and negative ions, minimizing the junction potential of the electrode [96]. A reference electrode functioning in this manner is known as a reference electrode of the second kind, and is the basis for all of the electrode designs that will be studied in this work. It is important to note that if the electrode is contaminated, or poisoned, by another anion or cation, the activities of these extraneous species will affect the measured potential of the electrode, leading to drift from the theoretical potential. For example, the aqueous Ag|AgCl reference electrode is rapidly degraded by the presence of

minute quantities of Br^- ions and is not easily regenerated after poisoning of the electrode has occurred [96].

Alternatively, the equilibrium between a gas and liquid phase can also be used as a reference couple, as is the case with the standard hydrogen electrode [96, 97]. An electrode of this type is known as a reference electrode of the first kind. Detailed description of the theory behind hydrogen electrode operation is beyond the scope of the current discussion, but it is mentioned here for completeness. It is possible to build a reference electrode of the first kind for a molten salt electrolyte, and in the case of a LiCl based electrolyte the gas would necessarily be Cl_2 [97]. Working with using gaseous chlorine at 650°C raises obvious safety concerns, however, a small number of researchers have utilized chlorine electrodes in the past for fundamental electrochemical studies in other systems [97]. Numerous difficulties with repeatability were encountered as a result of the sensitivity of the electrode to surface chemistry and the highly corrosive nature of high temperature Cl_2 gas. As the goal of the present work is to devise a stable, repeatable, and easily fabricated design to allow for its implementation in experimental work and engineering scale facilities, the danger, difficulties, and problems with reproducibility associated with a gaseous Cl_2 electrode eliminate this design from further investigation.

If the reference couple is isolated from the bulk electrolyte, the thermodynamic considerations do not have to take the presence of metallic Li in the system into account, and it is possible to use a reference couple that would

be driven from equilibrium if in direct contact with metallic Li. This is extremely attractive theoretically, as the simultaneous presence of both Li and Li_2O leads to a paradoxical thermodynamic situation where no redox couple other than $Li|Li^+$ can exist in true equilibrium with the melt, as any species with a more negative Gibbs free energy of formation than Li_2O would cause its reduction to metallic Li, while a species with a more positive Gibbs free energy of formation than Li_2O would itself be reduced by the metallic Li in the system. This is summarized by equations A1.4 and A1.5 below.

If $\Delta G_{M|M^+} > \Delta G_{Li|Li^+}$ then $M + Li_2O \rightarrow MO + 2Li$

Equation A1.4

If $\Delta G_{M|M^+} < \Delta G_{Li|Li^+}$ then $MO + 2Li \rightarrow M + Li_2O$ Equation A1.5

Depending on the valence state of the species, M^{n+}, the stoichiometry of the reactions would change, but a general case of a divalent cation is given here for simplicity. The direct contact of the reference couple with the bulk electrolyte also causes other issues with potential stability in response to changing electrolyte conditions, and possible contamination of the electrolyte with constituent species of the reference electrode. This is especially important for the present work, as a number of salt soluble fission products accumulate in the electroreduction step and contaminate the electrolyte, including Cs, Ba, Sr, Rb, Te, I, and Eu [50, 98]. The presence of these species in the electrolyte will affect the equilibrium

potential of the reference electrode if they were allowed to contact the reference couple directly.

A commonly used reference electrode design, particularly in Japan and Korea, is a Li | Li^+ based electrode consisting of a 35at%Li-Bi alloy contained in a closed end MgO tube with a small 0.7mm diameter hole drilled in the side slightly above the level of the molten Li-Bi alloy [99]. Similar electrodes utilizing Pb in place of Bi function essentially identically. By examining the Li-Bi phase diagram in Figure A2.1, below [100], it can be observed that the 35at%Li-Bi alloy is a homogenous liquid at 650°C.

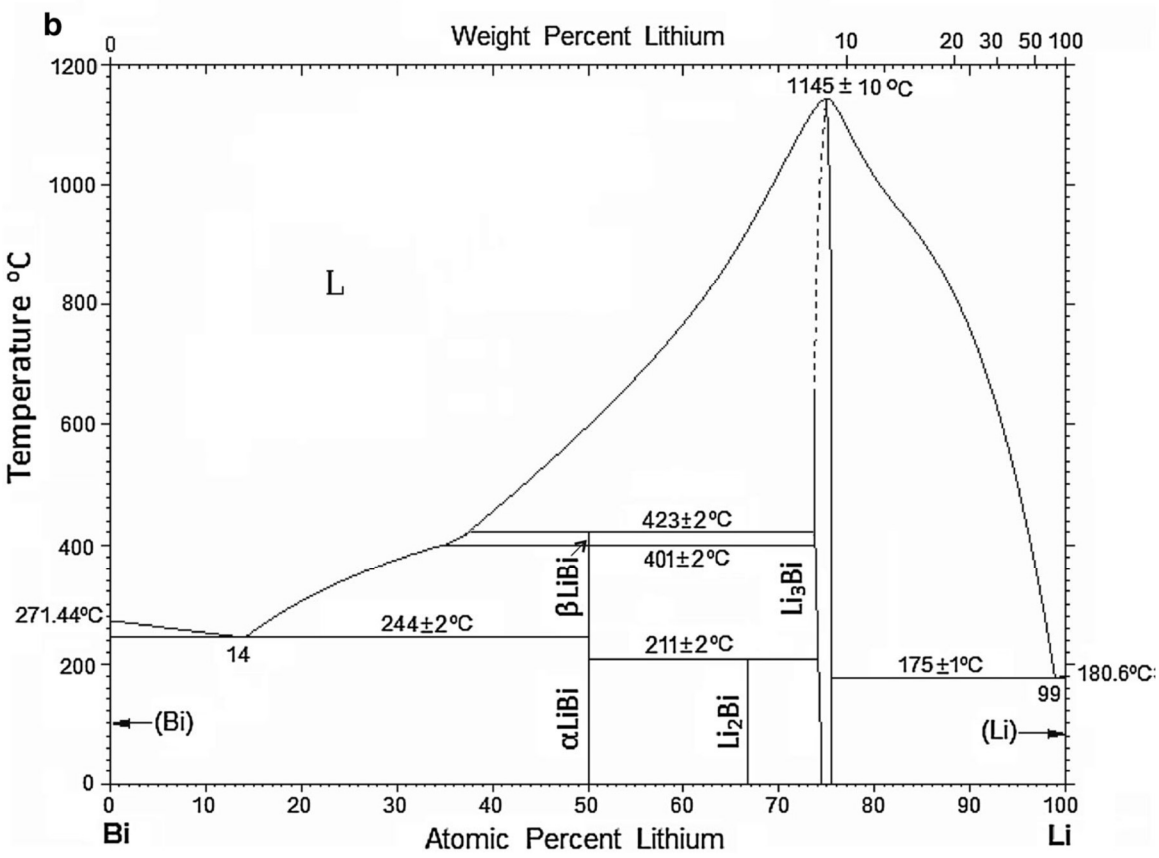

Figure A2.1: Phase diagram for the Li-Bi system [100].

Consequently, the activity of Li in Bi at this composition is not stable according to the Gibbs phase rule, meaning that the potential of the electrode will fluctuate as the activity of Li in the salt phase varies, as this electrode design is in direct contact with the bulk electrolyte [101]. The authors of the paper in which this reference electrode is described note these concerns but state that the 35at%Li-Bi electrode provided adequate stability over a week of experimentation, although no direct evidence is given to support this claim.

In the work of Foster, *et al.*, the potential variance of a similar 5at%Li-Bi electrode due to transport of Li through a porous BeO crucible was unacceptable for precise thermodynamic measurements in a LiCl-LiF electrolyte, and they devised an improved Li-Bi reference electrode by increasing the Li content to 60at%Li-Bi [101]. Re-examination of the Li-Bi phase diagram shows that at this composition, the alloy exists in an equilibrium between two phases: a solid intermetallic compound, Li_3Bi, and a liquid solution of Li_3Bi in Bi. Due to the presence of these two phases, the activity of Li is held constant over a fairly broad range of compositions, allowing for a stable potential to be achieved despite transfer of Li into or out of the electrode. Liu and Poignet utilized a similar 68at%Li-Bi reference electrode design in their work, substituting a thin walled BN crucible for containment, and found the characteristics of this electrode to be sufficient for the determination of Li activity in LiCl over a comprehensive range of Li concentrations and temperatures [21]. Despite the attractive characteristics of the Li_3Bi-Bi reference electrode, little mention of it has been made since Liu and Poignet's work in the early 1990's, and no comprehensive evaluation of its

performance has been published in the open literature. For this reason, one of the reference electrode designs studied for this work is based on the 60at%Li-Bi reference electrode designed by Foster.

A2.2: Current progress on the Li-Bi reference electrode

The lack of use of the intermetallic region of the Li-Bi system as a reference electrode may be in large part due to the difficulty associated with its fabrication. Neither Foster nor Liu mention the method with which they fabricated their reference electrodes. Initial attempts at fabricating a Li_3Bi-Bi reference electrode for this study were based on direct reaction of Li and Bi in their molten states. The intermetallic compound Li_3Bi has an enthalpy of formation of -251.3 kJ/mol at room temperature, which McDeavitt notes is sufficient to cause a 2000°C temperature rise under adiabatic conditions, and the reaction proceeds rapidly upon melting of Li if the two components are mixed directly [102]. Additionally, Li_3Bi has a melting point of ~1145°C and a high vapor pressure at this temperature, which leads to significant difficulties associated with its casting. Work with Li_3Bi thus far has confirmed the difficulty of controlling the reaction and forming a heterogeneous product. All attempts to form the compound inside the desired containment tube for the reference electrode have resulted in the tube cracking due to the large temperature gradient upon reaction between Li and Bi, and melting the compound upon formation has not been attempted in our laboratory due to the temperature limits of the furnaces in place in our gloveboxes and the sensitivity of the compound to moisture. The most successful

experiments on this work to date have utilized a two piece graphite mold in which a charge of Li was first melted around a Ta rod used for electrical contact, and then the correct amount of Bi was subsequently added incrementally, after which the assembly was annealed at 850°C for 2 hours and allowed to cool. After removing the as-formed electrode, it was obvious that a reaction with the graphite had occurred, likely the formation of Li_2C_2 [103], and that the Li-Bi slug was heterogeneous, with a high degree of porosity. Further difficulties arise from the high vapor pressures of both Li and Bi at the elevated temperatures present during the reaction which leads to the evaporation of both components and consequent difficulties with producing parts with exact compositions. This is exasperated by the disparity in the atomic mass of Li and Bi of 6.94 and 208.98, respectively, which makes small errors in weight fraction translate to large errors in atomic fraction.

To overcome these difficulties, future work on this electrode will focus on the electrochemical deposition of Li into molten Bi to form the desired 66at%Li-Bi reference in a controlled manner and in the proper geometry. Precise control of the stoichiometry is possible by stopping deposition upon transfer of the desired amount of charge, and the reaction rate is easily controlled by limiting the current and/or controlling the potential. This design would benefit from the stability of the $Li \mid Li^+$ couple in the LiCl-Li_2O-Li system, be easily fabricable, and be simple to regenerate *in-situ* if necessary.

A2.3: The $Mg|Mg^{2+}$ electrode

In addition to the Li-Bi reference electrode described above, reference electrodes based on the $Mg\,|\,Mg^{2+}$ couple were also studied. MgO is commonly used to fabricate parts such as crucibles, reference electrode containment vessels, and anode shrouds for use in experiments on the electroreduction of UO_2 [9, 99]. MgO has been shown to slowly degrade when in contact with LiCl-Li_2O-Li solutions; however, the presence of Mg^{2+} in small quantities in the electrolyte presents an opportunity to utilize the $Mg\,|\,Mg^{2+}$ couple as a reference electrode. Dr. Willit of ANL suggested a design of an electrode to take advantage of this. The proposed electrode was to be composed of a MgO tube to isolate the electrode from the bulk solution and filled with a LiCl-1wt%Li_2O electrolyte to prevent the formation of a concentration cell, while the electrode itself will consisted of an intermetallic Mg-Ni rod. The purpose of using a Mg-Ni intermetallic rather than pure Mg is to lower its chemical activity, as pure Mg is highly reducing and melts at 650°C and would therefore cause significant problems. The Mg-Ni phase diagram, shown in Figure A2.2 below, indicates that Mg_2Ni and $MgNi_2$ are the stable intermetallic phases, both of which have melting points well above the operating temperature of 650°C.

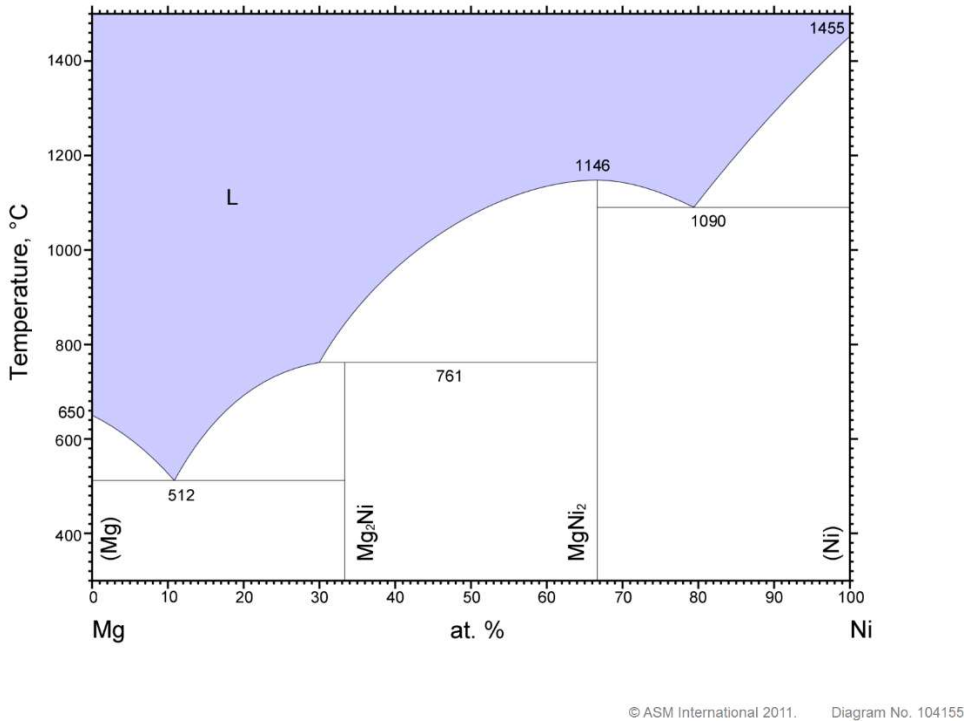

Figure A2.2: Phase diagram for the Mg-Ni system [104]

Fabrication of either of these intermetallic compounds in the laboratory poses difficulty beyond that of Li_3Bi described above due to the much higher melting points of the constituent elements. Fortunately, high purity Mg_2Ni is available from Sigma Aldrich in rod form.

A2.4: Experimental: Mg|MgO Reference electrode

All experiments were conducted in the Vacuum Atmospheres gloveboxes used in the previous chapters. For these experiments, the Ar atmosphere was maintained at less than 0.5ppm H_2O and less than 1ppm O_2. Two identical $Mg|Mg^{2+}$ reference electrodes based on Mg_2Ni were constructed, with a schematic diagram of the design shown in Figure A2.3 (not to scale). Mg_2Ni rods of ¾" diameter and 2" length of 99.9% purity were purchased from Sigma Aldrich.

1/16” diameter x 2” long rods were machined from the bulk material via electrical discharge machining (EDM). Ni plated high temperature crimp connectors were used to connect the short Mg_2Ni rods to 1/16” diameter 99.99% purity Ni rods obtained from ESPI metals for electrical contact to the potentiostat. Custom made ¼” OD MgO tubes with ½” long porous frits at one end were obtained from Tateho Ozark for use as the electrode casing. LiCl of 99% purity was obtained from Alfa Aesar and dried in a vacuum oven for 24 hours at 200°C prior to use. Li_2O of 99.5% purity was obtained from Strem chemicals. The EDM machined bulk Mg_2Ni rod and the electrodes prior to insertion into the MgO sheaths are shown in Figure A2.4.

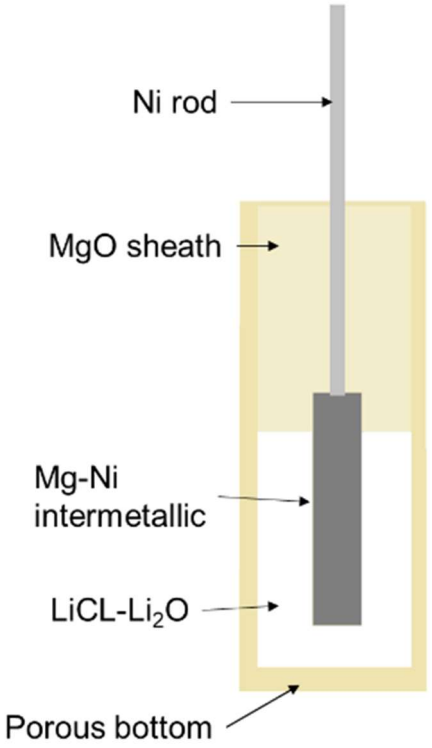

Figure A2.3: Design of the Mg|MgO reference electrode used in this study.

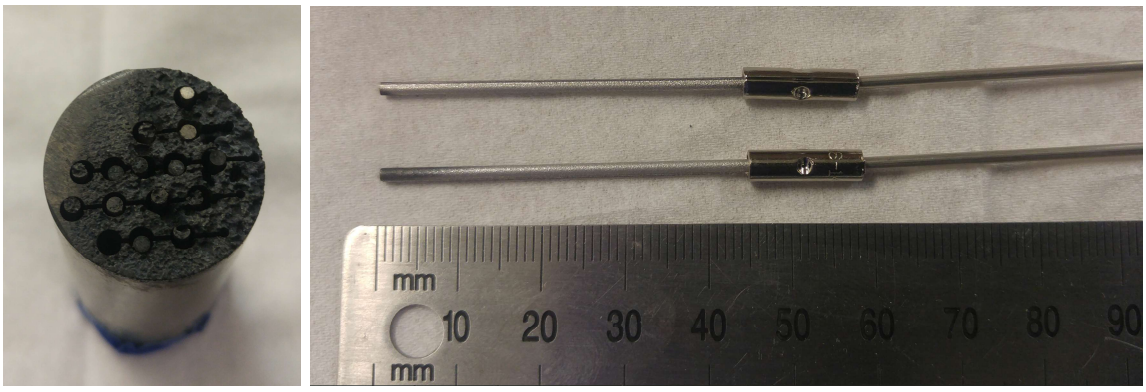

Figure A2.4: 1/16” dia x 2” long Mg_2Ni rods machined via EDM from bulk Mg_2Ni (left) and $MgNi_2$ rods connected to Ni rods via Ni plated crimp connectors prior to use in the reference electrodes used in this study.

The electrodes shown in Figure A2.4 were pre-inserted into the MgO sheath such that the gap between the end of the electrode and the porous frit at the bottom of the sheath was approximately 1/8”. The electrode was then wrapped in Teflon tape to guarantee a reliable insertion depth during final assembly. As the design of this electrode calls for the same electrolyte composition in the bulk as well as inside the electrode, a batch of 50g of LiCl-Li_2O was premade in the MgO crucible obtained from Alfa Aesar. Masses were weighed to mg precision. Pre-dried LiCl was baked at 550°C for four hours prior to raising the temperature to 650°C for one hour to melt. The weighed amount of Li_2O was then added to the molten LiCl and allowed to equilibrate for 1 hour. Samples of the salt were then taken using a cold graphite rod immersed quickly into the melt to collect the desired amount of electrolyte for construction of the Mg|MgO reference electrodes. These samples were then crushed and weighed prior to pouring into the MgO sheaths. Both electrodes contained 0.5g of LiCl-1wt%Li_2O.

The electrode sheaths were then suspended in the melt overnight prior to final assembly to allow for diffusion of the salt through the porous frit. Subsequently, the electrodes were inserted into the MgO sheaths and allowed to equilibrate for 4 hours prior to the start of open circuit potential (OCP) measurement. A Gamry Ref600 potentiostat was used for collection of the OCP data. Direct connection of the potentiostat cell cable to the electrodes was facilitated by a custom made feedthrough with a 3 meter cell cable. A Faraday cage was also constructed to isolate the electrochemical cell from electromagnetic interference. OCP measurement was conducted over a period of 24 hours.

A2.5: Results

The OCP of the two electrodes as a function of time is shown in Figure A2.5, with the time corresponding to the absolute time from the insertion of the electrodes into the MgO sheaths. Data collection was started at 4 hours after insertion. The potential between the two electrodes at the beginning of the measurement was 4mV, indicating that the initial conditions in the electrodes was near to identical. However, the potential between the two electrodes drifted in a continual manner over time, indicating that equilibrium was not obtained.

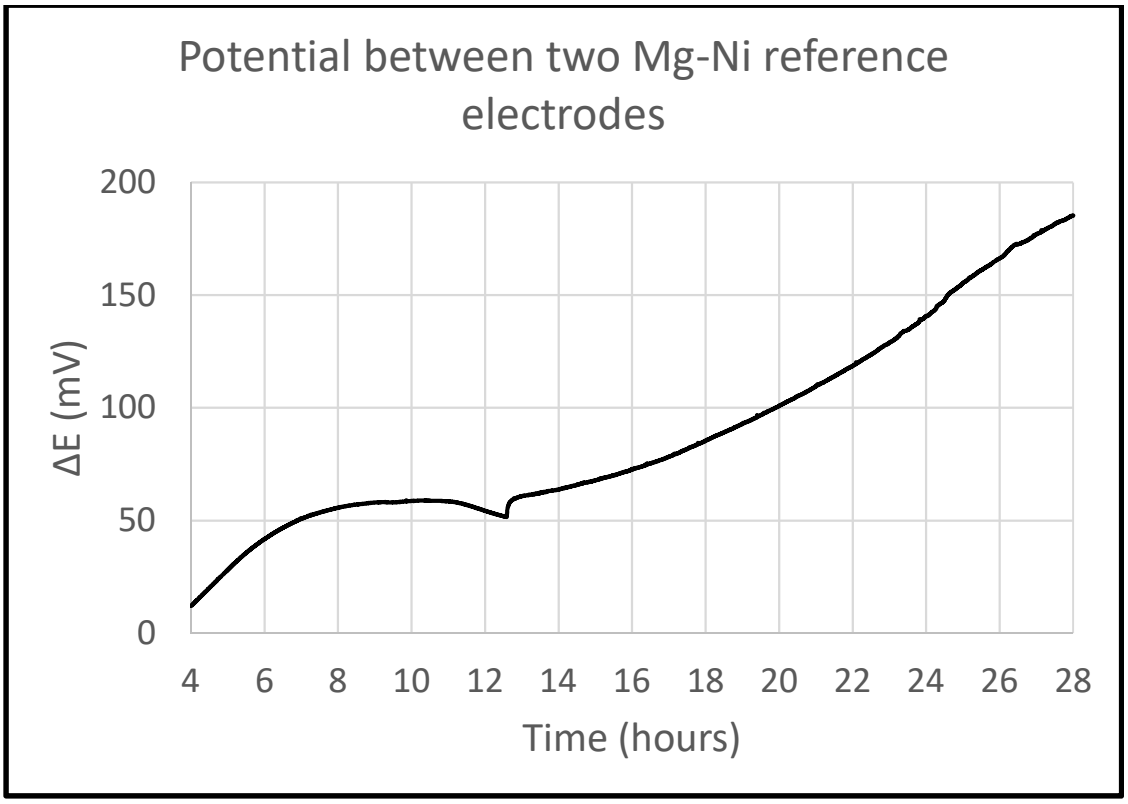

Figure A2.5: Open circuit potential recorded between two identical Mg|MgO reference electrodes immersed in LiCl-1wt%Li_2O at 650°C over the course of 24 hours. The x-axis gives the time from the initial insertion of the electrodes into the sheaths while at temperature.

The cause for the potential instability was quickly determined upon removal of the electrodes from the melt. The MgO sheaths showed signs of reaction with Mg metal, and the Ni leads showed signs of heat discoloration, as can be seen in Figure A2.6. Additionally, the Mg_2Ni electrodes had completely melted away, with some re-solidified metal on the Ni-plated crimp connectors. An exothermic reaction of the Mg in Mg_2Ni with one of the components of the electrode design resulted in a large increase in temperature, which melted the electrode. The cause of this is likely due to the high activity of Mg, which may have not been sufficiently reduced by alloying with Ni. Additionally, it is possible that the composition of the Mg_2Ni rods were slightly off the stoichiometric value,

as the Mg_2Ni intermetallic compound is in equilibrium with a Mg-Ni liquid at 650°C in the case of a slightly Mg rich composition.

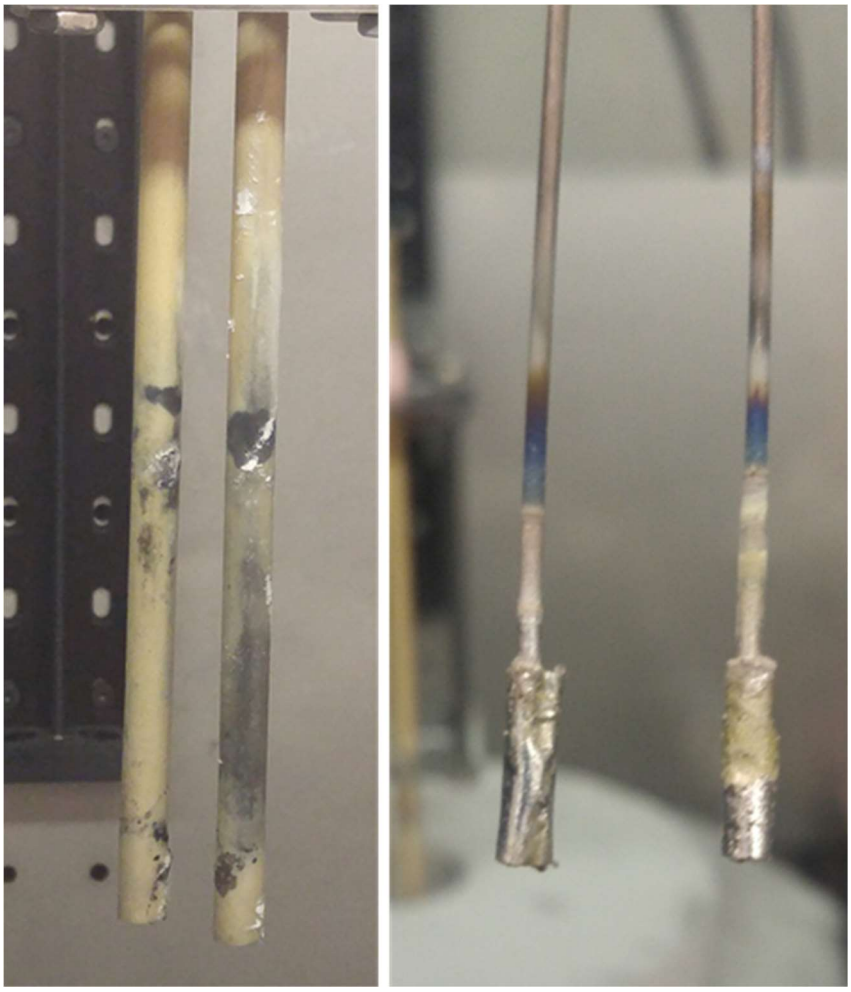

Figure A2.6: Degradation of Mg_2Ni-based Mg|MgO reference electrodes following 28 hours of immersion in LiCl-1wt%Li_2O at 650°C for 28 hours. Severe degradation of both the electrode sheaths and electrode assemblies can be observed. Additionally, the Mg_2Ni portion of the electrode had completely melted away, indicating a highly exothermic reaction with one of the electrolyte components.

Due to the failure of this experiment, further investigation of this electrode design was not pursued. However, the initial similarity of the potentials (~4mV) indicates that the Mg|MgO couple may be able to serve as a reference couple if the activity of Mg can be controlled sufficiently. If $MgNi_2$ were used rather than

Mg_2Ni, it is possible that the electrode would have functioned as desired. Unfortunately, the lack of a commercial supplier of the higher Ni content Mg-Ni intermetallic makes further study of this design impractical.

A2.6: Reference Electrode Design: Conclusions and future work

Significant progress has been made in the theoretical understanding of the design constraints of a reference electrode for the oxide reduction of used nuclear fuel. The Mg_2Ni-based electrode investigated in this study did not perform as intended due to the high activity of Mg in this intermetallic compound and the low melting point of the Mg-rich Mg-Ni liquid phase it is in equilibrium with. However, the small initial potential difference between the two identically constructed electrodes indicates that the $Mg|Mg^{2+}$ couple may be able to function as a stable reference couple if the activity of Mg is sufficiently constrained. The Li_3Bi-based $Li|Li^+$ electrode has not yet been successfully fabricated due to the difficulties associated with the direct chemical formation of the Li_3Bi intermetallic phase. Future studies will focus on the electrochemical formation of this compound via pulsed galvanostatic deposition of Li into a pool of molten Bi.

Appendix 3 : Degradation of Ceramic Materials in LiCl-Li_2O-Li

As the oxide reduction of used nuclear fuel is inherently an electrochemical process, there are a number of locations in the design of any such system where an electrically insulating material is required to withstand these harsh conditions. Components such as electrical insulators in electrodes, anode shrouds, and others will be made of some sort of ceramic material, and while this section focuses specifically on the selection of a ceramic material for the reference electrode sheath, many of the same material compatibility issues mentioned here are directly applicable to other components in this system.

Selection of the Reference Electrode casing material

As mentioned in Appendix 1, one of the most challenging aspects of reference electrode design for the LiCl-Li_2O-Li system is the selection of the ceramic material used for the reference electrode sheath. The primary function of the reference electrode casing material is to isolate the reference electrode and its electrolyte from the bulk electrolyte so that cross-contamination of both is avoided [96, 97]. In order to do this effectively, the material must be resistant to chemical attack by the electrolyte, be insoluble, allow for the diffusion of ions to allow for ionic conductivity, and prevent direct electrical contact between the electrode and the bulk electrolyte. An additional criterion that affects the design is that the ionic resistivity must be sufficiently low to allow for proper functioning of the potentiostat, with typical maximum acceptable resistivity values being

approximately 20kΩ [105]. This can be accomplished through thinning of a section of the casing or using a porous plug at the end, although techniques are available to lower the impedance of a high resistivity reference electrode using an auxiliary capacitively coupled Pt wire if neither of these techniques provide sufficient conductivity [106]. In aqueous systems, silica glass is typically used due to its inertness and the ease with which it can be fabricated, and a porous Vycor glass frit at the end of the electrode allows for ionic contact with the electrolyte [97]. In the LiCl-Li_2O-Li system, the material chosen has a number of extremely difficult challenges that must be overcome to succeed in providing adequate performance for the electrode, which eliminate silica as an option. Most importantly, the material must be inert to the highly reducing nature of metallic Li, while also being insoluble in LiCl-Li_2O and electrically insulating. While quartz can withstand exposure to molten LiCl-Li_2O at 650°C, the presence of Li rapidly degrades this material. Most other commonly used high temperature insulating materials, such as ceramic oxides or nitrides are also rapidly degraded by metallic Li, and most oxides that are more thermodynamically stable in contact with Li are salt soluble. By examining previous thermodynamic calculations on the compatibility of ceramics with metallic Li, shown in Figure A3.1 below, it can be observed that the oxides most likely to be stable are ThO_2, BeO, and MgO, while the most stable nitrides are BN and AlN [107].

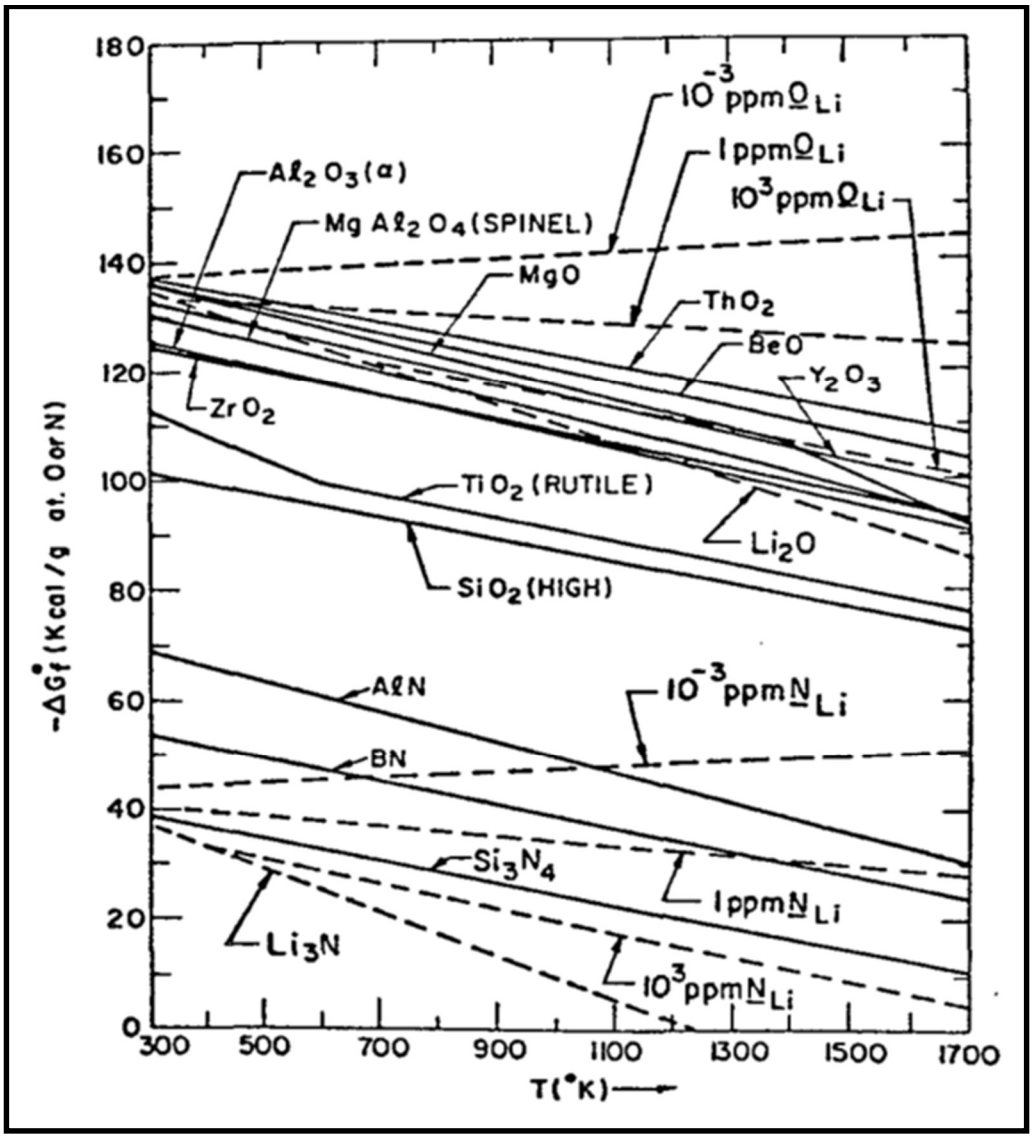

Figure A3.1: Calculated thermodynamic Lithium-Ceramic stability diagram [107].

Although the radioactivity of ThO_2 is not of primary concern during the reprocessing of used fuel, it has limited the commercial use of Th in other industries. Consequently ThO_2 is not readily commercially available, which has eliminated this material from consideration in the current study. By quantifying the stability of BeO, MgO, BN, and AlN in molten LiCl-Li_2O-Li, this work will

facilitate the design of ceramic equipment such as reference electrodes, anode shrouds, and crucibles for use in electroreduction experiments.

Examples of Ceramic Degradation in LiCl-Li_2O-Li

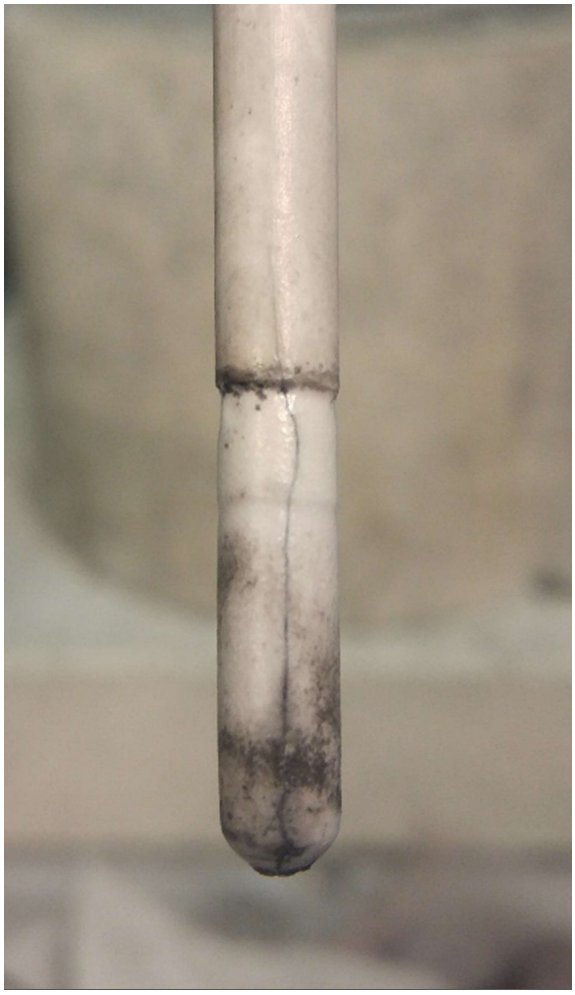

Figure A3.2: Mullite ($3Al_2O_32SiO_2$) reference electrode casing after exposure to LiCl-2wt%Li_2O-0.2wt%Li for 8 hours.

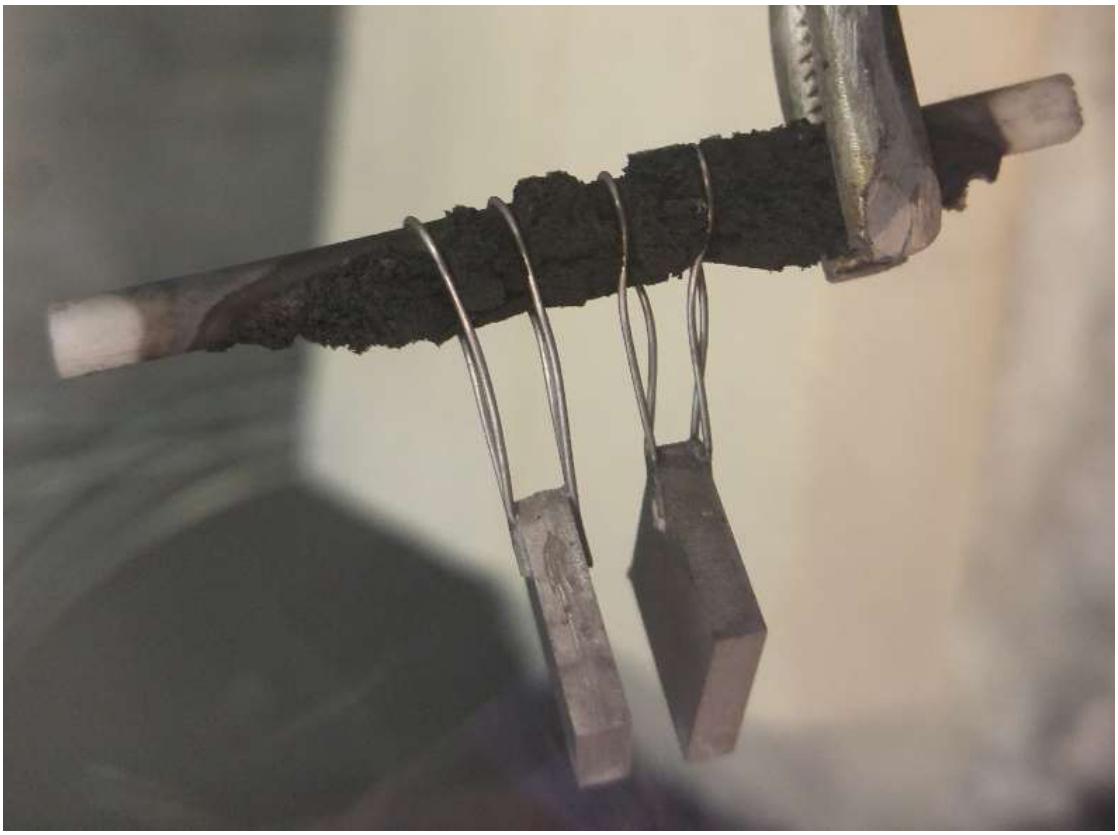

Figure A3.3: Degradation of alumina (Al_2O_3) rod used to hang samples for exposure testing in LiCl-2wt%Li_2O-0.6wt%Li for Chapters 2, 3, and 4, demonstrating the incompatibility of Al_2O_3 with the conditions in this system. The attack shown here was from the vapor phase above the salt, and was caused by metallic Li and Na vapors (Na is present as the major impurity in all Li compounds used for this study). This degradation occurred in less than 72 hours, and resulted in the complete failure of 6 out of 8 identical rods, resulting in failure of these experiments.

Investigation of the Performance of BeO during exposure to molten LiCl-Li_2O-Li

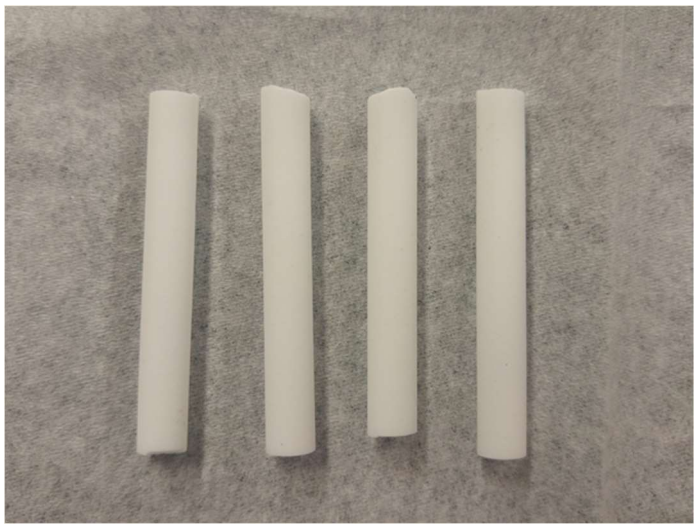

Figure A3.4: BeO rods obtained from American Beryllia Corporation prior to exposure to LiCl-1wt%Li_2O-Li solutions at 650°C for 100hr.

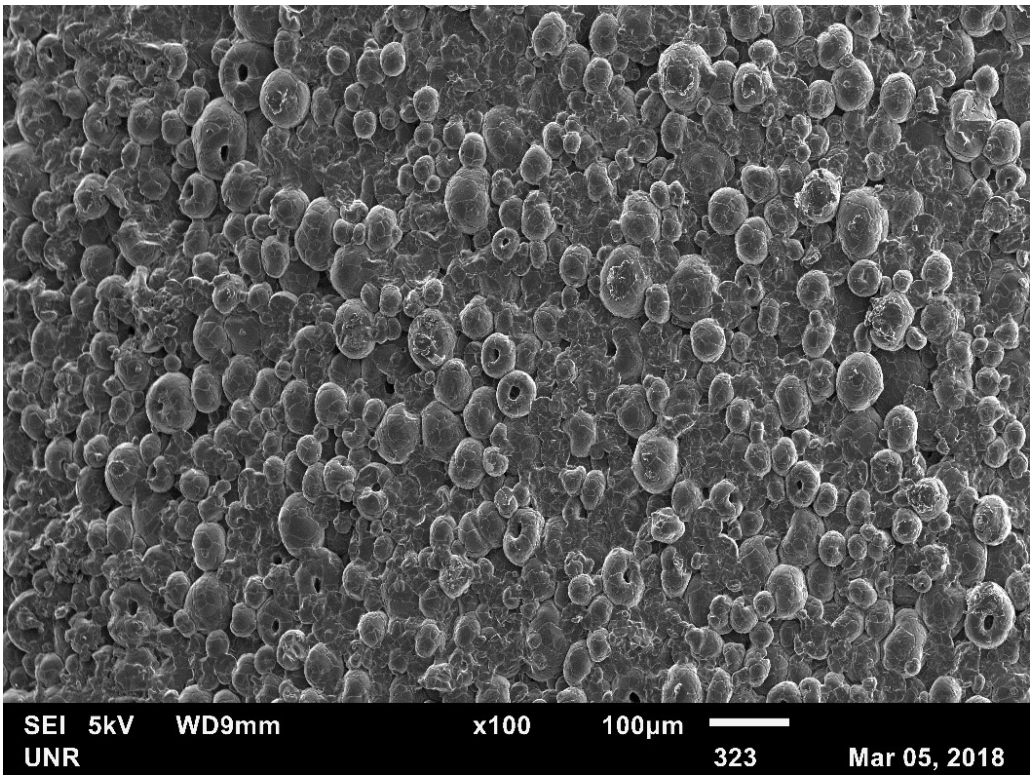

Figure A3.5: Low magnification SEM micrograph of a BeO surface after cleaning and sputter coating with 10nm of carbon, prior to exposure to LiCl-Li_2O-Li solutions for 100hr.

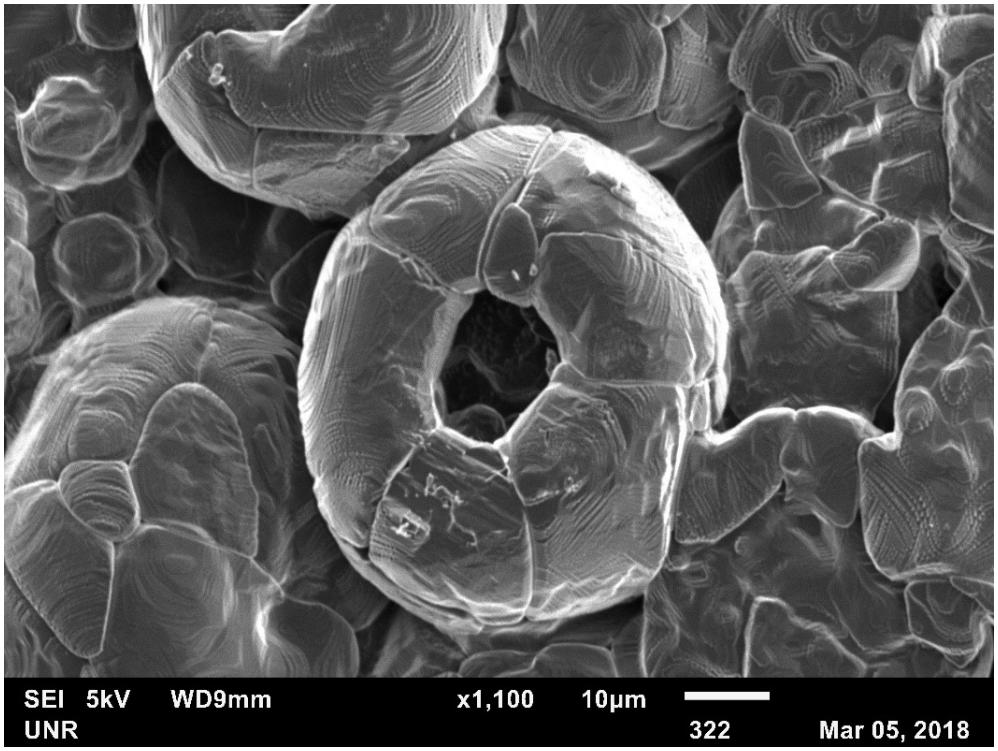

Figure A3.6: High magnification SEM micrograph of a BeO surface after cleaning and sputter coating with 10nm of carbon, prior to exposure to LiCl-Li_2O-Li solutions for 100hr.

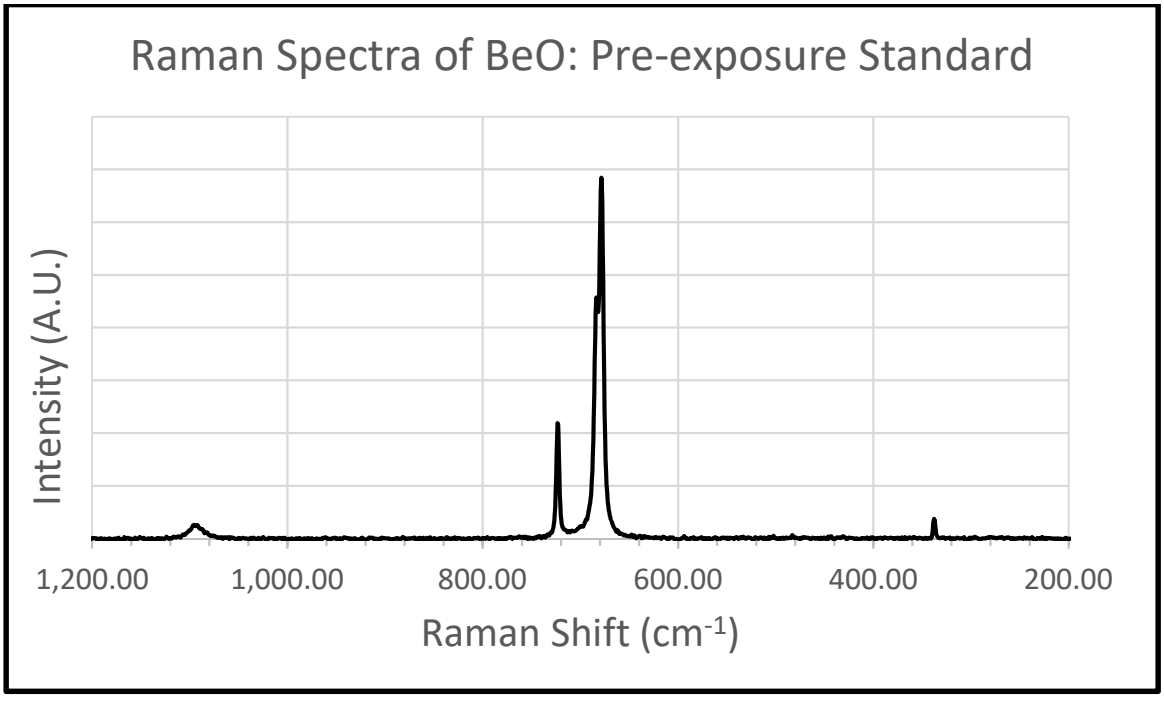

Figure A3.7: Raman spectrum of the as received BeO rods used in this study prior to exposure to molten LiCl-Li_2O-Li solutions.

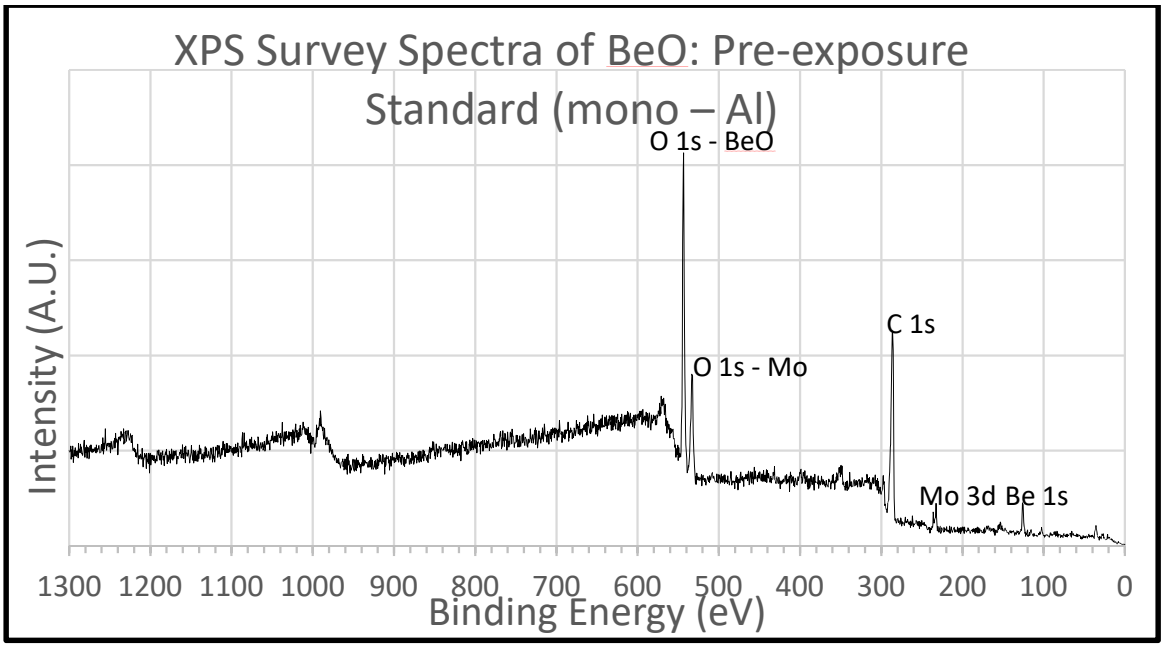

Figure A3.8: XPS survey spectrum of BeO standard. Due to the insulating nature of BeO, the spectrum was obtained at the edge of the sample, which was covered with a Mo plate. This minimized charging of the sample during acquisition, but meant the spectrum included Mo from the sample holder. No Mo was present in the BeO sample, and the photoelectron emission lines do not overlap for Be and Mo.

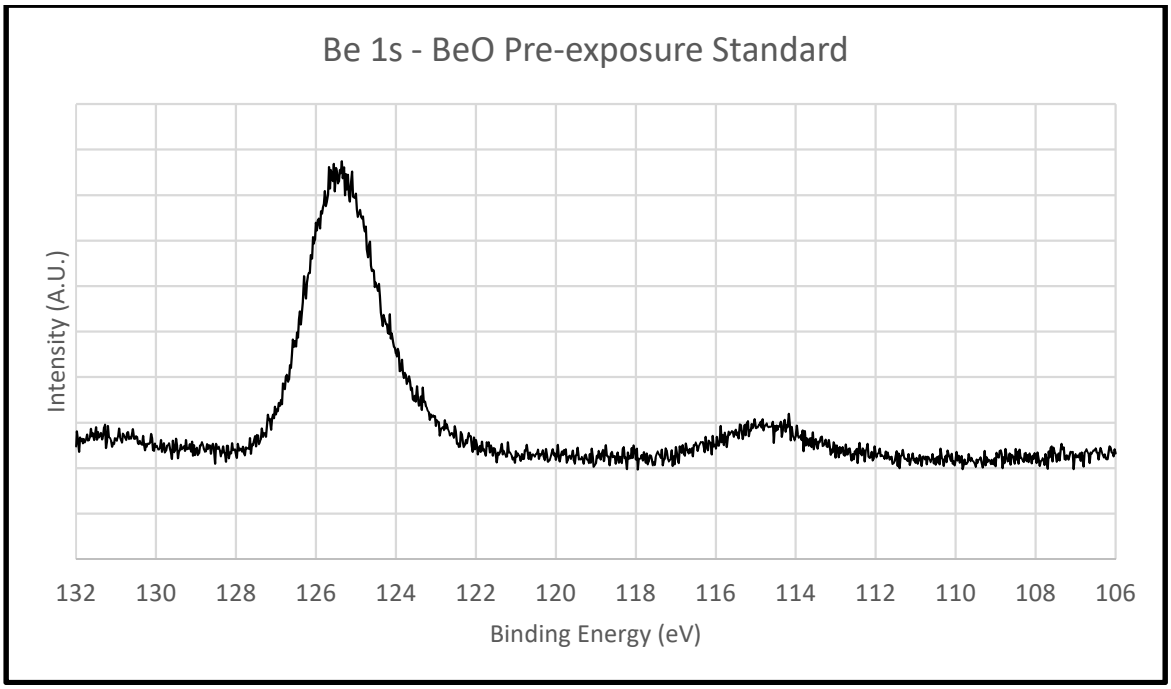

Figure A3.9: Be 1s XPS spectra obtained from the standard BeO rod prior to exposure to molten LiCl-Li_2O-Li. The two peaks are indicative of the high degree of differential charging associated with photoelectron emission from ceramic materials.

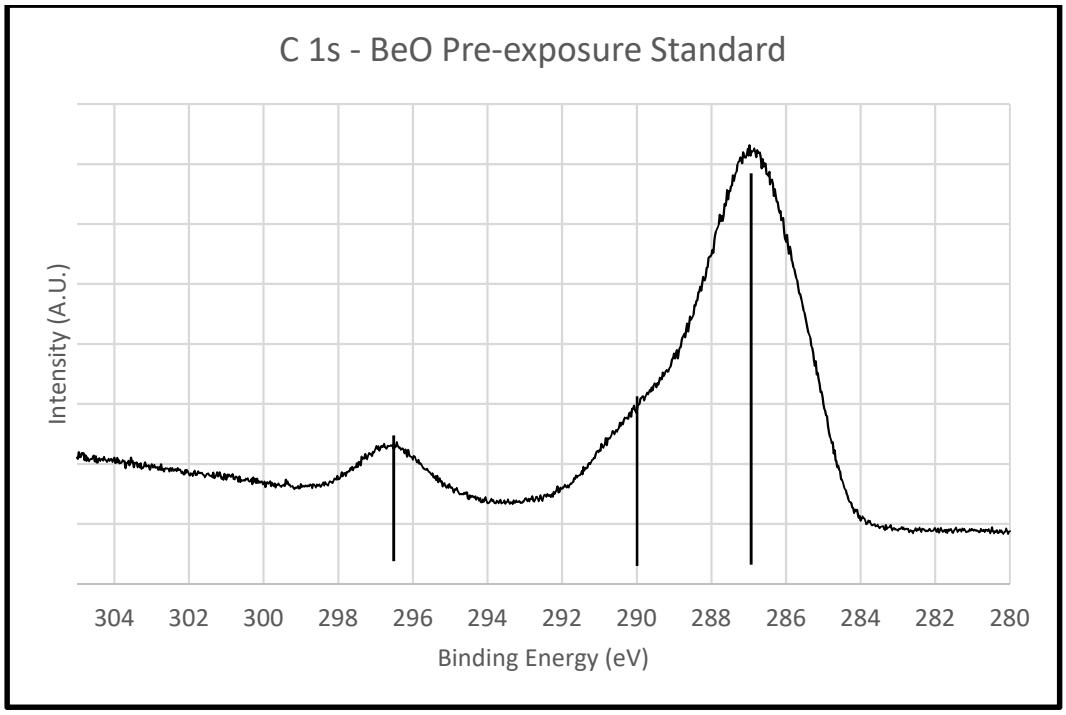

Figure A3.10: C 1s XPS spectra obtained from the standard BeO rod prior to exposure to molten LiCl-Li_2O-Li. Multiple peaks were observed, indicative of the high degree of differential charging associated with photoelectron emission from ceramic materials.

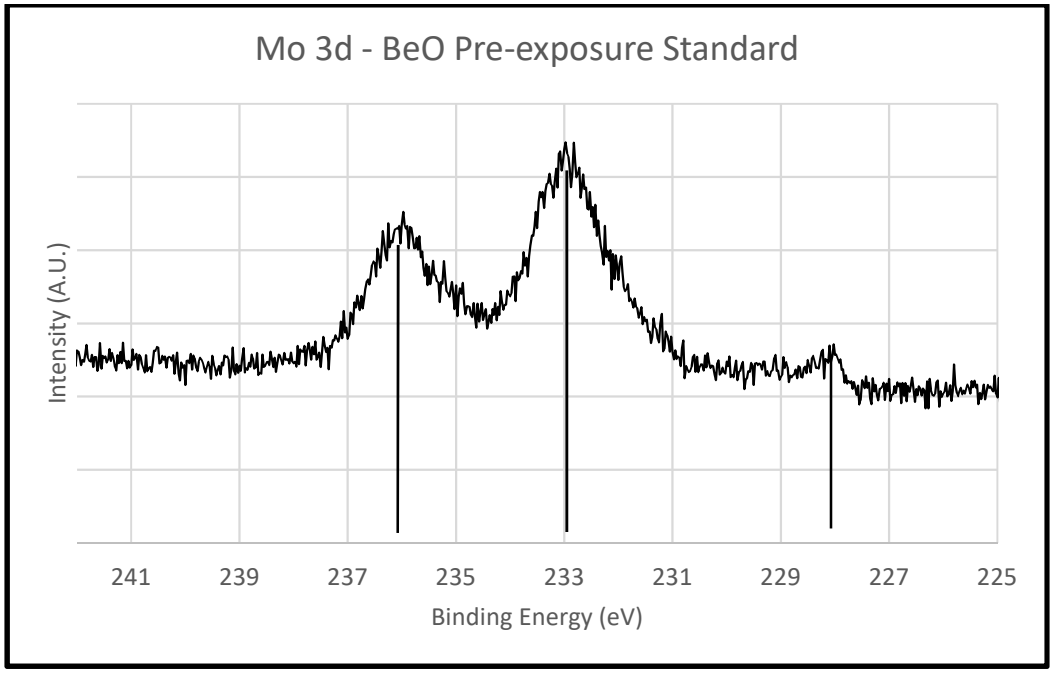

Figure A3.11: Mo 3d XPS spectra obtained from the standard Mo sample holder used to affix the BeO rod for analysis prior to exposure to molten LiCl-Li_2O-Li.

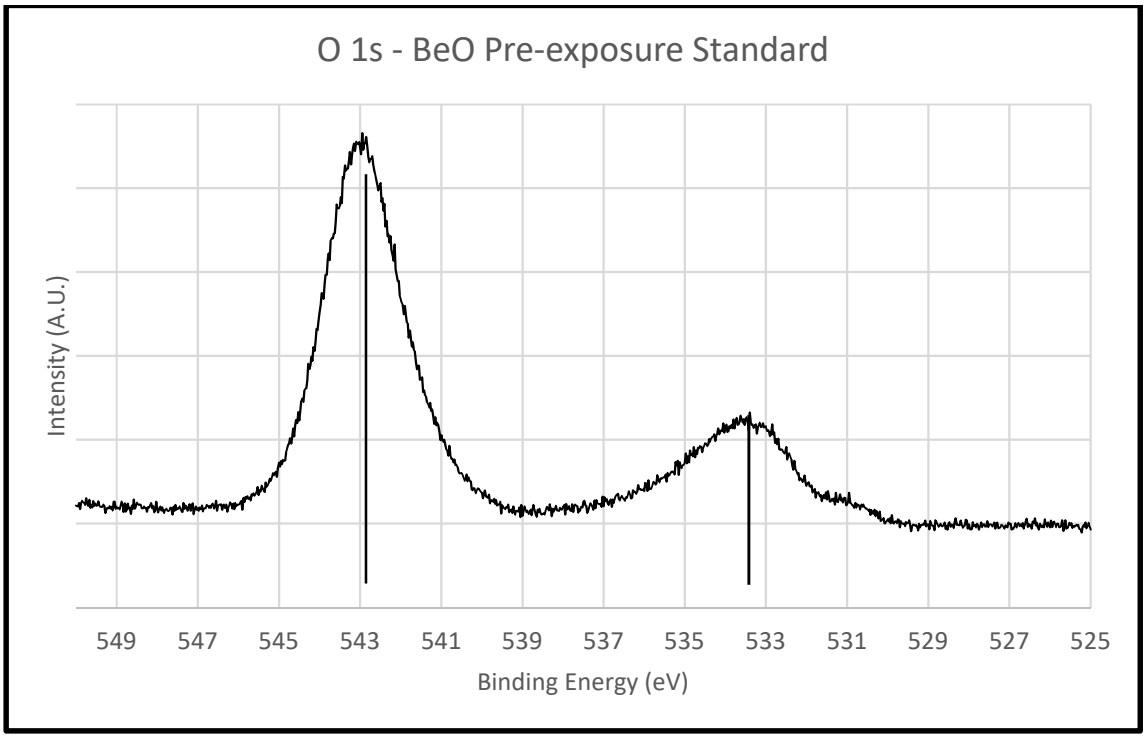

Figure A3.12: O 1s XPS spectra obtained from the standard BeO rod prior to exposure to molten LiCl-Li_2O-Li. The peak at approximately 533.5eV is due to the oxide layer on the Mo sample holder, while the highly charged O 1s peak at 543eV is a result of the high degree of charging on the BeO rod.

Figure A3.13: Optical images of BeO rods exposed to LiCl-1wt%Li_2O containing 0, 0.3, and 0.6wt%Li at 650°C for 100hr. Severe degradation of all samples was observed, with the most pronounced degradation occurring at the melt line. The reaction products were highly crystalline

in nature for the samples exposed to melts containing metallic Li, which made sample characterization hazardous due to the Be content. As such, only Raman analysis was performed on these samples.

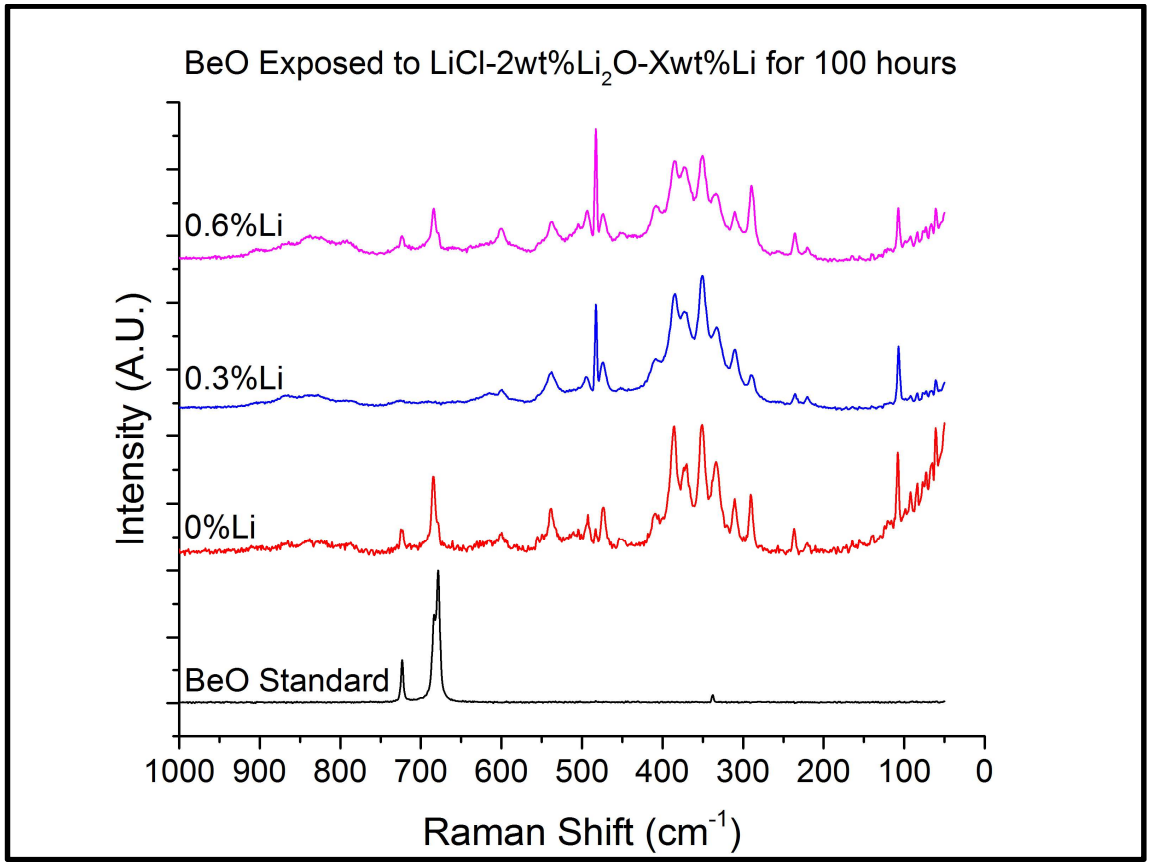

Figure A3.14: Raman spectra of BeO rods prior to and after exposure to LiCl-Li_2O-Li solutions at 650°C. Bottom spectrum is of the BeO standard shown in Figure A2.4, while the spectra above were taken from the surface of the samples exposed to LiCl-1wt%Li_2O containing 0, 0.3, or 0.6wt%Li, as indicated. The similarity of the spectra independent of the presence or absence of Li indicate that the degradation of the BeO in this system is likely due to the presence of Li_2O. The compound may be a ternary mixture of Li, Be, and O. Further characterization of these samples was not performed due to the health hazards associated with handling and working with the dust from the sample surfaces.

Appendix 4 : Supplemental Information from SS316L Studies

This Appendix gives additional surface analytical data obtained over the course of the exposure studies on SS316L in molten LiCl-Li_2O-Li solutions at 650°C. This information is supplemental to that presented in Chapter 2. The samples analyzed here are the same samples as those analyzed in Chapter 2, and the methods used are the same as those detailed in the experimental section of that Chapter. Discussion is presented as necessary to explain the findings from this data.

Micro-Vickers Hardness Testing

In an attempt to obtain information on the degradation of mechanical properties as a result of exposure to LiCl-Li_2O-Li solutions, micro-Vickers hardness testing was performed on all samples after methanol rinsing. These measurements were performed on a Wilson Tukon 1202 hardness tester using a micro-Vickers square pyramidal indenter. The load force of 500g was applied for 10s per indentation, and 10 indentations were made per sample. Unfortunately, the results of this testing were directly influenced by the morphologies of the samples, meaning that no conclusions about the bulk mechanical properties of the samples could be obtained. The presence of the oxide layer on the surface artificially increased the measured hardness values for all SS316L and I625 samples exposed to LiCl-Li_2O in the absence of Li due to the higher hardness of covalently bonded compounds compared to metals. Similarly, the highly porous morphologies observed on the SS316L samples exposed to LiCl-Li_2O solutions

containing 0.3wt%Li, as well as all I625 samples exposed to LiCl-Li_2O in the presence of Li, lead to artificially lower hardness values. As the SS316L samples exposed to LiCl-Li_2O solutions containing 0.6 and 1 wt%Li showed less porous morphology, the softening due to the microstructure was reduced when compared to the 0.3wt%Li samples. This can be observed in Figure A4.1, which shows the hardness measurements made for SS316 samples exposed to LiCl-2wt%Li_2O solutions containing 0, 0.3, 0.6, and 1wt%Li for 1000hr.

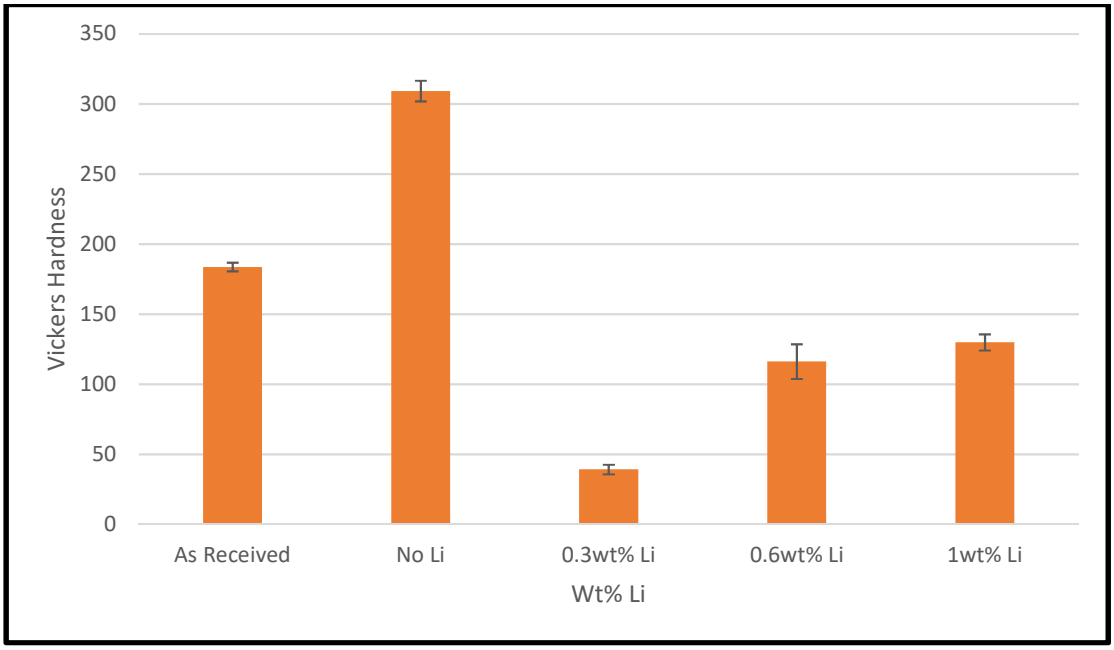

Figure A4.1: Micro-Vickers hardness measurements made for as received SS316 and SS316 samples exposed to LiCl-2wt%Li_2O containing 0, 0.3, 0.6, and 1wt%Li for 1000hr. Comparison to the morphologies shown in the SEM images presented above shows a direct correlation between surface morphology and hardness, indicating that the hardness measurements made are not representative of the base material.

SEM-EDS data

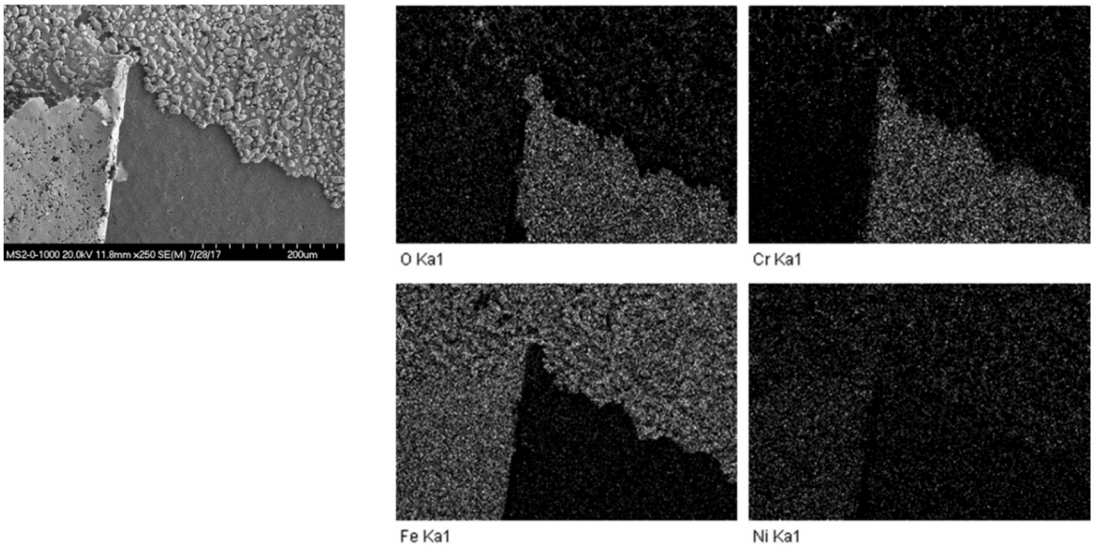

Figure A4.2: SEM image (left) and EDS maps of O, Cr, Fe, and Ni for an area above the salt level of the SS316L sample exposed to LiCl-2wt%Li_2O-0wt%Li for 1000hr. This area exhibited partial delamination of the surface layer, showing that the surface was composed of Fe and Ni metal, with a Cr based oxide layer underneath.

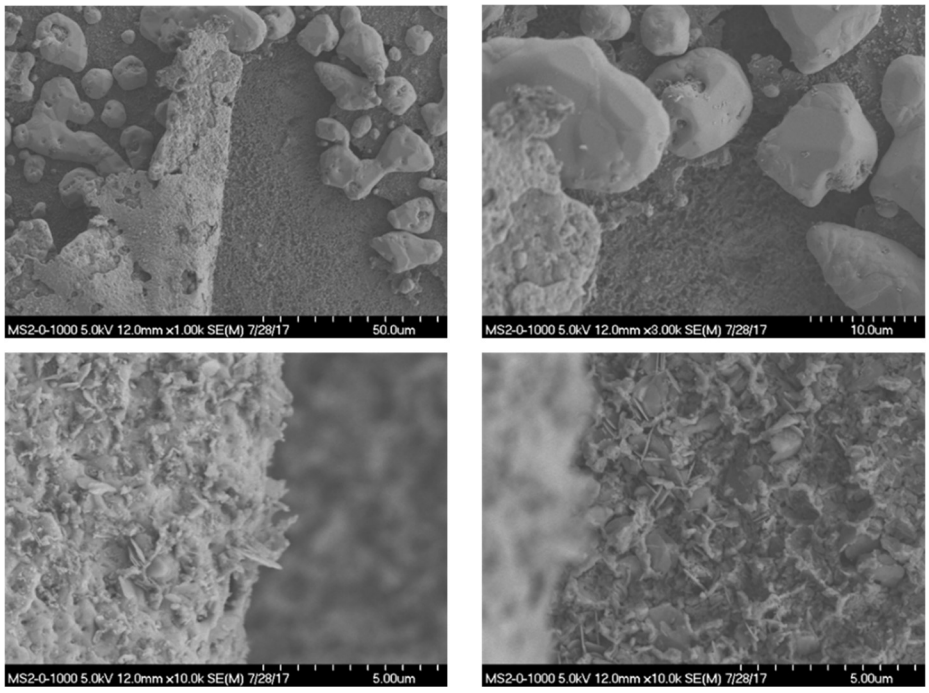

Figure A4.3: High magnification SEM images of the area shown in Figure A4.2 above the salt level of the SS316L sample exposed to LiCl-2wt%Li_2O-0wt%Li for 1000hr. This figure shows detailed morphology of the area shown in Figure A4.2.

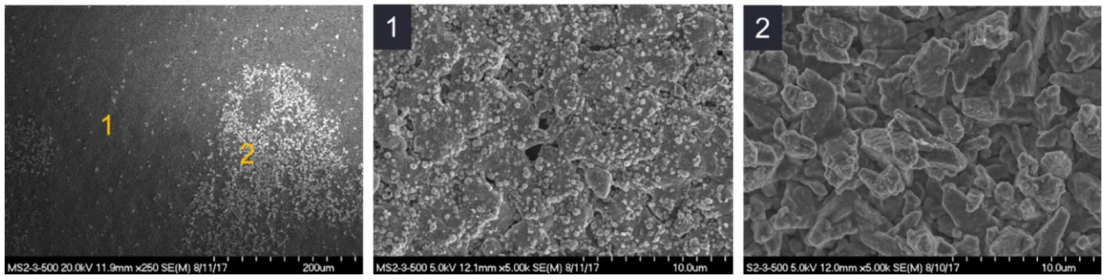

Figure A4.4: SEM images of area on the SS316L sample exposed to LiCl-2wt%Li_2O-0.3wt%Li for 500hr. This area showed a unique morphology, the composition of which indicates the possibility of a chromium oxynitride surface layer. This compound was removed during the methanol rinsing procedure, indicating poor adhesion to the base metal.

Table A4.1: EDS map average composition for location 1 in Figure A4.4.

Element	Weight%	Atomic%
N K	5.34	12.28
O K	3.72	7.49
S K	0.22	0.22
Cl K	0.20	0.19
Ti K	2.26	1.52
Cr K	11.34	7.02
Mn K	2.29	1.34
Fe K	106.20	61.26
Ni K	15.83	8.69
Totals	147.41	

Table A4.2: EDS map average composition for location 2 in Figure A4.4

Element	Weight%	Atomic%
N K	58.49	43.30
O K	45.81	29.68
Si K	1.17	0.43
Cl K	12.86	3.76
Ti K	1.19	0.26
V K	0.29	0.06
Cr K	107.26	21.39
Mn K	0.70	0.13
Fe K	3.84	0.71
Ni K	0.61	0.11
Mo L	1.60	0.17
Totals	233.83	

XRD Data

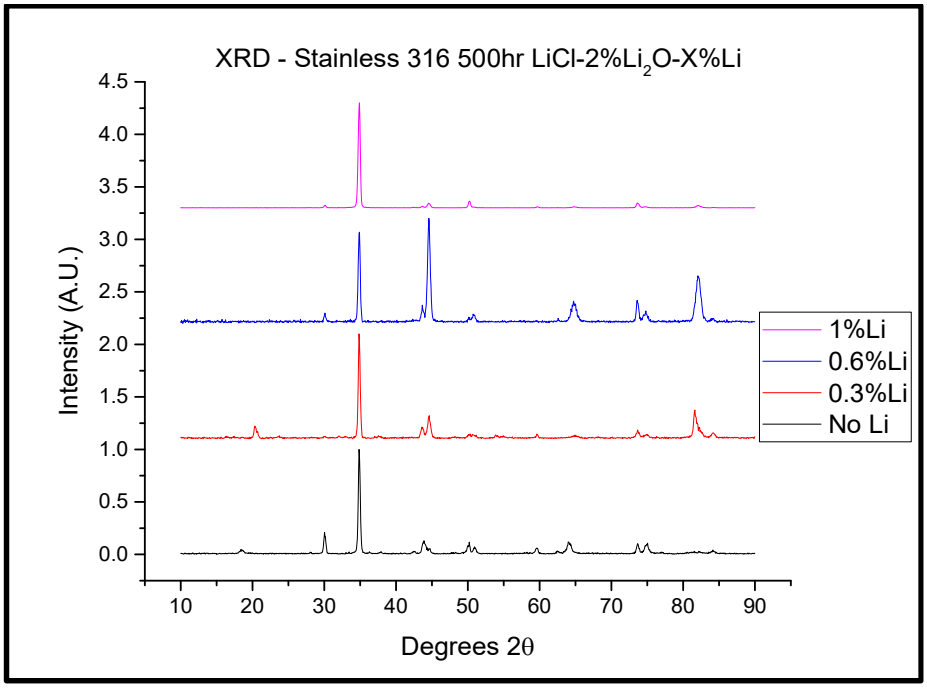

Figure A4.5: GI-XRD of SS316L samples exposed to LiCl-2wt%Li_2O solutions containing 0, 0.3, 0.6, and 1wt%Li at 650°C for 500hr prior to the removal of the residual salt layer with methanol.

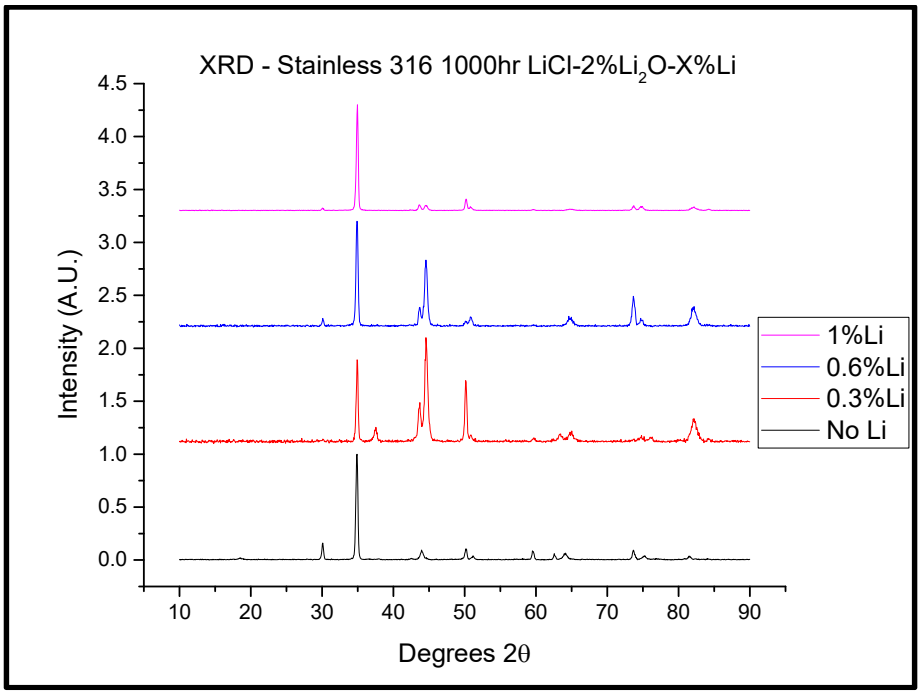

Figure A4.6: GI-XRD of SS316L samples exposed to LiCl-2wt%Li_2O solutions containing 0, 0.3, 0.6, and 1wt%Li at 650°C for 1000hr prior to the removal of the residual salt layer with methanol.

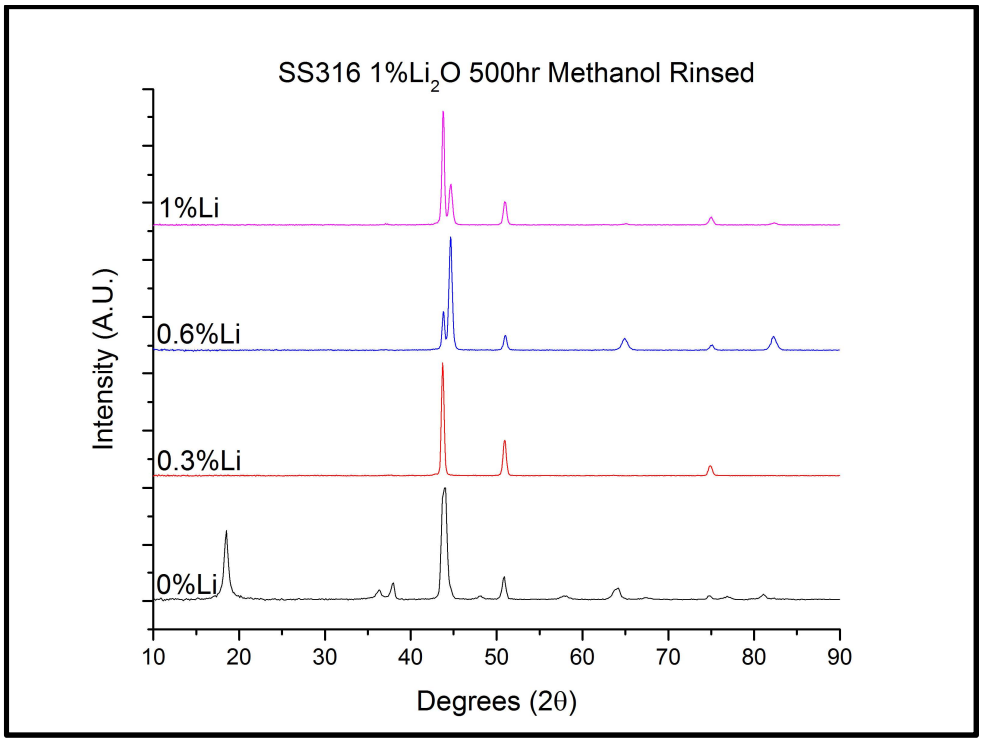

Figure A4.7: GI-XRD of SS316L samples exposed to LiCl-1wt%Li_2O solutions containing 0, 0.3, 0.6, and 1wt%Li at 650°C for 500hr after removal of the residual salt layer with methanol.

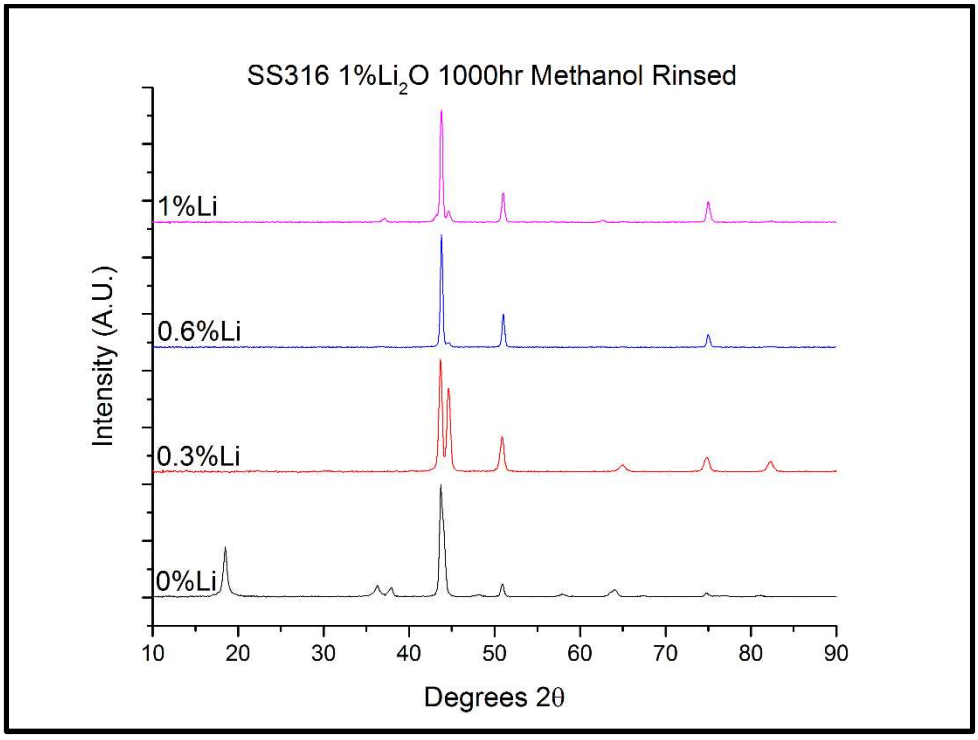

Figure A4.8: GI-XRD of SS316L samples exposed to LiCl-1wt%Li_2O solutions containing 0, 0.3, 0.6, and 1wt%Li at 650°C for 1000hr after removal of the residual salt layer with methanol.

Raman Data

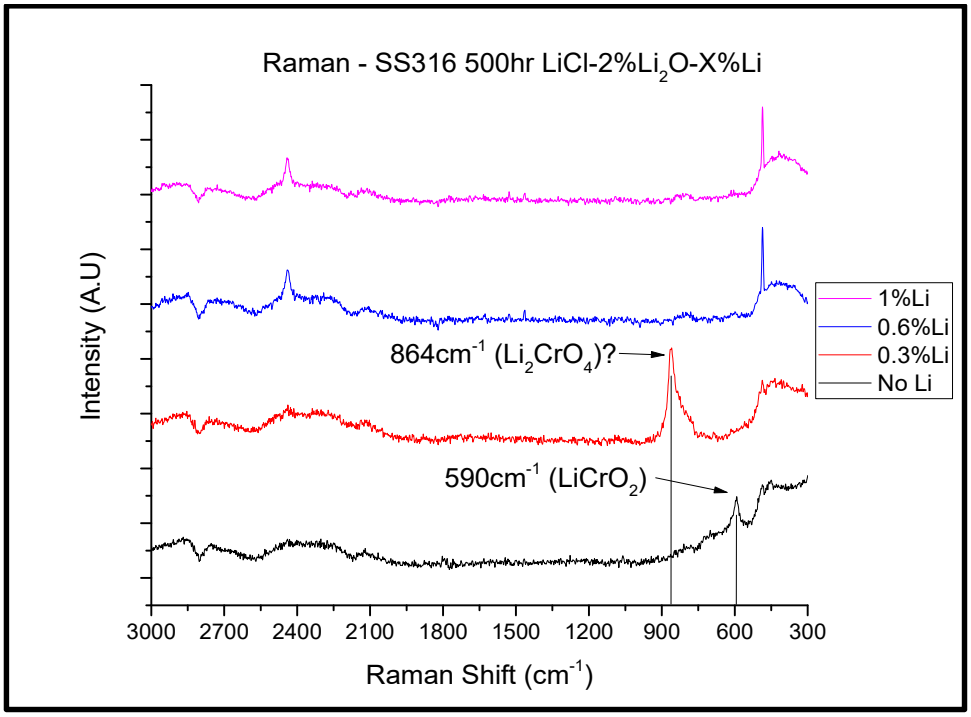

Figure A4.9: Raman spectra of SS316L samples exposed to LiCl-2wt%Li_2O solutions containing 0, 0.3, 0.6, and 1wt%Li at 650°C for 500hr prior to the removal of the residual salt layer with methanol.

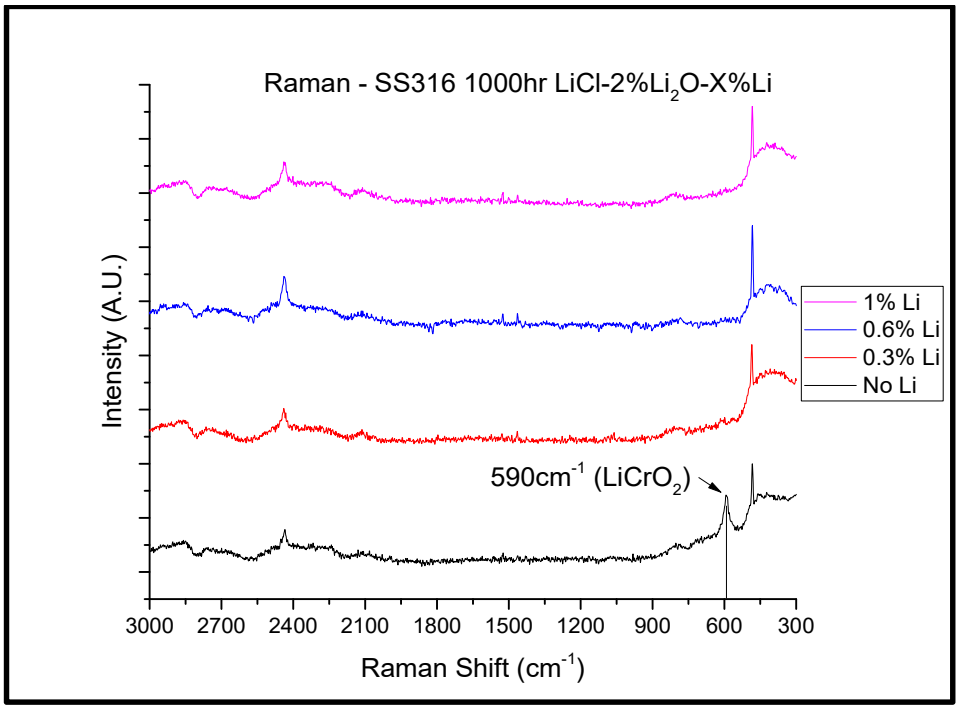

Figure A4.10: Raman spectra of SS316L samples exposed to LiCl-2wt%Li_2O solutions containing 0, 0.3, 0.6, and 1wt%Li at 650°C for 1000hr prior to the removal of the residual salt layer with methanol.

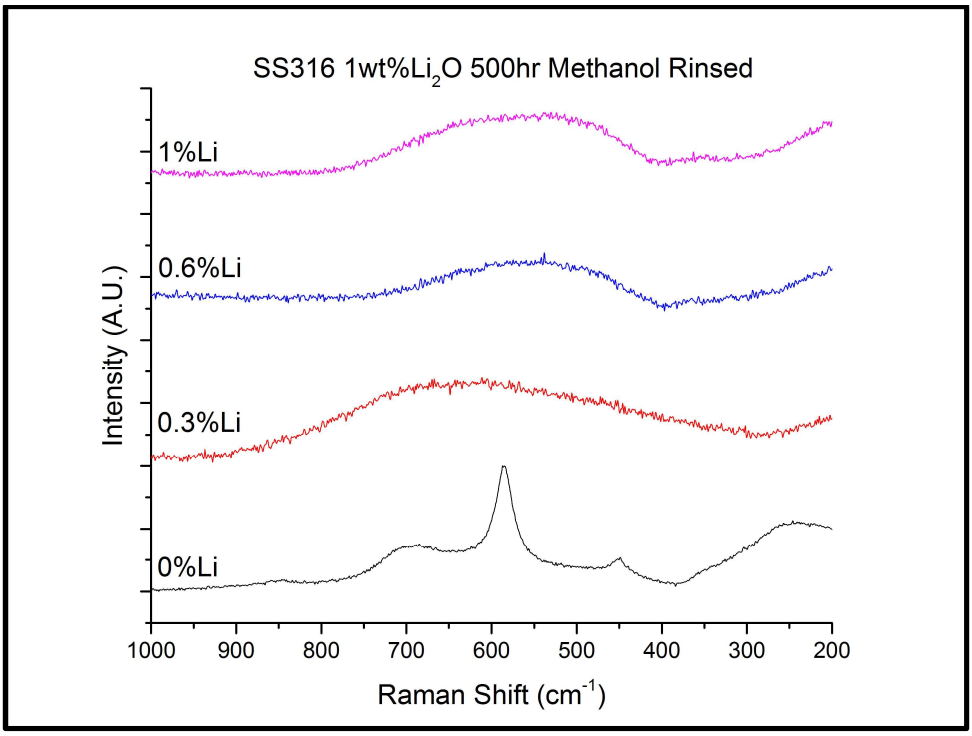

Figure A4.11: Raman spectra of SS316L samples exposed to LiCl-1wt%Li_2O solutions containing 0, 0.3, 0.6, and 1wt%Li at 650°C for 500hr following the removal of the residual salt layer with methanol.

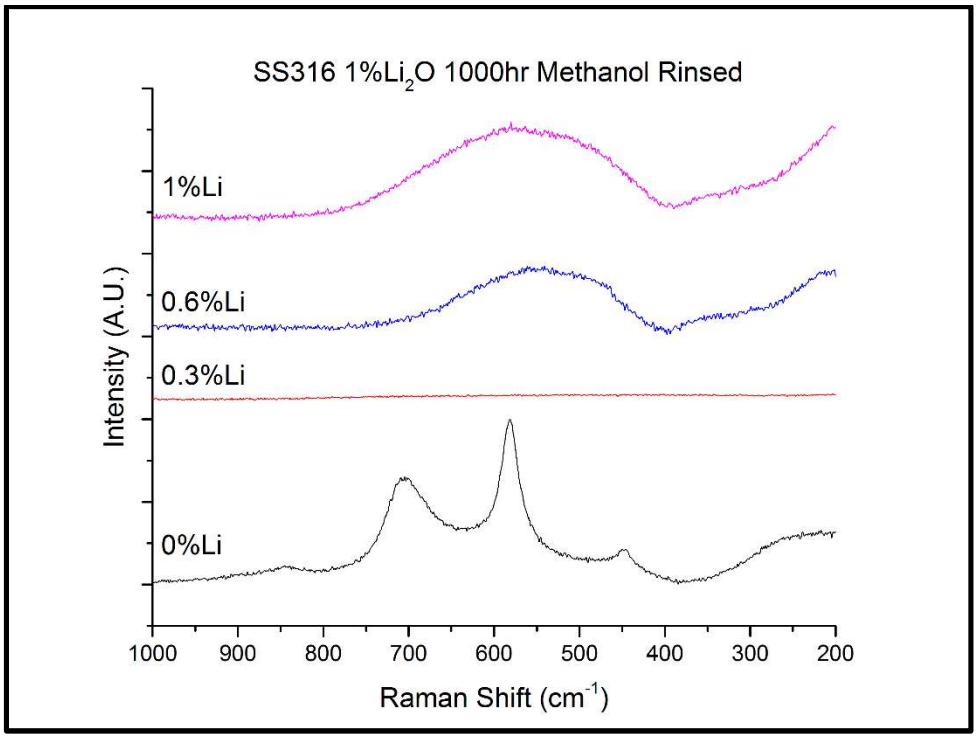

Figure A4.12: Raman spectra of SS316L samples exposed to LiCl-1wt%Li_2O solutions containing 0, 0.3, 0.6, and 1wt%Li at 650°C for 1000hr following the removal of the residual salt layer with methanol.

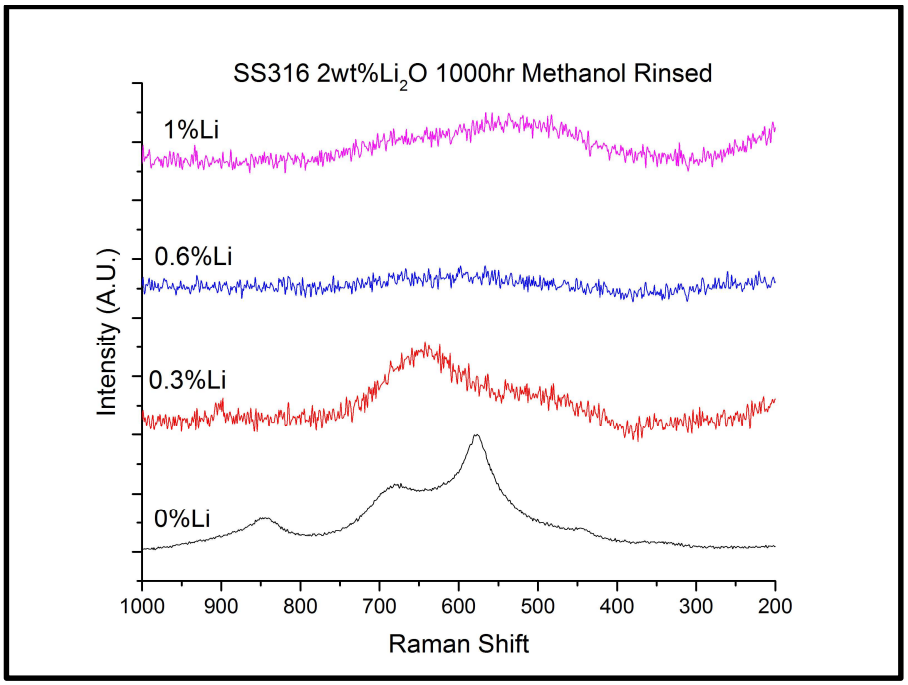

Figure A4.13: Raman spectra of SS316L samples exposed to LiCl-2wt%Li_2O solutions containing 0, 0.3, 0.6, and 1wt%Li at 650°C for 1000hr following the removal of the residual salt layer with methanol.

XPS Data

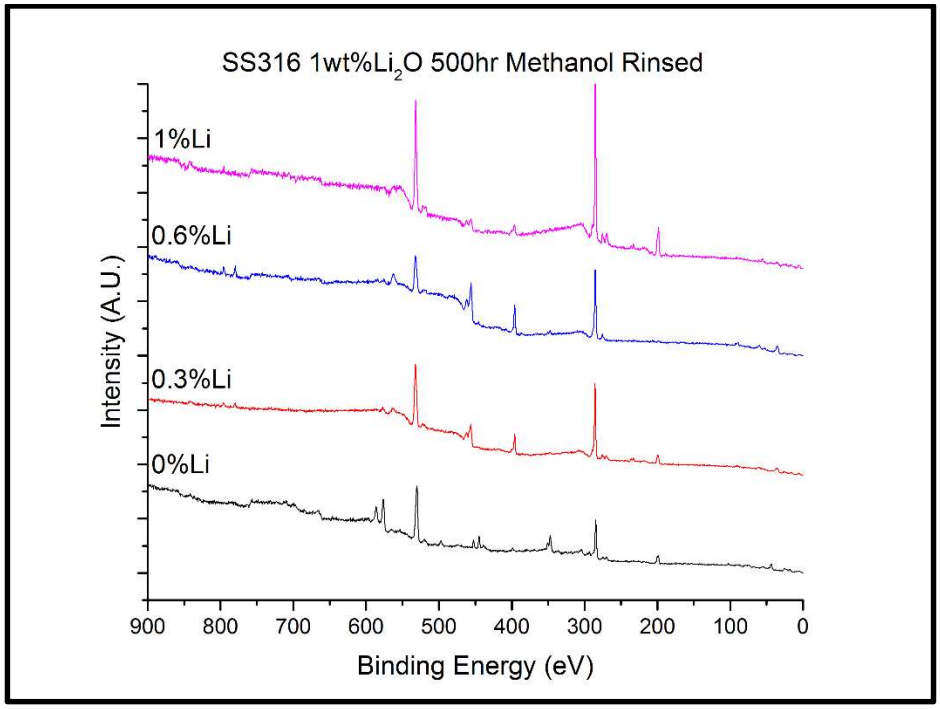

Figure A4.14: XPS survey spectra of SS316L samples exposed to LiCl-1wt%Li_2O solutions containing 0, 0.3, 0.6, and 1wt%Li at 650°C for 500hr following the removal of the residual salt layer with methanol.

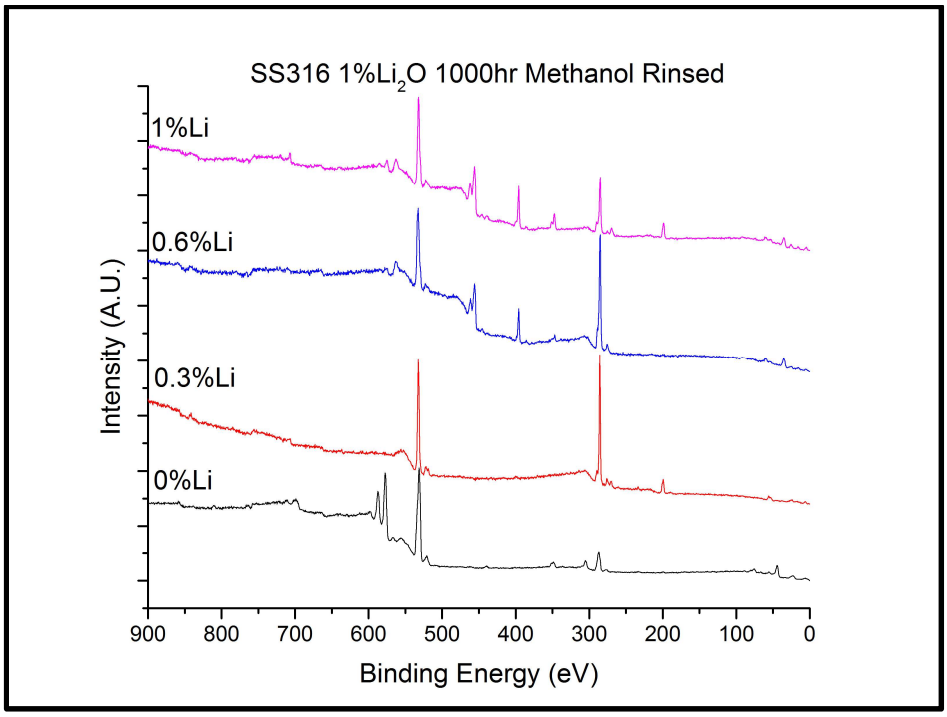

Figure A4.15: XPS survey spectra of SS316L samples exposed to LiCl-1wt%Li_2O solutions containing 0, 0.3, 0.6, and 1wt%Li at 650°C for 1000hr following the removal of the residual salt layer with methanol.

ICP-OES data

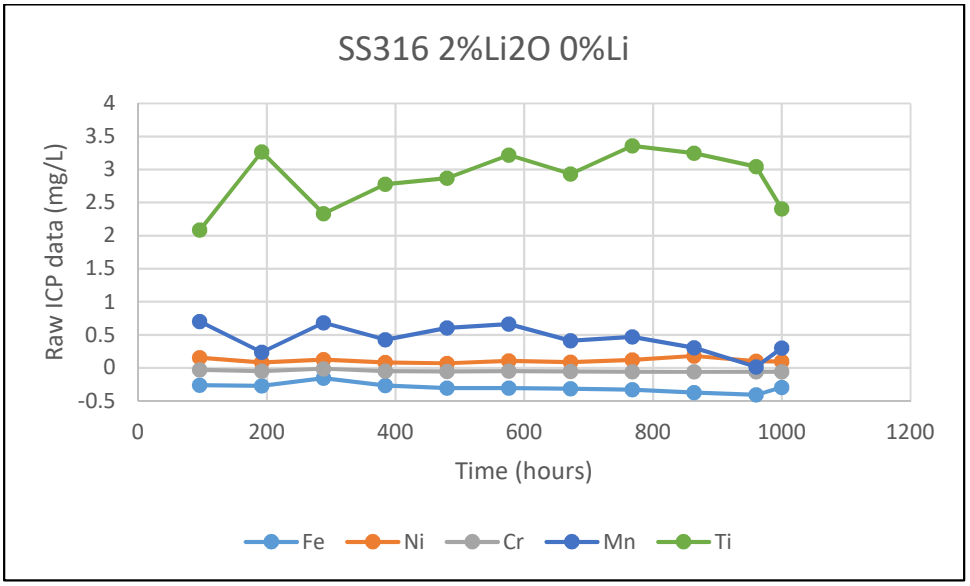

Figure A4.16: ICP-OES data of the concentration of alloying elements and impurity Ti in the salt ingots dissolved during the exposure of SS316L samples exposed to LiCl-2wt%Li_2O-0wt%Li at 650°C. Samples were taken every 96 hours over the course of the 1000hr exposures.

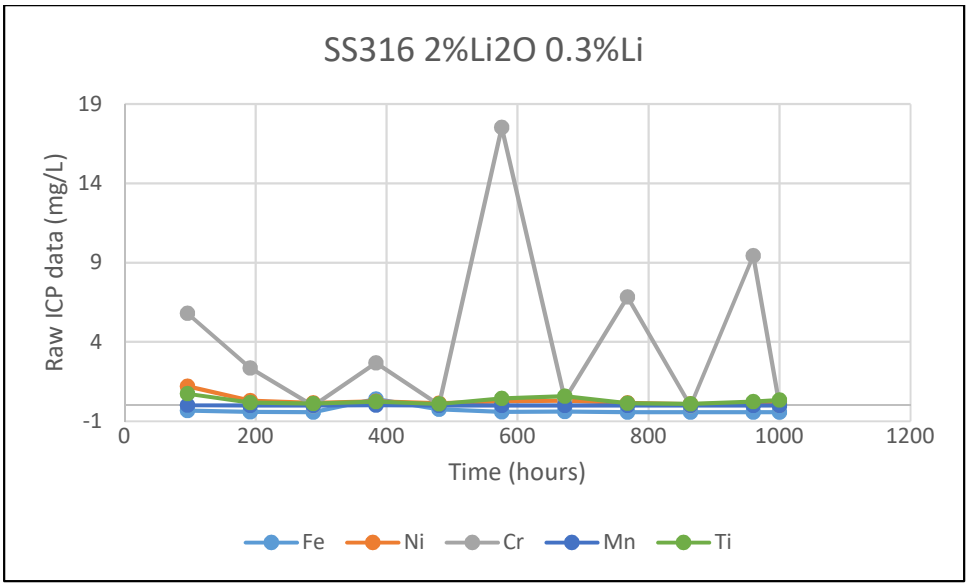

Figure A4.17: ICP-OES data of the concentration of alloying elements and impurity Ti in the salt ingots dissolved during the exposure of SS316L samples exposed to LiCl-2wt%Li_2O-0.3wt%Li at 650°C. Samples were taken every 96 hours over the course of the 1000hr exposures.

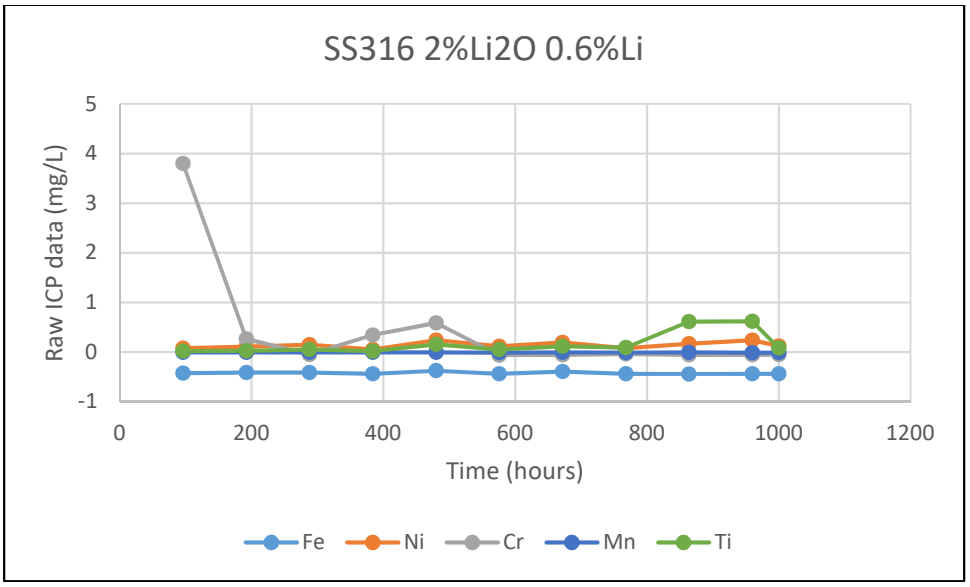

Figure A4.18: : ICP-OES data of the concentration of alloying elements and impurity Ti in the salt ingots dissolved during the exposure of SS316L samples exposed to LiCl-2wt%Li_2O-0.6wt%Li at 650°C. Samples were taken every 96 hours over the course of the 1000hr exposures.

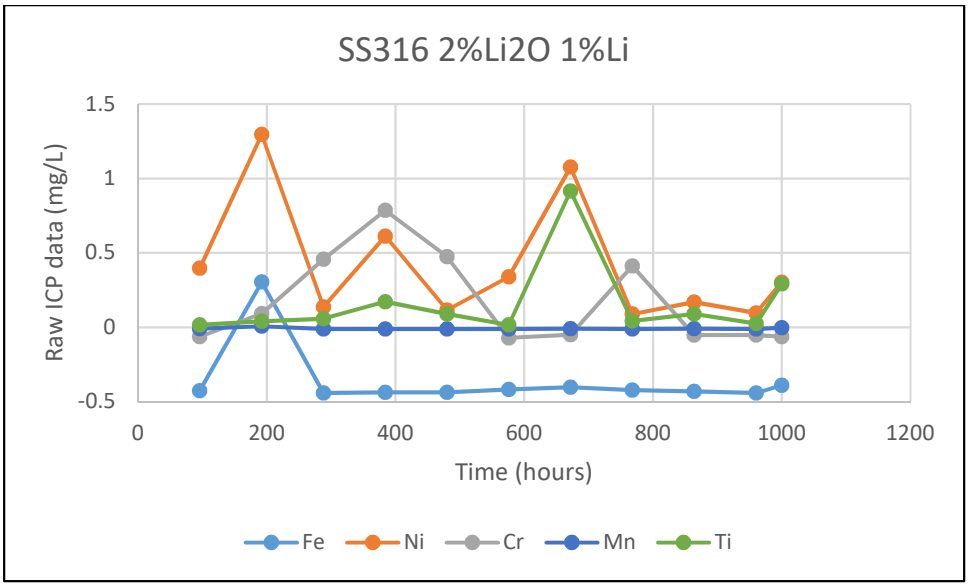

Figure A4.19: ICP-OES data of the concentration of alloying elements and impurity Ti in the salt ingots dissolved during the exposure of SS316L samples exposed to LiCl-2wt%Li_2O-1wt%Li at 650°C. Samples were taken every 96 hours over the course of the 1000hr exposures.

Appendix 5 : Supplemental Information from I625 Studies

Crucible Pictures

Figure A5.1: Image of Ni Crucible used to expose I625 samples to LiCl-2wt%Li_2O-1wt%Li for 1000hr. Severe degradation was observed, both above and below the melt line. Below the melt line, precipitation of corrosion products was observed which show a purple color. This may be indicative of lithium molybdenum purple bronze ($Li_{0.9}Mo_6O_{17}$), but further analysis would need to be conducted to determine the composition of this corrosion product. Above the melt line, dendritic structures were observed to be etched into the crucible wall, with apparent growth up and over the side of the crucible. This can be most readily observed in the figure on the right.

Appendix 6 : Li evaporation study

In the short term exposure studies of SS316L, I625, and M400 conducted prior to the longer duration exposure experiments presented here, the required mass of Li and Li_2O necessary to achieve a desired melt composition were added at the beginning of the experiment 1 hour prior to the immersion of the samples [25, 39, 46]. Due to the reactive and volatile nature of metallic Li at the operating temperature of 650°C, the mass of metallic Li present in the initial salt charge is depleted over time if no additional action is taken. Li_2O also has a significant vapor pressure at these temperatures, and consequently the solution chemistry will necessarily vary over extended time periods. In our previous work, the length of exposure (20-100 hours) was short enough to allow the depletion of Li and Li_2O to be negated. However, as the primary objective of the present study is to investigate the effects of metallic Li on container materials in the LiCl-Li_2O-Li system over exposure periods of 500 and 1000 hours, it was deemed necessary to replenish the salt periodically to maintain the desired composition. To ensure the accuracy of the salt composition, it was determined that the entire salt charge would be replaced periodically, and the addition of make-up Li and/or Li_2O to the existing melt was to be avoided.

To determine the frequency with which the salt must be replaced for these exposures, the evaporation rate of Li in our system was qualitatively observed by calculating the Li concentration in LiCl based on the volume of H_2 gas generated upon reaction of a salt sample with water. This was performed by sampling the

salt using a room temperature graphite dipstick, weighing the resulting salt sample, and measuring the H_2 volume generation upon reaction with water using the apparatus shown in Figure A6.1.

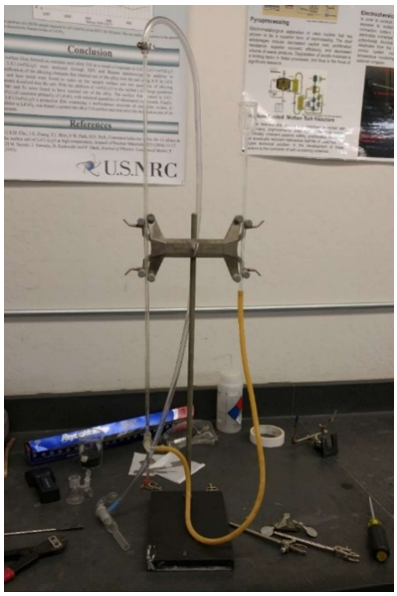

Figure A6.1: Gas measurement apparatus used for determination of H_2 volume generated from reaction of Li with H_2O. The salt sample is placed in a sealed reaction vessel with 10mL of DI H_2O that is connected via a flexible tube to the top of a 5mL burette, which is filled with water. The pressure inside the closed system is maintained at atmospheric pressure via a movable reservoir connected to the bottom of the burette via a second piece of flexible tubing.

The sample masses were recorded to 1 mg precision, and the burette used for measuring the volume of H_2 produced was accurate to 0.05 ml. The calculation of the mass of Li necessary to evolve the volume of gas produced was performed using the ideal gas law, accounting for the atmospheric pressure and the temperature of the laboratory, and assuming complete reaction according to the equation:

$$2Li(s) + 2H_2O(l) \rightarrow 2LiOH(aq.) + H_2(g)$$

The conversion factor was updated daily based on barometric pressure data from the National Weather Service. The value of the conversion factor varied between 0.484 and 0.488 mg Li/mL H_2 over the course of the study. The results of this analysis are shown in Figure A6.2. It is important to note that the solubility limit of Li in LiCl is approximately 0.3wt%, but is not well defined due to the possibility of multiple dissolution mechanisms [16, 22]. This accounts for the upper limit of around 0.35wt%Li observed, and the high variance associated with the measurements at high Li concentrations.

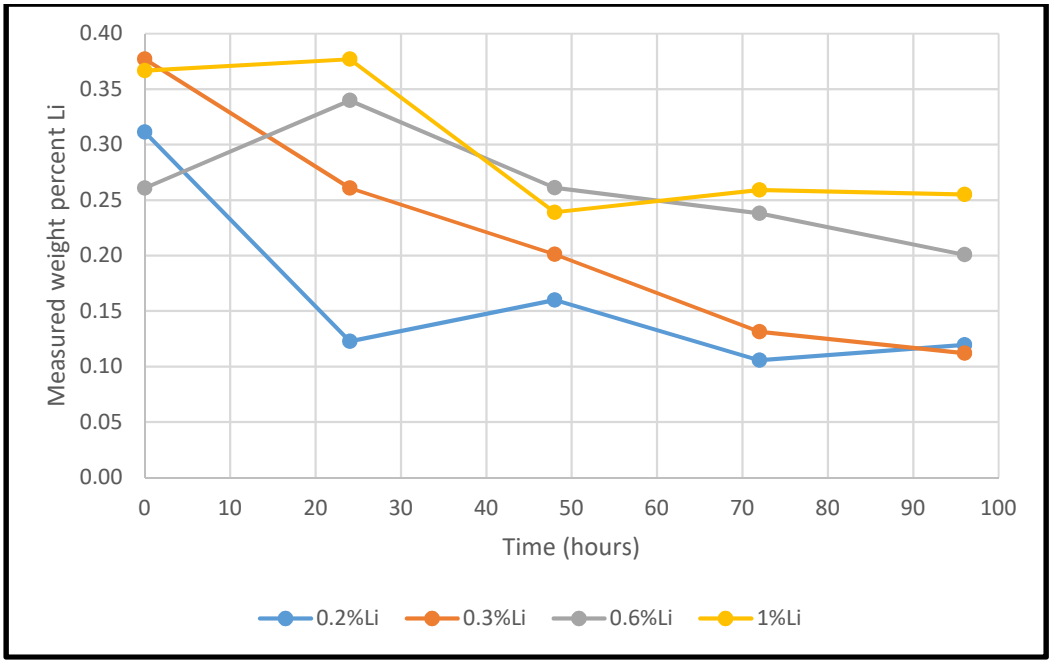

Figure A6.2: Measured Li concentration vs. time for four initial starting compositions of Li.

Based on the results of this study, the salt replacement interval was set to once every 96 hours. In practice, this was the absolute minimum salt change interval due to the large number of experiments that were ran in parallel during these studies.

Appendix 7 : Published Journal Articles

A7.1: Corrosion of stainless steel 316L in molten LiCl-Li_2O-Li

Journal of Nuclear Materials 517 (2019) 241–253

Contents lists available at ScienceDirect

Journal of Nuclear Materials

journal homepage: www.elsevier.com/locate/jnucmat

Corrosion of stainless steel 316L in molten LiCl-Li_2O-Li

William Phillips, Dev Chidambaram*

Materials Science and Engineering, University of Nevada, Reno, 1664 N. Virginia St., Reno, NV, 89557 MS0388, United States

HIGHLIGHTS

- SS316L exposed to molten LiCl-Li_2O-Li undergoes intergranular attack.
- Attack rates as high as 2.9 mm/year were observed in the presence of Li^0.
- $LiCrO_2$, Li_2CrO_4, and $NiFe_xCr_{2-x}O_4$ were seen on SS316L surfaces in absence of Li^0.
- In the presence of Li^0, no bulk oxide film forms to prevent further corrosion.
- A transition between electrochemical and liquid metal attack occurs based on [Li^0].

ARTICLE INFO

Article history:
Received 7 November 2018
Accepted 5 February 2019
Available online 8 February 2019

Keywords:
Pyroprocessing
Electroreduction
SS316L
High temperature
XPS

ABSTRACT

Exposure testing of Stainless Steel 316L was performed in LiCl-Li_2O-Li solutions at 650 °C for periods of 500 and 1000 h to investigate the effect of metallic Li on corrosion of materials used to contain the LiCl-Li_2O electrolyte for the electrolytic reduction of used nuclear fuel. Melt compositions studied consisted of LiCl containing 1 or 2 wt% Li_2O and 0, 0.3, 0.6, or 1 wt% Li. Post exposure surface analysis was performed using scanning electron microscopy coupled with energy dispersive X-ray spectroscopy, Raman spectroscopy, X-ray photoelectron spectroscopy, and X-ray diffraction. Focused ion beam and mechanical cross sections of the samples and gravimetric analyses were performed to determine the time-averaged corrosion rate for each sample. Lithium metal induced attack rates were found to be as high as 2.91 mm/y. In the absence of solvated Li in the LiCl-Li_2O system, $LiCrO_2$, Li_2CrO_4, and $NiFe_xCr_{2-x}O_4$ were observed to be the primary corrosion products. When Li was present in the melt, the oxidized alloying elements were only detectable via X-ray photoelectron spectroscopy, and the surface was primarily comprised of bare metal.

1. Introduction

Reduction of used oxide-based nuclear fuel is a necessary step for the incorporation of the large stockpile of used fuel from light water reactors into a pyrometallurgical-based fuel cycle [1–3]. The electrolytic oxide reduction operation developed by Argonne National Laboratory is the preferred method for the reduction of used nuclear fuel (UNF) and has been the subject of continued development [1,4–12]. In this process, declad, crushed, and pelletized UNF is placed in a stainless steel basket and cathodically polarized versus a suitable anode at a potential sufficient to reduce the oxides present at the cathode [12]. Li_2O is added in concentrations of 1-2 wt% to provide an initial source of O^{2-} ions, which are then oxidized at the anode to form oxygen gas. The concentration of Li_2O must be carefully controlled, as the reduction of the lanthanides and minor actinides becomes thermodynamically unfavorable at high O^{2-} activities, and the anodic dissolution of Pt becomes problematic at low O^{2-} activities [11,13–15]. As the reduction proceeds, the actinide and lanthanide oxides are reduced to metallic form, while the salt soluble fission products (i.e. Cs, Sr, I, Br, etc.) form salts and dissolve into the electrolyte. Due to the close reduction potentials of Li_2O and UO_2 of −2.40 V and −2.47 V vs. $O^{2-}|O_2$, respectively, and the necessity of applying a high overpotential to achieve a high reduction yield, metallic Li is generated at the cathode [2,12,16,17].

The Li generated at the cathode acts as an additional reduction pathway for UO_2 through direct chemical means; however, due to the solubility of Li in LiCl, some of the metallic Li dissolves into the electrolyte [15,16,18–23]. Dissolution of Li into LiCl has been noted

* Corresponding author.
E-mail address: dcc@unr.edu (D. Chidambaram).

https://doi.org/10.1016/j.jnucmat.2019.02.007
0022-3115/

by a number of researchers, and causes a number of changes in physical, electrical, and chemical properties of the electrolyte, as well as causing current inefficiency [16]. The exact solubility limit of Li in LiCl has proven to be experimentally difficult to determine [18,19,24]. A number of different dissolution mechanisms have been proposed by other researchers, but a consensus has yet to be reached within the community. The f-center model proposed by Bredig, *et Al.* treats the excess electron from solvated Li^0 as an anion vacancy, with the electron delocalized from any individual Li^+ ion core [18,25]. In this model, the solution behaves somewhat similarly to a liquid metal, with free electrons contributing to increased electrical conductivity. This model has successfully predicted the increase in solution conductivity for other alkali halide – alkali metal systems, however, the solution conductivity of the LiCl-Li system is anomalous in that it does not increase at the rate predicted by the f-center model [16,18]. Previous work in our laboratory using *in-situ* Raman spectroscopy has provided evidence of the presence of Li_8 nanoclusters in solution as a colloidal suspension [26]. If Li_8 clusters are present in the LiCl-Li system, they would act to keep the valence electrons of the Li_8 cluster localized, thus reducing the rate of electrical conductivity increase associated with the progressive addition of Li^0 to LiCl. As the clusters would be present as a colloid, the solubility of Li^0 in LiCl would be dependent on the specific experimental parameters, leading to the variation in the measured values for solubility reported by other researchers [26].

Regardless of the molecular interactions at place within the LiCl-Li system, understanding of the effect the solution chemistry has on materials exposed to the molten LiCl-Li_2O-Li system is important for the safe and economical design of vessels and other components for use during the electrolytic reduction of used nuclear fuel. Corrosion in LiCl-Li_2O under oxidizing conditions has been widely investigated [27–34]. The most successful model of corrosion in this system is based on the Lux-Flood model of salt basicity where the rate of material degradation is dependent upon the activity of the O^{2-} anion [27,35,36]. In addition to O^{2-} activity, corrosion in molten salts is also governed by the inclusion of impurities in the melt, such as moisture or metal chlorides [35]. While the literature concerning corrosion in chloride salts is rich in diversity and discussion of corrosion mechanisms, very few studies have investigated the effect of solvated lithium metal in lithium chloride [37–44]. The studies that have been reported have been mainly of short-term duration and have been conducted under widely varying experimental parameters. Consequently, these studies conflict in their analysis on the effect of Li^0 on the corrosion of various materials in the molten LiCl-Li_2O-Li system.

Previous work in our laboratory has attempted to elucidate the effect of Li^0 and Li_2O on the corrosion of Stainless Steel 316L (SS316L), Inconel 625, and Monel 400 by parametrically varying the concentrations of Li_2O, Li, and impurity H_2O independently [41,42,44]. These studies showed that material degradation depends on the concentration of H_2O, Li_2O and Li, and that a transition from corrosion based primarily on the O^{2-} activity in the melt at low Li^0 concentrations to corrosion more similar to liquid metal attack occurs at high Li^0 concentrations. However, the short-term nature of these exposure tests necessitated the continuation of this work to verify our previous findings. In this light, the current study focuses on the corrosion of SS316L over extended time periods when exposed to LiCl containing Li_2O and Li at various concentrations. This paper presents the information gathered from SEM-EDS of the sample surfaces and cross sections, as well as XRD, XPS, and Raman spectroscopy of the surfaces to elucidate the mechanisms responsible for material degradation.

2. Materials and methods

All experiments were performed in a Vacuum Atmospheres OMNI-LAB glovebox under an Ar atmosphere containing less than 2 ppm O_2 and less than 1 ppm H_2O. Anhydrous LiCl and Li_2O were obtained from Alfa-Aesar and were of 99% and 99.5% purity, respectively. Li metal of 99% purity was purchased from Strem Chemicals. 99% purity Ni crucibles were obtained from Alfa-Aesar. SS316L coupons were cut from a 3.048 mm plate obtained from McMaster-Carr, with the certified composition given in Table 1.

The salt compositions studied consisted of LiCl containing 1 and 2 wt% Li_2O and 0, 0.3, 0.6, and 1 wt% Li, with exposure periods of 500 and 1000 h. Total salt mass contained in each crucible was 50 g. Duplicate samples were exposed for each data point, and 500 h and 1000 h exposures were conducted in parallel, with the 500 h samples removed from the experiment upon completion of the allotted exposure period. The furnace configuration used for this study is shown in Fig. 1. A 6.5 inch inner diameter, 6 inch tall cylindrical heater from Watlow (1500 W) was used to maintain a temperature of 650 ± 5 °C for the duration of the exposure period. A 6 inch diameter graphite block was machined to accommodate 5 Ni crucibles, with slots machined to accommodate the sample hanging rods. This configuration allowed for repeatable placement of the samples within the melt during the salt replacement procedure outlined below. Two identical furnaces were constructed to maximize the number of experiments that could be ran in parallel. In operation, four experiments were ran simultaneously in each furnace, which allowed for an additional crucible location to be used for salt replacement purposes.

Prior to exposure, the metal samples were cut into 1.27 cm by 1.27 cm squares using a CO_2 laser. The samples were then polished to a 1 μm surface finish on both sides using a diamond abrasive and spot welded to loops of SS316L wire for suspension from the sample hanging rods, as was performed in our previous studies [41,42,44]. Sample hanging rods were made of like material to the samples, as alumina rods proved to be incapable of withstanding the highly reducing atmosphere directly over the molten solutions containing metallic Li for the duration of these experiments. The mass of each sample was recorded immediately prior to exposure using a high precision balance.

3. Experimental

Due to the evaporation of Li and Li_2O over time and the extended exposure periods of this study, the salt charge for each test was replaced once every 96 h to maintain the solution chemistry. To minimize the effects of impurity H_2O, LiCl was dried in a vacuum oven in air at 200 °C for 24 h before being transferred into the glovebox for storage [41,45]. Immediately prior to insertion in the primary furnace, a cleaned Ni crucible (99% purity, Alfa Aesar) containing the weighed amount of LiCl was dried under Ar for 2hr in a dedicated furnace maintained at 550 °C. After insertion into the primary furnace, the LiCl was allowed 1 h to reach thermal equilibrium, after which time the required mass of Li_2O and Li were added to the molten salt. The melt was allowed to equilibrate for another hour prior to the transfer of the corrosion specimens from the old salt charge to the new salt charge. Sample transfer was accomplished through the use of specially fabricated tongs.

Table 1
Certified composition of the SS316L plate used in this study.

Fe	Cr	Ni	Mo	Mn	C
70.1	16.5	10	2	1.3	0.014

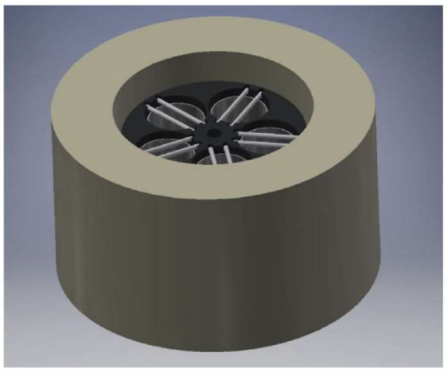

Fig. 1. A model of the long term exposure furnace, graphite crucible holder, Ni crucibles, and sample hanging rods.

Following transfer of the samples to the new salt charge, the old salt charge was removed from the furnace and allowed to cool to room temperature.

Following completion of the exposure period, the samples were removed from the furnace and allowed to cool to room temperature in the glovebox atmosphere. All samples were stored in the Ar glovebox between analytical procedures. As it was unknown if the surface films formed on the corrosion specimens would be stable in atmosphere, surface analysis was performed both prior to and following removal of the residual salt layer. Following the initial surface analytical procedures, residual LiCl was removed by placing each sample in 25 ml of HPLC grade methanol for 15 min with constant agitation. Prior to the methanol rinsing procedure, all surface analysis was performed under inert atmosphere or vacuum conditions, depending on technique. The data presented here was collected following the methanol rinsing procedure, as the residual salt layer significantly interfered with surface analysis. No chemical or morphological changes were observed as a result of the methanol rinsing procedure. Gravimetric weight change measurements were performed following the methanol rinsing procedure.

Post exposure surface analysis was performed using scanning electron microscopy (SEM) coupled with energy dispersive X-ray spectroscopy (EDS), Raman Spectroscopy, X-ray diffraction (XRD), and X-ray photoelectron spectroscopy (XPS). Following the completion of all surface analytical techniques performed in this study, the samples were cross sectioned to investigate the nature and depth of degradation of the samples. Initially, focused ion beam (FIB) milling was used to mill a trench in the samples to minimize possible morphological and chemical changes to the internal structure of the samples; however, it was found that the depth of attack for samples exposed to melts containing Li was much greater than practical to investigate using this technique alone. Consequently, all samples exposed to Li containing melts were cross sectioned using a Buehler cubic-BN wafering blade on a slow speed saw and polished according to Buehler's recommended polishing techniques to a 0.05 μm surface finish prior to analysis. Samples exposed to LiCl-Li_2O in the absence of Li were investigated using only FIB milling for cross sectional analysis due to the relatively shallow depth of attack.

SEM of the sample surfaces was performed using a Hitachi S-4700, while EDS data was collected via the attached Oxford Instruments energy dispersive X-ray spectrometer. The W cold field emission source was operated at an accelerating voltage of 5 kV for surface morphology images, while 20 kV was used for collection of EDS spectra. Emission current was maintained at 10 mA. FIB milling and subsequent SEM-EDS analysis for cross sectional images was performed using a FEI Scios dual-beam FIB/SEM equipped with a TEAM Pegasus Integrated EDS-EBSD. The same dual-beam FIB/SEM was used to perform the SEM-EDS analysis of all of the cross sectioned samples, including those mechanically cross sectioned and polished. The electron beam was operated at 20 kV for both imaging and EDS analysis.

Following the methanol rinsing procedure, the final mass of each sample was recorded, and the exposed surface area was calculated based on the measured submersion depth of each sample. The average corrosion rate in mm/year and the mass loss rate in mg cm^{-1} hr^{-1} was then calculated based on the mass change, density of the alloy, exposed surface area, and length of exposure.

X-ray diffraction was performed using a Rigaku Smartlab X-ray diffractometer with a Cu kα source operating at 44 kV and 40 mA. Parallel beam optics in a grazing incidence angle configuration were used for detection of the thin surface films formed on the samples in this study. The incidence angle was set at 1°, and the diffraction pattern was recorded over a 2θ range of 10°–90° for all diffraction patterns. For each diffraction pattern, the scan speed was optimized to yield an intensity of 5000 counts for the highest peak, while the step size was varied to give 5 steps at the full width at half-maximum intensity of the narrowest peak.

Raman spectroscopy was performed using a Thermo-Scientific DXR Raman microscope utilizing a 10 mW 532 nm continuous wave laser. Spectra were collected through the 50× objective lens of the microscope using a 50 μm incident beam slit. The collection time was 4 s per spectra, and 16 individual spectra were averaged to give the spectra reported here.

X-ray photoelectron spectroscopy was performed using a PHI 5600 spectrometer equipped with an Al-Kα source with a photon energy of 1486.6eV. The source was operated at an accelerating voltage of 14 kV and an anode power of 300 W. The spectrometer dispersion and work function were calibrated to the Au $4f_{7/2}$ peak at 84.00eV and the Cu $2p_{3/2}$ peak at 932.67eV to an accuracy of ±0.05eV. Survey spectra were recorded with a step size of 0.5eV, while narrow scans were collected at a step size of 0.025eV for the elements detected on the sample surfaces. Peak fitting was performed with SDP version 4.6 Gaussian fitting software. Charge correction was performed to the adventitious C 1s peak at 284.8eV unless noted otherwise.

4. Results

4.1. Scanning electron microscopy

The morphologies observed via SEM were highly dependent on the Li concentration in the molten salt solution. The SEM micrographs obtained from SS316L samples exposed to LiCl-2wt% Li_2O containing 0, 0.3, 0.6, and 1 wt% Li at 650 °C for 1000hr and washed with methanol are shown in Fig. 2, while the area averaged EDS composition of the primary constituents of the sample surface for these regions are given in Fig. 3. The differences in the surface morphology caused by the varying concentrations of Li in LiCl-2wt% Li_2O correlates to the changes in surface chemistry observed via Raman, XPS, and XRD presented below. The unique surface morphology observed at 0.3 wt% Li may be indicative of the simultaneous action of electrochemical corrosion and liquid metal attack, while the similarity between the morphologies observed at 0.6 and 1 wt% Li indicate that corrosion at these concentrations is firmly within the liquid metal attack regime. Morphologies similar

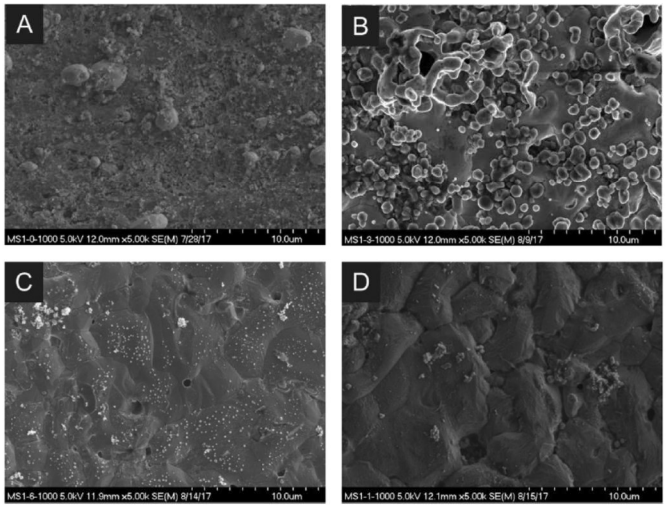

Fig. 2. SEM micrographs of SS316L exposed to LiCl-1wt% Li2O at 650 °C containing A) no Li, B) 0.3 wt% Li, C) 0.6 wt% Li, and D) 1 wt% Li for 1000hr, following the methanol rinsing procedure.

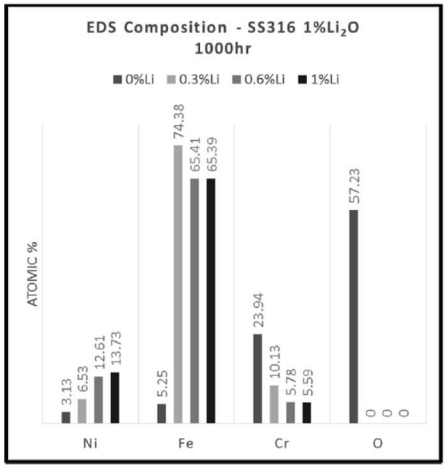

Fig. 3. Average composition of the SS316L samples exposed to LiCl-1wt% Li_2O-Li solutions for 1000hr for the regions shown in Fig. 2.

to those observed here were reported in a recent publication by researchers at KAERI who investigated the corrosion behavior of Ni in molten LiCl-Li_2O-Li [43]. A number of void spaces were also observed on the surface of all samples exposed to melts containing metallic Li, indicating possible locations where the intergranular corrosion observed on the sample cross sections was initiated. These voids were typically located at high angle grain boundaries, further supporting this hypothesis.

From Fig. 3, it can be observed that the surface of the SS316L sample exposed to LiCl-1wt% Li_2O-0wt% Li at 650 °C for 1000hr is primarily composed of Cr-based oxide films, with minor contributions of Ni and Fe. This is in good agreement with the Raman, XRD, and XPS data presented in their respective sections, which all indicate that these surfaces are composed primarily of $LiCrO_2$, while small quantities of Li_2CrO_4 and $NiFe_xCr_{2-x}O_4$ are predicted by Raman and XPS. When the Li concentration in the molten salt solution is 0.3 wt%, the Cr content of the surface is depleted compared to the base alloy while the Fe content is increased. Beyond the solubility limit of Li, at 0.6 and 1 wt% Li, Cr is depleted slightly further and O is not detectable, while both Fe and Ni are present at levels nominal for SS316L, indicating a bare metallic surface. A slight enrichment of Ni on the SS316L sample exposed to LiCl-2wt% Li_2O-1wt% Li for 1000hr is in agreement with our previous work, and is indicative of liquid metal like attack by Li [41]. Similar trends were observed for samples exposed to LiCl-Li_2O-Li containing 1 and 2 wt% Li_2O and 0, 0.3, 0.6, and 1 wt% Li for 500 and 1000hr.

Also of interest is the observation of sensitization on a small area on the SS316L sample exposed to LiCl-2wt% Li_2O-0.6 wt% Li at 650 °C for 1000hr. Sensitization of austenitic stainless steels is a well-known issue at high temperatures, where the formation of chromium carbides and their subsequent concentration at the grain boundaries leads to intergranular corrosion and loss of strength [46]. The characteristic enrichment of Cr at the grain boundaries typical of sensitization can clearly be observed in the Cr Kα EDS map in Fig. 4, while the specific compositions for spots 1 and 2 marked on the SEM micrograph and EDS map are given in Table 2.

The detection of S along with chromium carbide formation at Spot 1 is in good agreement with literature, as S is known to accelerate the sensitization of austenitic stainless steels [46]. As expected, the area around spot 1 (spot 2) has much lower concentration of chromium, which is below the concentration in base alloy. The low carbon content of the SS316L used for this study is intended to minimize this issue by preventing the formation of

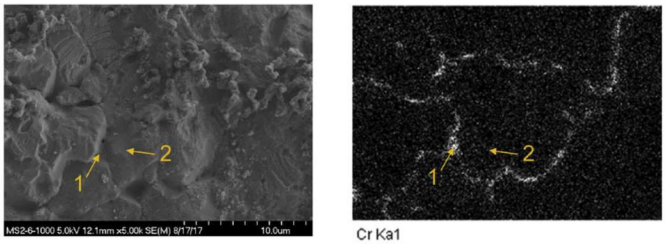

Fig. 4. SEM micrograph (left) and EDS map of Cr of the same location (right) for the SS316L sample exposed to LiCl-2wt% Li_2O-0.6 wt% Li at 650 °C for 1000hr. The elemental compositions obtained via EDS analysis for spots 1 and 2 are given in Table 2.

Table 2
EDS composition spot analysis for the locations marked on the SEM micrograph in Fig. 4, above.

Element	Spot 1	Spot 2
	Atomic%	Atomic%
C	26.69	–
S	1.21	–
Cr	27.05	4.28
Mn	1.09	1.46
Fe	28.52	50.05
Ni	15.44	44.21

carbides. Of great importance to the present work, the operating temperature of the electrolytic reduction of UNF at 650 °C is also ideal to cause sensitization of austenitic stainless steels, as chromium carbides are insoluble at this temperature and the diffusion of C through the microstructure allows for their formation and migration to the grain boundaries.

4.2. Cross section SEM-EDS

The SEM image obtained for the FIB milled trench from the SS316L samples exposed to LiCl-1wt% Li_2O-0% Li for 500hr and 1000hr are shown in Fig. 5. It can be observed that the attack first proceeds inward from the sample surface in an intergrannular fashion prior to consuming the grains themselves, likely assisted by the sensitization of the material seen in Fig. 4. The depth of attack into the sample is approximately linear with length of exposure, with the total depth of attack being 13 μm and 27 μm for 500hr and 1000hr, respectively, while the thickness of the outer oxide layer is approximately 3 μm for the 500hr sample and 7.5 μm for the 1000hr sample.

EDS mapping results for the corroded region of the SS316L sample exposed to LiCl-1wt% Li_2O for 1000hr are shown in Fig. 6. Here, it can be observed that the corrosion products (dark regions) are enriched in Cr, Mo and O, while the bulk material is relatively depleted in Cr and Mo. This agrees with the findings of previous studies that corrosion in LiCl-Li_2O occurs primarily through preferential attack of the most active alloying elements, namely Cr and Mo [35,41].

In the presence of Li, intergrannular corrosion was again observed to be the primary method of material degradation, as can be observed in Fig. 7. However, the lack of a protective oxide layer severely accelerated the attack of the base material.

From Fig. 7, it can be observed that the depth of attack on the base material is approximately linear with time and does not depend on the concentration of Li; however, the severity of the degradation is proportional to the Li concentration in the melt. In all cases, the rate of attack was approximately 2.2–2.9 mm/year in the presence of Li. The outer layers of the SS316L samples exposed to melts containing Li were depleted in Cr, while small, localized areas of high Cr concentration were observed in intergranular regions, further corroborating the observations of sensitization made in Fig. 4. A high magnification EDS map of one of these regions on the SS316L sample exposed to LiCl-1wt%Li_2O-0.6 wt%Li for 500hr is shown in Fig. 8, while the spot EDS analysis for the area highlighted in red in the SEM image is given in Table 3.

From the SEM-EDS images in Fig. 8 and spot analysis in Table 3, it is apparent that corrosion of the base material is facilitated by the precipitation of Cr and Mn at the grain boundaries in the form of metal carbides and nitrides. These carbides and nitrides are then preferentially attacked by the molten salt, leaving a channel for further intrusion of the salt along the grain boundary. N was likely incorporated as an impurity from the glovebox atmosphere which reacted with Li^0 to form Li_3N, which is known to accelerate corrosion in the LiCl-Li_2O-Li system [47]. Also, titanium nitride surface

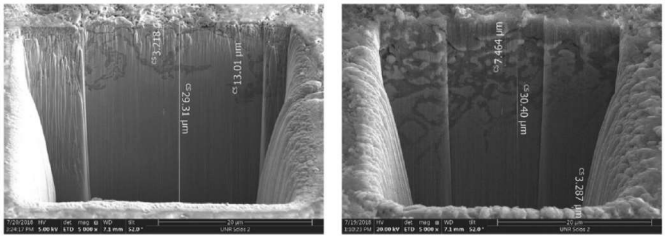

Fig. 5. FIB milled and SEM imaged cross sections of SS316L samples exposed to LiCl-1wt% Li_2O for 500hr (left) and 1000hr (right).

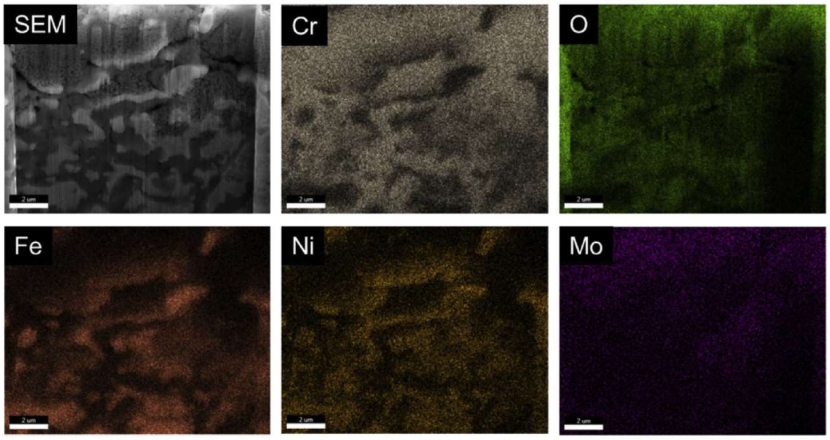

Fig. 6. EDS mapping results for the SS316L sample exposed to LiCl-1wt% Li_2O for 1000hr.

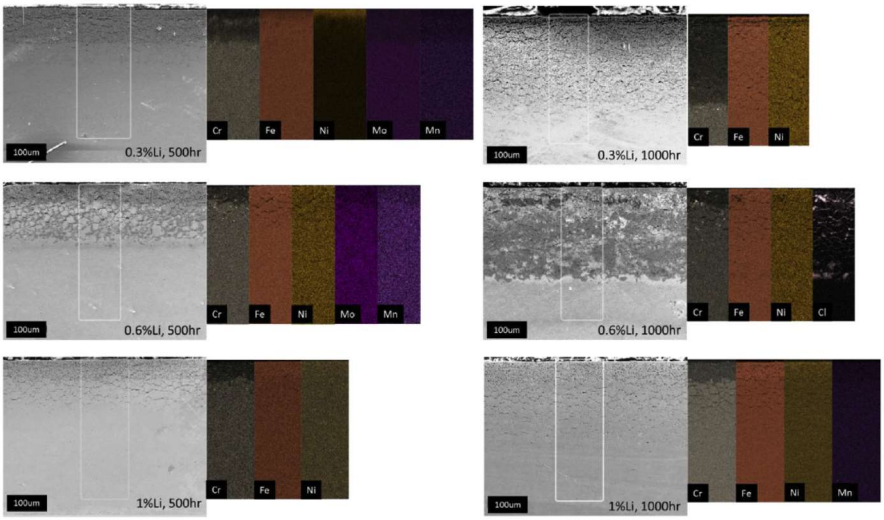

Fig. 7. Cross section SEM images and EDS maps of SS316L samples exposed to LiCl-1wt% Li_2O containing 0.3, 0.6, and 1 wt% Li for 500 and 1000hr. Areas selected for EDS mapping are delimited in SEM image. Brightness has been adjusted for clarity.

films were observed in previous studies, as well as during XPS analysis of these samples [48]. Some of these samples were observed to spontaneously form droplets of water from the cross sectioned surface when exposed to atmosphere, implying LiCl was entrapped within the sample. LiCl is extremely hygroscopic, and will absorb enough water to form a solution, even in relatively dry air, so the formation of water droplets on the cross sectioned surface is indicative of the entrapment of LiCl within the bulk sample. As most other metal chlorides are not hygroscopic to the same extent as Li, this indicates that the Cl observed in Figs. 7 and 8 is primarily in the form of LiCl.

4.3. Depth of attack analysis

Based on the depth of attack observed in Fig. 7, the penetration rate was calculated for each sample and are tabulated in Table 4. For comparison, the corrosion rates based on gravimetric analysis are presented in Table 5.

The lack of spallation of the material based on the gravimetric analysis presented below, along with the morphological changes to

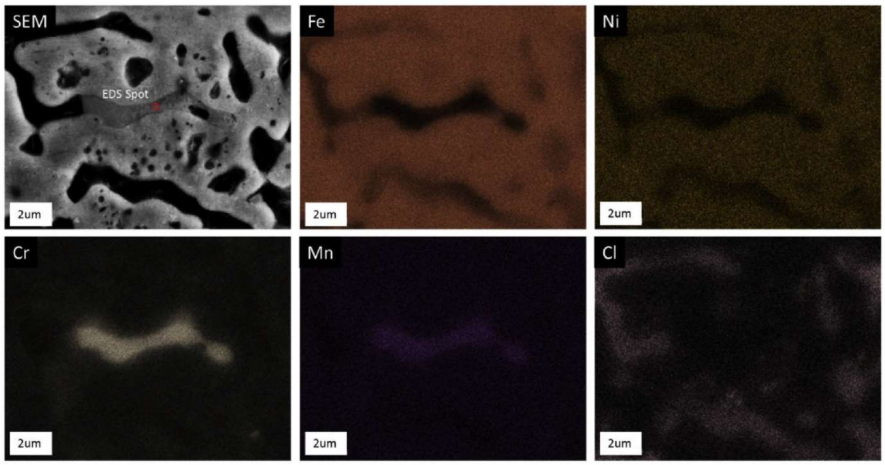

Fig. 8. Hi-magnification SEM-EDS maps of Fe, Ni, Cr, Mn, and Cl for a Cr rich region of the SS316L sample exposed to LiCl-1wt%Li_2O-0.6 wt%Li for 500hr. The red spot on the SEM image indicates the location of the spot EDS analysis summarized in Table 3. (For interpretation of the references to colour in this figure legend, the reader is referred to the Web version of this article.)

Table 3
Spot EDS analysis for the location on the SS316L sample exposed to LiCl-1wt%Li_2O-0.6%Li for 500hr shown in Fig. 8.

Element	Weight %	Atomic %	Error %
C	9.72	26.31	8.88
N	10.88	25.23	8.87
Cr	53.57	33.48	1.64
Mn	1.36	0.81	7.84
Fe	21.91	12.75	2.74
Ni	2.56	1.42	5.82

Table 4
Depth of attack observed for SS316L samples exposed to LiCl-1wt% Li_2O solutions containing 0, 0.3, 0.6, and 1 wt% Li for 500 and 1000hr, and the penetration rate based on this depth of attack.

Li Concentration in Salt (wt%)	Exposure Duration (hr)	Depth of Attack (μm)	Penetration Rate (mm $year^{-1}$)
0	500	13	0.23
0	1000	27	0.24
0.3	500	140	2.45
0.3	1000	275	2.41
0.6	500	166	2.91
0.6	1000	250	2.19
1	500	120	2.10
1	1000	225	1.97

the base material shown above indicates that simple mass loss or thickness measurements are not sufficient for assessing corrosion damage in this system. The maximum corrosion rate observed gravimetrically was for the SS316L sample exposed to LiCl-1wt% Li_2O-1wt% Li for 500hr, where the corrosion rate was 0.665 mm/year, which is well below the attack rate calculated for this sample based on the ingress of attack observed in cross sectional imaging. The high variance observed is thought to be a result of the relatively low absolute weight change per sample, which was on the order of 10s of mg for most samples, as well as ingress of salt into the material. No overall trend in gravimetric weight loss as a function of material, Li_2O concentration, Li concentration, or exposure period was observed.

Table 5
Calculated corrosion rates for SS316L samples exposed to LiCl-Li_2O-Li solutions at 650 °C for 500hr and 1000hr. Positive corrosion rates indicate weight loss, while negative corrosion rates indicate weight gain.

Wt% Li2O	Wt% Li	Exposure (hr)	Mass Loss Rate (mg cm^{-1} hr^{-1})	Corrosion Rate (mm $year^{-1}$)
1	0	500	0.000	−0.005
1	0.3	500	−0.019	0.211
1	0.6	500	−0.012	0.126
1	1	500	−0.061	0.665
2	0	500	−0.010	0.115
2	0.3	500	−0.005	0.055
2	0.6	500	−0.001	0.016
2	1	500	0.012	−0.134
1	0	1000	−0.005	0.050
1	0.3	1000	−0.006	0.062
1	0.6	1000	−0.016	0.179
1	1	1000	−0.010	0.112
2	0	1000	−0.008	0.082
2	0.3	1000	−0.012	0.130
2	0.6	1000	−0.009	0.101
2	1	1000	−0.007	0.073

4.4. X-ray diffraction

Fig. 9 shows the diffraction pattern obtained for SS316L exposed to LiCl-2wt%Li_2O-0wt%Li at 650 °C for 500hr. Peaks characteristic of $LiCrO_2$, based on PDF card number 01-072-7839, and the base material were observed [49]. No other phases were detected on the sample surface, indicating that the $NiFe_xCr_{2-x}O_4$ and Li_2CrO_4 phases predicted by Raman spectroscopy, SEM-EDS, and XPS observations presented below are minor components of the oxide layer present on samples exposed to LiCl-Li_2O solutions in the absence of Li. Similar patterns were obtained for all samples exposed to LiCl-Li_2O

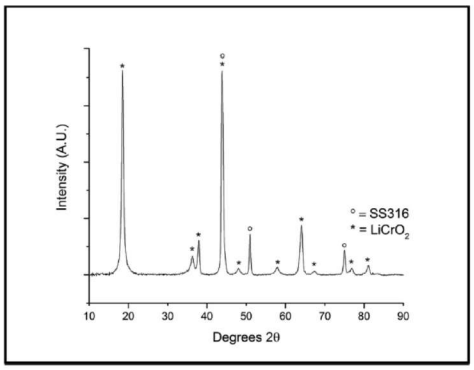

Fig. 9. GI-XRD pattern of SS316L exposed to LiCl-2%Li_2O-0%Li for 500hr after methanol rinsing. Peaks corresponding to $LiCrO_2$ and the base material were observed.

solutions in the absence of Li^0.

The XRD patterns for SS316L samples exposed to LiCl-1wt%Li_2O solutions containing 0, 0.3, 0.6, or 1 wt%Li at 650 °C for 500hr are shown in Fig. 10, while Fig. 11 shows the diffraction patterns for SS316L samples exposed to identical conditions for 1000hr.

From these figures, it can be observed that the $LiCrO_2$ surface films that form in the absence of Li are not detectable via XRD in the presence of Li, corroborating SEM-EDS as well as the Raman spectroscopy and XPS analysis presented in this work [41]. These techniques all show that the presence of Li prevents the formation of appreciable oxide surface films, resulting in severe degradation to the base material. Additionally, de-austenization of the base material was observed on the SS316L samples exposed to LiCl-1wt%Li_2O containing 0, 0.6, and 1 wt%Li for 500hr, and LiCl-1wt%Li_2O containing 0 and 0.3 wt%Li for 1000hr. This effect was also observed in short term testing of SS316L in molten LiCl-Li_2O-Li [41]. The inconsistency with which this phenomena was observed indicates

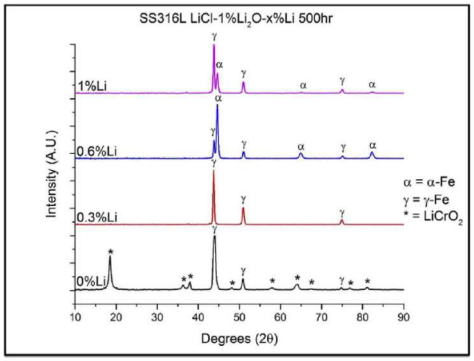

Fig. 10. High resolution grazing incidence XRD patterns for SS316L samples exposed to LiCl-1wt%Li_2O solutions containing 0, 0.3, 0.6, or 1 wt%Li at 650 °C for 500hr. The diffraction pattern for the SS316L sample exposed to LiCl-1wt%Li_2O-0wt%Li shows the peaks identified as $LiCrO_2$ in Fig. 10, above. The peaks of $LiCrO_2$ were not observed on any sample exposed to LiCl-Li_2O in the presence of Li. De-austenization of samples exposed to LiCl-1wt%Li_2O containing 0, 0.6, and 1 wt%Li for 500hr was observed.

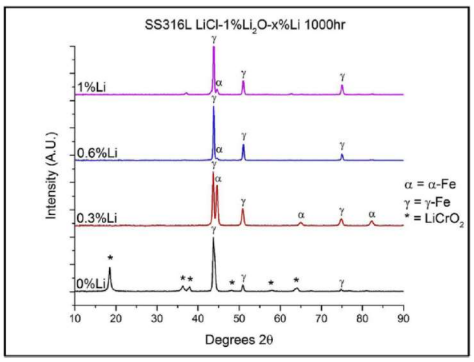

Fig. 11. High resolution grazing incidence XRD patterns for SS316L samples exposed to LiCl-1wt%Li_2O solutions containing 0, 0.3, 0.6, or 1 wt%Li at 650 °C for 1000hr. The diffraction pattern for the SS316L sample exposed to LiCl-1wt%Li_2O-0wt%Li shows the peaks identified as $LiCrO_2$ in Fig. 9, above. The extent of de-austenization of the base material varied among samples exposed to identical conditions, but otherwise the trends observed in Fig. 10 remain consistent at longer exposure periods.

that the solution chemistry does not affect the probability that a particular sample will undergo de-austenization. This is particularly highlighted by the SS316L samples exposed to LiCl-1wt%Li_2O containing 0.3, 0.6, and 1 wt%Li for 500 or 1000hr, as the samples exposed to identical solution chemistries for different exposure periods did not display similar de-austenization behavior.

The samples exposed to LiCl-2wt%Li_2O solutions containing 0, 0.3, 0.6, and 1 wt% Li displayed similar diffraction patterns as those presented here.

4.5. Raman Spectroscopy

The Raman spectrum of the SS316L sample exposed to LiCl-1wt%Li_2O-0wt%Li at 650 °C for 500hr is shown in Fig. 12. This spectrum displays peaks that were observed in various ratios on all samples exposed to LiCl-Li_2O solutions in the absence of Li and is therefore used here as representative of the samples exposed to similar

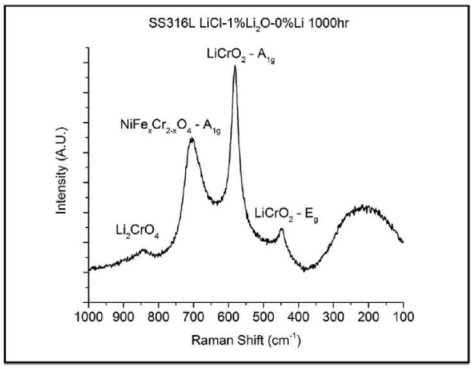

Fig. 12. Raman spectra of the SS316L sample exposed to LiCl-1wt%Li_2O in the absence of Li for 1000hr.

conditions. Both the A_{1g} mode at 572 cm^{-1} and the E_g mode at 445 cm^{-1} of $LiCrO_2$ are clearly defined [50]. Broad peaks centered at 250 cm^{-1}, 690 cm^{-1}, and 845 cm^{-1} were also observed. Based on EDS and XPS analysis shown in their respective sections, the peak at 690 cm^{-1} can be attributed to the A_{1g} mode of a mixed Ni, Fe, Cr spinel of the form $NiFe_xCr_{2-x}O_4$, although the exact composition of this oxide is not easily identified [51]. The position of this peak was also observed to shift slightly on other samples, which can likely be attributed to variations in the stoichiometry of the spinel due to differing exposure periods, melt compositions, and base materials. The peak at 845 cm^{-1} is hypothesized to originate from Li_2CrO_4, based on the presence of Cr^{6+} in the XPS spectra collected from SS316L samples exposed to LiCl-Li_2O solutions in the absence of Li. The broad feature centered around 250 cm^{-1} could not be positively attributed to any single compound, but may be caused by the combination of the minor modes of Li_2CrO_4 and minor components of the $NiFe_xCr_{2-x}O_4$ spectrum.

When exposed to LiCl-Li_2O solutions containing Li, these oxide based surface films are destabilized due to the highly reducing nature of metallic Li. To illustrate the changes to the surface layer present on samples exposed to LiCl-Li_2O solutions as a function of Li concentration, Fig. 13 shows the Raman spectra obtained from SS316L samples exposed to LiCl-1wt%Li_2O solutions containing 0, 0.3, 0.6, and 1 wt%Li at 650 °C for 500hr. The spectra collected from samples exposed to LiCl-Li_2O in the presence of Li do not display any discernible features indicative of the well-developed oxide layer observed in Fig. 12. Rather, the features observed are broad and are close to the baseline of the instrument, indicating that the oxide layer is tenuously present on these samples.

As no investigations into the Raman spectra of Li_2CrO_4 could be found in literature, the spectra of a commercially purchased Li_2CrO_4 standard was collected to confirm that the peak seen at 845 cm^{-1} in Figs. 12 and 13 could be attributed to this compound. The Raman spectrum collected from pure Li_2CrO_4 is shown in Fig. 14. The assignment of specific vibrational and rotational modes to each of the peaks observed in Fig. 14 is beyond the scope of this study. However, it can be seen that the primary features of pure Li_2CrO_4 occur between 1000 cm^{-1} and 800 cm^{-1}, with the dominant peak occurring at approximately 850 cm^{-1}. Additional minor features are present between 450 cm^{-1} and 275 cm^{-1}. As the oxide layer of the samples is non-homogenous and consists primarily of $LiCrO_2$ with small amounts of $NiFe_xCr_{2-x}O_4$ and Li_2CrO_4, the smearing of the features of the Li_2CrO_4 spectrum to form the single, broad peak centered around 850 cm^{-1} observed on the samples exposed to LiCl-Li_2O is plausible [51].

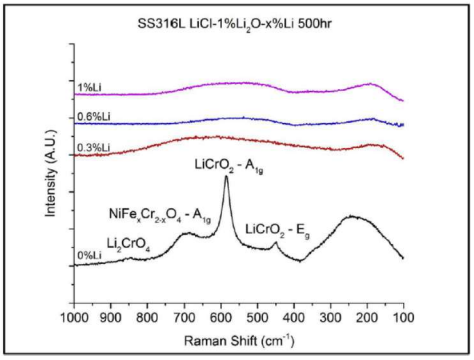

Fig. 13. Raman spectra of SS316L samples exposed to molten LiCl-1wt% Li_2O containing 0, 0.3, 0.6, and 1 wt% Li for 500 h. The distinctive peaks characteristic of $LiCrO_2$, Li_2CrO_4 and $NiFe_xCr_{2-x}O_4$ observed on samples exposed to LiCl-Li_2O in the absence of Li are seen to be eliminated by the presence of Li in the melt.

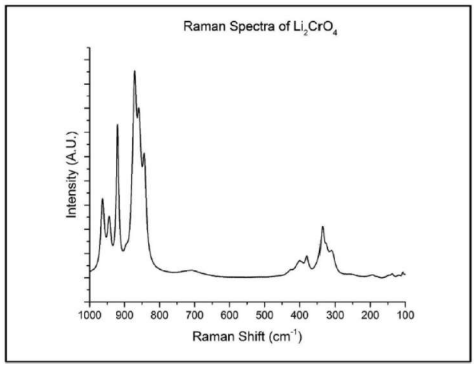

Fig. 14. Raman spectrum obtained from Li_2CrO_4. Collection parameters were identical to those used for methanol rinsed samples. The primary features of the Li_2CrO_4 spectrum occur around 850 cm^{-1}, with minor features in the range of 450 cm^{-1} to 300 cm^{-1}.

4.6. X-ray photoelectron spectroscopy

XPS survey scans of the SS316L samples exposed to LiCl-1wt% Li_2O containing 0, 0.3, 0.6, and 1 wt% Li at 650 °C for 1000hr are shown in Fig. 15. For the SS316L sample exposed to LiCl-1wt%Li_2O at 650 °C for 1000hr in the absence of Li, the surface is primarily composed of Cr and O, with Ni and Fe detectable in small quantities. For the SS316L samples exposed to LiCl-1wt%Li_2O containing 0.6 and 1 wt% Li at 650 °C for 1000hr, the surface shows a relatively thick Ti-based surface deposit, with high quantities of N and O present. In the case of the SS316L sample exposed to LiCl-1wt%Li_2O-0.6 wt%Li for 1000hr, this Ti surface film was sufficiently thick to prevent the analysis of the underlying base material. TiO_2 is a common impurity in Li_2O, and the deposition of Ti based

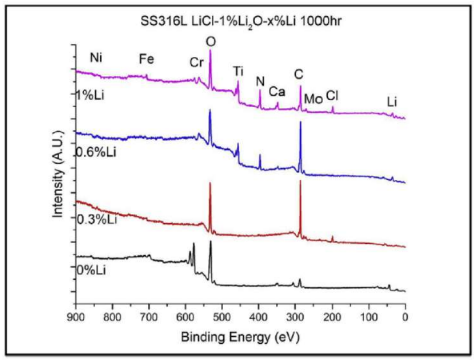

Fig. 15. XPS survey spectra recorded on SS316L samples exposed to LiCl-1wt%Li_2O containing 0, 0.3, 0.6, and 1 wt%Li at 650 °C for 1000hr after rinsing in methanol.

compounds on samples exposed to LiCl-Li_2O in the presence of Li was extensively studied during our previous short term studies [48].

Analysis of the alloying elements, especially the Cr 2p spectra, is necessary to determine the corrosion mechanisms of SS316L in LiCl-Li_2O-Li, as Cr is the primary element responsible for the formation of oxide films in the absence of Li. Identification of the oxidation state of Cr present on the surface of the SS316L sample exposed to LiCl-1wt%Li_2O-Li at 650 °C for 500hr was performed by peak fitting the Cr $2p_{3/2}$ spectra using previously published peak fitting parameters [52]. The peak fit data for all Cr spectra collected on the samples in this study are shown in Fig. 16, while the peak fitting parameters are given in Table 6 [52].

As can be observed in Fig. 16, both Cr^{3+} and Cr^{6+} are simultaneously present on all SS316L samples exposed to LiCl-Li_2O solutions in the absence of Li^0. The presence of Cr^{3+} and Cr^{6+} on the samples further supports the presence of both $LiCrO_2$ (Cr^{3+}) and Li_2CrO_4 (Cr^{6+}) on the surfaces of samples exposed to LiCl-Li_2O solutions in the absence of Li. In the presence of Li, the highly reducing nature of metallic Li destabilizes the oxide films that are present on the sample surfaces in the absence of Li. However, the transition between electrochemical oxidation of the samples in the absence of Li and liquid metal attack in the presence of high Li concentrations is not abrupt. Our previous short term studies have shown that at concentrations at or below the apparent solubility limit of Li in the system (around 0.3 wt%Li) [24], there exists a transition region where both modes of attack occur simultaneously [41,42]. The Cr $2p_{3/2}$ spectra shown in Fig. 16 give further evidence for this hypothesis, although there was no discernible trend in the relative ratios of Cr^0, Cr^{3+}, and Cr^{6+} based on the concentration of Li, Li_2O, or exposure period.

The presence of Cr^{3+} is also required for the formation of $NiFe_xCr_{2-x}O_4$, as both Fe and Cr are in the 3 + oxidation state in this compound, while Ni is present in the 2 + oxidation state. Further confirmation of the presence of $NiFe_xCr_{2-x}O_4$ is given by the narrow scans of the Ni 2p and Fe 2p spectra for SS316L exposed to LiCl-1wt%Li_2O-0wt%Li for 500hr, which are shown in Fig. 17, along with the Ni 2p and Fe 2p narrow scans for the SS316L sample exposed to LiCl-1wt%Li_2O-0.3 wt%Li for 500hr. In the absence of Li, the Ni $2p_{3/2}$ peak is located at 853.5eV, while the Fe $2p_{3/2}$ peak is located at 710.1eV. These binding energies and peak shapes correspond to Ni^{2+} and Fe^{3+}, respectively [53]. Neither element was detected in the metallic state, confirming the presence of Ni and Fe based oxides on the sample surface. In conjunction with Raman spectroscopy and EDS analysis, this is further evidence supporting the presence of a $NiFe_xCr_{2-x}O_4$ based spinel present on the surface of

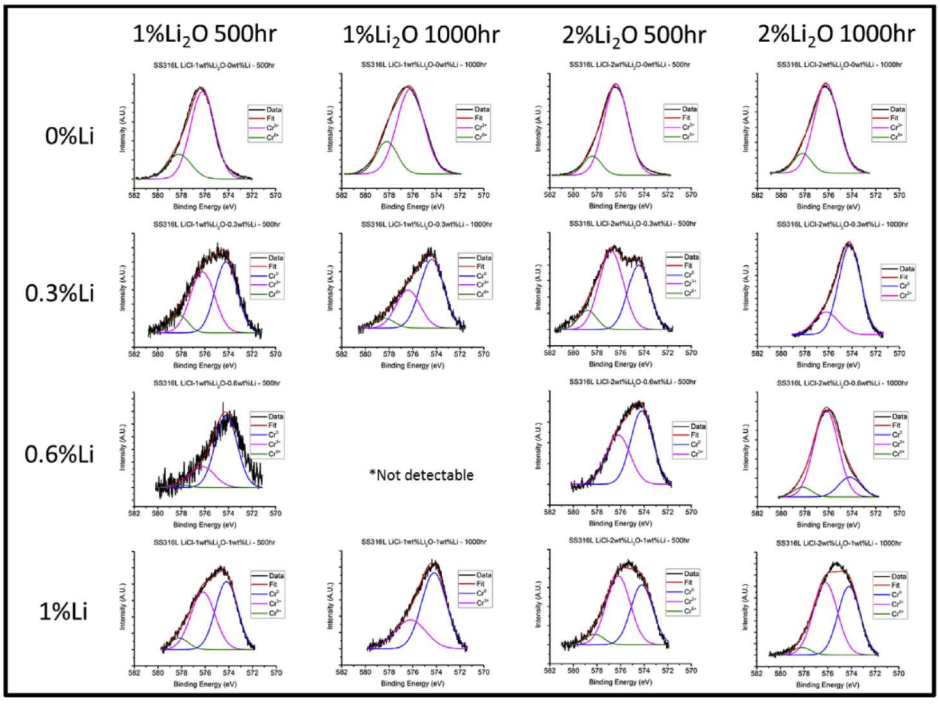

Fig. 16. Cr 2p XPS spectra collected from SS316L samples exposed to all LiCl-Li_2O-Li compositions and exposure periods studied in this work. Charge correction was performed to the adventitious C 1s peak at 284.8eV, and peak fitting parameters for Cr^0, Cr^{3+}, and Cr^{6+} listed in Table 2 were used for all spectra. Cr^{3+} and Cr^{6+} are the only species present in the absence of Li. Cr spectra of SS316L samples exposed to molten LiCl-Li_2O in the presence of Li indicate both metallic and oxidized components; however, no discernible trend in oxidation state based on Li concentration, Li_2O concentration or exposure period could be determined. Cr was not detectable on the SS316L sample exposed to LiCl-1wt% Li_2O-0.6 wt%Li for 1000hr due to the thickness of the overlying Tl surface deposit.

Table 6
Peak fitting parameters used for Cr $2p_{3/2}$ spectra reported in Fig. 9 [52].

Peak	BE	FWHM
Cr^0	574.2	2.2
Cr^{3+}	576.2	2.4
Cr^{6+}	578.2	1.8

the samples exposed to LiCl-Li_2O in the absence of Li. However, when Li was present in the molten salt, only metallically bonded Ni and Fe are present on the sample surface. No charge correction was necessary for the Ni and Fe 2p spectra, indicating that these elements were in direct electrical contact with the base material. Similar spectra were recorded for all other SS316L samples exposed to LiCl-Li_2O-Li, indicating that any quantity of Li^0 in the melt is sufficient to reduce $NiFe_xCr_{2-x}O_4$.

In our previous work, Mo was observed to behave similarly to Cr in some respects, becoming enriched on the surface in the absence of Li, and depleted at higher Li concentrations. As Mo is a minor alloying element of SS316L at around 2 wt%, Mo was not observed on all samples. Additionally, in the absence of Li, Mo was not detectable via XPS on any sample due to the thick $LiCrO_2$ surface layer. However, the samples exposed to molten LiCl-2wt%Li_2O solutions containing 0.3, 0.6, and 1 wt%Li for 500hr all had detectable levels of Mo, the narrow scans of which are presented in Fig. 18. From the spectra in Fig. 18, it can be observed that when 0.3 wt% Li is present in solution, Mo^{6+} is the only Mo species observable on the sample surface [54]. However, as Li concentration increases the stability of oxidized Mo is decreased, resulting in a mixed Mo^{6+}/Mo^0 spectra at 0.6 wt% Li and a fully metallic Mo^0 spectra at 1 wt% Li [54,55]. The observation of Mo^{6+} on samples exposed to high concentrations of Li indicates that Mo is highly active in the LiCl-Li_2O-Li system, which could explain the depletion of Mo from the surface of SS316L observed via SEM-EDS analysis of the cross section of these samples in section 4.2.

Co was also observed on some samples exposed to LiCl-Li_2O in the presence of Li. Co is not an alloying element of SS316L, but is present as the primary impurity in the Ni crucibles used for these studies at concentrations of less than 1 wt%. Consequently, the presence of Co on the surface of the samples exposed to LiCl-Li_2O solutions in the presence of Li indicates that there is mass transport from the crucible to the samples. Mass transport of Co from the crucible to the samples had not been observed in our previous short term experiments [41,42,44]. The Co 2p spectra of the SS316L sample exposed to LiCl-1wt%Li_2O-0.3 wt%Li for 500hr is presented in Fig. 19, and is typical of Co^{3+}, due to its binding energy and peak shape [53]. The cause of the transport of Co from the crucible to the samples and its implications to the degradation of materials in the LiCl-Li_2O-Li system as a whole requires further investigation.

5. Conclusions

Exposure testing of SS316L samples was performed for 500 and 1000hr intervals in molten LiCl-Li_2O-Li solutions containing 1 and 2 wt% Li_2O and 0, 0.3, 0.6, and 1 wt% Li. Morphological and elemental changes to the sample surfaces and cross sections were

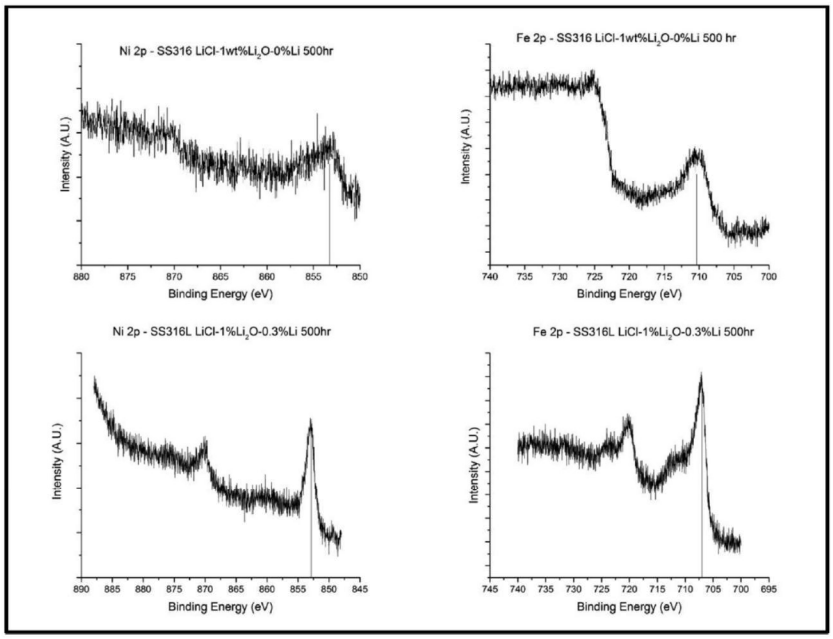

Fig. 17. XPS narrow scans for Ni 2p (left) and Fe 2p (right) collected from SS316L exposed to LiCl-1%Li_2O-0%Li (Top) and LiCl-1wt%Li_2O-0.3 wt%Li (Bottom) at 650 °C for 500hr. In the absence of Li, Ni is present in the 2 + oxidation state and Fe is present in the 3 + oxidation state based on their binding energies of 853.5eV and 710.1eV, respectively. However, in the presence of Li, all Ni and Fe spectra indicate the presence only of metallic Ni and Fe.

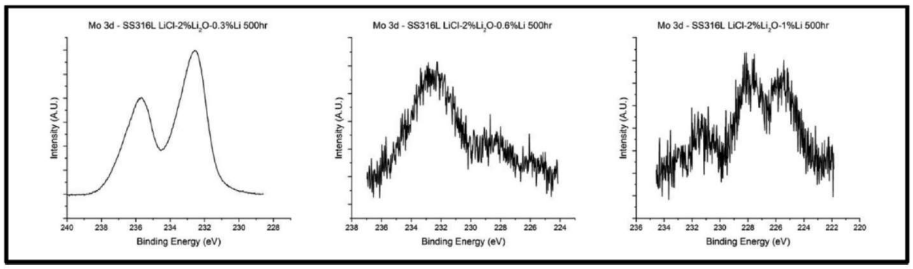

Fig. 18. Mo 3d XPS spectra of SS316L samples exposed to molten LiCl-2wt%Li_2O solutions containing 0.3, 0.6, and 1 wt%Li for 500hr. As Li concentration in the melt is increased, the Mo oxidation state shifts towards more reduced species. The peak shape for the SS316L sample exposed to LiCl-2wt%Li_2O-1wt%Li for 500hr is likely the result of differential charging and the charge correction performed to the adventitious C 1S peak at 284.8eV.

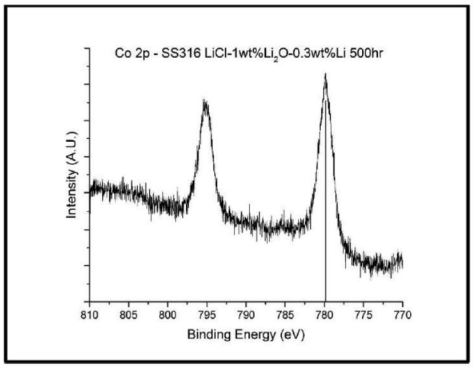

Fig. 19. XPS narrow scan of the Co 2p peak observed on SS316L exposed to LiCl-1wt% Li_2O-0.3 wt%Li at 650 °C for 500hr and rinsed with methanol. The binding energy and shape of the $2p_{3/2}$ peak of 789.8eV is consistent with the presence of Co^{3+} [56].

investigated via SEM and EDS, respectively, while XRD, Raman spectroscopy, and XPS were used to provide further insight into the effect of Li^0 on the degradation mechanisms of materials in LiCl-Li_2O-Li. Upon exposure to LiCl-Li_2O solutions in the absence of Li, SS316L was observed to form a $LiCrO_2$ based surface film, with minor contributions of Li_2CrO_4 and $NiFe_xCr_{2-x}O_4$. The oxide layer limited corrosion to a rate of approximately 0.24 mm/year during exposure to molten LiCl-Li_2O solutions. The presence of Li in the melt resulted in the destabilization of the protective oxide film formed in LiCl-Li_2O solutions, causing substantial damage to the samples in the form of intergranular corrosion. XPS analysis observed that metallically bonded Ni and Fe were present on the surface of all SS316L samples exposed to LiCl-Li_2O in the presence of Li, however both Cr and Mo displayed varying degrees of oxidation in the presence of Li. Mass loss rates were low, but cross sectioned samples displayed significant ingress of LiCl and damage to the sample surface, indicating that mass loss measurements alone are not sufficient to characterize corrosion in this system. Intergranular corrosion was facilitated by the precipitation of metal carbides and nitrides along the grain boundaries, resulting in the selective depletion of alloying elements, such as Cr, Mo, and Mn. The rate of material damage was on the order of 2–3 mm/year, indicating that the presence of high concentrations of Li during the electrolytic reduction of UNF will dramatically reduce the lifetime of any SS316L components exposed to the electrolyte. The ingress of intergranular corrosion into the material will likely have a marked effect on the strength of the material due to the effective loss of structural thickness, however, further investigation would be necessary to validate this hypothesis. From the combination of analytical techniques presented in this work, it is hypothesized that cyclical oxidation by O^{2-} ions and reduction by Li^0 is responsible for the high levels of material degradation in the LiCl-Li_2O-Li system.

Data availability

The raw/processed data required to reproduce these findings cannot be shared at this time as the data also forms part of an ongoing study.

Acknowledgements

The authors gratefully thank Zachary Karmiol, Research Scientist at Materials Characterization Nevada, for analyses of the cross sectioned samples.

This work was performed under the auspices of the Department of Energy (DOE), United States under contracts DE-NE0008262 and DE-NE0008236, and the US Nuclear Regulatory Commission (USNRC), United States under contracts NRCHQ-11-G-38-0039 and NRC-HQ-13-G-38-0027. W.P. acknowledges the Fellowship Award from the USNRC. Dr. Kenny Osborne serves as the program manager for the DOE award and Ms. Nancy Hebron-Isreal serves as the grants program officer for the NRC awards.

Appendix A. Supplementary data

Supplementary data to this article can be found online at https://doi.org/10.1016/j.jnucmat.2019.02.007.

References

[1] K. Gourishankar, L. Redey, M. Williamson, Electrolytic reduction of metal oxides in molten salts, in: W.A. Schneider (Ed.), Light Metals, the Minerals, Metals & Materials Society, 2002.
[2] S.D. Herrmann, S.X. Li, M.F. Simpson, Electrolytic Reduction of Spent Oxide Fuel - Bench-Scale Test Results, GLOBAL 2005, Tsukuba, Japan, 2005.
[3] H. Lee, G.-I. Park, K.-H. Kang, J.-M. Hur, J.-G. Kim, D.-H. Ahn, Y.-Z. Cho, E.H. Kim, Nucl. Eng. Technol. 43 (2011) 317–328.
[4] M. Kurata, T. Inoue, J. Serp, M. Ougier, J.P. Glatz, J. Nucl. Mater. 328 (2004) 97–102.
[5] S.D. Herrmann, S.X. Li, M.F. Simpson, S. Phongikaroon, Separ. Sci. Technol. 41 (2006) 1965–1983.
[6] M. Iizuka, Y. Sakamura, T. Inoue, J. Nucl. Mater. 359 (2006) 102–113.
[7] B. Park, S. Park, S. Jeong, C. Seo, J. Radioanal. Nucl. Chem. 270 (2006) 575–583.

[8] C.S. Seo, S.B. Park, B.H. Park, K.J. Jung, S.W. Park, S.H. Kim, J. Nucl. Sci. Technol. 43 (2006) 587–595.
[9] S. Jeong, J. Hur, S. Hong, D. Kang, M. Choung, X. Seo, J. Yoon, S. Park, Nucl. Technol. 162 (2007) 184–191.
[10] B.H. Park, I.W. Lee, C.S. Seo, Chem. Eng. Sci. 63 (2008) 3485–3492.
[11] S. Herrmann, S. Li, B. Serrano-Rodriguez, Observations of Oxygen Ion Behavior in the Lithium-Based Electrolytic Reduction of Uranium Oxide, GLOBAL 2009, Idaho National Labs, Paris, France, 2009, pp. 1198–1206.
[12] S. Herrmann, S. Li, D. Sell, B. Westphal, Electrolytic Reduction of Spent Nuclear Oxide Fuel – Effects of Fuel Form and Cathode Containment Materials on Bench-Scale Operations, Idaho National Laboratory, 2007.
[13] S.X. Li, M.F. Simpson, S.D. Hermann, Oxygen ion oxidation process on a platinum electrode in LiCl-Li2O at 650C, in: R.A. Mantz (Ed.), Electrochemical Society Proceedings, vol. 24, 2004.
[14] A. Merwin, D. Chidambaram, Metall. Mater. Trans. 46 (2015) 536–544.
[15] T. Usami, T. Kato, M. Kurata, T. Inoue, H.E. Sims, S.A. Beetham, J.A. Jenkins, J. Nucl. Mater. 304 (2002) 50–55.
[16] A. Merwin, M.A. Williamson, J.L. Willit, D. Chidambaram, J. Electrochem. Soc. 164 (2017) H5236–H5246.
[17] W. Park, J.-M. Hur, S.-S. Hong, E.-Y. Choi, H.S. Im, S.-C. Oh, J.-W. Lee, J. Nucl. Mater. 441 (2013) 232–239.
[18] A.S. Dworkin, H.R. Bronstein, M.A. Bredig, J. Phys. Chem. 66 (1962) 572–573.
[19] T. Nakajima, R. Minami, K. Nakanishi, N. Watanabe, Bull. Chem. Soc. Jpn. 47 (1974) 2071–2072.
[20] T. Nakajima, K. Nakanishi, N. Watanabe, Nippon Kagaku Kaishi 1975 (1975) 617–621.
[21] T. Nakajima, K. Nakanishi, N. Watanabe, Bull. Chem. Soc. Jpn. 49 (1975) 994–997.
[22] J. Liu, J.C. Poignet, J. Appl. Electrochem. 20 (1990) 864–867.
[23] T. Usami, M. Kurata, T. Inoue, H.E. Sims, S.A. Beetham, J.A. Jenkins, J. Nucl. Mater. 300 (2002) 15–26.
[24] T.N. Nakajima, N. Watanabe, Nippon Kagaku Kaishi 1974 (1974) 401–404.
[25] M.A. Bredig, in: M. Blander (Ed.), Molten Salt Chemistry, John Wiley and Sons, 1964, pp. 367–425, 1964.
[26] A. Merwin, W.C. Phillips, M.A. Williamson, J.L. Willit, P.N. Motsegood, D. Chidambaram, Sci. Rep. 6 (2016) 25435.
[27] S.H. Cho, J.S. Zhang, Y.J. Shin, S.W. Park, H.S. Park, J. Nucl. Mater. 325 (2004) 13–17.
[28] R.Y. Liu, X. Wang, J.S. Zhang, X.M. Wang, J. Nucl. Mater. 327 (2004) 194–201.
[29] C. Soo-Haeng, L. Jong-Ho, P. Sung-Bin, J. Ki-Jung, P. Seong-Won, J. Kor. Inst. Met. Mater. 43 (2005) 449–454.
[30] Q. Gao, R.Y. Liu, J.S. Zhang, J.T. Guo, Mater. Lett. 59 (2005) 2052–2058.
[31] S.H. Cho, S.B. Park, J.H. Lee, J.M. Hur, H.S. Lee, Mater. Chem. Phys. 131 (2012) 743–751.
[32] C. Soo-Haeng, P. Seong-Bin, L. Jong-Hyeon, H. Jin-Mok, L. Han-Soo, Oxid. Metals 78 (2012) 153–165.
[33] P. SangKyu, L. TaeHyuk, S. MoonSoo, N. JaeSoo, C. SooHaeng, L. JongHyeon, Adv. Mater. Res. 886 (2014) 41–44.
[34] H.-Y. Lee, K.-H. Baik, Met. Mater. Int. 15 (2009) 783–787.
[35] T.R. Allen, K. Sridharan, Corrosion in molten salts, in: Molten Salts Chemistry from Lab to Applications, Elsevier, Burlington, MA, 2013.
[36] Y.S. Zhang, J. Electrochem. Soc. 133 (1986) 655.
[37] J.E. Indacochea, J.L. Smith, K.R. Litko, E.J. Karell, J. Mater. Res. 14 (1999) 1990–1995. M1993 - 1910.1557/JMR.1999.0268.
[38] J.E. Indacochea, J.L. Smith, K.R. Litko, E.J. Karell, A.G. Raraz, Oxid. Metals 55 (1999) 1–16.
[39] B. Mishra, D.L. Olson, Miner. Process. Extr. Metall. Rev. 22 (2001) 369–388.
[40] S.H. Cho, S.B. Park, J.H. Lee, J.M. Hur, H.S. Lee, J. Nucl. Mater. 412 (2011) 157–164.
[41] A. Merwin, D. Chidambaram, Corros. Sci. 126 (2016) 1–9.
[42] A. Merwin, D. Chidambaram, Nucl. Technol. 195 (2016) 204–212.
[43] E.-Y. Choi, J. Lee, J. Nucl. Mater. 495 (2017) 85–90.
[44] W. Phillips, A. Merwin, D. Chidambaram, Metall. Mater. Trans. 49 (2018) 2384–2392.
[45] N.J. Gese, The Electrochemistry of Li-LiCl-Li2O Molten Salt Systems and the Role of Moisture, Nuclear Engineering, University of Idaho, 2015.
[46] D.A. Jones, Principles and Prevention of Corrosion, Prentice Hall, Upper Saddle River, NJ, 1996.
[47] J.E. Indacochea, J.L. Smith, K.R. Litko, E.J. Karell, A.G. Rarez, Oxid. Metals 55 (2001) 1–16.
[48] A. Merwin, Material Interactions with Molten LiCl-Li_2O-Li, Materials Science and Engineering, Vol Doctor of Philosophy in Materials Science and Engineering, University of Nevada, Reno, 2016, p. 241.
[49] PDF Card No. : 01-072-7839, The International Centre for Diffraction Data.
[50] M. Suzuki, I. Yamada, H. Kadowaki, F. Takei, J. Phys. Condens. Matter 5 (1993) 4225–4232.
[51] B.D. Hosterman, Raman Spectroscopic Study of Solid Solution Spinel Oxides, Physics and Astronomy, Vol Doctor of Philosophy in Physics, UNLV, 2011, p. 155.
[52] D. Chidambaram, C.R. Clayton, G.P. Halada, J. Electrochem. Soc. 150 (2003) B224–B237.
[53] M.C. Biesinger, B.P. Payne, A.P. Grosvenor, L.W.M. Lau, A.R. Gerson, R.S.C. Smart, Appl. Surf. Sci. 257 (2011) 2717–2730.
[54] B. Brox, I. Olefjord, Surf. Interface Anal. 13 (1988) 3–6.
[55] J. Baltrusaitis, B. Mendoza-Sanchez, V. Fernandez, R. Veenstra, N. Dukstiene, A. Roberts, N. Fairley, Appl. Surf. Sci. 326 (2015) 151–161.
[56] M.C. Biesinger, B.P. Payne, A.P. Grosvenor, L.W.M. Lau, A.R. Gerson, R.S.C. Smart, Appl. Surf. Sci. 257 (2011) 2717–2730.

A7.2: Effect of Metallic Li on the Corrosion of Behavior of Inconel 625 in Molten LiCl-Li_2O-Li

C162 *Journal of The Electrochemical Society*, **166** (6) C162-C168 (2019)

Effect of Metallic Li on the Corrosion Behavior of Inconel 625 in Molten LiCl-Li_2O-Li

William Phillips,[1,*] Zachary Karmiol,[1,2,*] and Dev Chidambaram [1,3,,z]**

[1] *Materials Science and Engineering, University of Nevada, Reno, Nevada 89557-0388, USA*
[2] *University of Nevada, Reno Electron Microscopy and Microanalysis Facility, Reno, Nevada, USA*
[3] *Nevada Institute For Sustainability, Reno, Nevada 89557-0388, USA*

The corrosion behavior of Inconel 625 in molten LiCl solutions maintained at 650°C and containing various quantities of Li_2O and metallic Li was studied for possible application in the electroreduction of used oxide-based nuclear fuel. This study focusses on the morphological and elemental changes on the surface of the samples with an emphasis on cross-sectional analyses conducted using focused ion beam microscopy. In the absence of metallic Li, a stable oxide film is formed that limits the corrosion of the base material to 0.07mm/year. However, in the presence of metallic Li, the formation of this film is impeded, resulting in dealloying of the base material and the formation of a highly porous microstructure composed primarily of Ni.

 [DOI: 10.1149/2.0201906jes]

Manuscript submitted January 31, 2019; revised manuscript received March 7, 2019. Published April 3, 2019.

In order to reprocess used nuclear fuel (UNF) from light water reactors using pyrometallurgical techniques, a reduction operation is necessary to convert UO_2-based UNF into a metallic product that can then be processed in subsequent unit operations.[1–5] The prototypical process by which the reduction of UO_2 is conducted is via the electrolytic reduction operation developed at Argonne National Laboratory (ANL).[2,6] In this process, LiCl containing 1 to 2wt% Li_2O and maintained at 650°C serves as the electrolyte.[7,8] The reduction is performed with UNF loaded in a stainless steel cathode basket which is polarized vs. a suitable anode, typically made of Pt, either galvanostatically or potentiostatically.[3,9] To achieve high reduction yields, it has been shown by a number of researchers that it is necessary to polarize UO_2 at potentials beyond the electrochemical window of Li_2O, which results in the formation of metallic Li at the cathode.[3,9,10] Some of the metallic Li thus generated then metalothermically reduces the UNF in the cathode; however, LiCl is capable of solvating Li to a limited degree, which leads to the formation of a tertiary LiCl-Li_2O-Li electrolyte.[3,9,10] As the process goes to completion, the electrolyte eventually reaches Li saturated conditions, and may even form and be present as clusters.[11]

The dissolution of alkali metals in their respective alkali halides has been well studied over the last century, notably by M.A. Bredig at Oak Ridge National Laboratory, among others.[12–14] The two primary models of alkali metal – alkali halide systems are the f- center model and the sub-halide model.[13] In the f- center model typical for alkali metal – alkali halide systems, the excess electron is delocalized from any particular cation core, leaving a free electron that imparts a metallic character to the molten solution.[13] This leads to several orders of magnitude increase in electrical conductivity of solution as the concentration of the alkali metal increases toward saturation, as well as causing a number of other changes in physical and chemical properties. The sub-halide model is typically representative of transition metals and post-transition metals in their respective halides and gives rise to the formation of abnormally reduced species due to the formation of complex molecules that keep electrons localized to the molecular scale, as is typical for the Bi-$BiCl_3$ system.[13] Sub-halide forming systems are not associated with an increase in electrical conductivity in the same manner as the f- center model predicts. Other dissolution mechanisms have also been reported, such as the formation of colloidal suspensions of nanoclusters of Na_2 or Li_8 in the Na-NaCl and Li-LiCl systems, respectively.[11,13] It is important to note that none of these effects are mutually exclusive, and it is possible that the simultaneous action of multiple dissolution mechanisms may occur simultaneously in the same system. Of the alkali metal – alkali halide systems, the Li-LiCl system has proven to be particularly challenging in the determination of the solubility limit of the metal in the metal salt, with the apparent solubility limit seeming to vary depending on the experimental methods; however, approximately 0.3wt% has been shown to be a useful estimate at the temperatures of the electrolytic reduction operation.[12,13,15–19] Importantly, the concentration of Li_2O has been shown to have minimal effect on the measured solubility limit of Li in LiCl-Li_2O.[19] The discrepancy between the various reported values of the solubility limit of Li in LiCl may be due to the simultaneous action of the various dissolution mechanisms theorized for this system.[11]

For the electrolytic reduction of UNF to be implemented on a large scale, knowledge of the degradation of materials in contact with the electrolyte is necessary, particularly for the container material. Corrosion in molten LiCl-Li_2O under inert or oxidizing atmospheres has been fairly well studied, and the corrosion of various materials has been found to follow similar mechanisms to those observed in other molten salt systems.[20–26] Primarily, the dissolution of alloying elements, and consequently the corrosion rate, is governed primarily by the activity of the O^{2-} ion in the solution according to the Lux-Flood model of salt basicity, as well as by the presence of impurities such as moisture or transition metal halides.[20,27,28] For the electroreduction process, such models are insufficient to completely describe corrosion due to the presence of dissolved Li. To date, very few investigations into the effects of Li on the corrosion of materials exposed to this system have been performed.[29–34] The initial studies conducted by Indocochea, et al. conflicted with studies conducted by Mishra and Olson due to widely varying experimental parameters, leading to confusion about the effect Li had on the degradation observed.[29,30] Recent studies have been performed to address these issues, but were of short term in nature and did not investigate the degradation of the materials studied in cross section.[31–33] These studies showed that a transition from molten salt based corrosion to a liquid metal attack induced degradation occurred at approximately 0.6wt%Li, and that the concentration of both Li and Li_2O affected the corrosion processes that were observed. Recent work by researchers at the Korean Atomic Energy Research Institute showed that Ni displayed minimal corrosion in the absence of Li, but underwent significant degradation in the presence of metallic Li.[34] In this light, the current study investigates the corrosion behavior of Inconel 625 (I625) in the LiCl-Li_2O-Li system at 650°C. To understand the effect of oxide concentration, metal concentration and the period of exposure, the solution chemistries studied consisted of LiCl containing 1 or 2wt% Li_2O and 0, 0.3, 0.6, or 1wt% Li, with samples exposure periods of 500 and 1000hr. This study focusses on the

*Electrochemical Society Student Member.
**Electrochemical Society Member.
[z]E-mail: dcc@unr.edu

observed degradation of I625 under these conditions by determining the changes to the microstructure and elemental composition using scanning electron microscopy (SEM) coupled with energy dispersive X-ray spectroscopy (EDS) of the sample surfaces as well as their cross sections.

Experimental

Experiments were conducted in a Vacuum Atmospheres OMNI-LAB glove box under Ar containing less than 2ppm O_2 and less than 1ppm H_2O. Anhydrous LiCl, Li_2O, and Ni crucibles were obtained from Alfa-Aesar and were of 99%, 99.5%, and 99% purity, respectively. Li metal of 99% purity was purchased from Strem Chemicals. I625 coupons were cut from a 3.175mm thick plate obtained from High Performance Alloys. The composition of this alloy as measured via the EDS used for cross sectional investigation was 62.3wt% Ni 23.5wt% Cr, 6.5wt% Mo, 5.1% Fe, and 2.6wt% Nb.

Studies were conducted using duplicate samples, and 500 hour and 1000 hour exposures were conducted in parallel, with the 500 hour samples removed from the experiment upon completion of the allotted exposure period. A 6.5 inch inner diameter, 6 inch tall cylindrical heater from Watlow (1500 watts) was used to maintain a temperature of 650 ± 5°C for the duration of the exposure period. A 6 inch diameter graphite block was machined to accommodate 5 Ni crucibles, with slots machined to accommodate the sample hanging rods. This configuration allowed for repeatable placement of the samples within the melt during the salt replacement procedure outlined below. Two identical furnaces were constructed to maximize the number of experiments that could be ran in parallel. In operation, four experiments were ran simultaneously in each furnace, which allowed for the extra 5th crucible location to be used for salt replacement purposes.

Prior to exposure, the metal samples were cut into 1.27cm by 1.27cm squares using a CO_2 laser. The samples were then polished to a 1 μm surface finish on both sides using a diamond abrasive and spot welded to loops of SS316L wire for suspension from the sample hanging rods, as was performed in our previous studies.[31–33] Sample hanging rods were made of like material to the samples, as alumina rods proved to be incapable of withstanding the highly reducing atmosphere directly over the molten solutions containing metallic Li for the duration of these experiments. The mass of each sample was recorded immediately prior to exposure.

Considering the evaporation of Li and Li_2O over time that was observed in other short-term studies and the extended exposure periods of this study, the salt charge for each test was replaced at a period of once every 96 hours to maintain the solution chemistry.[31–33,35,36] To minimize the effects of impurity H_2O, LiCl was dried in a vacuum oven in air at 200°C for 24 hours before being transferred into the glove box for storage.[31,37] Immediately prior to insertion in the primary furnace, a cleaned Ni crucible containing the weighed amount of LiCl was dried under Ar for 2hr in a dedicated furnace maintained at 550°C. After insertion into the primary furnace, the LiCl was allowed 1 hour to reach thermal equilibrium, after which time the required mass of Li_2O and Li were added to the molten salt by placing the Li_2O powder and Li pellets on top of the solution. Total salt mass contained in each crucible was 50g. The melt was allowed to equilibrate for another hour prior to the transfer of the corrosion specimens from the old salt charge to the new salt charge. As the concentration of Li was above the solubility limit for the 0.6 and 1wt% tests, a significant fraction was likely present as a colloidal suspension. Sample transfer was accomplished via specially fabricated tongs, which allowed for the transfer time to be less than 5 seconds on average. Following transfer of the samples to the new salt charge, the old salt charge was removed from the furnace and allowed to cool to room temperature. The cooled salt ingot was then dissolved in deionized (DI) water. The Ni crucible was then sanded with 600 grit SiC paper, rinsed with DI water, cleaned with isopropyl alcohol, and dried under vacuum prior to re-use for the next salt charge for the same solution chemistry conditions. Two Ni crucibles were alternated between for each solution chemistry.

Following completion of the exposure period, the samples were removed from the furnace and allowed to cool to room temperature in the glove box atmosphere. All samples were stored in the Ar glove box between analytical procedures. As it was unknown if the surface films formed on the corrosion specimens would be stable in atmosphere, surface analysis was performed both prior to and following removal of the residual salt layer. Following the initial surface analytical procedures, residual LiCl was removed by placing each sample in 25ml of HPLC grade methanol for 15 minutes with constant agitation. Prior to the methanol rinsing procedure, all surface analysis was performed under inert atmosphere or vacuum conditions, depending on technique. The data presented here were collected following the methanol rinsing procedure, as the residual salt layer significantly interfered with surface analysis as has been described earlier.[31] No chemical or morphological changes were observed as a result of the methanol rinsing procedure. Gravimetric weight change measurements were performed following the methanol rinsing procedure.

All samples exposed to Li containing melts were cross sectioned using a Buehler cubic-BN wafering blade on a slow speed saw and polished according to Buehler's recommended polishing techniques to a 0.05μm surface finish prior to analysis. Samples exposed to LiCl-Li_2O in the absence of Li were investigated using only FIB milling for cross sectional analysis due to the relatively shallow depth of attack.

SEM of the sample surfaces was performed using a Hitachi S-4700 and EDS data was collected via the attached Oxford Instruments energy dispersive X-ray spectrometer. The electron beam was operated at an accelerating voltage of 5kV for surface morphology images, while 20kV was used for collection of EDS spectra. Emission current was maintained at 10mA. FIB milling and subsequent SEM-EDS analysis for cross sectional images was performed using a FEI Scios dual-beam FIB/SEM equipped with a TEAM Pegasus Integrated EDS-EBSD. The same dual-beam FIB/SEM was used to perform the SEM-EDS analysis of all of the cross sectioned samples, including those mechanically cross sectioned and polished. The electron beam was operated at 20kV for both imaging and EDS analysis.

The exposed surface area was calculated based on the measured submersion depth of each sample. The average corrosion rate in mm/year and the mass loss rate in mg cm^{-2} hr^{-1} was then calculated based on the mass change, density of the alloy, exposed surface area, and length of exposure.

Results

The surface of I625 samples exposed to LiCl-Li_2O solutions in the absence of Li displayed a high degree of crystallinity indicative of a well-formed oxide layer, while the surfaces of samples exposed to LiCl-Li_2O in the presence of metallic Li showed a very porous, almost sponge-like microstructure. To illustrate these points, the SEM micrographs taken of the I625 samples exposed to LiCl-1wt%Li_2O containing 0, 0.3, 0.6, or 1wt%Li for 500hr are shown in Figure 1.

In the absence of Li, the oxide layer is well formed and shows evidence of a multi layered structure that is discussed in greater detail below. EDS analysis of the area shown in Figure 1a showed that the surface was composed of 22at% Cr, 66at%O, and 13at%Ni, with minor quantities of other elements, indicating a primarily Cr based oxide layer. Li is not detectable via EDS, however, spectroscopic analysis has definitively shown this compound to be $LiCrO_2$.[38] The presence of Li in the molten LiCl-Li_2O solution destabilizes the oxide layer and forms a very porous microstructure that is similar in appearance to a Ni foam. EDS analysis of these areas consistently showed greater than 80at%Ni, with high depletion of Cr, Mo, and Nb, although the Ni:Fe ratio remained close to that of the base material. There was little difference between the microstructures observed at low and high Li concentrations, with the microstructure of the I625 samples exposed to melts containing 0.3wt%Li displaying microstructures nearly identical to samples exposed to melts containing 1wt%Li. Exposure periods of 500hr and 1000hr both yielded nearly indistinguishable microstructures, as can be observed by comparing the micrographs of I625 samples exposed to LiCl-1wt%Li_2O containing 0, 0.3, 0.6, and

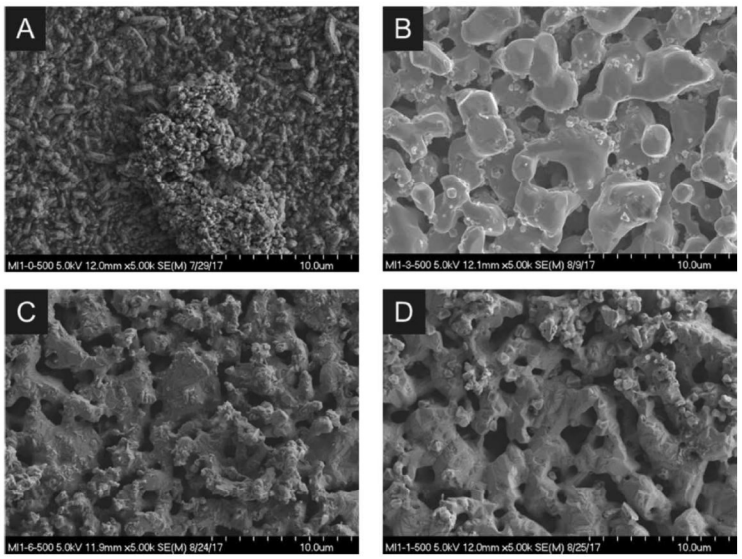

Figure 1. SEM micrographs of I625 exposed to LiCl-1wt%Li_2O at 650°C containing A) no Li, B) 0.3wt%Li, C) 0.6wt%Li, and D) 1wt%Li for 500hr and rinsed with methanol.

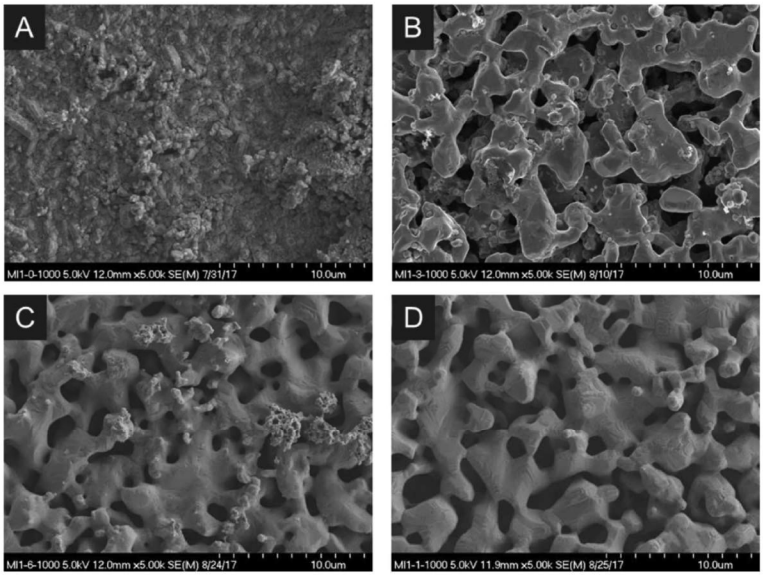

Figure 2. SEM micrographs of I625 exposed to LiCl-1wt%Li_2O at 650°C containing A) no Li, B) 0.3wt%Li, C) 0.6wt%Li, and D) 1wt%Li for 1000hr and rinsed with methanol.

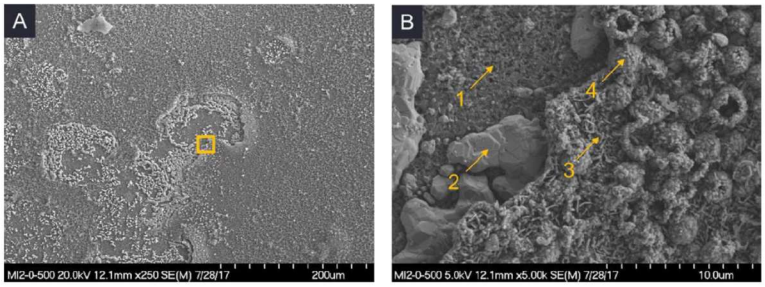

Figure 3. SEM micrographs taken at (A) low magnification and (B) high magnification of the highlighted area on the I625 sample exposed to LiCl-2wt%Li_2O-0wt%Li at 650°C for 500hr after methanol rinsing. The delamination of the outer surface layer on this sample provided a unique opportunity to examine the layered structure of the oxide films that form on I625 upon exposure to molten LiCl-Li_2O in the absence of Li. The compositions of Layers 1 through 4 in image B were obtained via EDS analysis and are given in Table II, below.

1wt%Li for 1000hr shown in Figure 2 to the micrographs presented in Figure 1.

Variations in Li_2O concentration and exposure length did not dramatically alter the morphology observed on I625 samples exposed to LiCl-Li_2O-Li compared to those shown in Figures 1 and 2. Consistent morphology was observed in the presence of Li, with all samples displaying similar structures. Likewise, in the absence of Li, a well-developed, highly crystalline oxide layer was consistently observed. Additionally, the surface of the I625 sample exposed to LiCl-2wt%Li_2O-0wt%Li for 500hr had a small number of locations where the oxide layer had partially delaminated, which allowed for direct observation of the layered structure of the oxide films formed on I625 during exposure to LiCl-Li_2O in the absence of Li. SEM micrographs of one of these locations are shown in Figure 3, and the compositions of locations 1 through 4 detected via EDS are given in Table I.

The presence of a multilayered oxide structure is easily discernable in this image. Each layer was analyzed using EDS at the spots marked by the arrows. The layers were numbered 1 through 4 starting with the innermost and proceeding outward. Due to the composition of Layer 2 and the lack of Ti in both Layers 1 and 2, which is present as an impurity in the Li_2O used in this study, it is thought that Layer 1 is the result of the inward diffusion of O into the base material. The O concentration of Layer 2 is much lower than in any of the other layers observed here, and its composition is the most similar to the base alloy, although all areas analyzed were notably depleted in Mo and Nb. The size of the grains in Layer 2 and their relative orientations are also similar to the morphology of the I625 samples exposed to LiCl-Li_2O in the presence of Li, as can be observed by comparison with Figures 1 and 2, indicating that this is likely the base material which has been depleted in Cr to facilitate the outward growth of Layers 3 and 4. These outermost layers differ in both morphology and composition, suggesting a difference in the compounds that compose them. Layer 3 is the layer closest to the base material, and has a plate-like morphology. The high Ni content of Layer 3 compared to Layer 4 implies that Layer 3 is composed of primarily $NiFe_xCr_{2-x}O_4$ with a relatively low value of x, while Layer 4 is primarily $LiCrO_2$ based. Both Layer 3 and Layer 4 have incorporated Ti from the impurities present in the Li_2O used in this study. The spheroidal morphology of Layer 4 suggests that its growth begins at specific nucleation sites. Some of these spheroids from Layer 4 appear to be broken or incompletely formed, showing that they are hollow. Figure 4 shows the results of EDS mapping of Ni, Fe, Cr, and O for the same location shown in Figure 3 which further highlights the differences between the layers observed on this sample.

Table I. EDS compositional analysis obtained for locations 1 through 4 marked in Figure 3B for the I625 sample exposed to LiCl-2wt%Li_2O-0wt%Li at 650°C for 500hr.

Element	Layer 1 Atomic%	Layer 2 Atomic%	Layer 3 Atomic%	Layer 4 Atomic%
C				5.07
O	62.43	11.22	61.07	65.48
Mg	1.35		2.56	3.14
Cl	0.41		0.27	0.47
Cr	18.34	3.33	12.99	20.07
Fe	0.61	3.74	1.21	0.32
Ni	15.23	80.97	21.44	5.13
Nb	0.9			
Mo	0.73	0.74		
Ti			0.46	0.32

Cross section SEM-EDS.—The cross sections of the samples were investigated to determine the depth to which the degradation of the surface penetrated into the bulk of the sample. In the absence of Li, the penetration into the bulk of the sample was minimal, as evidenced by Figures 5 and 6, which show the FIB milled cross section of the I625 samples exposed to LiCl-1wt%Li_2O-0wt%Li at 650°C for 500hr and 1000hr, respectively. Small pores of less than 2μm in diameter were observed immediately below the outer oxide layer for the 500hr sample, corresponding to a layer of Mo enrichment as evidenced in Figure 5d. As shown in the EDS analysis of this sample previously, the oxide layer does not incorporate a significant amount of Mo, indicating that the surface enrichment of Mo is deleterious to the integrity of the base material. At an exposure period of 500hr, the thickness of the oxide layer is approximately 1μm, while the thickness of the Mo enriched layer containing the pores is approximately 2μm. Based on a total thickness of 3μm, the corrosion rate was calculated to be 0.05mm/year.

Careful observation of the EDS maps in Figures 5b through 5f show that Cr is depleted in this region. Consequently, our hypothesis is that the pores are a result of the diffusion of Cr toward the surface to form the outer oxide layer, causing contraction of the base material at the interface between the base alloy and the oxide layer. As corrosion proceeds, the diffusion of Cr from the bulk alloy becomes the limiting factor, and the surface of these voids then offer the path of least resistance to allow reaction of Cr with the salt to form the Cr-based oxide layer. The increased volume of the oxide eventually fills in the void space. The growth and subsequent infill of these voids may give rise to the multi-layered oxide structure observed on the samples exposed to identical conditions for 1000hr in Figure 6. The lack of voids observed in Figure 6 may be due to the path required for diffusion of Cr from the alloy. This is supported by near complete depletion of Cr in the Ni and Fe rich layers between the Cr-based oxides.

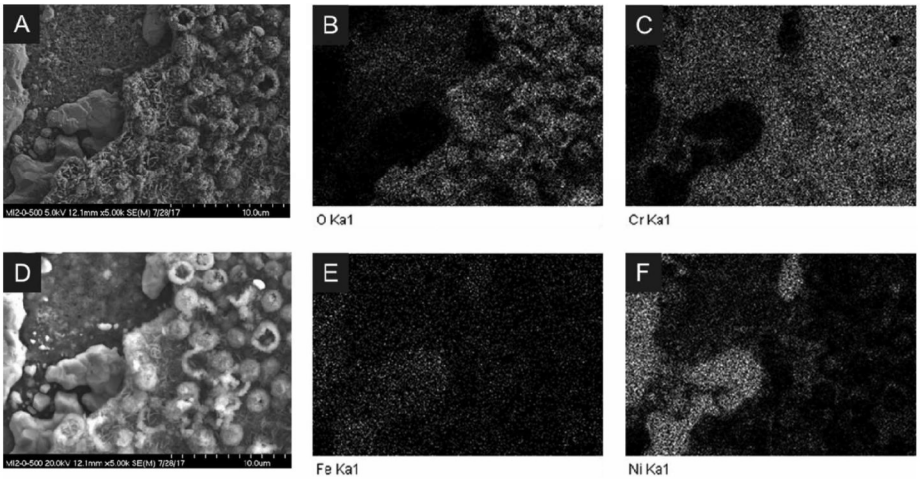

Figure 4. SEM images and EDS maps of the same area for the I625 sample exposed to LiCl-2wt%Li_2O-0wt%Li for 500hr. (A) SEM micrograph same as in Figure 3B given for reference, taken at 5kV accelerating voltage, (B) EDS map of O Kα, (C) EDS map of Cr Kα, (D) SEM micrograph of same area, taken at 20kV accelerating voltage (E) EDS map of Fe Kα, and (F) EDS map of Ni Kα. For the EDS maps, lighter tones indicate higher concentrations of that element.

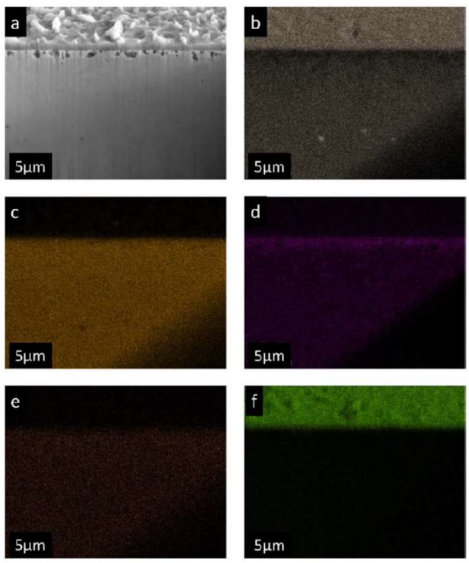

Figure 5. SEM micrograph (a) and EDS mapping analysis of the FIB milled trench on the I625 sample exposed to LiCl-1wt%Li_2O-0wt%Li for 500hr showing variations in concentration of (b) Cr, (c) Ni, (d) Mo, (e) Fe, and (f) O. The sample surface is observed as the image was taken at an angle of 52° from normal to the plane of the sample. The delineation between sample surface and cross section is demarked by the location of the abrupt change in intensity of all elements. Cr is seen to be enriched on the surface of the sample, while Mo is slightly enriched just below the outer corrosion layer. Oxide thickness is approximately 1µm, while the depth to the bottom of the lowest void space is 2.25µm.

For the I625 sample exposed to LiCl-1wt%Li_2O-0wt%Li for 1000hr, the corrosion rate was approximately 0.07mm per year, indicating that corrosion was approximately linear for these experiments. The oxide film was well developed, and showed a multi-layered structure similar to that shown for the I625 sample exposed to LiCl-2wt%Li_2O-0wt%Li for 500hr in Figures 3 and 4. The Mo enriched layer below the outer corrosion layer was still observed, however, there were no voids located in this area as there were on the 500hr sample. Mo accumulation was also observed at the grain boundaries, along with Cr and Nb, which is likely due to thermal aging of the microstructure, rather than a result of exposure to the molten LiCl-Li_2O solution.[39] Although enrichment of Cr, Mo, and Nb were observed along the grain boundaries, carbon was not observed at these locations, so it cannot be concluded that sensitization was observed. Corrosion did not proceed along the grain boundaries, so it seems that the enrichment of the grain boundaries in Cr, Mo, and Nb did not negatively impact the observed corrosion rate. However, sensitization followed by intergranular corrosion was observed in our previous work on SS316L under similar conditions.[36]

As was observed via SEM imaging of the sample surfaces, the cross sections of the I625 samples exposed to LiCl-Li_2O in the presence of Li were consistent in morphology and showed an outer layer of a highly porous Ni rich foam-like structure. The formation of this porous layer is believed to be a result of the selective dissolution of Cr, Mo, and Nb from the base material, leaving the Ni-Fe matrix in place, similar to the formation of Rainey Nickel by the selective dissolution of Al from Ni-Al alloys.[40] This mechanism is likely similar to the void formation observed in Figure 5a, as diffusion of elements within the alloy is unlikely to be affected by the solution chemistry. The SEM images of the cross sections of the I625 samples exposed to LiCl-1wt%Li_2O containing 0.3, 0.6, or 1wt% Li at 650°C for 500 and 1000hr are shown in Figure 7. For the sample exposed to LiCl-1wt%Li_2O-0.3wt%Li for 500hr, the porosity penetrated into the surface to a depth of approximately 30µm, corresponding to a corrosion rate of 0.53mm/year. However, all other samples consistently showed a penetration depth of 15µm, regardless of Li concentration or period of exposure, indicating that a direct measure of the corrosion rate is not necessarily applicable for these specimens. The similarity in the morphology and depth of attack regardless of Li concentration or

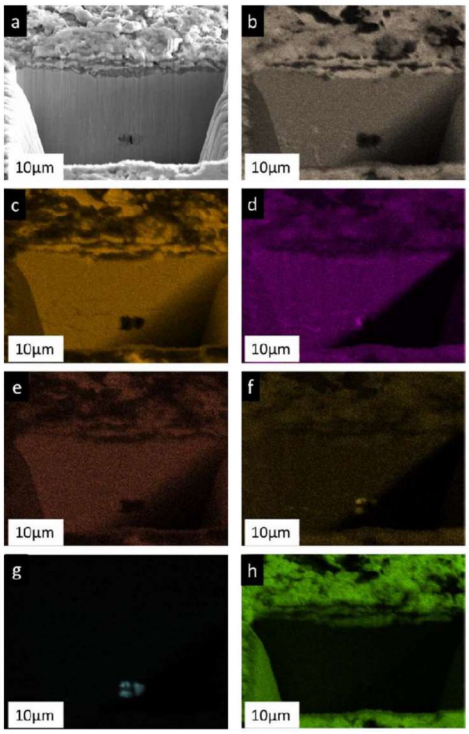

Figure 6. SEM micrograph (a) and EDS mapping analysis of the FIB milled trench on the I625 sample exposed to LiCl-1wt%Li_2O-0wt%Li for 1000hr showing variations in concentration of (b) Cr, (c) Ni, (d) Mo, (e) Fe, (f) Nb, (g) Ti, and (h) O. The multi-layered structure observed here corresponds to a similar oxide layer structure observed in Figures 3 and 4. Again, Mo enrichment is seen immediately below the corrosion layer, without significant incorporation of Mo into the oxide layer itself. The precipitate seen at a depth of 17µm consists largely of Ti, Mo, and Nb. Cr, Mo, and Nb were also observed to be enriched along the grain boundaries.

exposure period indicates that there may be a threshold concentration of Li necessary to cause this morphology and that threshold is likely below 0.3wt%, and the reactions responsible for pore formation may not be diffusion controlled. Further studies at Li concentrations below 0.3wt% would be necessary to determine at what concentration this morphology begins to be observed as well as the mechanisms responsible for pore formation. Due to the presence of metallic Li, liquid metal embrittlement may play a role in the formation of the microstructures observed here, although verification of this hypothesis would require further investigation.

The variation in composition as a function of depth was investigated via EDS of the cross sections. As all samples exposed to LiCl-Li_2O in the presence of Li displayed similar variations in composition, the SEM-EDS results for the I625 sample exposed to LiCl-1wt%Li_2O-1wt%Li at 650°C for 1000hr are shown in Figure 8, while spot EDS analysis for the locations shown in Figure 8a are given in Table II. Cr, Mo, and Nb are all significantly depleted from the material remaining in the porous layer, leaving primarily Ni, with Fe remaining at approximately the same ratio as in the base material. The depletion of Cr, Mo, and Nb was also observed to irregularly penetrate into the sample beyond the depth of the porous layer. The loss of the amount

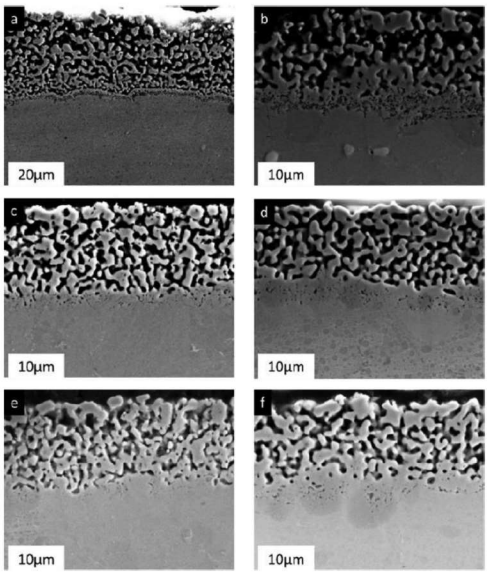

Figure 7. Cross section SEM images for I625 samples exposed to LiCl-1wt%Li_2O containing 0.3wt% Li for (a) 500hr or (b) 1000hr, 0.6wt%Li for (c) 500hr or (d) 1000hr, or 1wt%Li for (e) 500hr or (f) 1000hr. The porous microsctructure observed via SEM of the sample surface was also observed in cross section, and was consistent amongst sample exposed to LiCl-Li_2O in the presence of Li.

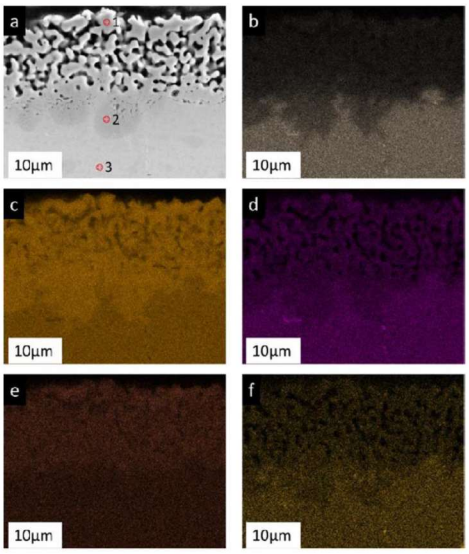

Figure 8. SEM micrograph (a) and EDS mapping analysis of the cross section of the I625 sample exposed to LiCl-1wt%Li_2O-1wt%Li for 1000hr showing variations in concentration of (b) Cr, (c) Ni, (d) Mo, (e) Fe, and (f) Nb. Locations marked 1, 2, and 3, were analyzed via point analysis, which is presented in Table II.

Table II. EDS spot analysis of the locations demarked in Figure 8a for the I625 sample exposed to LiCl-1wt%Li_2O-1wt%Li for 1000hr. The outermost layer was depleted in Cr compared to the base material, while the dark spots seen in some locations on these samples did not show any observable variation in composition compared to the base material.

Element	Spot 1 (wt%)	Spot 2 (wt%)	Spot 3 (wt%)
Nb	-	2.87	2.97
Mo	4.86	7.18	7.19
Cr	5.31	22.34	23.7
Fe	8.35	5.17	5.17
Ni	81.48	62.45	60.98

of Cr, Mo, and Nb necessary to reach the composition of spot 1 shown in Figure 8a represents the loss of a significant fraction of the material, which may account for the porous microstructure seen on this sample and other I625 samples exposed to LiCl-Li_2O in the presence of Li.

Conclusions

I625 samples were exposed to molten LiCl solutions containing 1 or 2wt% Li_2O and 0, 0.3, 0.6, or 1wt% Li maintained at 650°C for periods of 500 and 1000hr to investigate the effect of metallic Li on the degradation of the material. In the absence of metallic Li, I625 formed a highly crystalline, stable oxide film with a multi-layered structure that limited corrosion to approximately 0.05 to 0.07mm/year. The presence of metallic Li in solution prevented the formation of any substantial oxide film, resulting in a highly porous, foam-like structure. The depletion of Cr, Mo, and Nb from the surface was also observed on these samples via EDS, indicating that these elements were preferentially leached from the base material by the molten solution. The loss of these elements from the sample surface, which together constitute one-third of the material, is likely responsible for the highly porous microstructure observed.

Acknowledgments

This work was performed under the auspices of the Department of Energy (DOE) under contracts DE-NE0008262 and DE-NE0008236, and the US Nuclear Regulatory Commission (USNRC) under contracts NRCHQ-11-G-38-0039 and NRC-HQ-13-G-38-0027. W.P. acknowledges the Fellowship Award from the USNRC. Dr. Kenny Osborne serves as the program manager for the DOE award and Nancy Hebron-Isreal serves as the grants program officer for the NRC awards.

ORCID

Dev Chidambaram https://orcid.org/0000-0002-3918-3559

References

1. J. J. Laidler, J. E. Battles, W. E. Miller, J. P. Ackerman, and E. L. Carls, *Progress in Nuclear Energy*, **31**, 131 (1997).
2. K. Gourishankar, L. Redey, and M. Williamson, *Electrolytic Reduction of Metal Oxides in Molten Salts*, in: W. A. Schneider (Ed.) Light Metals, The Minerals, Metals & Materials Society, 2002.
3. S. D. Herrmann, S. X. Li, and M. F. Simpson, *Electrolytic Reduction of Spent Oxide Fuel - Bench-Scale Test Results*, GLOBAL 2005, Tsukuba, Japan, 2005.
4. H. Lee, G.-I. Park, K.-H. Kang, J.-M. Hur, J.-G. Kim, D.-H. Ahn, Y.-Z. Cho, and E. H. Kim, *Nuclear Engineering and Technology*, **43**, 317 (2011).
5. S. D. Herrmann, S. X. Li, M. F. Simpson, and S. Phongikaroon, *Separation Science and Technology*, **41**, 1965 (2006).
6. M. Kurata, T. Inoue, J. Serp, M. Ougier, and J. P. Glatz, *Journal of Nuclear Materials*, **328**, 97 (2004).
7. S. M. Jeong, H. S. Shin, S. H. Cho, J. M. Hur, and H. S. Lee, *Electrochimica Acta*, **54**, 6335 (2009).
8. S. X. Li, M. F. Simpson, and S. D. Hermann, *Oxygen Ion Oxidation Process on a Platinum Electrode in LiCl-Li_2O At 650C*, in: R. A Mantz (Ed.) *Electrochemical Society Proceedings*, vol **24**, 2004.
9. A. Merwin, M. A. Williamson, J. L. Willit, and D. Chidambaram, *Journal of the Electrochemical Society*, **164**, H5236 (2017).
10. W. Park, J.-M. Hur, S.-S. Hong, E.-Y. Choi, H. S. Im, S.-C. Oh, and J.-W. Lee, *Journal of Nuclear Materials*, **441**, 232 (2013).
11. A. Merwin, W. C. Phillips, M. A. Williamson, J. L. Willit, P. N. Motsegood, and D. Chidambaram, *Scientific Reports*, **6**, 25435 (2016).
12. A. S. Dworkin, H. R. Bronstein, and M. A. Bredig, *The Journal of Physical Chemistry*, **66**, 572 (1962).
13. M. A. Bredig, *Mixtures of Metals with Molten Salts*, United States, 1963.
14. L. M. Ferris, M. A. Bredig, and F. J. Smith, *The Journal of Physical Chemistry*, **77**, 2351 (1973).
15. T. N. Nakajima and N. Watanabe K., *Nippon Kagaku Kaishi*, **1974**, 401 (1974).
16. T. Nakajima, R. Minami, K. Nakanishi, and N. Watanabe, *Bulletin of the Chemical Society of Japan*, **47**, 2071 (1974).
17. T. N. Nakajima and N. Watanabe K., *Bulletin of the Chemical Society of Japan*, **49**, 994 (1975).
18. T. Nakajima, K. Nakanishi, and N. Watanabe, *Nippon Kagaku Kaishi*, **1975**, 617 (1975).
19. A. J. Burak and M. F. Simpson, *JOM*, **68**, 2639 (2016).
20. S. H. Cho, J. S. Zhang, Y. J. Shin, S. W. Park, and H. S. Park, *Journal of Nuclear Materials*, **325**, 13 (2004).
21. R. Y. Liu, X. Wang, J. S. Zhang, and X. M. Wang, *Journal of Nuclear Materials*, **327**, 194 (2004).
22. C. Soo-Haeng, L. Jong-Ho, P. Sung-Bin, J. Ki-Jung, and P. Seong-Won, *Journal of the Korean Institute of Metals and Materials*, **43**, 449 (2005).
23. Q. Gao, R. Y. Liu, J. S. Zhang, and J. T. Guo, *Materials Letters*, **59**, 2052 (2005).
24. C. Soo-Haeng, P. Seong-Bin, L. Jong-Hyeon, H. Jin-Mok, and L. Han-Soo, *Oxidation of Metals*, **78**, 153 (2012).
25. P. SangKyu, L. TaeHyuk, S. MoonSoo, N. JaeSoo, C. SooHaeng, and L. JongHyeon, *Advanced Materials Research*, **886**, 41 (2014).
26. S.-H. Cho, S.-K. Lee, D.-Y. Kim, J.-H. Lee, and J.-M. Hur, *Journal of Alloys and Compounds*, **695**, 2878 (2017).
27. T. R. Allen and K. Sridharan, *Corrosion in Molten Salts, in Molten salts chemistry from lab to applications*, Elsevier, Burlington, MA, 2013.
28. Y. S. Zhang, *Journal of The Electrochemical Society*, **133**, 655 (1986).
29. J. E. Indacochea, J. L. Smith, K. R. Litko, and E. J. Karell, *Journal of Materials Research*, **14**, 1990 (1999) M1993 - 1910.1557/JMR.1999.0268.
30. B. Mishra and D. L. Olson, *Mineral Processing and Extractive Metallurgy Reviews*, **22**, 369 (2001).
31. A. Merwin and D. Chidambaram, *Corrosion Science*, **126**, 1 (2016).
32. A. Merwin and D. Chidambaram, *Nuclear Technology*, **195**, 204 (2016).
33. W. Phillips, A. Merwin, and D. Chidambaram, *Metallurgical and Materials Transactions A*, **49**, 2384 (2018).
34. E.-Y. Choi and J. Lee, *Journal of Nuclear Materials*, **495**, 85 (2017).
35. A. Merwin, *Material Interactions with Molten LiCl-Li_2O-Li, Materials Science and Engineering*, vol *Doctor of Philosophy in Materials Science and Engineering*, University of Nevada, Reno, 2016, p. 241.
36. W. Phillips and D. Chidambaram, *Journal of Nuclear Materials*, **517**, 241 (2019).
37. N. J. Gese, *The Electrochemistry of Li-LiCl-Li_2O Molten Salt Systems and the role of Moisture*, Nuclear Engineering, University of Idaho, 2015.
38. W. Phillips and D. Chidambaram, *Journal of the Electrochemical Society*, (*Under Review*).
39. S. Malej, J. Medved, B. Šetina Batič, F. Tehovnik, and M. Godec, *Microstructural evolution of inconel 625 during thermal aging*, 2017, p. 319.
40. H. Lei, Z. Song, D. Tan, X. Bao, X. Mu, B. Zong, and E. Min, *Applied Catalysis A: General*, **214**, 69 (2001).

A7.3: Effect of Metallic Li on the Surface Chemistry of Inconel 625 Exposed to LiCl-Li_2O-Li

Journal of The Electrochemical Society, **166** (11) C3193-C3199 (2019) C3193

JES Focus Issue on Electrochemical Techniques in Corrosion Science in Memory of Hugh Isaacs

Effect of Metallic Li on the Surface Chemistry of Inconel 625 Exposed to Molten LiCl-Li_2O-Li

William Phillips [1,*] **and Dev Chidambaram** [1,2,**,z]

[1] *Materials Science and Engineering, University of Nevada, Reno, Nevada 89557-0388, USA*
[2] *Nevada Institute for Sustainability, Reno, Nevada 89557-0388, USA*

This study explores the surface chemistry of Inconel 625 samples exposed to molten LiCl-Li_2O-Li solutions at 650°C for 500 and 1000hr and aims to understand the effect of solvated Li on corrosion behavior in molten LiCl-Li_2O-Li. The surfaces of Inconel 625 samples were analyzed using X-ray diffraction, Raman spectroscopy, and X-ray photoelectron spectroscopy. The oxide films formed on the surface of the samples in the absence of Li is composed of $LiCrO_2$, with small contributions of Li_2CrO_4 and $NiFe_xCr_{2-x}O_4$. The presence of Li was observed to destabilize these compounds, resulting in a primarily metallic surface with trace amounts of oxidized Cr, Mo, and Nb present depending on the concentration of Li in solution.

Manuscript submitted January 31, 2019; revised manuscript received April 19, 2019. Published May 7, 2019. *This paper is part of the JES Focus Issue on Electrochemical Techniques in Corrosion Science in Memory of Hugh Isaacs.*

This study discusses the effect of metallic Li dissolved in molten LiCl-Li_2O solutions on the corrosion behavior of Inconel alloy 625 (I625), as applies to the electrolytic reduction of oxide based used nuclear fuel (UNF). A thorough introduction including the motivation and background for this work is provided in an earlier study.[1] Briefly, the formation of metallic Li in the molten LiCl-Li_2O electrolyte used for the electrolytic reduction of oxide based UNF has been noted by a number of researchers to occur.[2,3] Formation of metallic lithium is a side reaction that occurs as a result of the high reduction potential in the process that is necessary to reduce uranium oxide to uranium metal. As the reduction proceeds, it can be assumed that the concentration of Li in the electrolyte approaches saturated conditions.[3] While the dissolution mechanism of Li in LiCl and its effects on the physical chemistry of the solution have been well studied, corrosion in this tertiary LiCl-Li_2O-Li solution has not been extensively studied.[4–7] Additionally, the studies that have been conducted have been of short duration and have shown conflicting results due to widely varying experimental conditions employed.[8–13] Consequently, this study was performed to elucidate the mechanisms responsible for material degradation in conditions applicable to the electrolytic reduction of UNF.

Previous work from our group reported the morphological and elemental changes to the base material surface and cross section via scanning electron microscopy (SEM) coupled with energy dispersive X-ray spectroscopy (EDS) for both stainless steel 316 (SS316) and I625.[1,14] The results presented there showed that a stable Cr-based oxide film forms on the surface of I625 upon exposure to molten LiCl-Li_2O solutions at 650°C in the absence of Li^0.[1] This oxide film was found to limit the corrosion of these samples to a rate of approximately 0.05 to 0.07 mm/year.[1] However, in the presence of Li, this oxide film was destabilized, resulting in the preferential dissolution of the active alloying elements, namely Cr, Mo, and Nb, and a porous microstructure at the sample surface (1, supplemental information Figs. S4 and S5). This porous structure extended into the surface to a depth of 15 to 30μm.[1] This study aims to better understand the corrosion mechanisms involved by understanding the surface chemistry of I625 using X-ray diffraction (XRD), Raman spectroscopy, and X-ray photoelectron spectroscopy (XPS). The results of these surface analytical techniques are presented in this work.

*Electrochemical Society Student Member.
**Electrochemical Society Member.
[z]E-mail: dcc@unr.edu

Experimental

I625 coupons were cut from a 3.175mm plate obtained from High Performance Alloys with the following nominal composition: 58wt% Ni, 20–23wt% Cr, 5wt% Fe, 8.0-10.0wt% Mo, 3.15-4.15wt% Nb, 0.5wt% Mn, 0.4wt% Al, 0.4wt% Ti, and 0.5wt% Si. The composition of this alloy as measured via the EDS used for cross sectional investigation was 62.3wt% Ni 23.5wt% Cr, 6.5wt% Mo, 5.1% Fe, and 2.6wt% Nb. Duplicate coupons were exposed molten solutions of LiCl containing either 1 or 2wt% Li_2O, and either 0, 0.3, 0.6, or 1wt% Li over exposure periods of either 500 or 1000 hours. Considering the evaporation of Li and Li_2O over time that was observed in other short-term studies and the extended exposure periods of this study, the salt charge for each test was replaced at a period of once every 96 hours to maintain the solution chemistry.[10–12,14,15] To minimize the effects of impurity H_2O, LiCl was dried in a vacuum oven in air at 200°C for 24 hours before being transferred into the glove box for storage. Additionally, the LiCl was baked for 2 hours at 550°C immediately prior to melting and subsequent addition of Li_2O and Li.[10,16] The surface analysis presented here was conducted on the samples prepared for our previous work.[1] More details on the experimental procedure and morphology of these samples can be found in that publication.[1] All surface analysis was performed prior to removal of the residual salt layer, as well as following removal of the salt layer, which was accomplished by rinsing the sample in 25mL of ACS grade methanol for 15 minutes with continuous agitation.

Great care was taken to maintain sample integrity at all times during analyses. Prior to methanol rinsing, all surface analyses was conducted under inert or ultra-high vacuum (UHV) conditions, as dictated by each technique. Raman studies were performed inside the Ar glove box using a fiber optic coupled probe. For XPS analyses, the samples were transferred from the glove box to the UHV chamber in a sealed transfer chamber to prevent atmospheric contamination (PHI Model 04-110). This transfer vessel has been extensively verified to protect reactive samples from atmospheric contamination during transfer under various conditions.[17] A glove bag was installed on the transfer port of the XPS and purged with dry nitrogen for 30 minutes prior to sample removal to reduce atmospheric contamination of the samples during removal from the instrument. The samples were then re-sealed inside the PHI 04–110 transfer chamber for transfer back to the glove box. As described in our earlier work, XRD studies were then conducted on samples which were sealed in plastic bags in the argon atmosphere of the glove box.[10–12,14,15] No hydrated LiCl peaks were detected via XRD, indicating that there was insignificant moisture contamination

on the samples to this point, however, peaks indicative of $LiCrO_2$ were observed on the samples exposed to LiCl-Li_2O in the absence of Li (see supplemental information). Finally, sample surfaces were studied using SEM-EDS prior to methanol rinsing.[1] Due to the design of the transfer port of this instrument, it was necessary to momentarily expose the samples to atmosphere prior to pumping down of the SEM entry chamber. Total exposure time to atmosphere was less than 30 seconds. After SEM studies, the samples were then immediately rinsed with methanol as described above to remove the residual salt layer. Moisture content of the methanol was not analyzed, but typical moisture concentration was specified to be lower than 100 ppm. Following removal of the salt layer, the samples were immediately re-analyzed via SEM-EDS. No morphological or compositional changes were detected following methanol rinsing. Samples were stored inside the Ar glove box at all times other than for analysis. The surface analytical results from post methanol rinse were consistent with the results from pre-methanol rinse; however, the removal of the residual salt allowed for more accurate determination of the surface chemistry, as in many cases, the residual salt layer partially obscured the surface from analysis, particularly with XPS (see supplemental information). The lack of substantial surface oxides on the samples exposed to LiCl-Li_2O solutions containing Li indicate that the surface analysis procedures outlined above had minimal impact on the surface chemistry of these samples. As has been shown previously, no chemical or morphological changes to the sample surface were observed to result from the methanol rinsing procedure.[10,15,18] As such, the spectra reported here were collected from the sample surfaces following removal of the salt layer due to the improved data quality afforded by the increased signal to noise ratio.

X-ray diffraction was performed using a Rigaku Smartlab X-ray diffractometer with a Cu kα source operating at 44kV and 40mA. Parallel beam optics in a grazing incidence angle configuration were used for detection of the thin surface films formed on the samples in this study. The incidence angle was set at 1°, and the diffraction pattern was recorded over a range of 10° to 90° 2θ for all diffraction patterns. For each diffraction pattern, the scan speed was optimized to yield an intensity of 5000 counts for the highest peak, while the step size was varied to give 5 steps at the full width at half-maximum intensity of the narrowest peak.

Raman spectroscopy was performed using a Thermo-Scientific DXR Raman microscope utilizing a 10mW 532nm continuous wave laser. Spectra were collected through the 50x objective lens of the microscope using a 50μm incident beam slit. The collection time was 4 seconds per spectra, and 16 individual spectra were averaged to give the spectra reported here.

X-ray photoelectron spectroscopy was performed using a PHI 5600 spectrometer equipped with an Al-Kα source with a photon energy of 1486.6eV. The source was operated at an accelerating voltage of 14kV and an anode power of 300W. The spectrometer dispersion and work function were calibrated to the Au $4f_{7/2}$ peak at 84.00eV and the Cu $2p_{3/2}$ peak at 932.67eV to an accuracy of ±0.05eV. Survey spectra were recorded with a step size of 0.5eV, while narrow scans were collected at a step size of 0.025eV for the elements detected on the sample surfaces. Peak fitting was performed with SDP version 4.6 Gaussian fitting software. Charge correction was performed to the adventitious C 1s peak at 284.8eV.

Results

XRD.—The X-ray diffraction pattern collected for the I625 sample exposed to LiCl-1wt% Li_2O-0wt% Li at 650°C for 1000hr is shown in Figure 1. The peaks displayed in this pattern are representative of those collected for all samples exposed to molten LiCl-Li_2O solutions in the absence of Li^0. The only crystalline phases detected on these samples were the base material and peaks consistent with $LiCrO_2$.[19] When this result is considered along with Raman and XPS analysis of these samples shown below, it can be concluded that the oxide scale is composed largely of $LiCrO_2$ when I625 is exposed to molten LiCl-Li_2O solutions in the absence of Li.

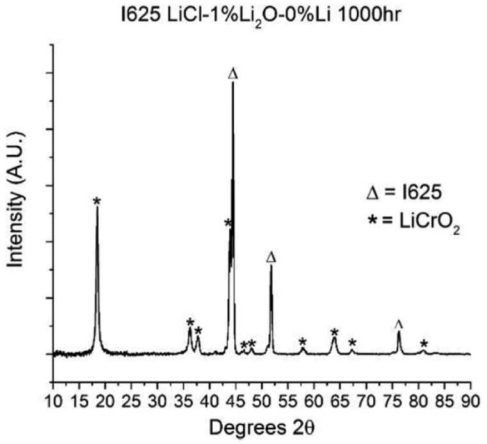

Figure 1. XRD pattern collected from the I625 sample exposed to LiCl-1wt% Li_2O-0wt% Li at 650°C for 1000hr. Peaks indicative of the base material and $LiCrO_2$ were observed.

The presence of Li^0 in solution creates a very reducing environment, preventing the formation of the well-developed $LiCrO_2$ films observed on these samples in the absence of Li. Consequently, the diffraction patterns for all samples exposed to LiCl-Li_2O solutions containing Li displayed diffraction patterns indicative only of the base material, as can be observed in Figures 2 and 3. These figures show the diffraction patterns of I625 samples exposed to LiCl-1wt% Li_2O solutions containing 0, 0.3, 0.6, or 1wt% Li for 500hr (Figure 2) or 1000hr (Figure 3). This corresponds with the observation made using SEM of the highly porous metallic surfaces on I625 samples exposed to LiCl-Li_2O in the presence of Li.[1,20]

Raman spectroscopy.—Raman spectra, shown in Figure 4, also confirms the presence of $LiCrO_2$ in the absence of Li, with the Raman spectra of the four samples exposed to molten LiCl-Li_2O solutions

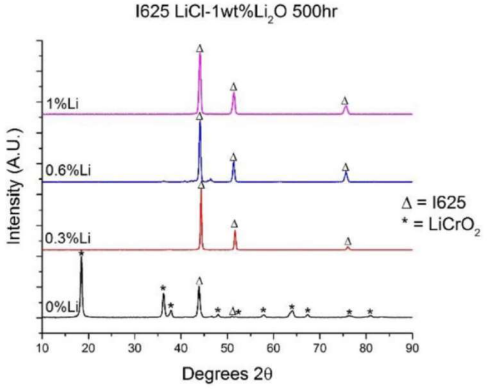

Figure 2. XRD spectra of I625 samples exposed to LiCl-1wt% Li_2O containing 0, 0.3, 0.6, and 1wt% Li at 650°C for 500hr. In the absence of Li, both $LiCrO_2$ and the base material were observed; however, in the presence of Li, on the base material was present.

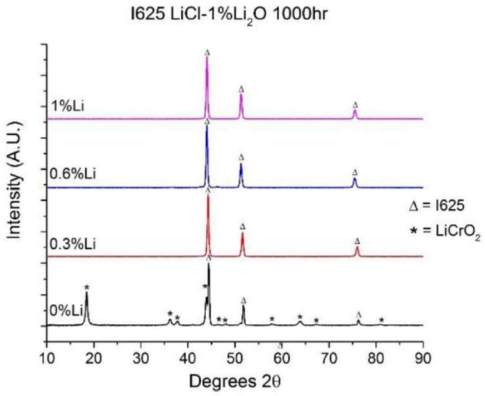

Figure 3. XRD spectra of I625 samples exposed to LiCl-1wt% Li_2O containing 0, 0.3, 0.6, and 1wt% Li at 650°C for 1000hr. In the absence of Li, both $LiCrO_2$ and the base material were observed; however, in the presence of Li, only the base material was present.

in the absence of Li displaying prominent peaks of both the $LiCrO_2$ A_{1g} and E_g modes at 572cm^{-1} and 445cm^{-1}, respectively.[21] An additional hump on the shoulder of the $LiCrO_2$ A_{1g} peak is believed to be indicative of a spinel of the type $NiFe_xCr_{2-x}O_4$ based on the work of Hosterman.[22] The exact composition of this compound is unknown, but is likely skewed toward Cr-rich compounds, due to the relatively low concentration of Fe in the I625 alloy. The I625 sample exposed to LiCl-1wt% Li_2O at 650°C also displayed features at 845cm^{-1} and 340cm^{-1} that indicate the presence of Li_2CrO_4 based on the collection of Raman spectra of this compound in our laboratory. It is currently unknown why the other I625 samples exposed to similar conditions did not display the features of Li_2CrO_4.

The effect of Li on the Raman spectra of I625 exposed to LiCl-Li_2O-Li solutions can be observed in Figure 5, which shows the Raman spectra of I625 samples exposed to LiCl-1wt% Li_2O solutions containing 0, 0.3, 0.6, and 1wt% Li at 650°C for 500hr. The well-defined Raman modes observed in Figure 4 are seen to be largely absent in the presence of Li. The broad features that roughly align with the positions of the compounds observed in the absence of Li may indicate minute quantities of these compounds on the sample surface. XPS analysis presented below confirms the presence of small amounts of oxidized Cr, Mo, and Nb on the surface of the I625 samples exposed to LiCl-Li_2O in the presence of Li.

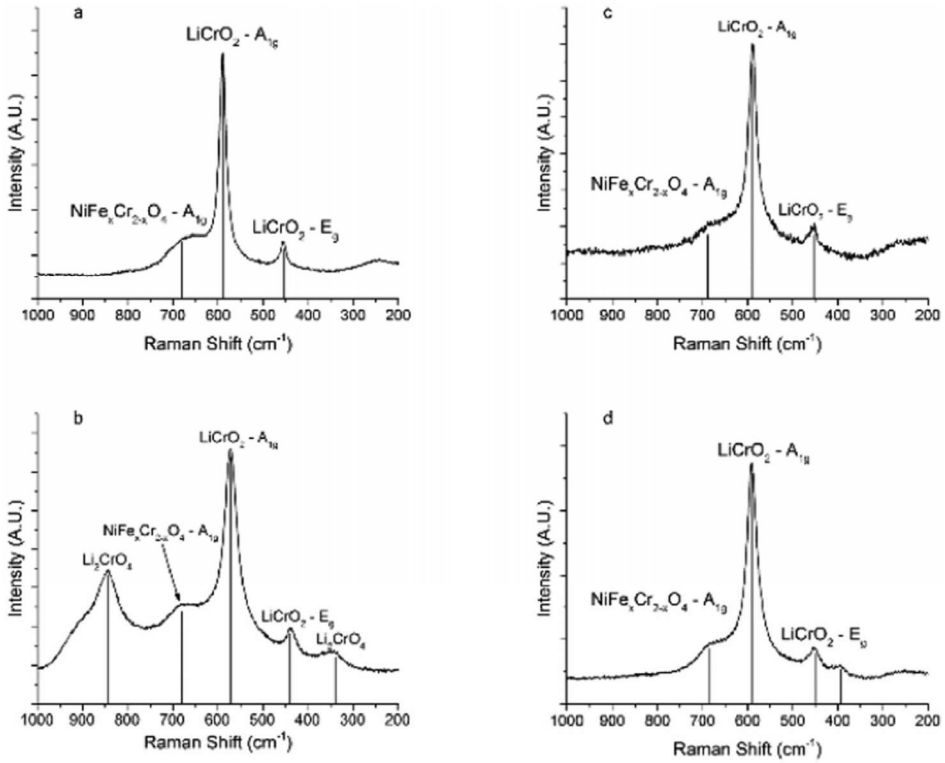

Figure 4. Raman spectra of I625 samples exposed at 650°C to LiCl containing a) 1wt% Li_2O for 500hr, b) 1wt% Li_2O for 1000hr, c) 2wt% Li_2O for 500hr and d) 2wt% Li_2O for 1000hr. The A_{1g} and E_g peaks of $LiCrO_2$ and a hump indicative of the A_{1g} peak of $NiFe_xCr_{2-x}O_4$ were observed on all samples exposed to LiCl-Li_2O solutions in the absence of Li. Additionally, the I625 sample exposed to LiCl-1wt% Li_2O for 1000hr displayed peaks indicative of Li_2CrO_4.

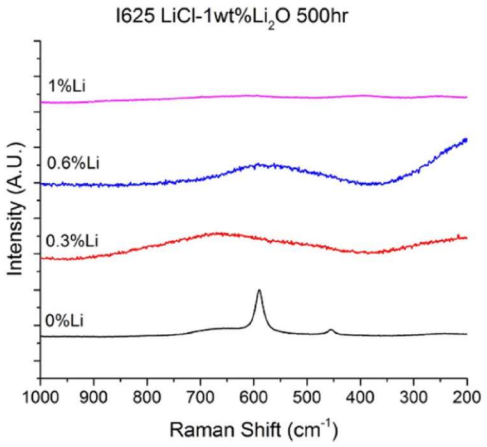

Figure 5. Raman spectra obtained from the surfaces of I625 samples exposed to LiCl-1wt% Li_2O containing 0, 0.3, 0.6, or 1wt% Li at 650°C for 500hr. The clearly defined Raman modes present in Raman spectra of samples exposed to LiCl-Li_2O in the absence of Li are not observed on the surface of samples exposed to LiCl-Li_2O in the presence of Li.

XPS.—The surface sensitivity and chemical state analysis provided by XPS allowed for the investigation of the corrosion products present on the surface of the samples, even at the low thicknesses observed on the I625 samples exposed to molten LiCl-Li_2O solutions containing Li. Comparison of spectra taken prior to and following methanol rinsing showed no change in surface chemistry caused by the rinsing procedure (see supplemental information), allowing for the chemical analysis presented below; however, the presence of a Ti-based deposit on some of the samples prevented accurate quantitative analysis of the surface composition. Figure 6 shows the XPS survey spectra recorded from the I625 samples exposed to LiCl-1wt% Li_2O solutions containing 0, 0.3, 0.6, and 1wt% Li at 650°C for 1000hr. Survey spectra of the I625 samples exposed to varying Li_2O concentrations and exposure periods showed similar features and trends. In

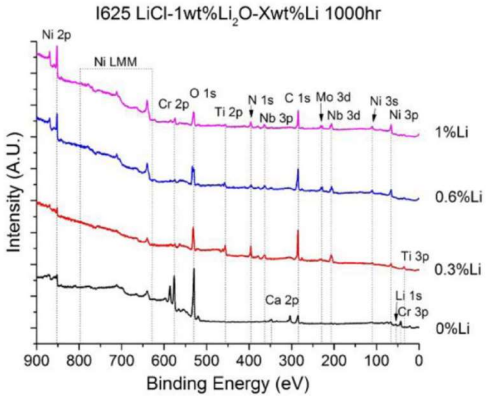

Figure 6. XPS survey spectra of I625 samples exposed to LiCl-1wt% Li_2O containing 0, 0.3, 0.6, or 1wt% Li at 650°C for 1000hr. Vertical lines denote the peak position of the spectral lines indicated.

Table I. Peak fitting parameters for Cr $2p_{3/2}$ spectra shown in Figures 7 and 8. Charge correction to the adventitious C 1s line at 284.6eV was performed.

Peak	BE	FWHM
Cr0	574.2	2.2
Cr^{3+}	576.2	2.4
Cr^{6+}	578.2	1.8

the case of the samples exposed to LiCl-Li_2O solutions in the absence of Li, the surface was primarily composed of Cr, O, and Li, further confirming the presence of $LiCrO_2$ on these samples. For the I625 sample exposed to LiCl-1wt% Li_2O for 1000hr, Ni was also detected via XPS; however, Ni was not detected on the surface of the other samples exposed to LiCl-Li_2O solutions in the absence of Li, further indicating that this sample had somewhat different surface chemistry when compared to the other samples exposed to similar conditions.

For I625 samples exposed to LiCl-Li_2O in the presence of Li, Ni was the primary element present, while the Cr level was depleted and most of the primary alloying elements were detected in trace amounts. Our previous work has shown these compounds were also detected on the surface of numerous samples that do not contain Ti as an alloying element, notably SS316L[14,15] and thus must be the be a result of electroless deposition of Ti oxide and nitride compounds from Ti impurities present in the Li_2O used in these studies.[15] This will not be discussed further in the present work.

The chemistry of Cr, being the primary alloying element in I625 as well as being responsible for corrosion inhibition through the formation of stable oxide films, is important to understand thoroughly. XPS narrow scans of the Cr $2p_{3/2}$ spectra obtained from the surface of the I625 samples exposed to LiCl containing 1 or 2wt% Li_2O and 0, 0.3, 0.6, or 1wt% Li for 500hr are shown in Figure 7, while the Cr $2p_{3/2}$ spectra of I625 samples exposed to similar conditions for 1000hr are shown in Figure 8. Peak fitting was performed using previously published fitting parameters given in Table I, with charge correction performed to the adventitious C 1s peak at 284.8eV.[23] In the absence of Li, the Cr spectra consistently showed the presence of Cr^{3+}, which is necessary for the formation of $LiCrO_2$, confirming the observations made via XRD and Raman spectroscopy that show this compound is present on the surface of these samples. Additionally, Cr^{6+} is also present to a minor degree on these samples, which supports the observation via Raman of the presence of Li_2CrO_4 in small amounts in the oxide film. As both Li_2O concentration and exposure period increase, the proportion of Cr^{6+} to Cr^{3+} increases, indicating that the formation of $LiCrO_2$ and Li_2CrO_4 are governed by the activity of the O^{2-} ion in solution, and that $LiCrO_2$ may be converted to Li_2CrO_4 over time. In the presence of Li^0, neither of these compounds are stable in bulk form, as indicated by XRD, Raman, and SEM-EDS observations; however, a nominal amount of Cr^{3+} and to a lesser extent Cr^{6+} were observed via XPS alongside metallic Cr^0, indicating that O^{2-} in solution continues to play a role in the corrosion process at concentrations of Li in solution of at least 1wt%. Cr^{6+} was not observed on all samples when Li metal was present in solution. While the formation of Cr^{6+} is unlikely from a thermodynamic perspective in pure LiCl-Li_2O, it was consistently observed in this study, as shown both via XPS and Raman. The formation of Li_2CrO_4 was also hypothesized to be the dissolution mechanism of the Cr-based oxide film by researchers at KAERI.[24] The solubility of CrO_4^{2-} in LiCl-Li_2O may lower the activation energy necessary to facilitate the formation of the Cr^{6+} oxidation state. Due to the difficulty associated with completely removing moisture from highly hygroscopic LiCl, the source of oxygen for the formation of the oxide layers observed in the absence of metallic Li was likely from impurity moisture remaining in the molten salt. In the case of the samples exposed to melts containing metallic Li, the excess Li would react with any moisture present in the salt to form Li_2O and H_2 gas, effectively eliminating this source of oxygen. The mechanism for the formation of the trace quantities of oxides present on the surface of

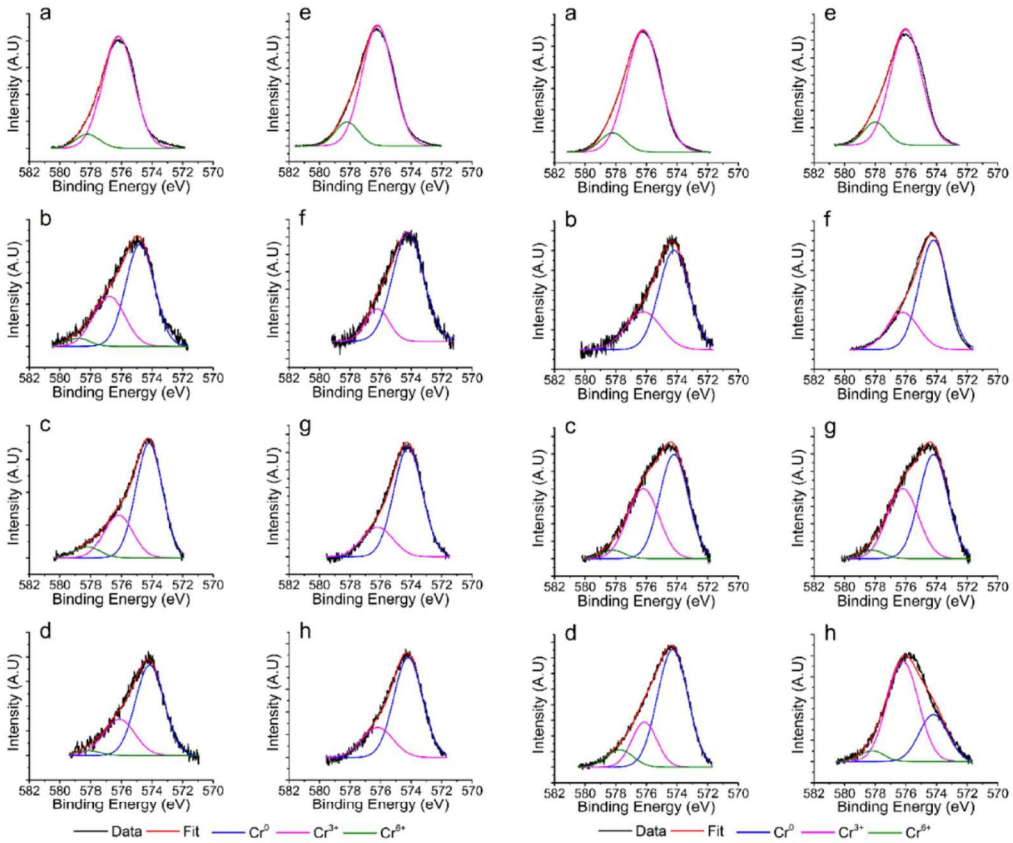

Figure 7. Cr $2p_{3/2}$ XPS spectra of I625 samples exposed for 500hr to LiCl containing a) 1% Li_2O 0% Li, b) 1% Li_2O 0.3% Li, c) 1% Li_2O 0.6% Li, d) 1% Li_2O 1% Li, e) 2% Li_2O 0% Li, f) 2% Li_2O 0.3% Li, g) 2% Li_2O 0.6% Li, and h) 2% Li_2O 1% Li.

Figure 8. Cr $2p_{3/2}$ XPS spectra of I625 samples exposed for 1000hr to LiCl containing a) 1% Li_2O 0% Li, b) 1% Li_2O 0.3% Li, c) 1% Li_2O 0.6% Li, d) 1% Li_2O 1% Li, e) 2% Li_2O 0% Li, f) 2% Li_2O 0.3% Li, g) 2% Li_2O 0.6% Li, and h) 2% Li_2O 1% Li.

the samples exposed to LiCl-Li_2O melts containing Li is currently unknown, and will require further investigation.

While Ni was not observed on the surface of most of the samples exposed to LiCl-Li_2O in the absence of Li, it was observed on the I625 sample exposed to LiCl-1wt% Li_2O for 1000hr, as well as on all samples exposed to LiCl-Li_2O-Li solutions. As shown in Figure 9, in the absence of Li, Ni was observed in a mixed valence state, showing both metallic as well as oxidized character. The presence of oxidized Ni on the surface of this sample supports the observations made via Raman of the presence of a spinel of the form $NiFe_xCr_{2-x}O_4$ in the oxide film of these samples. Fitting of these spectra was not performed due to the known difficulties associated with peak fitting Ni 2p XPS spectra without precise parameters obtained from standards with identical composition.[25] Peaks shapes and positions consistent with metallic Ni were observed on all samples exposed to LiCl-Li_2O in the presence of Li. No charge correction was necessary for the Ni spectra.

While Mo was not observed in detectable quantities via XPS of the surfaces of I625 samples exposed to LiCl-Li_2O solutions in the absence of Li due to the thick $LiCrO_2$ surface film and the relatively low concentration of Mo in the base alloy, it was observed on the surface of the majority of the samples exposed to LiCl-Li_2O in the presence of Li. The XPS narrow scans of the Mo 3d region are shown in Figure 10. At 0.3wt% Li, Mo behaved similarly to Cr in that it was present in a mixed metallic and oxidized state.[26,27] Due to the noise, presence of multiple overlapping peaks on these spectra, and the known tendency for photoreduction of Mo, peak fitting was not performed, although the apparent positions of the primary peaks are demarked by vertical lines on the charts in Figure 10. The I625 samples exposed to LiCl-Li_2O in the presence of 0.6 and 1wt% Li showed only the characteristic asymmetric peaks of metallic Mo. This transition from mixed metallic and oxidized character at low Li concentrations to a purely metallic state at higher Li concentrations indicates that the activity of Li in solution is not unity until beyond the solubility limit.

While both Cr and Mo were observed to be present in a mixed state containing oxidized and reduced species in the presence of Li, Nb was only observed in oxidized states.[28] The narrow scans of the Nb 3d region obtained from the surface of I625 samples exposed to molten LiCl solutions containing 1 or 2wt% Li_2O and 0.3, 0.6, or 1wt% Li for 1000hr are shown in Figure 11, with the exception of the I625 sample exposed to LiCl-1wt% Li_2O-1wt% Li for 1000hr, as Nb

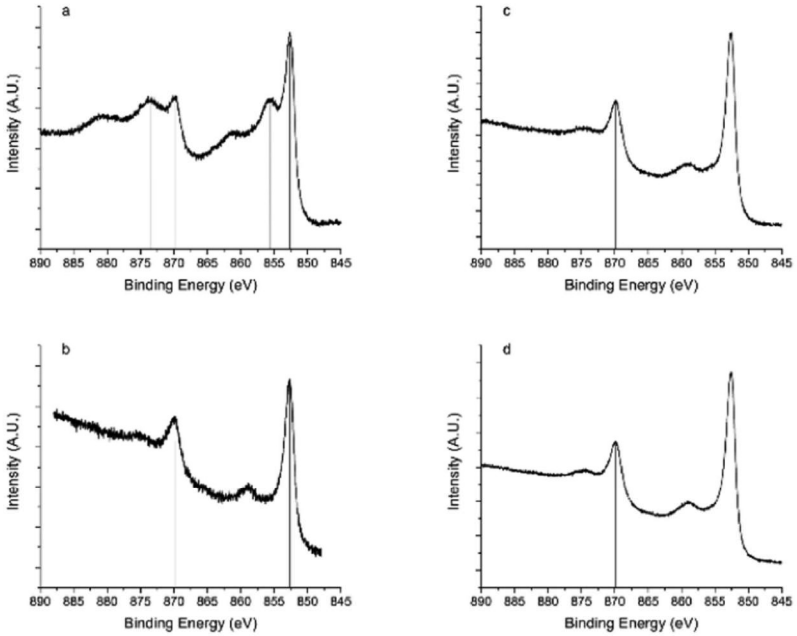

Figure 9. Ni 2p XPS narrow scans obtained from the I625 samples exposed to LiCl-1wt% Li_2O containing a) 0wt% Li, b) 0.3wt% Li, c) 0.6wt% Li, and d) 1wt% Li at 650°C for 1000hr. In the absence of Li, Ni is observed in a mixed metallic and oxidized state, indicating the presence of small amounts of Ni compounds in the oxide layer. In the presence of Li, Ni was only observed in the pure metallic state. No charge correction was performed necessary for Ni, indicating that it was consistently in electrical contact with the base material.

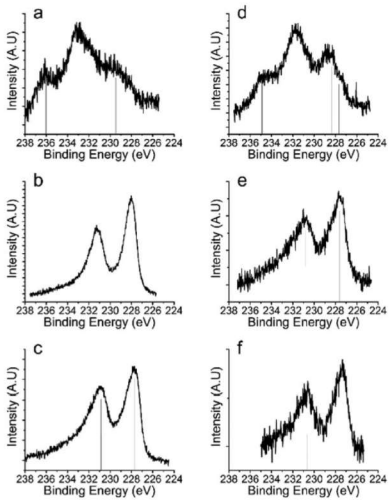

Figure 10. Mo 3d XPS narrow scans obtained from the surface of I625 samples exposed for 1000hr to molten LiCl containing a) 1wt% Li_2O and 0.3wt% Li, b) 1wt% Li_2O and 0.6wt% Li, c) 1wt% Li_2O and 1wt% Li, d) 2wt% Li_2O and 0.3wt% Li, e) 2wt% Li_2O and 0.6wt% Li, and f) 2wt% Li_2O and 1wt% Li. At concentrations of 0.3wt% Li Mo shows a mixed oxide state.

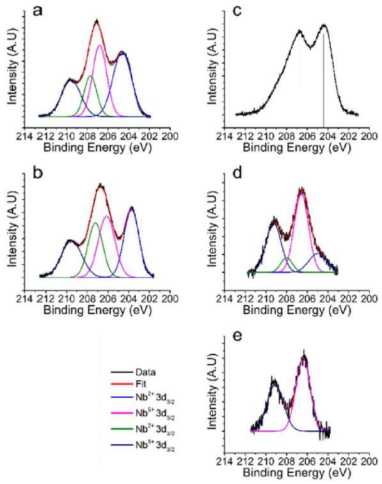

Figure 11. Nb 3d XPS narrow scans obtained from the surface of I625 samples exposed for 1000hr to molten LiCl containing a) 1wt% Li_2O and 0.3wt% Li, b) 1wt% Li_2O and 0.6wt% Li, c) 2wt% Li_2O and 0.3wt% Li, d) 2wt% Li_2O and 0.6wt% Li, and e) 2wt% Li_2O and 1wt% Li. Nb was not observed on the I625 sample exposed to LiCl-1wt% Li_2O-1wt% Li for 1000hr. Nb was observed to be present as Nb^{2+} and Nb^{5+}, however, metallic Nb was not observed.

was not detected on this sample. The presence of only oxidized Nb even in the presence of high Li concentrations is counter intuitive, as work by Jeong, et al. showed that the reduction of Nb_2O_5 to metallic Nb was able to be accomplished in LiCl-Li_2O, primarily through the indirect reaction with Li which was electrolytically generated at the cathode, similar to the reduction of UO_2.[29]

Minor alloying elements, Fe and Al, were not analyzed in this study. The oxide film on the samples exposed to LiCl-Li_2O in the absence of Li did not have detectable quantities of Fe on its surface, however Fe was detected in extremely small quantities on some of the samples exposed to LiCl-Li_2O solutions containing Li. Auger electrons from Ni using the Al Kα source interfered with these peaks, and switching the X-ray source to Mg Kα X-rays did not provide adequate signal intensity to reliably peak fit the Fe 2p spectra. Detection was not consistent from sample to sample. Consequently, interpretation of the Fe 2p spectra was not attempted. Al was not detected on the surface of any sample via XPS, regardless of X-ray source.

Conclusions

Investigation of the surface chemistry of I625 samples exposed to molten LiCl-Li_2O-Li solutions at 650°C for 500 and 1000hr was performed via XRD, Raman spectroscopy, and XPS. In the absence of solvated Li^0, the surface of I625 forms a stable $LiCrO_2$ based surface film with minor inclusions of Li_2CrO_4 and $NiFe_xCr_{2-x}O_4$ which acts to limit corrosion of the base alloy. Corrosion of the base alloy in molten LiCl-Li_2O is thus expected to be dictated by the O^{2-} activity and the presence of impurities, similar to the corrosion processes typical in other molten salt systems.[30] When Li is dissolved in the molten LiCl-Li_2O system, the formation of a bulk oxide film is not possible due to the highly reducing conditions caused by metallic Li; however, XPS analysis showed that the active alloying elements Cr, Mo, and Nb were all present to varying degrees in oxidized states on the sample surfaces, even up to high concentrations of Li in solution. This indicates that there is a synergistic effect between the oxidation caused by the O^{2-} ions and the reducing nature of solvated Li^0 that allows for the effective dissolution of Cr, Mo, and Nb, although further investigation would be necessary to confirm this hypothesis. Our earlier work showed that the alloy was depleted of these elements at the sample surface and in the regions displaying the highly porous microstructure seen via SEM-EDS. Consequently, it is likely that the diffusion of Cr, Mo, and Nb through the alloy microstructure and their subsequent dissolution in to the molten LiCl-Li_2O-Li system is responsible for the porosity observed in that study.

Acknowledgments

This work was performed under the auspices of the Department of Energy (DOE) under contracts DE-NE0008262 and DE-NE0008236, and the US Nuclear Regulatory Commission (USNRC) under contracts NRCHQ-11-G-38-0039 and NRC-HQ-13-G-38-0027. W.P. acknowledges the Fellowship Award from the USNRC. Dr. Kenny Osborne serves as the program manager for the DOE award and Nancy Hebron-Isreal serves as the grants program officer for the NRC awards.

ORCID

William Phillips https://orcid.org/0000-0003-1710-8061
Dev Chidambaram https://orcid.org/0000-0002-3918-3559

References

1. W. Phillips, Z. Karmiol, and D. Chidambaram, *Journal of the Electrochemical Society*, **166**, C162 (2019).
2. S. D. Herrmann, S. X. Li, and M. F. Simpson, in *GLOBAL 2005*, Tsukuba, Japan (2005).
3. A. Merwin, M. A. Williamson, J. L. Willit, and D. Chidambaram, *Journal of the Electrochemical Society*, **164**, H5236 (2017).
4. A. Merwin, W. C. Phillips, M. A. Williamson, J. L. Willit, P. N. Motsegood, and D. Chidambaram, *Scientific Reports*, **6**, 25435 (2016).
5. T. Nakajima, R. Minami, K. Nakanishi, and N. Watanabe, *Bulletin of the Chemical Society of Japan*, **47**, 2071 (1974).
6. M. A. Bredig, *Mixtures of Metals with Molten Salts*, in, United States (1963).
7. A. S. Dworkin, H. R. Bronstein, and M. A. Bredig, *The Journal of Physical Chemistry*, **66**, 572 (1962).
8. J. E. Indacochea, J. L. Smith, K. R. Litko, and E. J. Karell, *Journal of Materials Research*, **14**, 1990 (1999).
9. B. Mishra and D. L. Olson, *Mineral Processing and Extractive Metallurgy Reviews*, **22**, 369 (2001).
10. A. Merwin and D. Chidambaram, *Corrosion Science*, **126**, 1 (2016).
11. A. Merwin and D. Chidambaram, *Nuclear Technology*, **195**, 204 (2016).
12. W. Phillips, A. Merwin, and D. Chidambaram, *Metallurgical and Materials Transactions A*, **49**, 2384 (2018).
13. E.-Y. Choi and J. Lee, *Journal of Nuclear Materials*, **495**, 85 (2017).
14. W. Phillips and D. Chidambaram, *Journal of Nuclear Materials*, **517**, 241 (2019).
15. A. Merwin, Material Interactions with Molten LiCl-Li_2O-Li, in *Materials Science and Engineering*, p. 241, University of Nevada, Reno (2016).
16. N. J. Gese, The Electrochemistry of Li-LiCl-Li2O Molten Salt Systems and the role of Moisture, in *Nuclear Engineering*, University of Idaho (2015).
17. U. Vogel, E. Brachmann, S. Oswald, S. Menzel, T. Gemming, and J. Eckert, *Vacuum*, **117**, 81 (2015).
18. A. Merwin and D. Chidambaram, *Metallurgical and Materials Transactions A*, **46**, 536 (2015).
19. PDF Card No.: 01-072-7839, in, The International Centre for Diffraction Data.
20. W. Phillips, Z. Karmiol, and D. Chidambaram, *Journal of the Electrochemical Society*, **166**, C162 (2019).
21. M. Suzuki, I. Yamada, H. Kadowaki, and F. Takei, *Journal of Physics: Condensed Matter*, **5**, 4225 (1993).
22. B. D. Hosterman, Raman Spectroscopic Study of Solid Solution Spinel Oxides, in *Physics and Astronomy*, p. 155, UNLV (2011).
23. D. Chidambaram, C. R. Clayton, and G. P. Halada, *Journal of the Electrochemical Society*, **150**, B224 (2003).
24. S. H. Cho, J. S. Zhang, Y. J. Shin, S. W. Park, and H. S. Park, *Journal of Nuclear Materials*, **325**, 13 (2004).
25. M. C. Biesinger, B. P. Payne, A. P. Grosvenor, L. W. M. Lau, A. R. Gerson, and R. S. C. Smart, *Applied Surface Science*, **257**, 2717 (2011).
26. B. Brox and I. Olefjord, *Surface and Interface Analysis*, **13**, 3 (1988).
27. J. Baltrusaitis, B. Mendoza-Sanchez, V. Fernandez, R. Veenstra, N. Dukstiene, A. Roberts, and N. Fairley, *Applied Surface Science*, **326**, 151 (2015).
28. Z. P. Hu, Y. P. Li, M. R. Ji, and J. X. Wu, *Solid State Communications*, **71**, 849 (1989).
29. S. M. Jeong, H. Y. Yoo, J.-M. Hur, and C.-S. Seo, *Journal of Alloys and Compounds*, **452**, 27 (2008).
30. T. R. Allen and K. Sridharan, *Corrosion in Molten Salts, in Molten salts chemistry from lab to applications*, Elsevier, Burlington, MA (2013).

Appendix 8 : Copyright Permissions

SPRINGER NATURE LICENSE TERMS AND CONDITIONS

Mar 04, 2019

This Agreement between University of Nevada, Reno -- William Phillips ("You") and Springer Nature ("Springer Nature") consists of your license details and the terms and conditions provided by Springer Nature and Copyright Clearance Center.

The publisher has provided special terms related to this request that can be found at the end of the Publisher's Terms and Conditions.

License Number	4537090276024
License date	Feb 27, 2019
Licensed Content Publisher	Springer Nature
Licensed Content Publication	Journal of Phase Equilibria (and diffusion)
Licensed Content Title	Amendment of the Li-Bi Phase Diagram Crystal and Electronic Structure of Li2Bi
Licensed Content Author	Volodymyr Pavlyuk, Martyn Sozanskyi, Grygoriy Dmytriv et al
Licensed Content Date	Jan 1, 2015
Licensed Content Volume	36
Licensed Content Issue	6
Type of Use	Thesis/Dissertation
Requestor type	academic/university or research institute
Format	electronic
Portion	figures/tables/illustrations
Number of figures/tables/illustrations	1
Will you be translating?	no
Circulation/distribution	<501
Author of this Springer Nature content	no
Title	Degradation of Structural Alloys in LiCl-Li2O-Li
Institution name	n/a
Expected presentation date	May 2019
Portions	Figure 1
Requestor Location	University of Nevada, Reno 1664 N. Virginia St. Mailstop 0388 RENO, NV 89557 United States Attn: University of Nevada, Reno
Billing Type	Invoice
Billing Address	University of Nevada, Reno 1664 N. Virginia St. Mailstop 0388

RENO, NV 89557
United States
Attn: University of Nevada, Reno

Total 0.00 USD

Terms and Conditions

Springer Nature Terms and Conditions for RightsLink Permissions

Springer Nature Customer Service Centre GmbH (the Licensor) hereby grants you a non-exclusive, world-wide licence to reproduce the material and for the purpose and requirements specified in the attached copy of your order form, and for no other use, subject to the conditions below:

1. The Licensor warrants that it has, to the best of its knowledge, the rights to license reuse of this material. However, you should ensure that the material you are requesting is original to the Licensor and does not carry the copyright of another entity (as credited in the published version).

   If the credit line on any part of the material you have requested indicates that it was reprinted or adapted with permission from another source, then you should also seek permission from that source to reuse the material.

2. Where **print only** permission has been granted for a fee, separate permission must be obtained for any additional electronic re-use.

3. Permission granted **free of charge** for material in print is also usually granted for any electronic version of that work, provided that the material is incidental to your work as a whole and that the electronic version is essentially equivalent to, or substitutes for, the print version.

4. A licence for 'post on a website' is valid for 12 months from the licence date. This licence does not cover use of full text articles on websites.

5. Where **'reuse in a dissertation/thesis'** has been selected the following terms apply: Print rights of the final author's accepted manuscript (for clarity, NOT the published version) for up to 100 copies, electronic rights for use only on a personal website or institutional repository as defined by the Sherpa guideline (www.sherpa.ac.uk/romeo/).

6. Permission granted for books and journals is granted for the lifetime of the first edition and does not apply to second and subsequent editions (except where the first edition permission was granted free of charge or for signatories to the STM Permissions Guidelines http://www.stm-assoc.org/copyright-legal-affairs/permissions/permissions-guidelines/), and does not apply for editions in other languages unless additional translation rights have been granted separately in the licence.

7. Rights for additional components such as custom editions and derivatives require additional permission and may be subject to an additional fee. Please apply to Journalpermissions@springernature.com/bookpermissions@springernature.com for these rights.

8. The Licensor's permission must be acknowledged next to the licensed material in print. In electronic form, this acknowledgement must be visible at the same time as the figures/tables/illustrations or abstract, and must be hyperlinked to the journal/book's homepage. Our required acknowledgement format is in the Appendix below.

9. Use of the material for incidental promotional use, minor editing privileges (this does not include cropping, adapting, omitting material or any other changes that affect the meaning, intention or moral rights of the author) and copies for the disabled are permitted under this licence.

10. Minor adaptations of single figures (changes of format, colour and style) do not require the Licensor's approval. However, the adaptation should be credited as shown in Appendix below.

Appendix — Acknowledgements:

For Journal Content:
Reprinted by permission from [**the Licensor**]: [**Journal Publisher** (e.g. Nature/Springer/Palgrave)] [**JOURNAL NAME**] [**REFERENCE CITATION** (Article name, Author(s) Name), [**COPYRIGHT**] (year of publication)

For **Advance Online Publication papers:**
Reprinted by permission from [**the Licensor**]: [**Journal Publisher** (e.g. Nature/Springer/Palgrave)] [**JOURNAL NAME**] [**REFERENCE CITATION** (Article name, Author(s) Name), [**COPYRIGHT**] (year of publication), advance online publication, day month year (doi: 10.1038/sj.[JOURNAL ACRONYM].)

For Adaptations/Translations:
Adapted/Translated by permission from [**the Licensor**]: [**Journal Publisher** (e.g. Nature/Springer/Palgrave)] [**JOURNAL NAME**] [**REFERENCE CITATION** (Article name, Author(s) Name), [**COPYRIGHT**] (year of publication)

Note: For any republication from the British Journal of Cancer, the following credit line style applies:

Reprinted/adapted/translated by permission from [**the Licensor**]: on behalf of Cancer Research UK: : [**Journal Publisher** (e.g. Nature/Springer/Palgrave)] [**JOURNAL NAME**] [**REFERENCE CITATION** (Article name, Author(s) Name), [**COPYRIGHT**] (year of publication)

For **Advance Online Publication** papers:
Reprinted by permission from The [**the Licensor**]: on behalf of Cancer Research UK: [**Journal Publisher** (e.g. Nature/Springer/Palgrave)] [**JOURNAL NAME**] [**REFERENCE CITATION** (Article name, Author(s) Name), [**COPYRIGHT**] (year of publication), advance online publication, day month year (doi: 10.1038/sj.[JOURNAL ACRONYM])

For Book content:
Reprinted/adapted by permission from [**the Licensor**]: [**Book Publisher** (e.g. Palgrave Macmillan, Springer etc) [**Book Title**] by [**Book author**(s)] [**COPYRIGHT**] (year of publication)

Other Conditions: requestor will advise the society in writing and in advance of the exercise of any of the foregoing rights ASM International (ASM) Mr. Stanley C. Theobald, Managing Director, 9639 Kinsman Road Materials Park, OH 44073-002, USA; e-mail: stan.theobald@asminternational.org

Version 1.1

ELSEVIER LICENSE
TERMS AND CONDITIONS

Mar 04, 2019

This Agreement between University of Nevada, Reno -- William Phillips ("You") and Elsevier ("Elsevier") consists of your license details and the terms and conditions provided by Elsevier and Copyright Clearance Center.

License Number	4536740291252
License date	Feb 26, 2019
Licensed Content Publisher	Elsevier
Licensed Content Publication	Calphad
Licensed Content Title	Thermodynamic description of Cu–Mg–Ni and Cu–Mg–Zn systems
Licensed Content Author	Jyrki Miettinen
Licensed Content Date	Jun 1, 2008
Licensed Content Volume	32
Licensed Content Issue	2
Licensed Content Pages	10
Start Page	389
End Page	398
Type of Use	reuse in a thesis/dissertation
Portion	figures/tables/illustrations
Number of figures/tables/illustrations	1
Format	electronic
Are you the author of this Elsevier article?	No
Will you be translating?	No
Original figure numbers	Figure 1
Title of your thesis/dissertation	Degradation of Structural Alloys in LiCl-Li2O-Li
Expected completion date	May 2019
Estimated size (number of pages)	171
Requestor Location	University of Nevada, Reno 1664 N. Virginia St. Mailstop 0388 RENO, NV 89557 United States Attn: University of Nevada, Reno
Publisher Tax ID	98-0397604
Total	0.00 USD
Terms and Conditions	

INTRODUCTION

1. The publisher for this copyrighted material is Elsevier. By clicking "accept" in connection with completing this licensing transaction, you agree that the following terms and conditions apply to this transaction (along with the Billing and Payment terms and conditions established by Copyright Clearance Center, Inc. ("CCC"), at the time that you opened your Rightslink account and that are available at any time at http://myaccount.copyright.com).

GENERAL TERMS

2. Elsevier hereby grants you permission to reproduce the aforementioned material subject to the terms and conditions indicated.
3. Acknowledgement: If any part of the material to be used (for example, figures) has appeared in our publication with credit or acknowledgement to another source, permission must also be sought from that source. If such permission is not obtained then that material may not be included in your publication/copies. Suitable acknowledgement to the source must be made, either as a footnote or in a reference list at the end of your publication, as follows:
"Reprinted from Publication title, Vol /edition number, Author(s), Title of article / title of chapter, Pages No., Copyright (Year), with permission from Elsevier [OR APPLICABLE SOCIETY COPYRIGHT OWNER]." Also Lancet special credit - "Reprinted from The Lancet, Vol. number, Author(s), Title of article, Pages No., Copyright (Year), with permission from Elsevier."
4. Reproduction of this material is confined to the purpose and/or media for which permission is hereby given.
5. Altering/Modifying Material: Not Permitted. However figures and illustrations may be altered/adapted minimally to serve your work. Any other abbreviations, additions, deletions and/or any other alterations shall be made only with prior written authorization of Elsevier Ltd. (Please contact Elsevier at permissions@elsevier.com). No modifications can be made to any Lancet figures/tables and they must be reproduced in full.
6. If the permission fee for the requested use of our material is waived in this instance, please be advised that your future requests for Elsevier materials may attract a fee.
7. Reservation of Rights: Publisher reserves all rights not specifically granted in the combination of (i) the license details provided by you and accepted in the course of this licensing transaction, (ii) these terms and conditions and (iii) CCC's Billing and Payment terms and conditions.
8. License Contingent Upon Payment: While you may exercise the rights licensed immediately upon issuance of the license at the end of the licensing process for the transaction, provided that you have disclosed complete and accurate details of your proposed use, no license is finally effective unless and until full payment is received from you (either by publisher or by CCC) as provided in CCC's Billing and Payment terms and conditions. If full payment is not received on a timely basis, then any license preliminarily granted shall be deemed automatically revoked and shall be void as if never granted. Further, in the event that you breach any of these terms and conditions or any of CCC's Billing and Payment terms and conditions, the license is automatically revoked and shall be void as if never granted. Use of materials as described in a revoked license, as well as any use of the materials beyond the scope of an unrevoked license, may constitute copyright infringement and publisher reserves the right to take any and all action to protect its copyright in the materials.
9. Warranties: Publisher makes no representations or warranties with respect to the licensed material.
10. Indemnity: You hereby indemnify and agree to hold harmless publisher and CCC, and their respective officers, directors, employees and agents, from and against any and all claims arising out of your use of the licensed material other than as specifically authorized pursuant to this license.
11. No Transfer of License: This license is personal to you and may not be sublicensed, assigned, or transferred by you to any other person without publisher's written permission.

12. No Amendment Except in Writing: This license may not be amended except in a writing signed by both parties (or, in the case of publisher, by CCC on publisher's behalf).
13. Objection to Contrary Terms: Publisher hereby objects to any terms contained in any purchase order, acknowledgment, check endorsement or other writing prepared by you, which terms are inconsistent with these terms and conditions or CCC's Billing and Payment terms and conditions. These terms and conditions, together with CCC's Billing and Payment terms and conditions (which are incorporated herein), comprise the entire agreement between you and publisher (and CCC) concerning this licensing transaction. In the event of any conflict between your obligations established by these terms and conditions and those established by CCC's Billing and Payment terms and conditions, these terms and conditions shall control.
14. Revocation: Elsevier or Copyright Clearance Center may deny the permissions described in this License at their sole discretion, for any reason or no reason, with a full refund payable to you. Notice of such denial will be made using the contact information provided by you. Failure to receive such notice will not alter or invalidate the denial. In no event will Elsevier or Copyright Clearance Center be responsible or liable for any costs, expenses or damage incurred by you as a result of a denial of your permission request, other than a refund of the amount(s) paid by you to Elsevier and/or Copyright Clearance Center for denied permissions.

LIMITED LICENSE

The following terms and conditions apply only to specific license types:
15. **Translation**: This permission is granted for non-exclusive world **English** rights only unless your license was granted for translation rights. If you licensed translation rights you may only translate this content into the languages you requested. A professional translator must perform all translations and reproduce the content word for word preserving the integrity of the article.
16. **Posting licensed content on any Website**: The following terms and conditions apply as follows: Licensing material from an Elsevier journal: All content posted to the web site must maintain the copyright information line on the bottom of each image; A hyper-text must be included to the Homepage of the journal from which you are licensing at http://www.sciencedirect.com/science/journal/xxxxx or the Elsevier homepage for books at http://www.elsevier.com; Central Storage: This license does not include permission for a scanned version of the material to be stored in a central repository such as that provided by Heron/XanEdu.
Licensing material from an Elsevier book: A hyper-text link must be included to the Elsevier homepage at http://www.elsevier.com . All content posted to the web site must maintain the copyright information line on the bottom of each image.

Posting licensed content on Electronic reserve: In addition to the above the following clauses are applicable: The web site must be password-protected and made available only to bona fide students registered on a relevant course. This permission is granted for 1 year only. You may obtain a new license for future website posting.
17. **For journal authors:** the following clauses are applicable in addition to the above:
Preprints:
A preprint is an author's own write-up of research results and analysis, it has not been peer-reviewed, nor has it had any other value added to it by a publisher (such as formatting, copyright, technical enhancement etc.).
Authors can share their preprints anywhere at any time. Preprints should not be added to or enhanced in any way in order to appear more like, or to substitute for, the final versions of articles however authors can update their preprints on arXiv or RePEc with their Accepted Author Manuscript (see below).
If accepted for publication, we encourage authors to link from the preprint to their formal publication via its DOI. Millions of researchers have access to the formal publications on ScienceDirect, and so links will help users to find, access, cite and use the best available

version. Please note that Cell Press, The Lancet and some society-owned have different preprint policies. Information on these policies is available on the journal homepage.
Accepted Author Manuscripts: An accepted author manuscript is the manuscript of an article that has been accepted for publication and which typically includes author-incorporated changes suggested during submission, peer review and editor-author communications.
Authors can share their accepted author manuscript:

- immediately
  - via their non-commercial person homepage or blog
  - by updating a preprint in arXiv or RePEc with the accepted manuscript
  - via their research institute or institutional repository for internal institutional uses or as part of an invitation-only research collaboration work-group
  - directly by providing copies to their students or to research collaborators for their personal use
  - for private scholarly sharing as part of an invitation-only work group on commercial sites with which Elsevier has an agreement
- After the embargo period
  - via non-commercial hosting platforms such as their institutional repository
  - via commercial sites with which Elsevier has an agreement

In all cases accepted manuscripts should:

- link to the formal publication via its DOI
- bear a CC-BY-NC-ND license - this is easy to do
- if aggregated with other manuscripts, for example in a repository or other site, be shared in alignment with our hosting policy not be added to or enhanced in any way to appear more like, or to substitute for, the published journal article.

Published journal article (JPA): A published journal article (PJA) is the definitive final record of published research that appears or will appear in the journal and embodies all value-adding publishing activities including peer review co-ordination, copy-editing, formatting, (if relevant) pagination and online enrichment.
Policies for sharing publishing journal articles differ for subscription and gold open access articles:
Subscription Articles: If you are an author, please share a link to your article rather than the full-text. Millions of researchers have access to the formal publications on ScienceDirect, and so links will help your users to find, access, cite, and use the best available version.
Theses and dissertations which contain embedded PJAs as part of the formal submission can be posted publicly by the awarding institution with DOI links back to the formal publications on ScienceDirect.
If you are affiliated with a library that subscribes to ScienceDirect you have additional private sharing rights for others' research accessed under that agreement. This includes use for classroom teaching and internal training at the institution (including use in course packs and courseware programs), and inclusion of the article for grant funding purposes.
Gold Open Access Articles: May be shared according to the author-selected end-user license and should contain a CrossMark logo, the end user license, and a DOI link to the formal publication on ScienceDirect.
Please refer to Elsevier's posting policy for further information.
18. **For book authors** the following clauses are applicable in addition to the above:
Authors are permitted to place a brief summary of their work online only. You are not allowed to download and post the published electronic version of your chapter, nor may you scan the printed edition to create an electronic version. **Posting to a repository:** Authors are permitted to post a summary of their chapter only in their institution's repository.

19. **Thesis/Dissertation**: If your license is for use in a thesis/dissertation your thesis may be submitted to your institution in either print or electronic form. Should your thesis be published commercially, please reapply for permission. These requirements include permission for the Library and Archives of Canada to supply single copies, on demand, of the complete thesis and include permission for Proquest/UMI to supply single copies, on demand, of the complete thesis. Should your thesis be published commercially, please reapply for permission. Theses and dissertations which contain embedded PJAs as part of the formal submission can be posted publicly by the awarding institution with DOI links back to the formal publications on ScienceDirect.

Elsevier Open Access Terms and Conditions

You can publish open access with Elsevier in hundreds of open access journals or in nearly 2000 established subscription journals that support open access publishing. Permitted third party re-use of these open access articles is defined by the author's choice of Creative Commons user license. See our open access license policy for more information.

Terms & Conditions applicable to all Open Access articles published with Elsevier:

Any reuse of the article must not represent the author as endorsing the adaptation of the article nor should the article be modified in such a way as to damage the author's honour or reputation. If any changes have been made, such changes must be clearly indicated.

The author(s) must be appropriately credited and we ask that you include the end user license and a DOI link to the formal publication on ScienceDirect.

If any part of the material to be used (for example, figures) has appeared in our publication with credit or acknowledgement to another source it is the responsibility of the user to ensure their reuse complies with the terms and conditions determined by the rights holder.

Additional Terms & Conditions applicable to each Creative Commons user license:

CC BY: The CC-BY license allows users to copy, to create extracts, abstracts and new works from the Article, to alter and revise the Article and to make commercial use of the Article (including reuse and/or resale of the Article by commercial entities), provided the user gives appropriate credit (with a link to the formal publication through the relevant DOI), provides a link to the license, indicates if changes were made and the licensor is not represented as endorsing the use made of the work. The full details of the license are available at http://creativecommons.org/licenses/by/4.0.

CC BY NC SA: The CC BY-NC-SA license allows users to copy, to create extracts, abstracts and new works from the Article, to alter and revise the Article, provided this is not done for commercial purposes, and that the user gives appropriate credit (with a link to the formal publication through the relevant DOI), provides a link to the license, indicates if changes were made and the licensor is not represented as endorsing the use made of the work. Further, any new works must be made available on the same conditions. The full details of the license are available at http://creativecommons.org/licenses/by-nc-sa/4.0.

CC BY NC ND: The CC BY-NC-ND license allows users to copy and distribute the Article, provided this is not done for commercial purposes and further does not permit distribution of the Article if it is changed or edited in any way, and provided the user gives appropriate credit (with a link to the formal publication through the relevant DOI), provides a link to the license, and that the licensor is not represented as endorsing the use made of the work. The full details of the license are available at http://creativecommons.org/licenses/by-nc-nd/4.0.

Any commercial reuse of Open Access articles published with a CC BY NC SA or CC BY NC ND license requires permission from Elsevier and will be subject to a fee.

Commercial reuse includes:

- Associating advertising with the full text of the Article
- Charging fees for document delivery or access
- Article aggregation
- Systematic distribution via e-mail lists or share buttons

Posting or linking by commercial companies for use by customers of those companies.

20. **Other Conditions**:

v1.9

Questions? customercare@copyright.com or +1-855-239-3415 (toll free in the US) or +1-978-646-2777.

JOHN WILEY AND SONS LICENSE TERMS AND CONDITIONS

Mar 04, 2019

This Agreement between University of Nevada, Reno -- William Phillips ("You") and John Wiley and Sons ("John Wiley and Sons") consists of your license details and the terms and conditions provided by John Wiley and Sons and Copyright Clearance Center.

License Number	4542040161607
License date	Mar 04, 2019
Licensed Content Publisher	John Wiley and Sons
Licensed Content Publication	Journal of the American Ceramic Society
Licensed Content Title	Compatibility of Ceramics with Liquid Na and Li
Licensed Content Author	R. N. SINGH
Licensed Content Date	Jun 2, 2006
Licensed Content Volume	59
Licensed Content Issue	3-4
Licensed Content Pages	4
Type of use	Dissertation/Thesis
Requestor type	University/Academic
Format	Electronic
Portion	Figure/table
Number of figures/tables	1
Original Wiley figure/table number(s)	Figure 2 Calculated themodynamic Lithium-Ceramic stability diagram
Will you be translating?	No
Title of your thesis / dissertation	Degradation of Structural Alloys in LiCl-Li2O-Li
Expected completion date	May 2019
Expected size (number of pages)	171
Requestor Location	University of Nevada, Reno 1664 N. Virginia St. Mailstop 0388 RENO, NV 89557 United States Attn: University of Nevada, Reno
Publisher Tax ID	EU826007151
Total	0.00 USD
Terms and Conditions	

TERMS AND CONDITIONS

This copyrighted material is owned by or exclusively licensed to John Wiley & Sons, Inc. or one of its group companies (each a"Wiley Company") or handled on behalf of a society with which a Wiley Company has exclusive publishing rights in relation to a particular work

(collectively "WILEY"). By clicking "accept" in connection with completing this licensing transaction, you agree that the following terms and conditions apply to this transaction (along with the billing and payment terms and conditions established by the Copyright Clearance Center Inc., ("CCC's Billing and Payment terms and conditions"), at the time that you opened your RightsLink account (these are available at any time at http://myaccount.copyright.com).

Terms and Conditions

- The materials you have requested permission to reproduce or reuse (the "Wiley Materials") are protected by copyright.

- You are hereby granted a personal, non-exclusive, non-sub licensable (on a stand-alone basis), non-transferable, worldwide, limited license to reproduce the Wiley Materials for the purpose specified in the licensing process. This license, **and any CONTENT (PDF or image file) purchased as part of your order,** is for a one-time use only and limited to any maximum distribution number specified in the license. The first instance of republication or reuse granted by this license must be completed within two years of the date of the grant of this license (although copies prepared before the end date may be distributed thereafter). The Wiley Materials shall not be used in any other manner or for any other purpose, beyond what is granted in the license. Permission is granted subject to an appropriate acknowledgement given to the author, title of the material/book/journal and the publisher. You shall also duplicate the copyright notice that appears in the Wiley publication in your use of the Wiley Material. Permission is also granted on the understanding that nowhere in the text is a previously published source acknowledged for all or part of this Wiley Material. Any third party content is expressly excluded from this permission.

- With respect to the Wiley Materials, all rights are reserved. Except as expressly granted by the terms of the license, no part of the Wiley Materials may be copied, modified, adapted (except for minor reformatting required by the new Publication), translated, reproduced, transferred or distributed, in any form or by any means, and no derivative works may be made based on the Wiley Materials without the prior permission of the respective copyright owner.**For STM Signatory Publishers clearing permission under the terms of the STM Permissions Guidelines only, the terms of the license are extended to include subsequent editions and for editions in other languages, provided such editions are for the work as a whole in situ and does not involve the separate exploitation of the permitted figures or extracts,** You may not alter, remove or suppress in any manner any copyright, trademark or other notices displayed by the Wiley Materials. You may not license, rent, sell, loan, lease, pledge, offer as security, transfer or assign the Wiley Materials on a stand-alone basis, or any of the rights granted to you hereunder to any other person.

- The Wiley Materials and all of the intellectual property rights therein shall at all times remain the exclusive property of John Wiley & Sons Inc, the Wiley Companies, or their respective licensors, and your interest therein is only that of having possession of and the right to reproduce the Wiley Materials pursuant to Section 2 herein during the continuance of this Agreement. You agree that you own no right, title or interest in or to the Wiley Materials or any of the intellectual property rights therein. You shall have no rights hereunder other than the license as provided for above in Section 2. No right, license or interest to any trademark, trade name, service mark or other branding ("Marks") of WILEY or its licensors is granted hereunder, and you agree that you shall not assert any such right, license or interest with respect thereto

- NEITHER WILEY NOR ITS LICENSORS MAKES ANY WARRANTY OR REPRESENTATION OF ANY KIND TO YOU OR ANY THIRD PARTY, EXPRESS, IMPLIED OR STATUTORY, WITH RESPECT TO THE MATERIALS OR THE ACCURACY OF ANY INFORMATION CONTAINED IN THE MATERIALS, INCLUDING, WITHOUT LIMITATION, ANY IMPLIED WARRANTY OF MERCHANTABILITY, ACCURACY, SATISFACTORY QUALITY, FITNESS FOR A PARTICULAR PURPOSE, USABILITY, INTEGRATION OR NON-INFRINGEMENT AND ALL SUCH WARRANTIES ARE HEREBY EXCLUDED BY WILEY AND ITS LICENSORS AND WAIVED BY YOU.

- WILEY shall have the right to terminate this Agreement immediately upon breach of this Agreement by you.

- You shall indemnify, defend and hold harmless WILEY, its Licensors and their respective directors, officers, agents and employees, from and against any actual or threatened claims, demands, causes of action or proceedings arising from any breach of this Agreement by you.

- IN NO EVENT SHALL WILEY OR ITS LICENSORS BE LIABLE TO YOU OR ANY OTHER PARTY OR ANY OTHER PERSON OR ENTITY FOR ANY SPECIAL, CONSEQUENTIAL, INCIDENTAL, INDIRECT, EXEMPLARY OR PUNITIVE DAMAGES, HOWEVER CAUSED, ARISING OUT OF OR IN CONNECTION WITH THE DOWNLOADING, PROVISIONING, VIEWING OR USE OF THE MATERIALS REGARDLESS OF THE FORM OF ACTION, WHETHER FOR BREACH OF CONTRACT, BREACH OF WARRANTY, TORT, NEGLIGENCE, INFRINGEMENT OR OTHERWISE (INCLUDING, WITHOUT LIMITATION, DAMAGES BASED ON LOSS OF PROFITS, DATA, FILES, USE, BUSINESS OPPORTUNITY OR CLAIMS OF THIRD PARTIES), AND WHETHER OR NOT THE PARTY HAS BEEN ADVISED OF THE POSSIBILITY OF SUCH DAMAGES. THIS LIMITATION SHALL APPLY NOTWITHSTANDING ANY FAILURE OF ESSENTIAL PURPOSE OF ANY LIMITED REMEDY PROVIDED HEREIN.

- Should any provision of this Agreement be held by a court of competent jurisdiction to be illegal, invalid, or unenforceable, that provision shall be deemed amended to achieve as nearly as possible the same economic effect as the original provision, and the legality, validity and enforceability of the remaining provisions of this Agreement shall not be affected or impaired thereby.

- The failure of either party to enforce any term or condition of this Agreement shall not constitute a waiver of either party's right to enforce each and every term and condition of this Agreement. No breach under this agreement shall be deemed waived or excused by either party unless such waiver or consent is in writing signed by the party granting such waiver or consent. The waiver by or consent of a party to a breach of any provision of this Agreement shall not operate or be construed as a waiver of or consent to any other or subsequent breach by such other party.

- This Agreement may not be assigned (including by operation of law or otherwise) by you without WILEY's prior written consent.

- Any fee required for this permission shall be non-refundable after thirty (30) days from receipt by the CCC.

- These terms and conditions together with CCC's Billing and Payment terms and conditions (which are incorporated herein) form the entire agreement between you and WILEY concerning this licensing transaction and (in the absence of fraud) supersedes all prior agreements and representations of the parties, oral or written. This Agreement may not be amended except in writing signed by both parties. This Agreement shall be binding upon and inure to the benefit of the parties' successors, legal representatives, and authorized assigns.

- In the event of any conflict between your obligations established by these terms and conditions and those established by CCC's Billing and Payment terms and conditions, these terms and conditions shall prevail.

- WILEY expressly reserves all rights not specifically granted in the combination of (i) the license details provided by you and accepted in the course of this licensing transaction, (ii) these terms and conditions and (iii) CCC's Billing and Payment terms and conditions.

- This Agreement will be void if the Type of Use, Format, Circulation, or Requestor Type was misrepresented during the licensing process.

- This Agreement shall be governed by and construed in accordance with the laws of the State of New York, USA, without regards to such state's conflict of law rules. Any legal action, suit or proceeding arising out of or relating to these Terms and Conditions or the breach thereof shall be instituted in a court of competent jurisdiction in New York County in the State of New York in the United States of America and each party hereby consents and submits to the personal jurisdiction of such court, waives any objection to venue in such court and consents to service of process by registered or certified mail, return receipt requested, at the last known address of such party.

WILEY OPEN ACCESS TERMS AND CONDITIONS

Wiley Publishes Open Access Articles in fully Open Access Journals and in Subscription journals offering Online Open. Although most of the fully Open Access journals publish open access articles under the terms of the Creative Commons Attribution (CC BY) License only, the subscription journals and a few of the Open Access Journals offer a choice of Creative Commons Licenses. The license type is clearly identified on the article.

The Creative Commons Attribution License

The Creative Commons Attribution License (CC-BY) allows users to copy, distribute and transmit an article, adapt the article and make commercial use of the article. The CC-BY license permits commercial and non-

Creative Commons Attribution Non-Commercial License

The Creative Commons Attribution Non-Commercial (CC-BY-NC)License permits use, distribution and reproduction in any medium, provided the original work is properly cited and is not used for commercial purposes.(see below)

Creative Commons Attribution-Non-Commercial-NoDerivs License

The Creative Commons Attribution Non-Commercial-NoDerivs License (CC-BY-NC-ND) permits use, distribution and reproduction in any medium, provided the original work is properly cited, is not used for commercial purposes and no modifications or adaptations are made. (see below)

Use by commercial "for-profit" organizations

Use of Wiley Open Access articles for commercial, promotional, or marketing purposes requires further explicit permission from Wiley and will be subject to a fee.

Further details can be found on Wiley Online Library
http://olabout.wiley.com/WileyCDA/Section/id-410895.html

Other Terms and Conditions:

v1.10 Last updated September 2015

Questions? customercare@copyright.com or +1-855-239-3415 (toll free in the US) or +1-978-646-2777.